Electronic Structures of Perfunctionalized Dodecaborate Clusters

Thesis by

L. Josef Schwan

In Partial Fulfillment of the Requirements for
the degree of
Doctor of Philosophy

CALIFORNIA INSTITUTE OF TECHNOLOGY
Pasadena, California

2020
(Defended March 5, 2020)

To my father

ACKNOWLEDGEMENTS

First and foremost, I want to thank Harry Gray for his encouragement and unwavering support. Under his mentorship I have enjoyed near limitless freedom to pursue my own path and to discover what it means to be a truly independent scientist. Harry is always accessible and happy to help, both in and out of the lab. He is glad to talk on a moment's notice, and I have never had to wait for more than a day or two to get his comments on drafts and new data. He truly makes his students and post-docs the top priority. I could not imagine a better advisor. I also want to thank Jay Winkler, who in many ways is the scientific engine of the lab. His uncanny ability to pick apart problems and make complex relationships seem simple has been invaluable throughout my studies. Nate Lewis deserves my gratitude for being my formal co-advisor, even as I scientifically drifted far away from the Lewis lab. Nate and his group have continued to welcome me, and I have appreciated partaking in many social events with the Lewis group.

I am likewise grateful to the members of my thesis committee. Doug Rees, my committee chair, has been incredibly supportive and willing to offer his advice on the big picture questions. He was a great collaborator during the initial two years of my graduate studies, when I attempted to develop methods for investigating the mechanism of nitrogenase enzymes using flash-quench techniques. Sarah Reisman has been a great help in answering complex organic chemistry questions and giving perspective on how our work on photoredox catalysts relates to the needs of the organic chemistry community. I also appreciate that she made sure to push the difficult questions during committee meetings. Bob Grubbs, who was the final addition to my committee, offered valuable help in identifying career opportunities and in making connections outside of the academic environment. The support of Doug, Sarah and Bob has been instrumental in getting me to where I am today and finding my path post-Caltech.

I could not have gotten through my graduate work without the help of my friends in the Gray lab. In particular, I want to thank Wes Kramer, Brian Sanders, Brendon McNicholas, Jillian Clinton, Brad Brennan and Javier Fajardo, who have been my greatest friends and supporters during my time at Caltech. Brad was my lab and office mate during my first year and a fantastic mentor throughout that period. He helped me get settled in the lab and pushed me to find direction in my work. Brendon's support during my second year was key in building momentum in my research. I am also indebted to him for assisting last year, when I was struggling doing work in the lab due to health issues. I am thankful to Brian for mentoring me in the biochemistry lab while I was exploring nitrogenase enzymes, and for always being happy to assist in the laser lab. His calm presence provided refuge from the stressful reality of graduate school. Wes led the work on group 6 metal arylisocyanides, which was for a long time my main thesis project. Under his guidance I grew into a confident synthetic inorganic chemist and the independent scientist I am today. Javier was a great contributor and supporter during the later stages of my engagement in the metal arylisocyanide project and took over after I moved on to focus on the work presented in this thesis. It has been a pleasure to watch all the amazing research he has done over the past year. Jill has been a beacon of energy in the lab, and I am forever grateful for her support and for making our lab the fun and happy place it is today. I too owe thanks to all the other members of the Gray lab who have helped and supported me over the years (in no particular order): Sarah Del Ciello, Oliver Shafaat, Bryan Hunter, James Blakemore, Julian West, Katharina Brinkert, Patrycja Kielb, Dana Levine, Carl Blumenfeld, Emmanuelle Despagnet-Ayoub, Tony Vlcek, Jieun Shin, Astrid Mueller, Michelle DeBoever, and Michael Lichterman. I also want to thank two fantastic undergraduate researchers, Damien Berube and Joseph Schneider, who worked for me on the group 6 metal arylisocyanide project. Mentoring them was among enjoyable things I did at Caltech. Joseph helped develop synthetic schemes for naphthylisocyanides, while Damien worked on mixed carbonyl-arylisocyanide complexes. Their energy in the lab was a great inspiration.

During my time at Caltech I have sought out several collaborative projects. I am indebted to all my collaborators outside of the Gray lab. Most notably, I want to extend my gratitude to Alex Spokoyny at UCLA and his post-docs Jon Axtell and Julia Stauber. Alex, Jon and Julia have been key participants in developing this thesis. The Spokoyny lab developed the perfunctionalized dodecaborate clusters I explored and did all synthetic work. They have always been accessible and happy to provide compounds and assistance. Working with Alex and his group has been an amazing experience. I also owe gratitude to Christine Morrison from the Rees lab for all her encouragement and help while I was working on nitrogenase enzymes, and for Amylynn Chen, Andrey Vyatskikh and Julia Greer from the Greer lab who made reality out of my vision to use tungsten arylisocyanide complexes as two-photon lithography absorbers.

I am thankful to all the staff scientists and administrators who we depend on to keep Caltech running. Paul Oyala deserves special mention—his assistance with EPR experiments and interpretation has been a key part of my thesis research. He has also been a great friend over the past years. I additionally want to thank Mike Takase and Larry Henling who run the X-ray crystallography facility (special shout out to Larry for all the hours we have spent chatting in the Beckman Institute break room), Mona Shahgoli at the mass spec lab and Dave Vander Velde who supervises the NMR facility. They have all been incredibly helpful—always happy to assist with experiments and to discuss data. I am grateful to Rick Jackson, our group administrator, for taking care of us—his snack cabinet has saved me during many long nights in the lab. I also want to thank Siddharth Dasgupta, Alison Ross, Pat Andersson, Barbara Miralles, Kimberly Papadantonaki, Daniel Yoder, Laura Flower Kim, as well as everyone in the Graduate Office. They have all played important roles in helping me get through my studies without any administrative hiccups.

Beyond the scientific community around Caltech, I want to mention some of the people who helped me find my way to Caltech and provided personal support during my time here. First of all, I want to thank my mother for encouraging and supporting me, even when I spent my early twenties with no high school degree working in bars. She has visited me many times over the past few years and helped me remain connected to my roots. I want to thank my father, who regrettably passed away many years ago, for awakening my curiosity and inspiring me to question authority and ask challenging questions. My grandmother and my uncle Åke deserve special mention. Even though she is now 90, my grandmother twice made it out to visit California for Christmas and my thirtieth birthday. Åke has been a great supporter and has kept me updated on all that's ongoing back in Sweden.

Furthermore, I want to thank those who aided me during my undergraduate studies. Most importantly, I am forever grateful to Professors Leif Hammarström and Tomas Edvinsson at Uppsala University, who let me into their labs and gave me my first experiences with chemistry and chemical physics research. The graduate students and post-docs who guided me during my undergraduate research also deserve credit—Mohammad Mirmohades, Jesper Jacobsson and Starla Glover where both good friends and fantastic mentors. I am also grateful to my friends from the Chemical Engineering program: Erik Bamford, David Jonsson, Andreas Bengtsson, Daniel Hedbom and Emil Olsson. We spent countless hours studying and solving problems together and without their support I would have never gotten to where I am today.

Finally, I am eternally grateful to my amazing girlfriend Courtney who has supported and pushed me through the final stages of my graduate studies. Having her by my side allowed me to approach my work with confidence and stay calm during stressful periods. The structure and motivation she has brought to my life has been invaluable—without her I would have undoubtedly needed an additional year (or two) to finish this thesis.

ABSTRACT

This thesis summaries my exploration of hypoelectronic aryloxy-perfunctionalized dodecaborate clusters ([$B_{12}(OR)_{12}$]). *Closo*-dodecaborate (*closo*-[$B_{12}H_{12}$]$^{2-}$) is only stable as a dianionic closed-shell species. However, some perfunctionalized dodecaborate clusters can be isolated in hypoelectronic oxidation states, such as *hypocloso*-[$B_{12}(OR)_{12}$]$^{1-}$ and *hypercloso*-$B_{12}(OR)_{12}$ (R = alkyl or aryl). Depopulation of the [$B_{12}(OR)_{12}$] highest occupied molecular orbital (HOMO) give rise to strong visible absorption bands, which has opened up for their use as photoredox reagents. Furthermore, their inert nature and highly reversible redox behavior has inspired applications in charge–storage devices and as dopants in conducting polymers.

The work presented in Chapters 2–4 were part of a broad collaborative effort lead by Professor Alexander M. Spokoyny (University of California, Los Angeles). Chapter 2 discusses my early contributions, which aimed to spectroscopically investigate the photoredox properties of aryloxy-perfunctionalized *hypercloso*-$B_{12}(OR)_{12}$ clusters. Obtaining reliable photophysical data proved exceedingly difficult, due to formation of *hypercloso*-[$B_{12}(OR)_{12}$]$^{1-}$, disproportionation and solvent-cluster interactions. Chapter 2 summarizes discoveries made while attempting to understand these issues, as well as the final luminescence data collected for *hypercloso*-$B_{12}(OR)_{12}$ and *hypercloso*-[$B_{12}(OR)_{12}$]$^{1-}$ clusters. Much of the discussion is speculative, but we felt it should be published here so that other researchers can learn from our struggles.

Given the issues we had with photophysical characterization of the aryloxy-perfunctionalized clusters discussed in Chapter 2, we turned our attention to the alkyloxy-perfunctionalized analogues, which we hoped would be more amenable to spectroscopic characterization. These clusters did not help our investigation of the photoredox behavior, however, while electrochemically characterizing [$B_{12}(OEt)_{12}$] (Et = C_2H_5) we discovered a third reversible oxidation wave, corresponding to the [$B_{12}(OEt)_{12}$]$^{1+/0}$ couple. Chapter 3 discusses this discovery and the characterization of super-oxidized [$B_{12}(OR)$]$^{1+}$ clusters.

Up until now, electronic structure descriptions of hypoelectronic dodecaborate clusters have been largely limited to computational work. Attempts to access the distribution of the frontier orbitals through electron paramagnetic resonance (EPR) spectroscopy had been hindered by the lack of resolution in the continuous wave (CW) spectra of *hypocloso*-$[B_{12}]^{1-}$ species. In chapter 4, we present Q-band pulsed EPR results that give a quantitative measure of the spin distribution of both *hypocloso*-$[B_{12}(OR)_{12}]^{1-}$ and super-oxidized $[B_{12}(OR)_{12}]^{1+}$ clusters. This is to our knowledge the first time pulsed EPR techniques have been applied to hypoelectronic dodecaborate clusters. Our results indicate that the frontier orbitals of *hypocloso*-$[B_{12}(OR)_{12}]$ clusters are confined to the cluster core and delocalized evenly across the B_{12} pseudo-icosahedron. The data for the super-oxidized $[B_{12}(OR)_{12}]^{1+}$ indicate a somewhat more localized spin distribution, which we suggest stems from increased elongation along the z-axis resulting in a concentration of spin density around the equatorial boron atoms. Furthermore, we provide UV–vis–NIR evidence indicating that visible and NIR electronic transitions in $[B_{12}(OR)_{12}]$ occur between orbitals that are largely confined to the cluster core.

PUBLISHED CONTENT AND CONTRIBUTIONS

Axtell, J. C.; Messina, M. S.; Liu, J.-Y.; Galaktionova, D.; Schwan, J.; Porter, T. M.; Savage, M. D.; Wixtrom, A. I.; Rheingold, A. L.; Kubiak, C. P.; Winkler J. R.; Gray H. B.; Král P.; Alexandrova A. N.; Spokoyny A. M. Photooxidative Generation of Dodecaborate-Based Weakly Coordinating Anions. *Inorg. Chem.* **2019**, *58* (16), 10516–10526. DOI: 10.1021/acs.inorgchem.9b00935.

L. J. S. performed photophysical characterization and experimental investigation of intermolecular interactions. Additionally, L. J. S. assisted with data interpretation and development of the photooxidative mechanism.

Stauber, J. M.; Schwan, L. J.; Xhang, X.; Axtell, J. C.; Jung, D.; McNicholas, B. J.; Oyala, P. H.; Winkler, J. R.; Miller, T. F.; Gray H. B.; Spokoyny, A.M. Evidence for the Existence of Cationic Dodecaborate-based Clusters (*in preparation*).

L. J. S. performed electrochemical, spectroelectrochemical, EPR and chemical oxidation studies, including the initial discovery of the cationic dodecaborate.

Schwan, L. J.; Oyala P. H.; Axtell J. C.; McNicholas B. J.; Winkler, J. R.; Spokoyny A. M.; Gray H. B. Electronic Structures of Perfunctionalized Dodecaborates Clusters (*in preparation*).

L. J. S. participated in conception of the project, experiment design, collection and analysis of data, and writing of the manuscript.

Fajardo Jr. J.; Schwan, L. J.; Takase, M. K.; Winkler, J. R.; Gray, H. B. Third Generation $W(CNAr)_6$ Photosensitizers Featuring Fused-Ring and Alkynyl-Bridged Arylisocyanides (*in preparation).*

L. J. S. participated in conception of the project, synthesis and spectroscopic characterization.

TABLE OF CONTENTS

LIST OF FIGURES

LIST OF TABLES

INTRODUCTORY REMARKS

My time at Caltech has been defined by a number of collaborations spanning a range of topics. My first main project was developing flash-quench techniques for mechanistic investigation of nitrogenase enzymes together with colleagues from the Rees lab (Caltech) and Tezcan lab (UCSD). At the same time, I was involved in researching organic electrooxidation using metal catalysts, and semiconductor photochemistry together with members of the Lewis Lab. During my third year at Caltech, I became interested in doing more synthetic inorganic chemistry and transitioned into one of the Gray group's current focus areas—Group 6 Metal Arylisocyanide complexes. Within that project I developed new classes of alkyne-bridged arylisocyanide ligands, along with mixed ligand carbonyl-arylisocyanide complexes. Additionally, I initiated a partnership with the Greer lab (Caltech) to use metal arylisocyanide complexes as absorbers for two-photon nanofabrication.

The research presented in this thesis started during my second year but was until recently a side project of mine. It was part of a broad collaboration initiated by Professor Alex Spokoyny at UCLA, who develops perfunctionalized dodecaborate clusters and investigates their reactivity and applications. Chapter 2 covers much of my early work. At that time, we were fumbling in the dark trying to understand dodecaborate photoredox mechanisms and photophysics. I truly enjoyed all the little experiments I performed to test various hypothesis' and trying to patch together large sets of seemingly unrelated data. However, I never thought that work would lead to anything significant, much less an entire thesis.

Two key advances drove the dodecaborate work to the forefront of my research. The first discovery was made using the newly acquired Q-band pulsed EPR system at Caltech. We found that Electron Nuclear Double Resonance (ENDOR) techniques could be applied to obtain information on hyperfine interactions in open shell dodecaborate clusters, which allowed us to experimentally describe the dodecaborate frontier orbitals. The second development was my electrochemical observation of a new super-oxidized cationic state in the electrochemistry of alkyloxy-perfunctionalized dodecaborate clusters. Both were major breakthroughs; the pulsed

EPR data provided experimental insights that had previously been inaccessible, and the discovery of cationic dodecaborates demonstrated that the clusters could reversibly reach oxidation states that were previously thought be highly unstable.

About a year ago Harry suggested that the dodecaborate data I had was enough for a thesis and that I should "*just write it up*". It was a difficult choice as I really enjoyed the metal arylisocyanide project, but I could not resist the draw of an earlier graduation date. Today, putting down the final words of this thesis, I am very happy about that decision. It has allowed me to finish my studies in good time and focus my energy toward future career goals. Additionally, I am excited about how the metal arylisocyanide project has evolved after I stepped away. Javier Fajardo has made amazing progress, both in continuing my work on alkyne-bridged isocyanides and in developing his own systems.

As I turn away from academia to pursue a career in consulting, I will surely miss Caltech and my time at the bench. It has been some of the most rewarding years of my life.

I hope you will enjoy reading this account of my Caltech experience!

Chapter 1

PERFUNCTIONALIZED DODECABORATE CLUSTERS

This chapter provides a historical overview of dodecaborate clusters and summarizes research conducted over the past 70 years. Emphasis is on discussions around the electronic structure and stability of dodecaborates, as well as recent developments toward hypoelectronic perfunctionalized dodecaborates and their applications.

A range of theoretical and experimental studies followed Lipscomb's initial structural characterization of the closo-dodecaborate dianion (closo-$[B_{12}H_{12}]^{2-}$*) in 1960. These included the synthesis of a range of partially substituted closo-dodecaborates, as well as the persubstituted closo-dodecahalo-dodecaborates (*$[B_{12}X_{12}]^{2-}$*; X = F, Cl, Br, I). Up until the late 1990s, it was assumed that stable electronic configurations were reserved for closed-shell dianionic closo-dodecaborates. However, pioneering work conducted in the Hawthorne lab demonstrated that the alkyloxy- and aryloxy-perfunctionalized closo-*$[B_{12}(OR)_{12}]^{2-}$ *clusters could undergo two reversible single-electron oxidations to yield hypocloso-*$[B_{12}(OR)_{12}]^{1-}$ *and hypercloso-*$B_{12}(OR)_{12}$ *species. Following work by the Spokoyny lab and others have shown a range of promising applications for hypercloso-*$B_{12}(OR)_{12}$ *clusters, including their use as photoredox reagents, in charge-storage devices and as dopants in conducting polymers.*

1.1 Dodecaborate Clusters

The early 1950s saw an increasing interest in systematic investigation of boron hydrides and rationalization of their stability and bonding patterns. In 1954, Lipscomb and co-workers introduced the "three-center bond" concept.[1] They argued that a three-center bond description of electron-deficient boron hydrides may be more appropriate than previously suggested resonance based structures. Using the three-center bond approach, Lipscomb explored the binding patterns of a number of known boron hydrides: B_2H_6, B_4H_{10}, B_5H_9, B_5H_{11} and $B_{10}H_{14}$. Additionally, several at the time unknown structures were explored—including B_6H_6 and the icosahedral $B_{12}H_{12}$ dodecaborate. Linear combination of atomic orbitals (LCAO) calculations for B_6H_6 indicate a triply degenerate highest occupied molecular orbital (HOMO), partially filled with four electrons. Due to its unfilled B-B bonding HOMO, B_6H_6 is predicted to be unstable. The relative orbital energies of $B_{12}H_{12}$ were not obtained due the complexity of performing the required LCAO calculations. Lipscomb argued that the HOMO of $B_{12}H_{12}$ might be three-fold or four-fold degenerate—where the former would lead to a stable closed-shell configuration, while the latter would likely lead to an unstable open-shell species.

Following the theoretical investigations by Lipscomb, Longuet-Higgins and Roberts used more in-depth molecular orbital calculations to explore the stability of boron hydrides.[2] Based on the relative ordering of the B-B bonding orbitals, they reported that $B_{12}H_{12}$ would likely not be stable. However, their predictions indicated that a dianionic closed-shell $[B_{12}H_{12}]^{2-}$ species might exist. $B_{12}H_{12}$ has forty-eight valence electrons, of which twenty-four are localized to twelve two-center B-H bonds. This leaves twenty-four electrons for B-B bonding. Assuming near-icosahedral symmetry, Longuet-Higgins predicted thirteen B-B bonding orbitals, where the four highest energy orbitals create a four-fold degenerate g_u set. As postulated by Lipscomb, this leads to the conclusions that icosahedral $B_{12}H_{12}$ should not be stable, as the four-fold degenerate g_u would lead to a partially unfilled HOMO. However, a dianionic $[B_{12}H_{12}]^{2-}$ species may be stable as the two extra electrons would result in a fully occupied HOMO.

The first mention of experimentally observed $B_{12}H_{12}$ came from Shapiro and Williams.[3] Reacting diborane (B_2H_6) with decaborane ($B_{10}H_{14}$) at elevated temperatures resulted in the formation of a light yellow solid. The final product appeared to be a polymerized borane. However, based on gasometrical analysis the authors proposed that the initial product of the reaction was $B_{12}H_{12}$. In 1960 Pitochelli and Hawthorn confirmed Longuet-Higgins and Lipscombs predictions by isolating the icosahedral $[B_{12}H_{12}]^{2-}$ dodecaborate (henceforth referred to as *closo*-dodecaborate or *closo*-$[B_{12}H_{12}]^{2-}$), although in very low yield (3.8%).[4] Later that year, Lipscomb reported an X-ray diffraction study showing that the structure of *closo*-dodecaborate possessed near-icosahedral symmetry (Figure 1.1).[5] Spectroscopic investigations by Muetterties and co-workers followed soon thereafter.[6] Hoffmann and Lipscomb used the newly obtained experimental data to guide refinement of LCAO calculations. Their work confirmed Longuet-Higgins overall qualitative description of *closo*-dodecaborate and provided additional quantitative information, including a ~14 eV calculated band gap.[7,8] A calculated electronic structure for *closo*-dodecaborate by Bambakidis and Wagner is shown in Figure 1.2.[9]

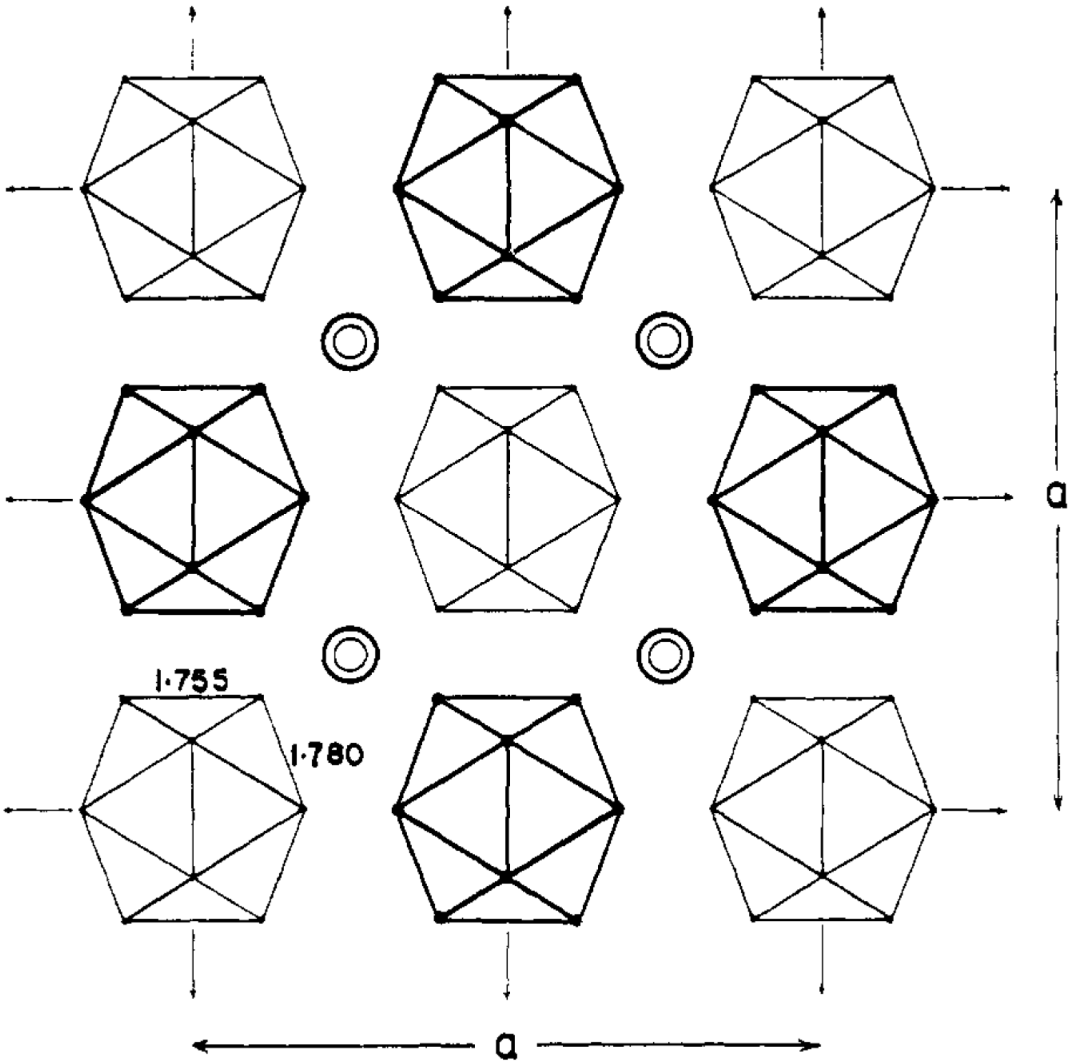

Figure 1.1. Crystallographic data reported by Lipscomb demonstrating the near-icosahedral symmetry of *closo*-$[B_{12}H_{12}]^{2-}$. Reprinted with permission from Wunderlich, J. A.; Lipscomb, W. N. STRUCTURE OF B12H12-2 ION. *J. Am. Chem. Soc.* **1960**, *82* (16), 4427–4428. Copyright (1960) American Chemical Society.

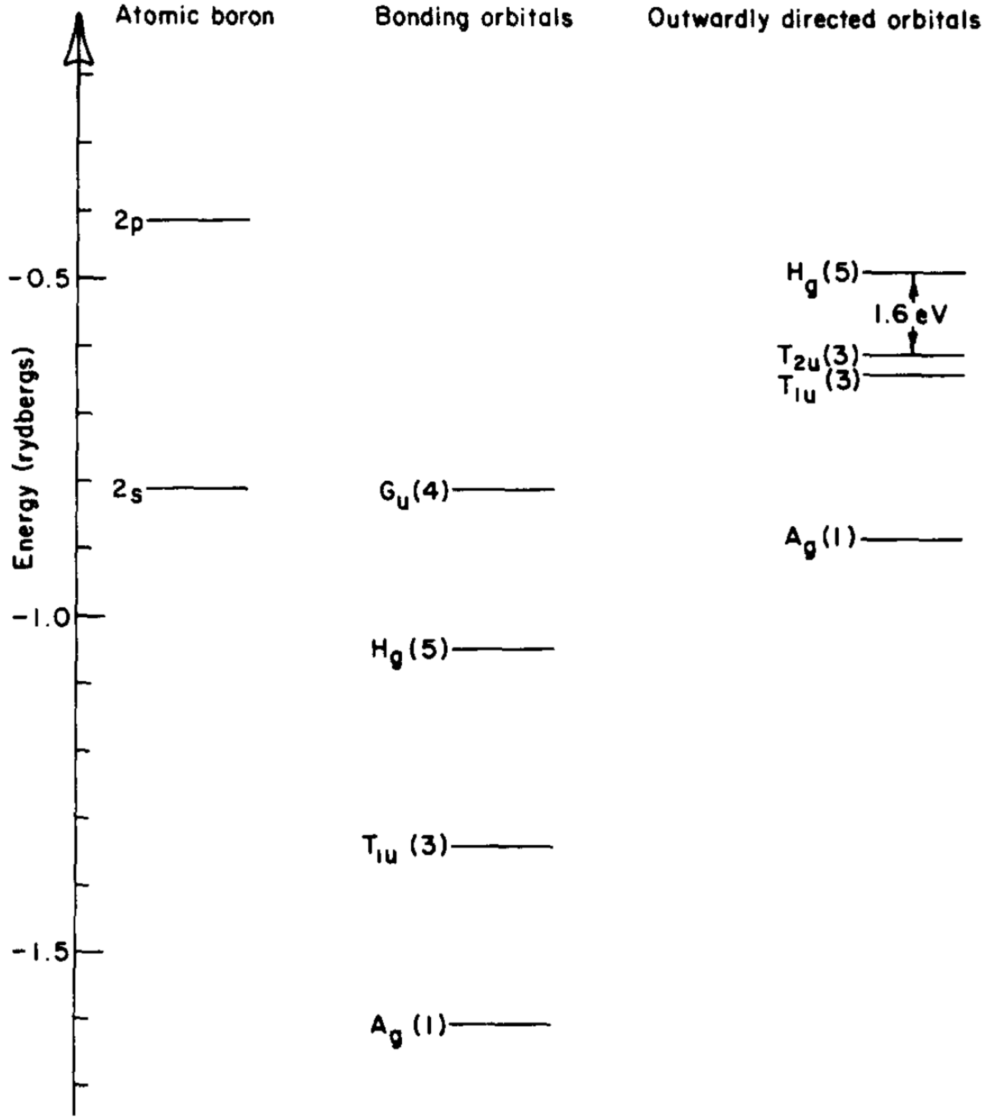

13 bonding orbitals (maximum of 26 electrons);
12 outwardly directed orbitals (maximum of 24 electrons)

Figure 1.2. Electronic structure of *closo*-$[B_{12}H_{12}]^{2-}$ calculated by Bambakidis and Wagner. Reprinted from Bambakidis, G.; Wagner, R. P. Electronic Structure and Binding Energy of the Icosahedral Boron Cluster B12. *Journal of Physics and Chemistry of Solids* **1981**, *42* (11), 1023–1025. Copyright (1981), with permission from Elsevier.

The interest in dodecaborates was further enhanced by the discovery of more convenient methods for synthesizing *closo*-$[B_{12}H_{12}]^{2-}$ salts. Two classes of high-yield reactions were reported, both relying on reacting diborane with a base in a pressurized reactor. In the first route (eq. 1) sodium borohydride is reacted with diborane in a basic solvent, typically triethylamine. The second route (eq. 2) involves reacting an alkylamine or a borane-alkylamine complex with diborane. Reactions yields of > 90% are readily achieved using optimized variations of these reactions.[10–12] Modern synthetic schemes replace diborane with larger boranes, commonly $B_{10}H_{14}$, which avoids the hazardous pressurized conditions required for the early synthetic pathways. Today, a wide range of synthetic methods have been reported and dozens of *closo*-$[B_{12}H_{12}]^{2-}$ salts have been prepared; including metal, ammonium, trimethylsulfonium, tetraphenylphosphonium and guanidinium salts.[13]

$$2NaBH_4 + 5B_2H_6 \rightarrow Na_2[B_{12}H_{12}] + 13H_2 \tag{1}$$

$$2R_3N + 6\mathrm{B}_2H_6 \rightarrow [R_3NH]_2[B_{12}H_{12}] + 11H_2 \tag{2}$$

As expected from the theoretical investigations discussed above, attempts to isolate oxidized forms of *closo*-$[B_{12}H_{12}]^{2-}$ have proved unsuccessful. Specifically, Wiersema and Middaugh demonstrated that one-electron electrochemical oxidation of *closo*-dodecaborate leads to irreversible formation of $[B_{24}H_{23}]^{3-}$. This species likely corresponds to the hydrogen-bridged dimer 1,1'-μ-hydro-bis(undecahydro-*closo*-dodecaborate)(3-).[14]

The 1970s saw further generalization of the theoretical framework for rationalizing structures and stability trends of electron-deficient polyhedral clusters. A landmark paper by Wade presented a set of principles for predicting the structure of cluster compounds by counting the number of vertices and the number of skeletal bonding orbitals. These guidelines, which have become known as “Wade’s rule”, state that the number of skeletal bonding pairs of stable *closo* (n-vertex), *nido* ((n - 1)-vertex) and *arachno* ((n - 2)-vertex) clusters must be (n + 1). Wade’s rule has been successfully applied to rationalize the structure of a wide variety of polyhedral cluster compounds.[15,16]

Models considering three-dimensional aromaticity also provided important insights toward understanding the stability of polyhedral boranes. Early theoretical work by Aihara showed that the resonance model could be extended into three dimensions using three-center bonding. Through this approach, resonance stabilization can be used to explain the stability of various boron polyhedra. The three-dimensional aromaticity of polyhedral boron compounds has gained additional support through later computational studies and is thought to be an important contributor to the inert nature of *closo*-dodecaborate.[17,18]

1.2 Functionalization of *closo*-Dodecaborate

A range of studies on the reactivity and physical properties of *closo*-dodecaborate were published in the decade following its initial isolation by Pitochelli and Hawthorn. Muetterties and co-workers performed several experimental studies on functionalization of *closo*-dodecaborate.[19,20] *Closo*-dodecaborate is exceptionally stable toward strong bases, strong acids and oxidizing agents. The cluster remains intact even in hot sodium hydroxide and sodium methoxide solutions. In fact, *closo*-dodecaborate can be converted into stable $(H_3O)_2[B_{12}H_{12}]\bullet x(H_2O)$ by reaction with strong acids, without compromising the integrity of the cluster. The stability toward acid is noteworthy, as most boron hydrides rapidly decompose under acidic conditions.

Closo-dodecaborate is susceptible to electrophilic substitution, where hydrogen atoms are replaced by an electrophilic reagent. *Closo*-$[B_{12}H_{12}]^{2-}$ can be reacted with halogens (X = F, Cl, Br, I) to yield fully substituted *closo*-$[B_{12}X_{12}]^{2-}$. Partially substituted haloborates ($[B_{12}X_nH_{12-n}]^{2-}$, n<12) can be prepared through similar procedures. However, the rapid reaction rates makes isolating species with a low degree of halogen substitution challenging, in particular for the smaller halogens (F, Cl). Certain partially substituted haloborates can be prepared using elemental halogens, like iodine monochloride and N-bromosuccinimide, or hydrogen fluoride in the case of fluoroborates. Additional reactivity can be afforded by using the acid derivative, $(H_3O)_2[B_{12}H_{12}]\bullet x(H_2O)$. For example, reacting these acidic clusters with alcohols or carboxylic acids yield $[B_{12}H_{11}(OH)]^{2-}$ and $[B_{12}H_{12-n}(OR)_n]^{2-}$ (n = 1, 2).[19–21]

Development of *closo*-dodecaborate derivatives has continued to be an active field of research. Many monosubstituted and disubstituted variants have been reported, including clusters carrying boron-carbon bonds, boron-nitrogen bonds, boron-oxygen bonds, boron-sulfur bonds, as well as boron-phosphorus and boron-arsenic bonds. Some interesting examples include carbonyl derivatives, amines, amides, alkyl and aryl derivatives. Notably, clusters carrying mercapto-functionalities have received much attention due to their potential applications in boron neutron capture therapy.[22]

This thesis is primarily concerned with persubstituted derivates of *closo*-dodecaborate. Up until the late 1990s the only examples of perfunctionalized dodecaborates were the dodecahalo-*closo*-dodecaborates discussed above. The first example of a non-halogen perfunctionalized dodecaborate came from Krebs and co-workers in 1997, who reported the selenoboratoborate *closo*-$[B_{12}(BSe_3)_6]^{8-}$, where the hydrogens had been substituted by six bidentate BSe_3 groups.[23] A year later, Hawthorne reported a permethylated *closo*-$[B_{12}Me_{12}]^{2-}$ cluster (Me = CH_3).[24,25]

A key breakthrough came in 1999 when Hawthorne and co-workers reported the isolation of dodecahydroxy-*closo*-dodecaborate (*closo*-$[B_{12}(OH)_{12}]^{2-}$).[26] The synthesis of *closo*-$[B_{12}(OH)_{12}]^{2-}$ is performed by refluxing $Cs_2[B_{12}H_{12}]$ in 30% hydrogen peroxide for several days and produces good to excellent yields (65-90%).[27] To mitigate risks involved with using concentrated hydrogen peroxide at elevated temperatures, the $Cs_2[B_{12}H_{12}]$ starting material must be rigorously purified before attempting the reactions. Researchers are advised to exercise caution when trying this synthesis as minor organic impurities may cause explosive mixtures. That said, this synthetic pathway is still used and has proven remarkably robust—provided appropriate safety measures are taken.[27,28] Following the isolation of dodecahydroxy-*closo*-dodecaborate, the Hawthorn group demonstrated that these clusters could be reacted with benzyl chloride to form $[B_{12}(OBz)_{12}]^{2-}$ (Bz = $CH_2C_6H_5$). Using the reaction pathways shown in Figure 1.3, the reactivity was expanded to a range of ether and ester derivatives of *closo*-$[B_{12}(OH)_{12}]^{2-}$. Table 1.1 shows examples of the ether derivatives published by the Hawthorne group.

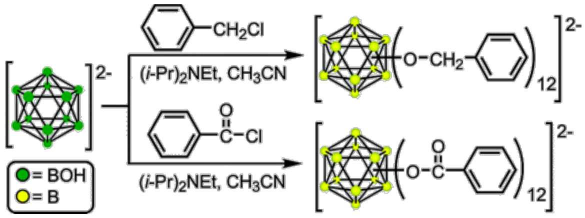

Figure 1.3. Synthetic method for perfunctionalized ether and ester derivatives of *closo*-$[B_{12}(OH)_{12}]^{2-}$ developed by Hawthorne and co-workers. An acetonitrile solution of *closo*-$[B_{12}(OH)_{12}]^{2-}$ and the relevant reactant is refluxed in the presence of base, yielding the desired *closo*-$[B_{12}(OR)_{12}]^{2-}$ cluster. Reprinted with permission from Farha, O. K.; Julius, R. L.; Lee, M. W.; Huertas, R. E.; Knobler, C. B.; Hawthorne, M. F. Synthesis of Stable Dodecaalkoxy Derivatives of Hypercloso-B12H12. *J. Am. Chem. Soc.* **2005**, *127* (51), 18243–18251. Copyright (2005) American Chemical Society.

Table 1.1. Examples of *closo*-$[B_{12}(OR)_{12}]^{2-}$ clusters developed by the Hawthrone lab. Method 1 refers to refluxing $[B_{12}(OH)_{12}]^{2-}$ with the appropriate alkyl or aryl halide and *N,N'*-diisopropylamine in acetonitrile. Method 2 involves performing the same reaction under mild argon pressure in an autoclave to achieve elevated temperature and reduced reaction times. Reprinted with permission from Farha, O. K.; Julius, R. L.; Lee, M. W.; Huertas, R. E.; Knobler, C. B.; Hawthorne, M. F. Synthesis of Stable Dodecaalkoxy Derivatives of Hypercloso-B12H12. *J. Am. Chem. Soc.* **2005**, *127* (51), 18243–18251. Copyright (2005) American Chemical Society.

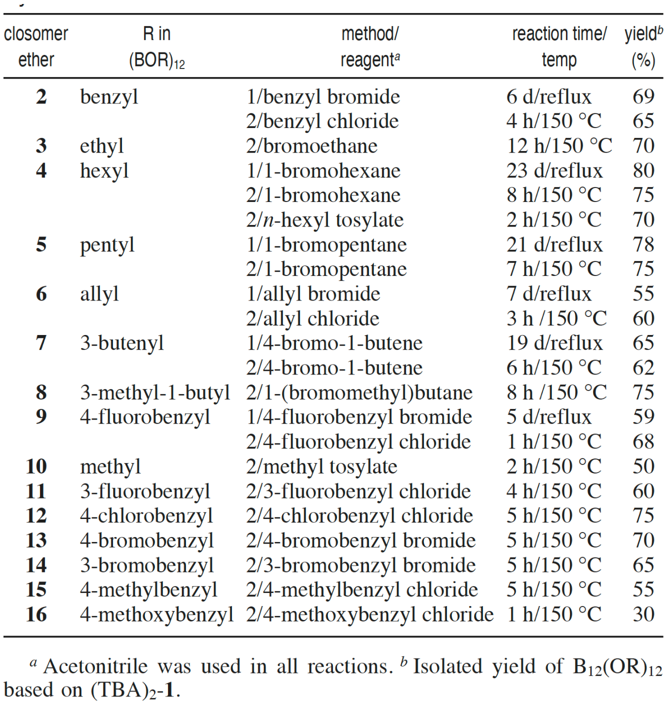

closomer ether	R in $(BOR)_{12}$	method/ reagent[a]	reaction time/ temp	yield[b] (%)
2	benzyl	1/benzyl bromide	6 d/reflux	69
		2/benzyl chloride	4 h/150 °C	65
3	ethyl	2/bromoethane	12 h/150 °C	70
4	hexyl	1/1-bromohexane	23 d/reflux	80
		2/1-bromohexane	8 h/150 °C	75
		2/*n*-hexyl tosylate	2 h/150 °C	70
5	pentyl	1/1-bromopentane	21 d/reflux	78
		2/1-bromopentane	7 h/150 °C	75
6	allyl	1/allyl bromide	7 d/reflux	55
		2/allyl chloride	3 h /150 °C	60
7	3-butenyl	1/4-bromo-1-butene	19 d/reflux	65
		2/4-bromo-1-butene	6 h/150 °C	62
8	3-methyl-1-butyl	2/1-(bromomethyl)butane	8 h /150 °C	75
9	4-fluorobenzyl	1/4-fluorobenzyl bromide	5 d/reflux	59
		2/4-fluorobenzyl chloride	1 h/150 °C	68
10	methyl	2/methyl tosylate	2 h/150 °C	50
11	3-fluorobenzyl	2/3-fluorobenzyl chloride	4 h/150 °C	60
12	4-chlorobenzyl	2/4-chlorobenzyl chloride	5 h/150 °C	75
13	4-bromobenzyl	2/4-bromobenzyl bromide	5 h/150 °C	70
14	3-bromobenzyl	2/3-bromobenzyl bromide	5 h/150 °C	65
15	4-methylbenzyl	2/4-methylbenzyl chloride	5 h/150 °C	55
16	4-methoxybenzyl	2/4-methoxybenzyl chloride	1 h/150 °C	30

[a] Acetonitrile was used in all reactions. [b] Isolated yield of $B_{12}(OR)_{12}$ based on $(TBA)_2$-**1**.

1.3 Hypoelectronic Dodecaborates

The first example of a stable hypoelectronic dodecaborate derivative came when the Hawthorne group reported the isolation a stable salt of the singly oxidized $[B_{12}Me_{12}]^{1-}$ cluster.[30] Quickly thereafter, in conjunction with their publications on alkoxy-perfunctionalized clusters, the same group showed that $[B_{12}(OBz)_{12}]^{2-}$ could undergo reversible one-electron oxidations to yield open-shell anionic $[B_{12}(OBz)_{12}]^{1-}$ and neutral $B_{12}(OBz)_{12}$ species. These oxidized pseudo-icosahedral species have since become known as *hypocloso*-dodecaborates ($[B_{12}]^{1-}$ monoanion) and *hypercloso*-dodecaborates (B_{12}^{0} neutral), to signify their deviation from Wade's rule.[31] Following publications demonstrated that the ability to form hypoelectronic *hypocloso*-$[B_{12}(OR)_{12}]^{1-}$ and *hypercloso*-$B_{12}(OR)_{12}$ states is a general feature of alkyloxy- and aryloxy-perfunctionalized dodecaborates.[29,32] Hypoelectronic states can also be isolated for perfunctionalized halide and hydroxyl derivatives of dodecaborate. Under certain conditions, synthesis of *closo*-$[B_{12}(OH)_{12}]^{2-}$ leads to formation of *hypocloso*-$[B_{12}(OH)_{12}]^{1-}$ as a side product, which can be isolated as the cesium salt $Cs[B_{12}(OH)_{12}]$.[33] The halide derivatives *closo*-$[B_{12}X_{12}]^{2-}$ (X = F, Cl, Br, I) undergo electrochemical single-electron oxidation to *hypocloso*-$[B_{12}X_{12}]^{1-}$ in liquid sulfur dioxide at highly oxidizing potentials (~1.7 V for X = F, ~2.1 V for X = Cl, ~2.3 V for X = Br; potentials referenced to the ferrocene-ferrocenium couple). In contrast to the reversible oxidations observed for $[B_{12}(OR)_{12}]$ clusters, the halide derivatives, at best, display pseudo-reversible redox events. The highest degree of reversibility is achieved when X = Cl or Br. In line with these results, *hypocloso*-$[B_{12}Cl_{12}]^{1-}$ and *hypocloso*-$[B_{12}Br_{12}]^{1-}$ can be chemically isolated through oxidation with arsenic pentafluoride in liquid sulfur dioxide.[34,35] *hypocloso*-$[B_{12}F_{12}]^{1-}$ is more challenging to generate chemically, however, a crystal structure of a cobaltocenium salt of *hypocloso*-$[B_{12}F_{12}]^{1-}$ has been reported.[36]

The next breakthrough came when the Spokoyny lab presented a convenient route for rapid generation of *hypercloso*-$B_{12}(OR)_{12}$ using microwave synthesis. Table 1.2 shows some of the clusters synthesized using this method and compares the reaction times to those reported for earlier methods. Reactions that used to take many hours, sometimes days, could now be achieved in a matter of minutes. Access to straightforward and scalable synthesis methods have facilitated systematic characterization and investigation into potential applications of $[B_{12}(OR)_{12}]$ clusters.

Table 1.2. *hypercloso*-$B_{12}(OR)_{12}$ clusters obtained through microwave synthesis. Previously reported reaction times and yields shown in parenthesis, when available. Reproduced from Ref. 27 with permission from The Royal Society of Chemistry.

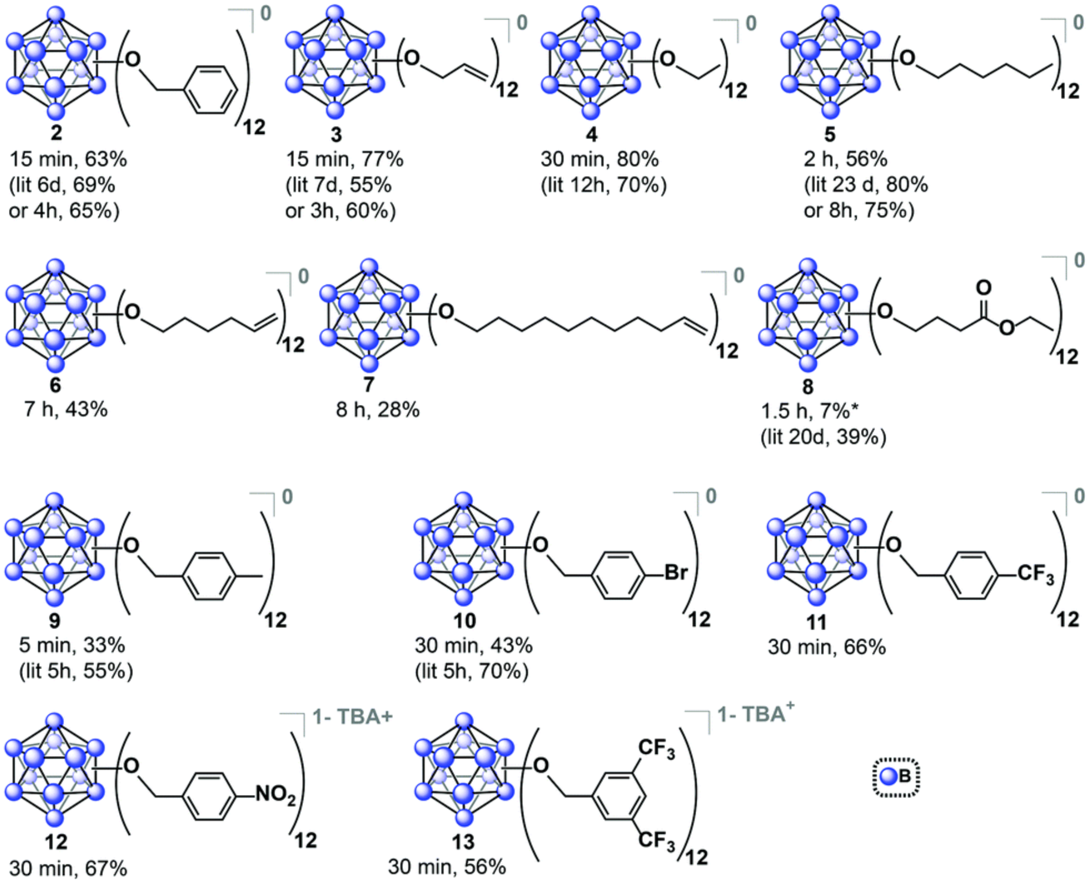

The majority of the *hypercloso*-$B_{12}(OR)_{12}$ clusters reported are indefinitely stable under ambient conditions, which is remarkable considering that even single-electron oxidation leads to immediate decomposition of *closo*-$[B_{12}H_{12}]^{2-}$. Multiple factors contribute to stabilizing the B_{12}^0 core in *hypercloso*-$B_{12}(OR)_{12}$. Electron donation from the R-groups modulates redox potentials and play an important role in increasing the electron density in B-B bonding orbitals. In line with this, the redox potential of $[B_{12}(OR)_{12}]$ clusters carrying aryl substituents can be systematically tuned based on the Hammett constant of the aryl groups, as demonstrated by the linear relationship between redox potentials and Hammett constants shown in Figure 1.4. Furthermore, upon oxidation the cluster is distorted, which lowers the overall energy and avoids energetically unfavorable open-shell configurations by breaking the icosahedral (I_h) symmetry. There has been some controversy around the nature of the distortion, however, most authors believe a $I_h \rightarrow D_{3d}$ transformation is involved in stabilizing oxidized $[B_{12}(OR)_{12}]$ clusters. This leads to a closed-shell *hypercloso*-$B_{12}(OR)_{12}$ $a_{1u}^0a_{2u}^2e_u^4$ configuration, avoiding the unstable open-shell g_u^4 configuration predicted for $B_{12}H_{12}$. An important consequence of depopulation of the a_{1u} is the appearance of a strong visible absorption band (~ 455 nm $\varepsilon > 2{*}10^4$ $M^{-1}cm^{-1}$). The reversible redox behavior and visible absorption have opened up for applications in a range of fields, including photochemistry,[37,38] charge storage[39] and as dopants in conducting polymers.[40]

1.4 Applications of *hypercloso*-$B_{12}(OR)_{12}$

To date, the most widely explored applications of *hypercloso*-$B_{12}(OR)_{12}$ involve using the clusters as photoredox reagents, and in particular, their use as photoinitiators for cationic polymerization.

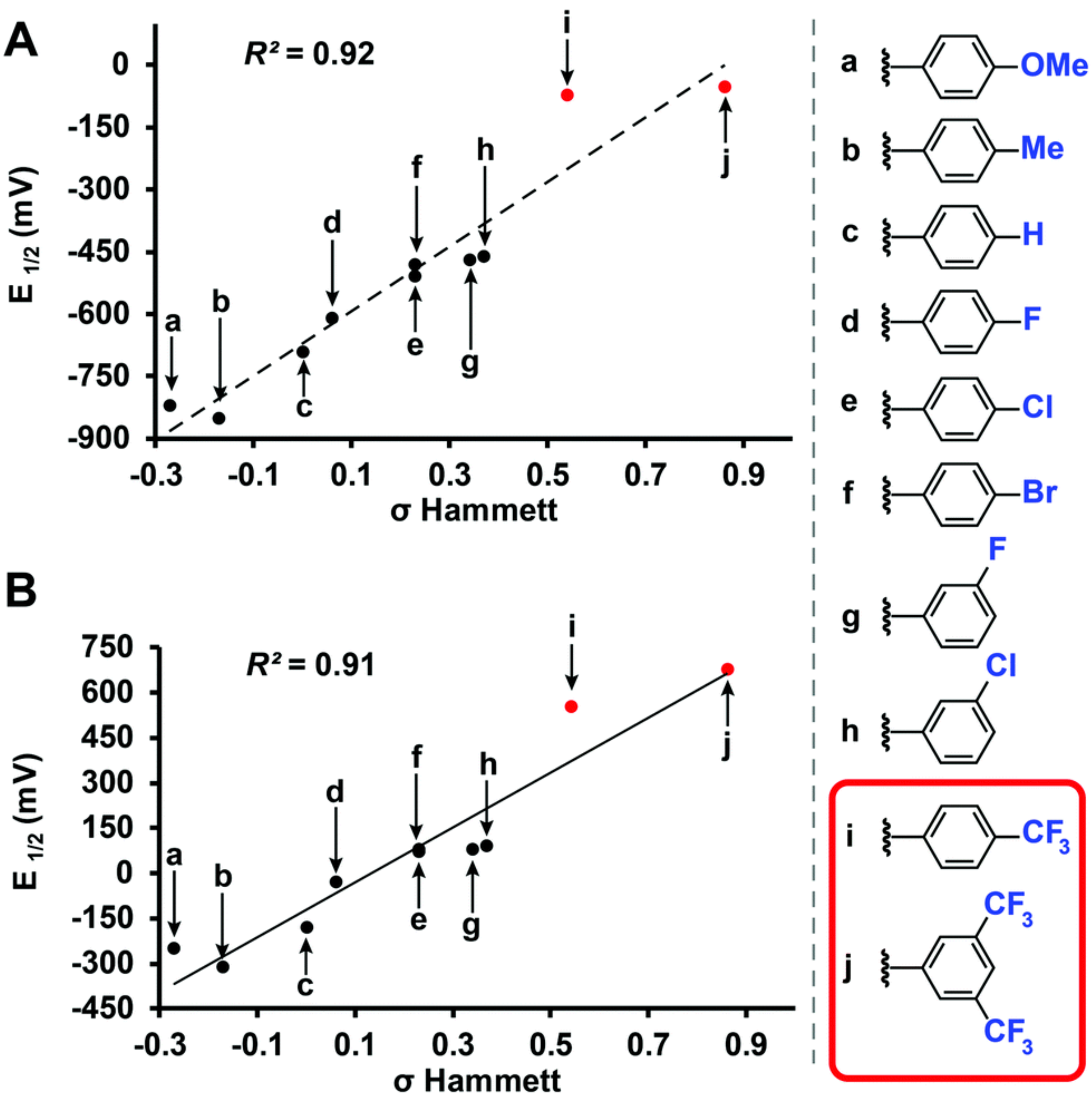

Figure 1.4 Relationship between $[B_{12}(OR)_{12}]$ redox potentials and substituent Hammett constants. Potentials are reported versus the ferrocene-ferrocenium couple. Reproduced from Ref. 27 with permission from The Royal Society of Chemistry.

The Spokoyny lab demonstrated polymerization of electron-rich styrenes using *hypercloso*-$B_{12}(OBz)_{12}$ as a photoinitiator. Using the more oxidizing perfluoro analogue, *hypercloso*-$B_{12}(OCH_2C_6F_5)_{12}$, they were able to expand the reactivity to less electron-rich styrenes. Remarkably, *hypercloso*-$B_{12}(OCH_2C_6F_5)_{12}$ is also able to photoinitiate polymerization of isobutylene, which had previously not been achieved in metal-free systems. Figure 1.5 shows a schematic of the photopolymerization reaction and the highly branched poly(isobutylene) product. Part of the work presented in this thesis aims to rationalize the photooxidative properties of *hypercloso*-$B_{12}(OR)_{12}$ clusters.[28,37]

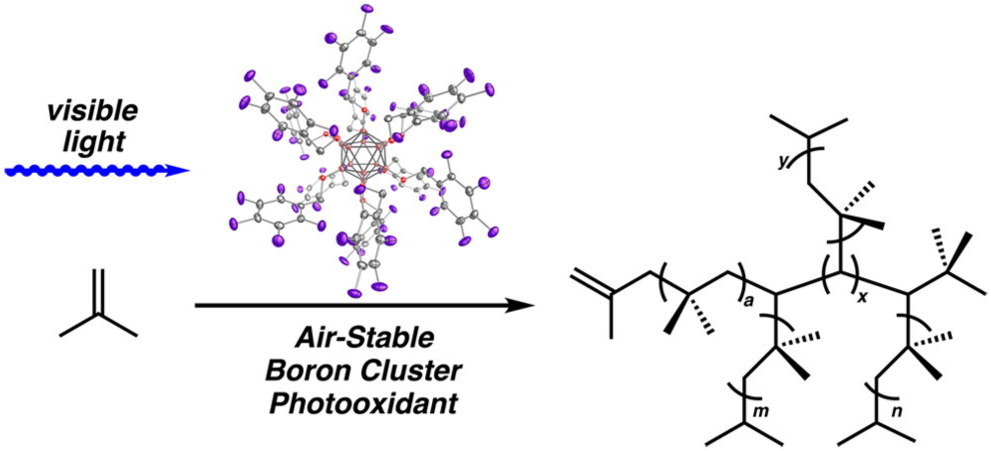

Figure 1.5. Photopolymerization of isobutylene using *hypercloso*-$B_{12}(OCH_2C_6F_5)_{12}$ results in a highly branched polymer. Reprinted with permission from Messina, M. S.; Axtell, J. C.; Wang, Y.; Chong, P.; Wixtrom, A. I.; Kirlikovali, K. O.; Upton, B. M.; Hunter, B. M.; Shafaat, O. S.; Khan, S. I.; et al. Visible-Light-Induced Olefin Activation Using 3D Aromatic Boron-Rich Cluster Photooxidants. *Journal of the American Chemical Society* **2016**, *138* (22), 6952–6955. Copyright (2016) American Chemical Society.

The highly reversible redox behavior of $[B_{12}(OR)_{12}]$ clusters have resulted in interesting applications as dopants in conducting polymers and in charge-storage devices. Recent work showed that P3HT (poly(3-hexylthiophene-2,5-diyl) films doped with the bulky dodecaborate *hypercloso*-$B_{12}(OCH_2$-3,5-$(CF_3)_2$-$C_6H_3)_{12}$ display conductivities roughly an order of magnitude higher than P3HT films prepared with the conventional dopant F_4TCNQ (2,3,5,6-tetrafluoro-tetracyanoquinodimethane). In these systems, introduction of the oxidizing *hypercloso*-B_{12}^{0} species produces a hole on the polymer and a negative charge confined to the B_{12} cluster core. The authors argue that the bulky 3,5-$(CF_3)_2$-C_6H_3 groups result in a highly shielded *hypocloso*-$[B_{12}]^{1-}$ core, which improves polymer hole conductivity.[40] Applications in redox flow batteries have also shown promising results. A single type of $[B_{12}(OR)_{12}]$ cluster can be used in both cell compartments, as shown in Figure 1.6, or the anodic and cathodic electrolytes can be prepared using clusters equipped with differing R-groups. The former utilizes the split between the $[B_{12}]^{1-/2-}$ couple and $[B_{12}]^{0/1-}$ couple to drive the voltage, while the latter uses the difference in redox potential provided by changing the R-group. Negligible cluster decomposition after > 1000 hours of battery cycling demonstrates the robustness of the $[B_{12}(OR)_{12}]^{0/1-/2-}$ redox system.

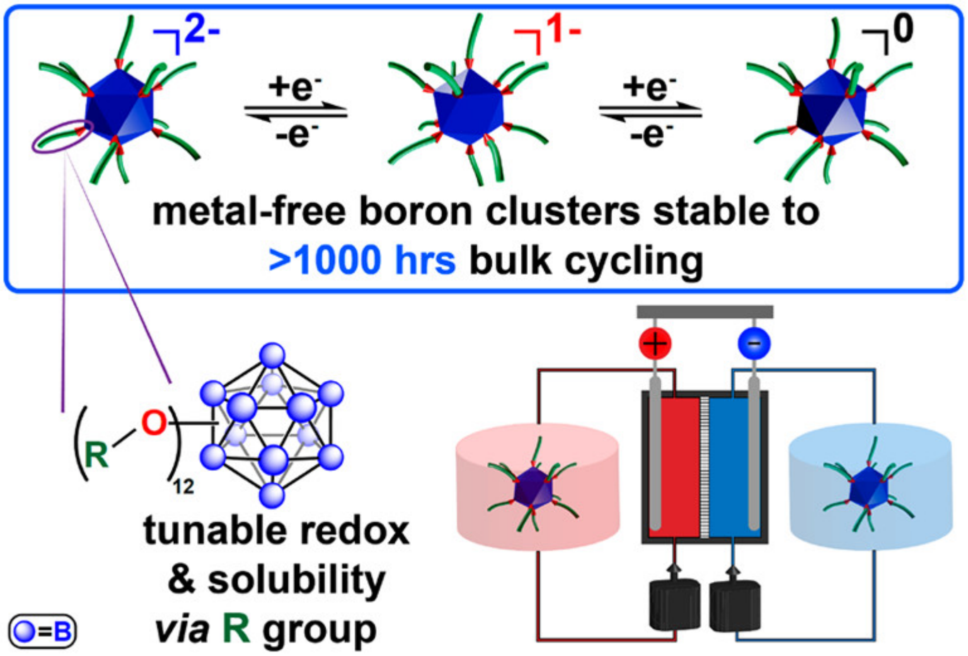

Figure 1.6. Schematic of a $[B_{12}(OR)_{12}]$ redox flow battery. The blue electrolyte contains $[B_{12}(OR)_{12}]^{2-}$, while the red electrolyte contains $B_{12}(OR)_{12}{}^{0}$. The battery voltage is obtained from the split between the $[B_{12}]^{1-/2-}$ and $[B_{12}]^{0/1-}$ redox couples. Reprinted with permission from Barton, J. L.; Wixtrom, A. I.; Kowalski, J. A.; Qian, E. A.; Jung, D.; Brushett, F. R.; Spokoyny, A. M. Perfunctionalized Dodecaborate Clusters as Stable Metal-Free Active Materials for Charge Storage. *ACS Appl. Energy Mater.* **2019**, *2* (7), 4907–4913. Copyright (2019) American Chemical Society.

1.5 Concluding Remarks

Dodecaborate clusters have been a lively field of research since the early 1950s. Several groundbreaking discoveries have been made over the past two decades, most notably, the isolation of alkyloxy-perfunctionalized dodecaborates and the discovery of hypoelectronic *hypocloso*-$[B_{12}(OR)_{12}]^{1-}$ and *hypercloso*-$B_{12}(OR)_{12}$ states. *hypercloso*-$B_{12}(OR)_{12}$ shows remarkable stability, considering the instability of oxidized $[B_{12}H_{12}]$ species and challenges associated with oxidizing dodecahalo-*closo*-dodecaborates. The tunability of the electrochemical properties, reversible redox behavior and strong visible absorption bands make *hypercloso*-$B_{12}(OR)_{12}$ clusters interesting for a range of applications. Recent reports include their use as photoredox reagents, as dopants in conducting polymers and in charge-storage devices. Understanding the electronic structure is key to rationalizing these properties. Regrettably, experimental evidence is currently lacking, and most electronic structure descriptions are based on often contradictory computational work. This thesis aims to address some of these issues using spectroscopic and electrochemical techniques.

BIBLIOGRAPHY

(1) Eberhardt, W. H.; Crawford, B.; Lipscomb, W. N. The Valence Structure of the Boron Hydrides. *J. Chem. Phys.* **1954**, *22* (6), 989–1001. https://doi.org/10.1063/1.1740320.

(2) Longuet-Higgins, H. C.; Roberts, M. D. V. The Electronic Structure of an Icosahedron of Boron Atoms. *Proc R Soc Lond A* **1955**, *230* (1180), 110–119. https://doi.org/10.1098/rspa.1955.0115.

(3) Shapiro, I.; Williams, R. E. The Nature of Boron Hydride Solids1. *J. Am. Chem. Soc.* **1959**, *81* (18), 4787–4790. https://doi.org/10.1021/ja01527a009.

(4) Pitochelli, A. R.; Hawthorne, F. M. THE ISOLATION OF THE ICOSAHEDRAL B12H12-2 ION. *J. Am. Chem. Soc.* **1960**, *82* (12), 3228–3229. https://doi.org/10.1021/ja01497a069.

(5) Wunderlich, J. A.; Lipscomb, W. N. STRUCTURE OF B12H12-2 ION. *J. Am. Chem. Soc.* **1960**, *82* (16), 4427–4428. https://doi.org/10.1021/ja01501a076.

(6) Muetterties, E. L.; Merrifield, R. E.; Miller, H. C.; Knoth, W. H.; Downing, J. R. Chemistry of Boranes. III.1 The Infrared and Raman Spectra of B12H12 - and Related Anions. *J. Am. Chem. Soc.* **1962**, *84* (13), 2506–2508. https://doi.org/10.1021/ja00872a011.

(7) Hoffmann, R.; Lipscomb, W. N. Boron Hydrides: LCAO—MO and Resonance Studies. *J. Chem. Phys.* **1962**, *37* (12), 2872–2883. https://doi.org/10.1063/1.1733113.

(8) Hoffmann, R.; Lipscomb, W. N. Theory of Polyhedral Molecules. I. Physical Factorizations of the Secular Equation. *J. Chem. Phys.* **1962**, *36* (8), 2179–2189. https://doi.org/10.1063/1.1732849.

(9) Bambakidis, G.; Wagner, R. P. Electronic Structure and Binding Energy of the Icosahedral Boron Cluster B12†. *J. Phys. Chem. Solids* **1981**, *42* (11), 1023–1025. https://doi.org/10.1016/0022-3697(81)90068-8.

(10) Miller, H. C.; Miller, N. E.; Muetterties, E. L. Synthesis of Polyhedral Boranes. *J. Am. Chem. Soc.* **1963**, *85* (23), 3885–3886. https://doi.org/10.1021/ja00906a033.

(11) Miller, H. C.; Miller, N. E.; Muetterties, E. L. Chemistry of Boranes. XX. Syntheses of Polyhedral Boranes. *Inorg. Chem.* **1964**, *3* (10), 1456–1463. https://doi.org/10.1021/ic50020a026.

(12) Ellis, I. A.; Gaines, D. F.; Schaeffer, Riley. A Convenient Preparation of B12H122- Salts. *J. Am. Chem. Soc.* **1963**, *85* (23), 3885–3885. https://doi.org/10.1021/ja00906a032.

(13) Sivaev, I. B.; Sjöberg, S.; Bregadze, V. I.; Gabel, D. Synthesis of Alkoxy Derivatives of Dodecahydro-Closo-Dodecaborate Anion [B12H12]2−. *Tetrahedron Lett.* **1999**, *40* (17), 3451–3454. https://doi.org/10.1016/S0040-4039(99)00420-7.

(14) Wiersema, R. J.; Middaugh, R. L. Electrochemical Preparation and Halogenation of 1,1'-.Mu.-Hydro-Bis(Undecahydro-Closo-Dodecaborate)(3-), B24H233-. *Inorg. Chem.* **1969**, *8* (10), 2074–2079. https://doi.org/10.1021/ic50080a009.

(15) Wade, K. The Structural Significance of the Number of Skeletal Bonding Electron-Pairs in Carboranes, the Higher Boranes and Borane Anions, and Various Transition-Metal Carbonyl Cluster Compounds. *J. Chem. Soc. Chem. Commun.* **1971**, No. 15, 792–793. https://doi.org/10.1039/C29710000792.

(16) J. Welch, A. The Significance and Impact of Wade's Rules. *Chem. Commun.* **2013**, *49* (35), 3615–3616. https://doi.org/10.1039/C3CC00069A.

(17) Aihara, J. Three-Dimensional Aromaticity of Polyhedral Boranes. *J. Am. Chem. Soc.* **1978**, *100* (11), 3339–3342. https://doi.org/10.1021/ja00479a015.

(18) King, R. B. Three-Dimensional Aromaticity in Polyhedral Boranes and Related Molecules. *Chem. Rev.* **2001**, *101* (5), 1119–1152. https://doi.org/10.1021/cr000442t.

(19) Knoth, W. H.; Miller, H. C.; England, D. C.; Parshall, G. W.; Muetterties, E. L. Derivative Chemistry of B10H10- and B12H12-. *J. Am. Chem. Soc.* **1962**, *84* (6), 1056–1057. https://doi.org/10.1021/ja00865a040.

(20) Knoth, W. H.; Miller, H. C.; Sauer, J. C.; Balthis, J. H.; Chia, Y. T.; Muetterties, E. L. Chemistry of Boranes. IX. Halogenation of B10H10-2 and B12H12-2. *Inorg. Chem.* **1964**, *3* (2), 159–167. https://doi.org/10.1021/ic50012a002.

(21) Muetterties, E. L.; Balthis, J. H.; Chia, Y. T.; Knoth, W. H.; Miller, H. C. Chemistry of Boranes. VIII. Salts and Acids of B10H10-2 and B1212-2. *Inorg. Chem.* **1964**, *3* (3), 444–451. https://doi.org/10.1021/ic50013a030.

(22) Sivaev, I. B.; Bregadze, V. I.; Sjöberg, S. Chemistry of *Closo*-Dodecaborate Anion $[B_{12}H_{12}]^{2-}$: A Review. *Collect. Czechoslov. Chem. Commun.* **2002**, *67* (6), 679–727. https://doi.org/10.1135/cccc20020679.

(23) Küper, J.; Conrad, O.; Krebs, B. Selenoboratoborates [B12(BSe3)6]8−: A New Class of Chalcogen-Substituted Icosahedral Boron Clusters. *Angew. Chem. Int. Ed. Engl.* **1997**, *36* (17), 1903–1904. https://doi.org/10.1002/anie.199719031.

(24) Peymann, T.; Knobler, C. B.; Khan, S. I.; Hawthorne, M. F. Dodecamethyl-Closo-Dodecaborate(2−). *Inorg. Chem.* **2001**, *40* (6), 1291–1294. https://doi.org/10.1021/ic0010398.

(25) Peymann, T.; Knobler, C. B.; Hawthorne, M. F. An Icosahedral Array of Methyl Groups Supported by an Aromatic Borane Scaffold: The [Closo-B12(CH3)12]2- Ion. *J. Am. Chem. Soc.* **1999**, *121* (23), 5601–5602. https://doi.org/10.1021/ja990884q.

(26) Peymann, T.; Herzog, A.; Knobler, C. B.; Hawthorne, M. F. Aromatic Polyhedral Hydroxyborates: Bridging Boron Oxides and Boron Hydrides. *Angew. Chem. Int. Ed.* **1999**, *38* (8), 1061–1064. https://doi.org/10.1002/(SICI)1521-3773(19990419)38:8<1061::AID-ANIE1061>3.0.CO;2-B.

(27) Peymann, T.; Knobler, C. B.; Khan, S. I.; Hawthorne, M. F. Dodecahydroxy-Closo-Dodecaborate(2−). *J. Am. Chem. Soc.* **2001**, *123* (10), 2182–2185. https://doi.org/10.1021/ja0014887.

(28) Wixtrom, A. I.; Shao, Y.; Jung, D.; Machan, C. W.; Kevork, S. N.; Qian, E. A.; Axtell, J. C.; Khan, S. I.; Kubiak, C. P.; Spokoyny, A. M. Rapid Synthesis of Redox-Active Dodecaborane B12(OR)12 Clusters under Ambient Conditions. *Inorg. Chem. Front.* **2016**, *3* (5), 711–717. https://doi.org/10.1039/C5QI00263J.

(29) Farha, O. K.; Julius, R. L.; Lee, M. W.; Huertas, R. E.; Knobler, C. B.; Hawthorne, M. F. Synthesis of Stable Dodecaalkoxy Derivatives of Hypercloso-B12H12. *J. Am. Chem. Soc.* **2005**, *127* (51), 18243–18251. https://doi.org/10.1021/ja0556373.

(30) Peymann, T.; Knobler, C. B.; Hawthorne, M. F. An Unpaired Electron Incarcerated within an Icosahedral Borane Cage: Synthesis and Crystal Structure of the Blue, Air-Stable {[Closo-B12(CH3)12]·}− Radical. *Chem. Commun.* **1999**, *0* (20), 2039–2040. https://doi.org/10.1039/A905406E.

(31) Peymann, T.; Knobler, C. B.; Khan, S. I.; Hawthorne, M. F. Dodeca(Benzyloxy)Dodecaborane, B12(OCH2Ph)12: A Stable Derivative of Hypercloso-B12H12. *Angew. Chem. Int. Ed.* **2001**, *40* (9), 1664–1667. https://doi.org/10.1002/1521-3773(20010504)40:9<1664::AID-ANIE16640>3.0.CO;2-O.

(32) Lee, M. W.; Farha, O. K.; Hawthorne, M. F.; Hansch, C. H. Alkoxy Derivatives of Dodecaborate: Discrete Nanomolecular Ions with Tunable Pseudometallic Properties. *Angew. Chem. Int. Ed.* **2007**, *46* (17), 3018–3022. https://doi.org/10.1002/anie.200605126.

(33) Van, N.; Tiritiris, I.; Winter, R. F.; Sarkar, B.; Singh, P.; Duboc, C.; Muñoz-Castro, A.; Arratia-Pérez, R.; Kaim, W.; Schleid, T. Oxidative Perhydroxylation of [Closo-B12H12]2− to the Stable Inorganic Cluster Redox System [B12(OH)12]2−/.−: Experiment and Theory. *Chem. – Eur. J.* **2010**, *16* (37), 11242–11245. https://doi.org/10.1002/chem.201001374.

(34) Boeré, R. T.; Kacprzak, S.; Keßler, M.; Knapp, C.; Riebau, R.; Riedel, S.; Roemmele, T. L.; Rühle, M.; Scherer, H.; Weber, S. Oxidation of Closo-[B12Cl12]2− to the Radical Anion [B12Cl12].− and to Neutral B12Cl12. *Angew. Chem. Int. Ed.* **2011**, *50* (2), 549–552. https://doi.org/10.1002/anie.201004755.

(35) Boeré, R. T.; Derendorf, J.; Jenne, C.; Kacprzak, S.; Keßler, M.; Riebau, R.; Riedel, S.; Roemmele, T. L.; Rühle, M.; Scherer, H.; et al. On the Oxidation of the Three-Dimensional Aromatics [B12X12]2− (X=F, Cl, Br, I). *Chem. – Eur. J.* **2014**, *20* (15), 4447–4459. https://doi.org/10.1002/chem.201304405.

(36) Malischewski, M.; Bukovsky, E. V.; Strauss, S. H.; Seppelt, K. Jahn–Teller Effect in the B12F12 Radical Anion and Energetic Preference of an Octahedral B6(BF2)6 Cluster Structure over an Icosahedral Structure for the Elusive Neutral B12F12. *Inorg. Chem.* **2015**, *54* (23), 11563–11566. https://doi.org/10.1021/acs.inorgchem.5b02256.

(37) Messina, M. S.; Axtell, J. C.; Wang, Y.; Chong, P.; Wixtrom, A. I.; Kirlikovali, K. O.; Upton, B. M.; Hunter, B. M.; Shafaat, O. S.; Khan, S. I.; et al. Visible-Light-Induced Olefin Activation Using 3D Aromatic Boron-Rich Cluster Photooxidants. *J. Am. Chem. Soc.* **2016**, *138* (22), 6952–6955. https://doi.org/10.1021/jacs.6b03568.

(38) Axtell, J. C.; Messina, M. S.; Liu, J.-Y.; Galaktionova, D.; Schwan, J.; Porter, T. M.; Savage, M. D.; Wixtrom, A. I.; Rheingold, A. L.; Kubiak, C. P.; et al. Photooxidative Generation of Dodecaborate-Based Weakly Coordinating Anions. *Inorg. Chem.* **2019**, *58* (16), 10516–10526. https://doi.org/10.1021/acs.inorgchem.9b00935.

(39) Barton, J. L.; Wixtrom, A. I.; Kowalski, J. A.; Qian, E. A.; Jung, D.; Brushett, F. R.; Spokoyny, A. M. Perfunctionalized Dodecaborate Clusters as Stable Metal-Free Active Materials for Charge Storage. *ACS Appl. Energy Mater.* **2019**, *2* (7), 4907–4913. https://doi.org/10.1021/acsaem.9b00610.

(40) Aubry, T. J.; Axtell, J. C.; Basile, V. M.; Winchell, K. J.; Lindemuth, J. R.; Porter, T. M.; Liu, J.-Y.; Alexandrova, A. N.; Kubiak, C. P.; Tolbert, S. H.; et al. Dodecaborane-Based Dopants Designed to Shield Anion Electrostatics Lead to Increased Carrier Mobility in a Doped Conjugated Polymer. *Adv. Mater.* **2019**, *31* (11), 1805647. https://doi.org/10.1002/adma.201805647.

Chapter 2

PHOTOCHEMISTRY OF $B_{12}(OR)_{12}$

Parts of the work discussed in this chapter was published in Axtell, J. C.; Messina, M. S.; Liu, J.-Y.; Galaktionova, D.; Schwan, J.; Porter, T. M.; Savage, M. D.; Wixtrom, A. I.; Rheingold, A. L.; Kubiak, C. P.; et al. Photooxidative Generation of Dodecaborate-Based Weakly Coordinating Anions. *Inorg. Chem.* **2019**, *58* (16), 10516–10526. The paper can be found in its entirety in Appendix A.

Chapter 2 summarizes my contributions to a broad collaborative effort exploring the photochemistry of $B_{12}(OR)_{12}$ *clusters. Much of the results presented here have not previously been published, and the discussion is at times speculative. That said, our observations helped direct mechanistic and computation work reported in the paper mentioned above and could assist in guiding future research.*

The hypercloso-$B_{12}(OR)_{12}$ *clusters* $B_{12}(OC_6F_5)_{12}$ (**F_{60}^{0}**), $B_{12}(4\text{-}CF_3\text{-}C_6H_4)_{12}$ (**F_{36}^{0}**), $B_{12}(3,5\text{-}(CF_3)_2\text{-}C_6H_3)_{12}$ (**F_{72}^{0}**) *and* $B_{12}(3,5\text{-}(CF_3)_2\text{-}C_6F_3)_{12}$ (**F_{84}^{0}**) *form small amounts of anionic* $[B_{12}]^{1-}$ *in many solvents.* $[B_{12}]^{1-}$ *show fluorescence centered at 600 nm. This complicates photophysical characterization of* B_{12}^{0}*, as the emission spectrum is often dominated by* $[B_{12}]^{1-}$*. We sought to understand what causes formation of* $[B_{12}]^{1-}$ *and find ways to eliminate its contribution to the emission spectra of* B_{12}^{0}*. Some instances of* $[B_{12}]^{1-}$ *formation can be explained by direct solvent oxidation or photooxidation, however, our results suggest that complex solvent-cluster interactions may also play a role. Furthermore, we found that* $[B_{12}]^{1-}$ *disproportionate in the presence of trifluoracetic acid, and at cryogenic temperatures in 2-methyltetrahydrofuran. Our work culminated in collection of emission data for* **F_{36}^{0}**, **F_{60}^{0}**, *and* **F_{72}^{0}** *at 77 K in 10:1 perfluorotoluene/perfluoro-methylcyclohexane glass.*

2.1 Background

Icosahedral dodecaborate clusters have been known since the late 1950s, when Lipscomb and co-workers first synthesized *closo*-$[B_{12}H_{12}]^{2-}$.[2–9] These closed-shell clusters display no visible absorption bands due to the large energy gap between the highest occupied molecular orbital (HOMO) and lowest unoccupied molecular orbital (LUMO). Over the past few decades, a range of hypoelectronic perfunctionalized dodecaborate clusters have been isolated in oxidized *hypocloso*-$[B_{12}]^{1-}$ and *hypercloso*-B_{12}^{0} states (B_{12} denotes a generic perfunctionalized dodecaborate cluster). Early examples include *hypocloso*-$[B_{12}Me_{12}]^{1-}$ (Me = CH_3),[10] *hypocloso*-$[B_{12}X_{12}]^{1-}$ (X = F, Cl, Br, I),[11–13] *hypocloso*-$[B_{12}(OH)_{12}]^{1-}$,[14] *hypocloso*-$[B_{12}(OBz)_{12}]^{1-}$ and *hypercloso*-$B_{12}(OBz)_{12}$ (Bz = $CH_2C_6H_5$).[15] These oxidized dodecaborate clusters undergo structural distortions breaking the fourfold degeneracy of the *closo*-$[B_{12}]^{2-}$ HOMO, which helps stabilize the hypoelectronic cluster core. They also display rich visible absorption spectra due to excitations between lower lying molecular orbitals and the HOMO vacancies resulting from oxidation.

Spokoyny and co-workers first reported the exceptional photooxidizing ability of perfunctionalized dodecaborate clusters in 2016 (Messina et al. 2016).[16] They realized that that *hypocloso*-$B_{12}(OBz)_{12}$ could photoinitiate polymerization of electron-rich styrenes, such as 4-methoxy-styrene (**2a**). Following these findings, they decided to explore whether more oxidizing $B_{12}(OR)_{12}$ clusters could initiate polymerization of less-accessible substrates. Indeed, they found that the perfluorophenyl derivative *hypercloso*-$B_{12}(OCH_2C_6F_5)_{12}$ ($\mathbf{F_{60}}^{0}$; nomenclature based on the number of fluorine atoms) could initiate polymerization of a range of styrenes, including both electron-rich and electron-poor variants (Table 2.1, **2b**-**2i**). Hoping to expand the reactivity to even more challenging monomers, they turned their attention to isobutylene. By ^{1}H- and ^{13}C-NMR, they showed that after 4 hours of 450 nm illumination a highly branched polymer had formed in a 2 mM solution of $\mathbf{F_{60}}^0$ under 1–4 psi isobutylene. A ^{1}H-NMR spectrum of the highly branched poly(isobutylene) product is shown in Figure 2.1. The ability to photoinitiate isobutylene polymerization in a metal-free system is noteworthy, as such reactivity had previously been reserved for transition metal photoinitiators. Time-dependent density functional theory (TD-DFT) was used explain the reactivity by comparing the LUMO energy of *hypercloso*-$B_{12}(OBz)_{12}$ and $\mathbf{F_{60}}^0$ with the HOMO energy of the styrene monomers. Attempts to use TD-DFT to examine the orbitals involved in photoexcitation indicated that the lowest energy electronic transition occur between a low-lying orbital (HOMO-27 in $\mathbf{F_{60}}^0$ and HOMO-15 in $B_{12}(OBz)_{12}$) and the LUMO. Photophysical characterization was performed using both steady-state fluorescence measurements and fluorescence decay measurements. Steady-state measurements with $\mathbf{F_{60}}^0$ in dichloromethane, benzene, trifluoromethylbenzene and 1,2-difluorobenzene showed a fluorescence maximum around 600 nm with highly solvent dependent intensity. $\mathbf{F_{60}}^0$ in dichloromethane showed near-zero fluorescence, while $\mathbf{F_{60}}^0$ in 1,2-difluorobenzene showed medium-to-intense fluorescence. Decay measurements using 355 nm laser excitation gave a lifetime of a few hundreds of picoseconds at 600 nm in acetonitrile and 1,2-dichlorobenzene. Based on the emission data, the excited-state reduction potential of $\mathbf{F_{60}}^0$ was estimated to around 3 V (vs the standard calomel electrode).[16]

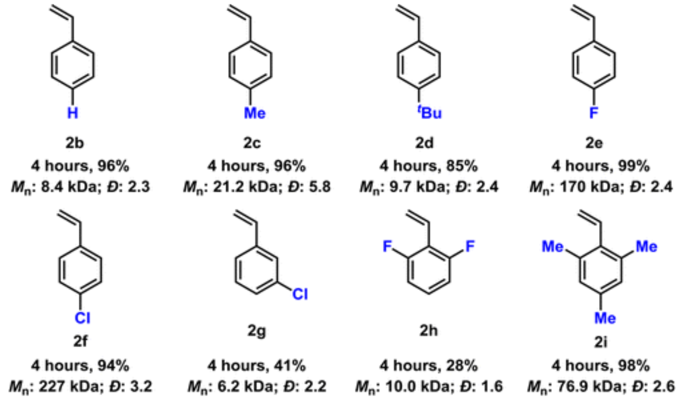

Table 2.1. Monomers polymerized by $\mathbf{F_{60}}^{\mathbf{0}}$ (0.1 mol%) in dichloromethane. Yield, molecular weight (M_n) and dispersity (Đ) shown for each monomer. Reprinted with permission from Messina, M. S.; Axtell, J. C.; Wang, Y.; Chong, P.; Wixtrom, A. I.; Kirlikovali, K. O.; Upton, B. M.; Hunter, B. M.; Shafaat, O. S.; Khan, S. I.; et al. Visible-Light-Induced Olefin Activation Using 3D Aromatic Boron-Rich Cluster Photooxidants. *Journal of the American Chemical Society* **2016**, *138* (22), 6952–6955. Copyright (2016) American Chemical Society.

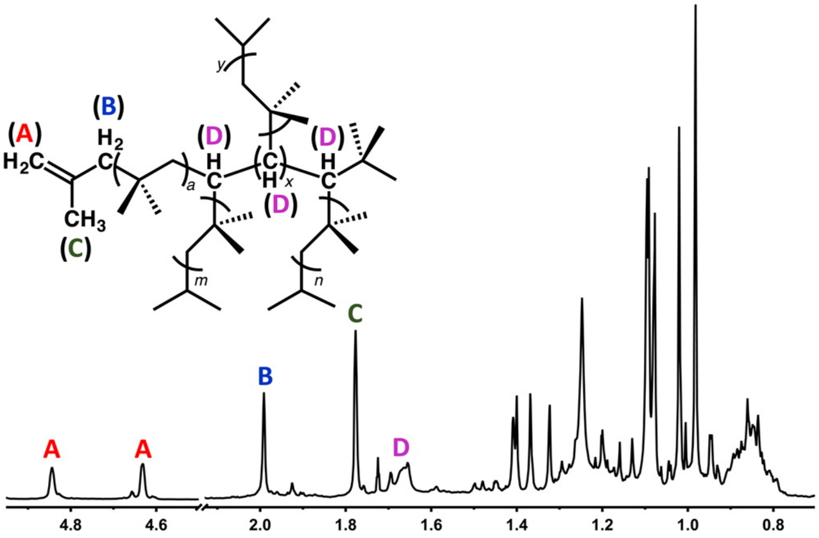

Figure 2.1. ^{1}H-NMR of poly(isobuylene) produced by irradiation of $\mathbf{F_{60}}^0$ with a 450 nm light-emitting diode (LED) under 4 psi isobutylene. Label A indicates protons of the olefinic chain end; B/C, allylic protons of the chain end; D, methine protons. Reprinted with permission from Messina, M. S.; Axtell, J. C.; Wang, Y.; Chong, P.; Wixtrom, A. I.; Kirlikovali, K. O.; Upton, B. M.; Hunter, B. M.; Shafaat, O. S.; Khan, S. I.; et al. Visible-Light-Induced Olefin Activation Using 3D Aromatic Boron-Rich Cluster Photooxidants. *Journal of the American Chemical Society* **2016**, *138* (22), 6952–6955. Copyright (2016) American Chemical Society

2.2 Preliminary Photophysical Studies

The original goal of the work presented in this Chapter was to improve on the results reported in the initial $B_{12}(OR)_{12}$ photooxidation paper (Messina et al. 2016).[16] We knew from our records that the samples used for the published data set had been changing color during collection. At the time, the hypothesis was that the relatively short lifetimes and inconsistent fluorescence spectra resulted from unwanted side reactions caused by trace impurities. We believed these issues could be circumvented by using more stringent sample preparation and handling methods, and that this would lead to lifetimes more consistent with a diffusion controlled photooxidation mechanism.

We started by attempting to collect reproducible emission data and lifetime measurements. In addition to $\mathbf{F_{60}}^0$, the study was expanded to *hypercloso*-$B_{12}(4\text{-}CF_3\text{-}C_6H_4)_{12}$ ($\mathbf{F_{36}}^0$), *hypercloso*-$B_{12}(3,5\text{-}(CF_3)_2\text{-}C_6H_3)_{12}$ ($\mathbf{F_{76}}^0$) and *hypercloso*-$B_{12}(3,5\text{-}(CF_3)_2\text{-}C_6F_3)_{12}$ ($\mathbf{F_{84}}^0$). Based on records from previous researchers we expected that $\mathbf{F_{76}}^0$ and, in particular, $\mathbf{F_{84}}^0$ would be significantly stronger emitters than $\mathbf{F_{60}}^0$. Hoping to combine the strongest emitter with the best solvent, we prepared samples of $\mathbf{F_{84}}^0$ in 1,2-difluorobenzene. Immediately, it became clear that $\mathbf{F_{84}}^0$ was not stable under these conditions, as the sample solution rapidly changed color from yellow to purple. Preliminary fluorescence measurements were, as expected, similar to the published spectra. Hoping to improve the data, we prepared samples of $\mathbf{F_{84}}^0$ under low-light conditions using dry and air-free 1,2-difluorobenzene. No significant color shifts were observed by eye when the samples were prepared under low-light conditions. In direct contrast to our expectations, preliminary fluorescence intensities for these samples were significantly lower than what we had observed for samples prepared under ambient conditions. However, samples turned purple during data collection and the fluorescence intensity rapidly increased as more scans were averaged. The low-light experiments were repeated for $\mathbf{F_{60}}^0$ and $\mathbf{F_{72}}^0$, again displaying significantly reduced fluorescence compared to samples prepared under ambient lighting. Notably, comparison of the three clusters indicated that increased fluorine content was correlated to both stronger preference for the purple state and more intense fluorescence. Reproducible spectra could not be collected under the given conditions and we were unable to obtain excitation spectra that matched the absorption spectra of the neutral clusters. We wonder what the nature of the purple species was and whether it could be responsible for the observed fluorescence spectra.

Comparison of the UV-visible absorption spectrum of the purple $\mathbf{F_{60}}$ samples showed an uncanny resemblance to the published spectrum of $[\mathbf{F_{60}}]^{1-}$. However, the extinction coefficients we observed were several times higher than what had previously been reported for $[\mathbf{F_{60}}]^{1-}$.[16] We hypothesized that the purple species' was the result of B_{12}^0 photoreduction to $[B_{12}]^{1-}$ and that the reported extinction coefficient for $[\mathbf{F_{60}}]^{1-}$ was incorrect. Although this explanation was attractive, we felt photoreduction alone might not be sufficient to rationalize our observations. Our primary concern was that in 1,2-difluorobenzene a weak 525 nm band immediately appeared after mixing, even in the dark. This behavior persisted regardless of solvent manufacturer, and whether the solvent had been dried and degassed. These observations lead to a competing hypothesis: the purple species is the result of cluster-solvent interactions, possibly involving solvent and concentration-dependent cluster aggregation.

2.3 Electrochemical Characterization and the $[B_{12}]^{1-}$ Monoanion

Cyclic voltammograms of $\mathbf{F_{60}}$ and $\mathbf{F_{72}}$ collected at 100 mV/s in 0.2 M $TBAPF_6$ (tetrabutylammonium hexafluorophosphate) dichloromethane electrolyte are shown in Figure

2.2 A-B. Two waves are observed for both clusters, representing the $[B_{12}]^{1-/2-}$ and $[B_{12}]^{0/1-}$ couples. The influence of scan rate (ν) on the peak potential (i_p) was explored to assess the reversibility of the redox events. The electrochemical reversibility is confirmed by the linear relationships between i_p and $(\nu)^{1/2}$, shown in Figure 2.3 (**F**$_{60}$) and 2.4 (**F**$_{72}$) along with individual cyclic voltammograms collected for each redox couple. Table 2.2 summarizes the redox potentials measured for **F**$_{60}$ and **F**$_{72}$.

Table 2.2. Redox potentials derived from a cyclic voltammograms collected at 100 mV/s in 0.2 M TBAPF$_6$ dichloromethane solution. E_p^{ox} and E_p^{red} are the oxidative and reductive peak potentials. $E_{1/2}$ is the mean of the peak potentials. All potentials are referenced to the ferrocene-ferrocenium couple.

	$[\mathbf{F}_{60}]^{1-/2-}$	$[\mathbf{F}_{60}]^{0/1-}$	$[\mathbf{F}_{72}]^{1-/2-}$	$[\mathbf{F}_{72}]^{0/1-}$
E_p^{ox} (V)	-0.124	0.593	0.182	0.922
E_p^{red} (V)	-0.196	0.515	0.097	0.776
$E_{1/2}$ (V)	-0.160	0.554	0.140	0.844

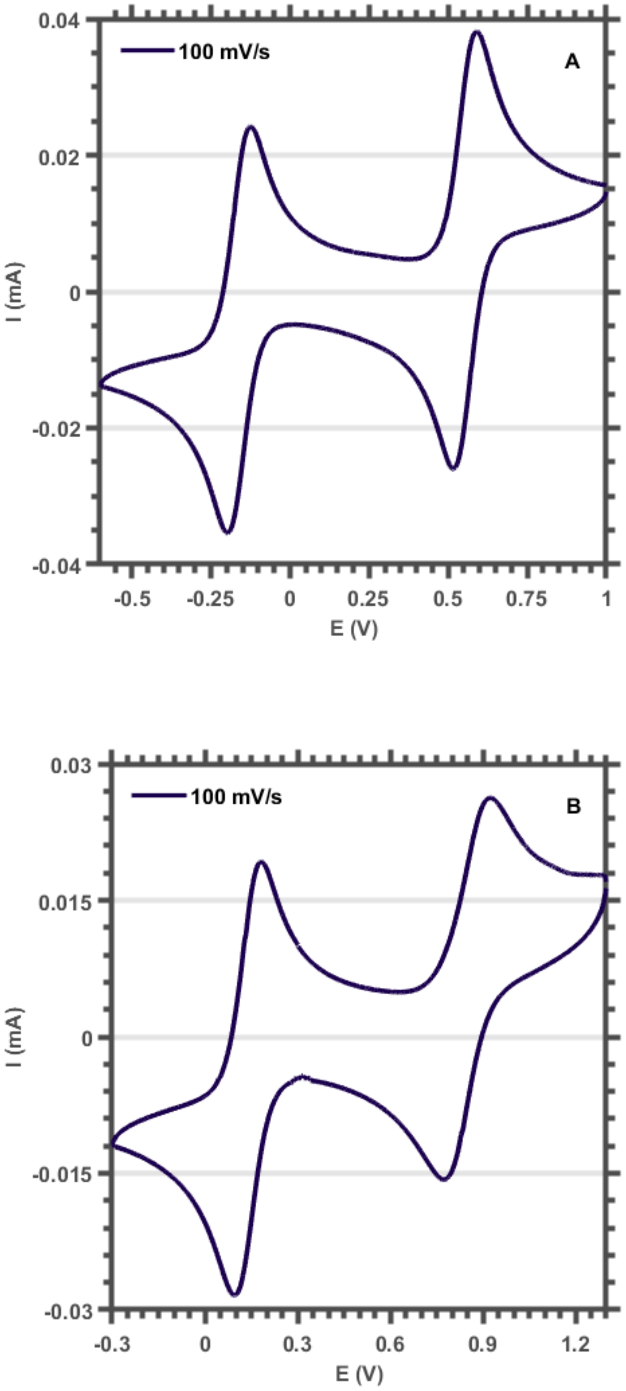

Figure 2.2. Cyclic voltammograms collected for (A) $\mathbf{F_{60}}$ and (B) $\mathbf{F_{72}}$ at 100 mV/s in 0.2 M $TBAPF_6$ dichloromethane electrolyte.

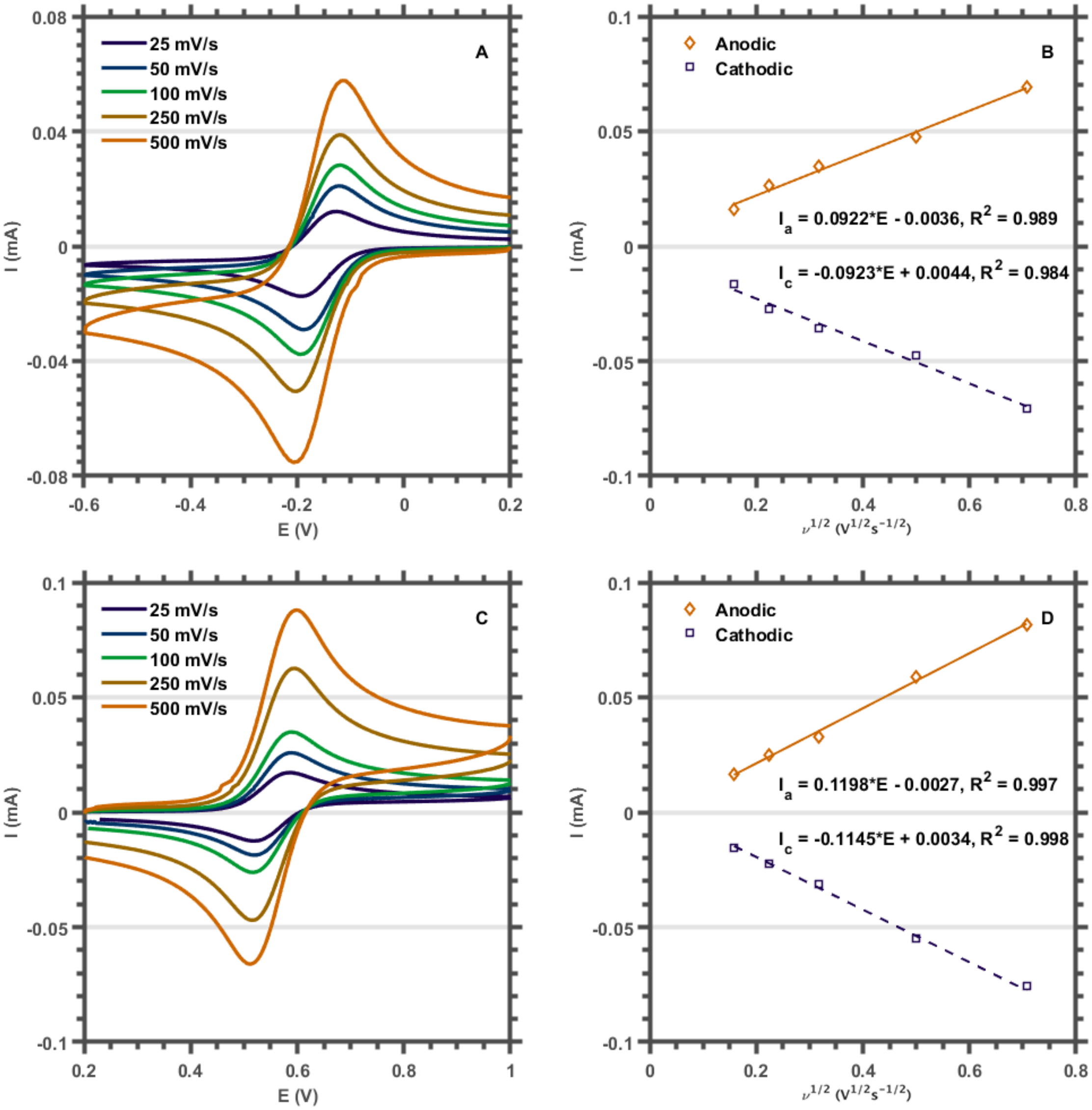

Figure 2.3. Scan rate dependence of 2.5 mM $\mathbf{F_{60}}$ in 0.2 M $TBAPF_6$/dichloromethane. i_a and i_c are the anodic and cathodic peak potentials. ν is the scan rate in V/s. (A) $[\mathbf{F_{60}}]^{1-/2-}$ cyclic voltammograms, (B) $i_p([\mathbf{F_{60}}]^{1-/2-})$ as a function of $(\nu)^{1/2}$, (C) $[\mathbf{F_{60}}]^{1-/2-}$ cyclic voltammograms, (D) $i_p([\mathbf{F_{60}}]^{0/1-})$ as a function of $(\nu)^{1/2}$.

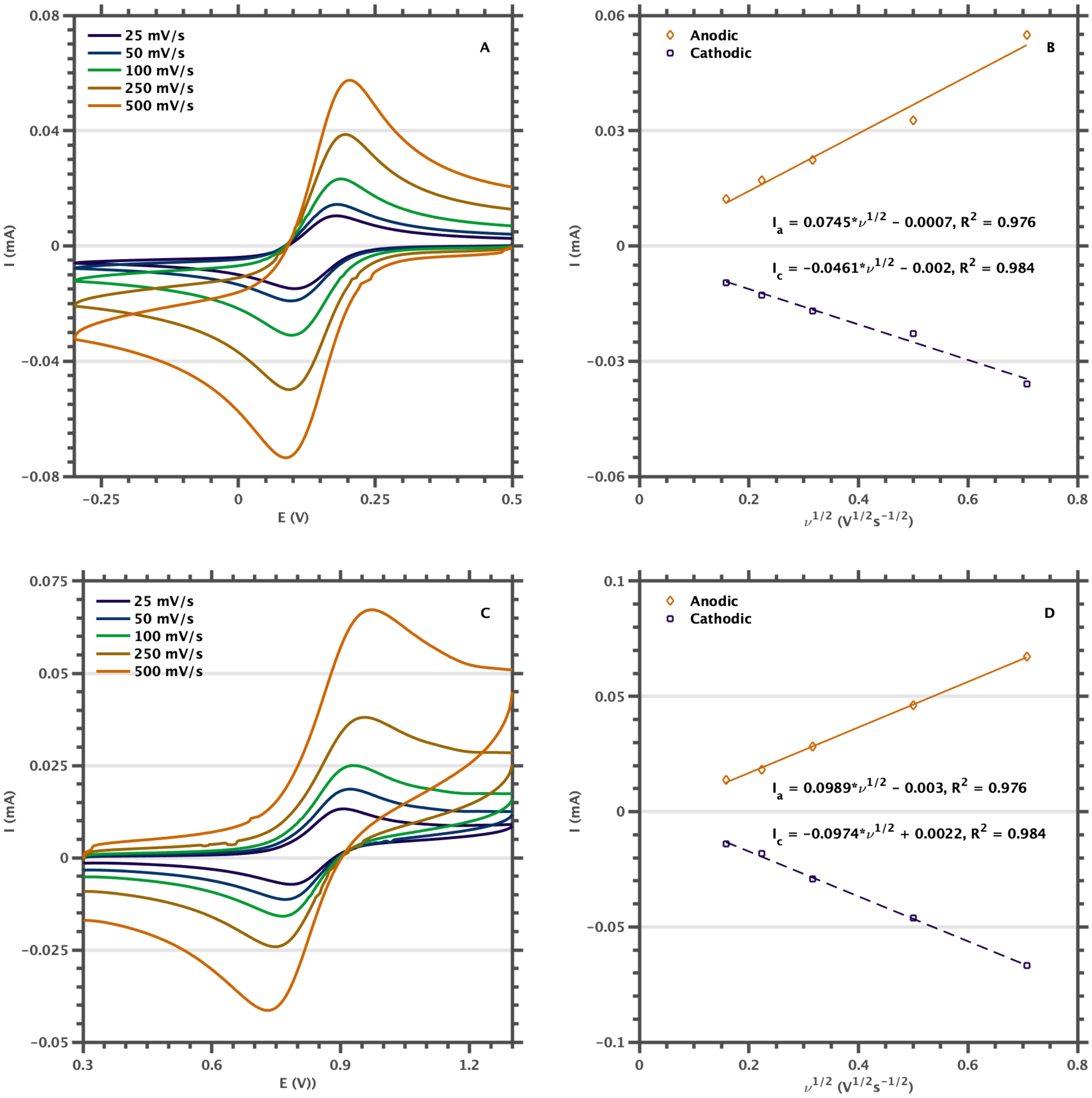

Figure 2.4. Scan rate dependence of ~2.3 mM **F**$_{72}$ in 0.2 M TBAPF$_6$/dichloromethane. i_a and i_c are the anodic and cathodic peak potentials. ν is the scan rate in V/s. (A) [**F**$_{72}$]$^{1-/2-}$ cyclic voltammograms, (B) i_p([**F**$_{72}$]$^{1-/2-}$) as a function of $(\nu)^{1/2}$, (C) [**F**$_{72}$]$^{1-/2-}$ cyclic voltammograms, (D) i_p([**F**$_{72}$]$^{0/1-}$) as a function of $(\nu)^{1/2}$.

Following electrochemical characterization, we used spectroelectrochemistry to show that the published extinction coefficient of the $[\mathbf{F_{60}}]^{1-}$ 525 nm band had been significantly underestimated, and that the true spectrum was in good agreement with the purple species we had observed during our preliminary work. Spectroelectrochemical data collected for $\mathbf{F_{60}}$ in benzonitrile is shown in Figure 2.5 A-B, while Figure 2.6 A-C shows data collected in dichloromethane. In benzonitrile, it proved challenging to achieve complete conversion to $[\mathbf{F_{60}}]^{2-}$ but we were able to successfully achieve near-complete conversion to $\mathbf{F_{60}}^{0}$ and $[\mathbf{F_{60}}]^{1-}$. Significant non-Coulombic currents were passed, indicating that side reactions may have been occurring. In dichloromethane, $\mathbf{F_{60}}$ was taken all the way from $[\mathbf{F_{60}}]^{2-}$ to $\mathbf{F_{60}}^{0}$. This data led us to conclude that $[\mathbf{F_{60}}]^{1-}$ has a visible absorption band at 525 nm with approximately half the extinction coefficient of the 455 nm band of $\mathbf{F_{60}}^{0}$. Later extinction coefficient measurements based on chemically isolated [TBA][$\mathbf{F_{60}}$] and [TBA][$\mathbf{F_{72}}$] further validate these results, finding a strong ~455 nm band for the neutral B_{12} clusters ($\varepsilon_{455nm} \approx 25{,}000\ M^{-1}cm^{-1}$) and a slightly weaker ~525 nm band for the monoanionic $[B_{12}]^{1-}$ clusters ($\varepsilon_{525nm} \approx 13{,}000\ M^{-1}cm^{-1}$). These observations strongly support that the 525 nm band stems from formation of monoanionic $[B_{12}]^{1-}$ cluster.

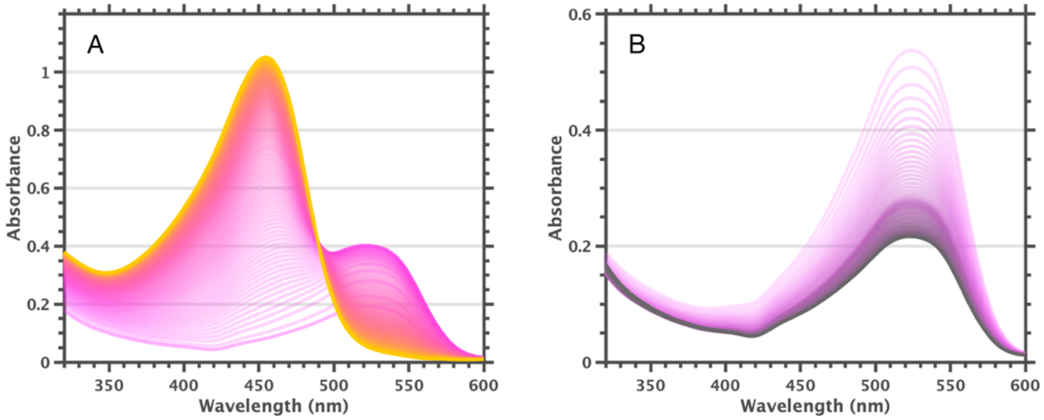

Figure 2.5. Electrochemically derived spectra of $\mathbf{F_{60}}$ collected in 0.1 M TBAPF$_6$/Benzonitrile. (a) [$\mathbf{F_{60}}$]$^{2-/1-}$ mixture oxidized to [$\mathbf{F_{60}}$]$^{1-}$, then $\mathbf{F_{60}}^0$. (b) [$\mathbf{F_{60}}$]$^{1-}$ reduced to a [$\mathbf{F_{60}}$]$^{2-/1-}$ mixture.

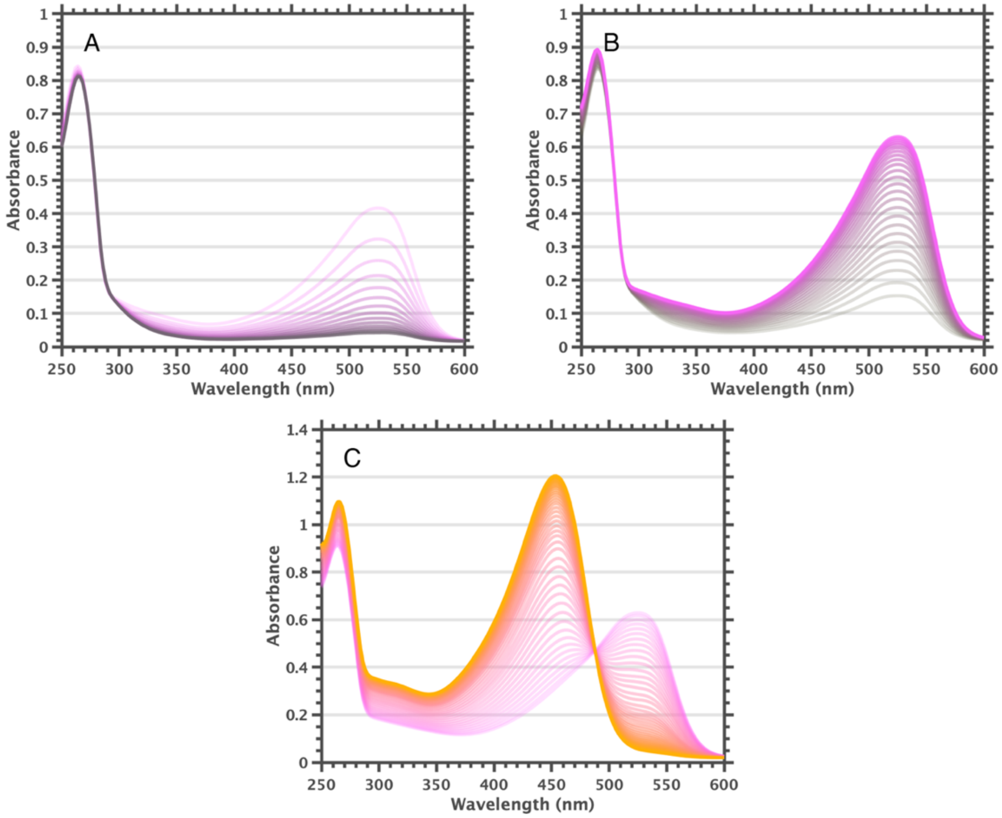

Figure 2.6. Electrochemically derived spectra of $\mathbf{F_{60}}$ collected in 0.1 M TBAPF$_6$/dichloromethane. (a) [$\mathbf{F_{60}}$]$^{1-}$ reduced to [$\mathbf{F_{60}}$]$^{2-}$. (b) [$\mathbf{F_{60}}$]$^{2-}$ oxidized to [$\mathbf{F_{60}}$]$^{1-}$. (c) [$\mathbf{F_{60}}$]$^{1-}$ oxidized to $\mathbf{F_{60}}^0$.

2.4 Interactions with Haloarenes

We now wanted to understand what caused formation $[B_{12}]^{1-}$. As our initial work indicated that conversion to $[B_{12}]^{1-}$ was most strongly favored in 1,2-difluorobezene, we wondered if other halogenated aromatic solvents would also favor $[B_{12}]^{1-}$ and whether concentration-dependent aggregation mechanisms where involved. To explore aggregation, we performed Beer's law measurements of $\mathbf{F_{60}}^0$ in benzene, toluene, chlorobenzene and 1,2-dichlorobenzene (Figure 2.7 A-D). Aggregation-induced spectral changes are unlikely if absorption is linearly dependent on concentration. The 455 nm absorption band showed good agreement with Beers' law (Figure 2.7 E-H) giving no indication of concentration-induced aggregation, although a small 525 nm shoulder was seen in all solvents except chlorobenzene.

A follow-up experiment was performed where a concentrated $\mathbf{F_{60}}^0$ solution in dry and degassed 1,2-dichlorobenzene was slowly added to neat solvent. The stock solution had a bright yellow color implying little contribution from the 525 nm band. UV-visible spectra collected after each addition are shown in Figure 2.8. Remarkably, $[\mathbf{F_{60}}]^{1-}$ dominates the spectrum throughout the concentration series indicating that $\mathbf{F_{60}}^0$ is kinetically inert at higher concentrations but readily converts to $[\mathbf{F_{60}}]^{1-}$ when diluted. This could indicate that, while aggregation does not shift the visible absorption bands, kinetically inert aggregated forms of $\mathbf{F_{60}}^0$ may be present at elevated concentrations.

To further test the cluster-solvent interaction hypothesis, we wanted to find a solvent where $[\mathbf{F_{60}}]^{1-}$ was strongly favored. The results from the Beer's law study indicated that a higher degree of halogenation led to a more pronounced 525 nm shoulder. To test this, we added

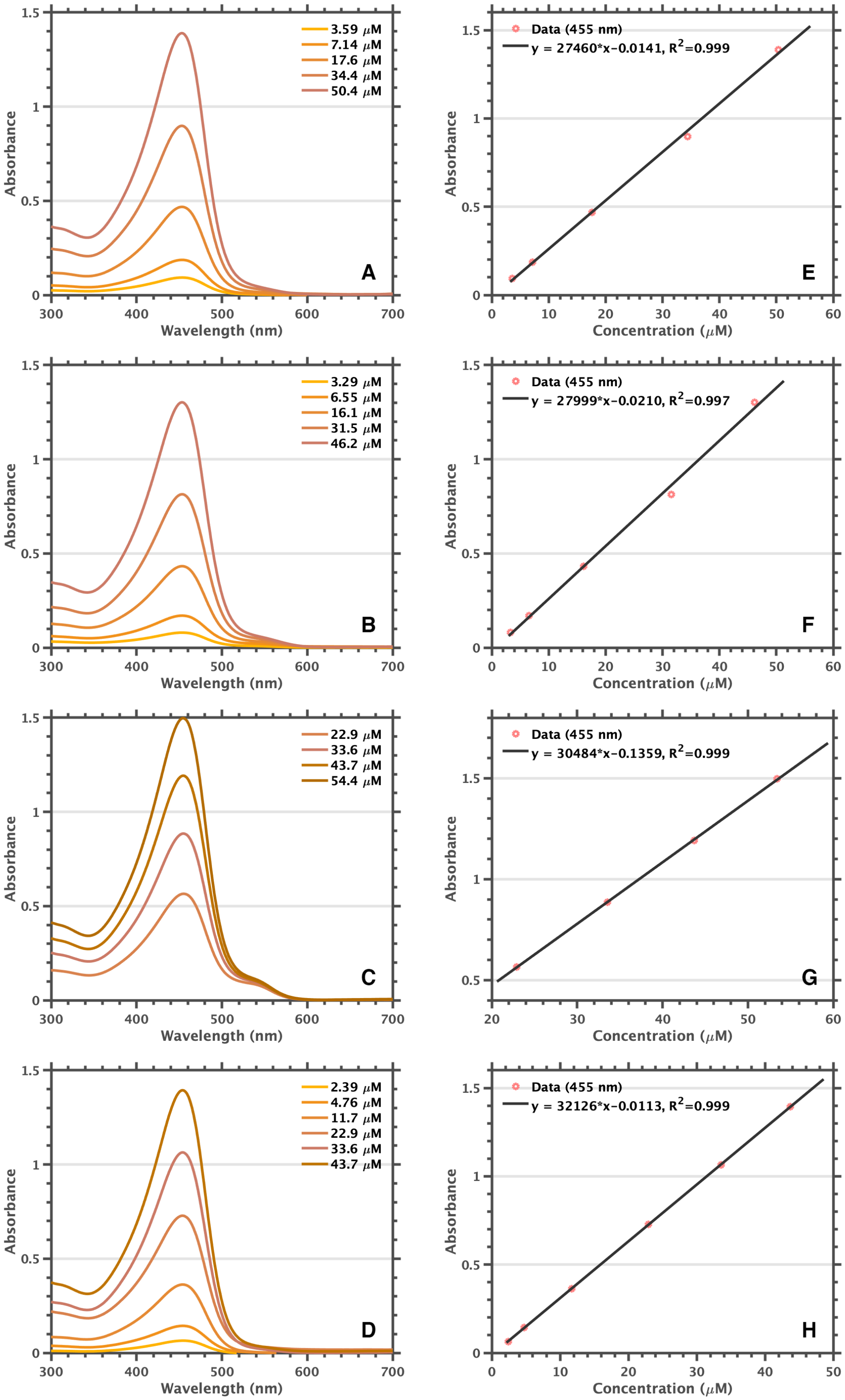

Figure 2.7. Beers' law study of $\mathbf{F_{60}}^0$ in (A, E) benzene, (B, F) toluene, (C, G) 1,2-dichlorobenzene and (D, H) chlorobenzene.

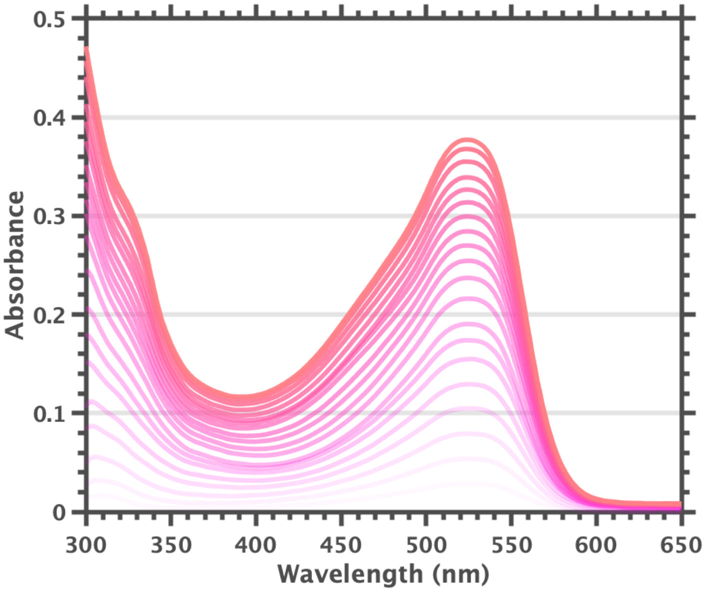

Figure 2.8. $\mathbf{F_{60}}^0$ in dry and degassed 1,2-dichlorobenzene. Slow addition of a concentrated solution to neat solvent. The 525 nm band indicates formation of $[\mathbf{F_{60}}]^{1-}$.

1,2-diiodo-tetrafluorobenzene to $\mathbf{F_{60}}^0$ and $\mathbf{F_{84}}^0$ samples prepared in 1,2-difluorobenzene. Spectra collect with and without 1,2-diiodo-tetrafluorobenzene are shown in Figure 2.9 (A-B). For $\mathbf{F_{60}}^0$ only a small 525 nm shoulder is present in neat 1,2-difluorobenzene. Addition of 1 mM 1,2-diiodo-tetrafluorobenzene leads to partial conversion to $[\mathbf{F_{60}}]^{1-}$. Increasing the 1,2-diiodo-tetrafluorobenzene concentration to 100 mM makes the effect more pronounced. $\mathbf{F_{84}}^0$ samples show a prominent 525 nm band even in neat 1,2-difluorobenzene and addition of a speck of 1,2-diiodo-tetrafluorobenzene leads to complete conversion to $[\mathbf{F_{84}}]^{1-}$.

Encouraged by these results we moved on to hexafluorobenzene, hoping to see a similar effect. Indeed, addition of a small amount of hexafluorobenzene caused bright yellow solutions of $\mathbf{F_{60}}^0$

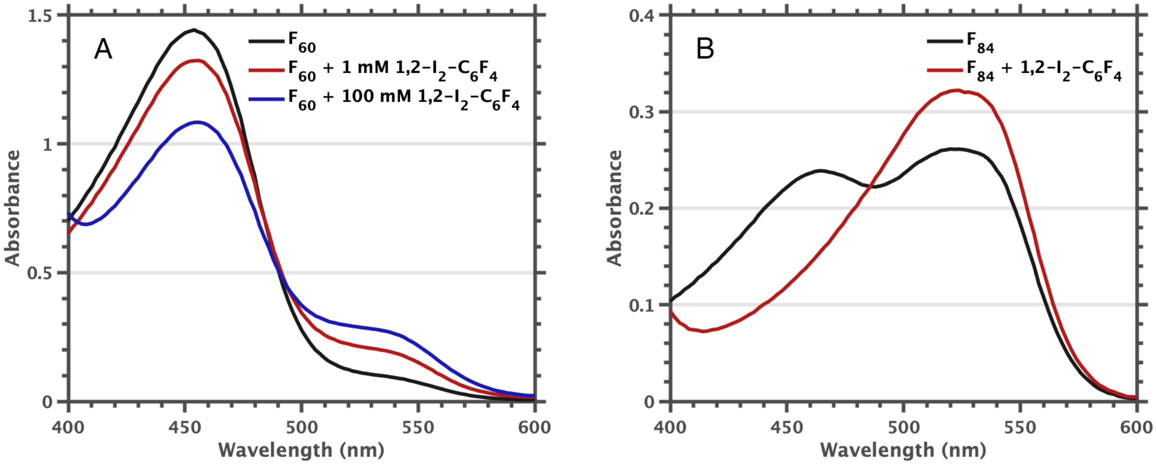

Figure 2.9 Addition of 1,2-diiodotetrafluorobezene to (A) $\mathbf{F}_{60}^{0}$ in 1,2-difluorobenzene and (B) $\mathbf{F}_{84}^{0}$ in 1,2-difluorobenzene.

to rapidly turn pink, indicating conversion to $[\mathbf{F}_{60}]^{1-}$. Figure 2.10 shows UV-visible spectra collected while titrating a chlorobenzene solution of $\mathbf{F}_{60}^{0}$ with hexafluorobenzene. At low hexafluorobenzene concentrations < 0.9 vol % (~80 mM) the absorption bands rapidly stabilize after each addition. However, conversion proceeds slowly at > 2 vol% (~170 mM) under low-light conditions, although rapid conversion can be achieved by illuminating the sample. Figure 2.11 shows the time-evolution of the absorption spectra after a rapid concentration increase from 0.9 vol% (~80 mM) to 2.2 vol% (~190 mM) hexafluorobenzene. The sample was kept in the dark between measurements and intermittent control spectra were taken to assure that the light absorbed during data collection did not significantly impact the spectrum.

The visible spectrum of $\mathbf{F}_{60}^{0}$ and $\mathbf{F}_{84}^{0}$ are very similar, displaying absorption maxima around 455 nm. However, a 525 nm shoulder is generally present in samples prepared in halogenated aromatic solvents. No evidence of aggregation-induced spectroscopic shifts are observed in the

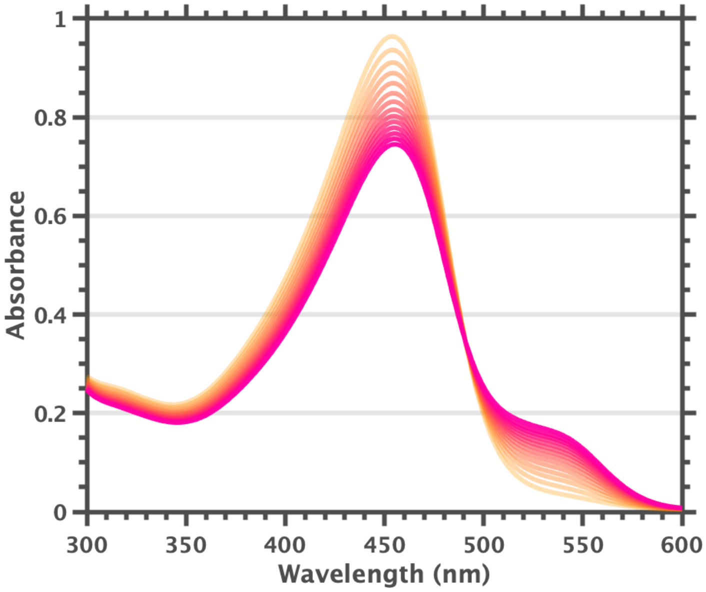

Figure 2.10. **F_{60}**^{0} in chlorobenzene. Titration with 0 – 0.9 vol% hexafluorobenzene.

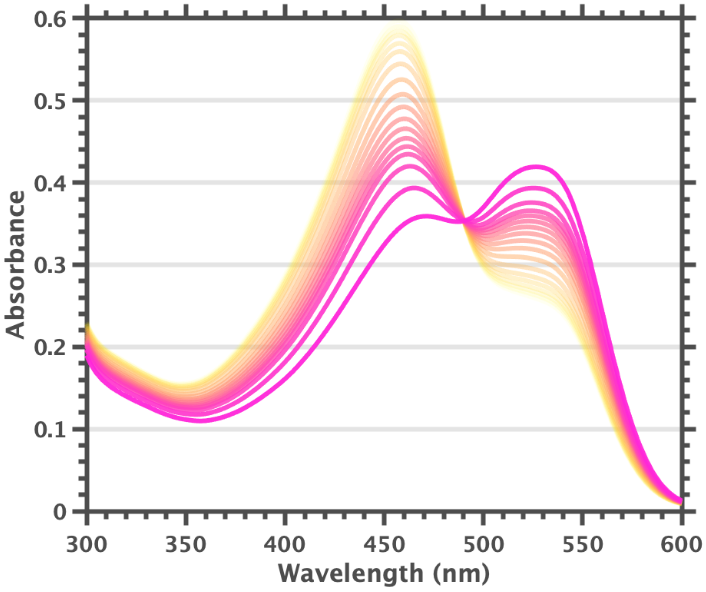

Figure 2.11. **F_{60}** in chlorobenzene. Time-evolution after increasing the hexafluorobenzene concentration from 0.9 vol% (~80 mM) to 2.2 vol% (~190 mM). Data points 1, 2, 3, 5, 7, 10, 15, 20, 25, 30, 35, 40, 45, 50, 60, 80 and 110 minutes after hexafluorobenzene addition.

Beer's Law studies, as expected assuming the 525 nm band stems from $[B_{12}]^{1-}$. However, the strong 525 nm band and near-complete 455 nm bleach resulting from slowly increasing the $\mathbf{F_{60}}^{0}$ concentration in 1,2-dichlorobenzene could signify that B_{12}^{0} in high-concentration solutions exists in a kinetically inert aggregated form. More halogenated haloarenes result in a higher degree of conversion to the $[B_{12}]^{1-}$ state (hexafluorobenzene ≈ 1,2-diiodo-tetrafluorobenzene > 1,2-difluorobenzene > 1,2-dichlorobenzene > chlorobenzene); no 525 nm shoulder is observed under low-light conditions for $\mathbf{F_{60}}^{0}$ in chlorobenzene, while solutions containing a few vol% hexafluorobenzene show a strong 525 nm band and a near-complete bleaching of the 455 nm band (at equilibrium). The effect is further enhanced for $\mathbf{F_{84}}^{0}$. These observations indicate that interactions between the clusters and haloarenes result in a new species displaying the 525 nm band, presumably $[B_{12}]^{1-}$. Non-covalent interactions involving halogenated arenas are well known.[17–19] π-π stacking may occur between the haloarene and the aromatic rings on the clusters, which could induce conformational changes, redistribution of energy levels or formation of charge-transfer complexes. We propose that such interaction may result in modulation of the ring and haloarene molecular orbitals, possibly forming a combined ring-arene orbital. These modulated and/or combined molecular orbitals could act as donor orbitals resulting in $[\mathbf{F_{60}}]^{1-}$-$[\text{haloarene}]^{1+}$ charge-transfer complexes. TD-DFT calculations performed by collaborators in the Král group show that such interactions may a play role in styrene polymerization (see Appendix A). The data we have so far supports this description, however, it remains speculative and requires further experimental validation.

2.5 $[\mathbf{F_{60}}]^{1-}$ Disproportionation

Addition of triethylamine to solutions of $\mathbf{F_{60}}^{0}$ results in rapid conversion to $[\mathbf{F_{60}}]^{1-}$ (high triethylamine concentration leads to reduction to colorless $[\mathbf{F_{60}}]^{2-}$). Titration with strong acids, like trifluoroacetic acid or trifluoromethanesulfonic acid, on the other hand, restores the 455 nm and completely bleaches the 525 nm band. In fact, reversible bleaching and in-growth of the 455 nm and 525 nm bands can be achieved by addition of base followed by addition of acid, or vice versa. Figure 2.12 shows a trifluoroacetic acid titration of a 2 ml 2.5 μM $\mathbf{F_{60}}^0$ solution in 1,2-dichlorobenzene. The sample had been prepared by slow addition of a concentrated stock solution, so that the spectrum was dominated by $[\mathbf{F_{60}}]^{1-}$ (*vide supra*). 500 μl of a 1 vol% trifluoroacetic acid in 1,2-dichlorobenzene solution was added in 25 μl increments, resulting in samples containing between 0 and 26 mM trifluoroacetic acid. At 26 mM trifluoroacetic acid a small 525 nm shoulder is observed along with a strong 455 nm band. Addition of a 1% solution of triethylamine in 1,2-dichlorobenzene (225 μl in 25 μl increments) fully restores the 525 nm band, indicating complete recovery of $[\mathbf{F_{60}}]^{1-}$ at approximately 60 mM triethylamine (Figure 2.13).

It is notable that the magnitude of the 455 nm band at 26 mM trifluoroacetic acid is approximately the same as the magnitude of the 525 nm band of the starting solution. 1:1 conversion between $[\mathbf{F_{60}}]^{1-}$ and $\mathbf{F_{60}}^0$ should result in a 455 nm band of approximately twice the magnitude, given that $\varepsilon_{455nm}(\mathbf{F_{60}}^0)/\varepsilon_{525nm}([\mathbf{F_{60}}]^{1-}) \approx 2$ (see Section 2.2). These results indicate that only about half of $[\mathbf{F_{60}}]^{1-}$ is converted into $\mathbf{F_{60}}^0$, which suggest acid-induced disproportion into $\mathbf{F_{60}}^0$ and colorless $[\mathbf{F_{60}}]^{2-}$ (eq. 2.1).

$$[\boldsymbol{F_{60}}]^{1-} \rightleftharpoons {}^{1}/_{2}\,\boldsymbol{F_{60}}^{0} + {}^{1}/_{2}\,[\boldsymbol{F_{60}}]^{2-} \tag{2.1}$$

To understand this reactivity, we have to consider that triethylamine can act both as a weak reductant and as a weak base. Alone triethylamine acts as a reductant, reducing $\mathbf{F_{60}}^0$ to $[\mathbf{F_{60}}]^{1-}$. However, if triethylamine is added to the solution after acid-induced disproportionation, it

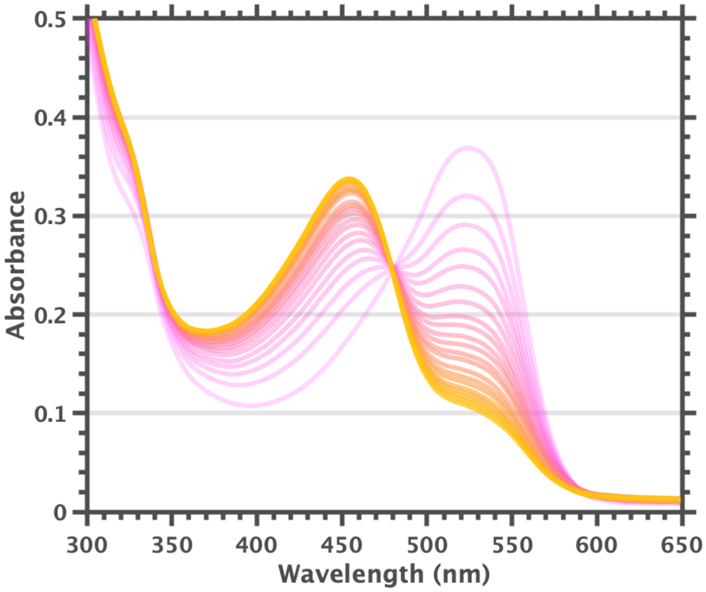

Figure 2.12. Titration of 2.5 μM [**F$_{60}$**]$^{1-}$ with trifluoroacetic acid. Each data point corresponds to addition of 25 μl 1% trifluoroacetic acid in 1,2-dichlorobenzene.

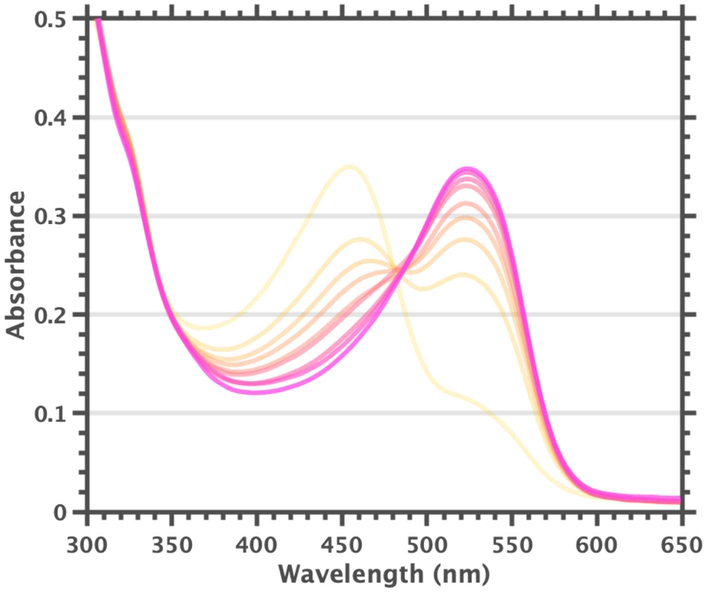

Figure 2.13. Recovery of [**F$_{60}$**]$^{1-}$ by addition of triethylamine. Each data point corresponds to addition of 25 μl 1% triethylamine in 1,2-dichlorobenzene.

instead acts as a base and reverses the disproportionation, either by decreasing the acidity or the ion strength of the solution. If $\mathbf{F_{60}}^0$ had instead been reduced by triethylamine, it would be apparent from following acid addition experiments, as multiple disproportionation-reduction cycles would result in accumulation of $[\mathbf{F_{60}}]^{2-}$ and lead to decoloration of the solution.

Variable temperature UV-visible studies in 2-methyltetrahydrofuran (2-MeTHF) show similar reversible color shifts. The room-temperature UV-visible spectrum of equilibrated 2-MeTHF solutions of $\mathbf{F_{60}}^0$ imply complete conversion to $[\mathbf{F_{60}}]^{1-}$. The conversion proceeds in the absence of light but is significantly faster under illumination. Intriguingly, visual observations suggest that cooling to 77 K (in 2-MeTHF glass) results in reoxidation to $\mathbf{F_{60}}^0$. In fact, the solution reversibly shifts color from deep purple at room temperature to bright yellow at 77 K. This behavior can be repeated over many freeze-thaw cycles. However, samples exposed to ambient lighting become paler over extended periods (hours) and remain purple at 77 K. A photograph displaying the prominent color shift observed upon freezing a fresh 2-MeTHF solution of $\mathbf{F_{60}}^0$ in liquid nitrogen is shown in Figure 2.11. Variable temperature UV-visible spectra (Figure 2.12) of $\mathbf{F_{60}}^0$ collected from 0ºC to -130ºC display a small 455 nm shoulder in the ≤ -100ºC range, suggesting that the yellow color stems from the 455 nm band. However, we are at this time unable to reach sufficiently low temperatures to clearly resolve the 455 nm band. (It is worth nothing that we observe vibrionic progression in the 525 nm band at cryogenic temperatures, with a spacing of ~500 cm^{-1}. This approximately matches the energy of B_{12}-core Raman breathing modes.[20]) Based on these observation, we hypothesize that $\mathbf{F_{60}}^0$ in 2-MeTHF fully converts to $[\mathbf{F_{60}}]^{1-}$ through (photo)oxidation of solvent, and that cooling to cryogenic temperatures result in disproportionation, yielding a spectrum dominated by the $\mathbf{F_{60}}^0$ 455 nm band. Over extended periods in ambient lighting, $[\mathbf{F_{60}}]^{1-}$ is converted to $[\mathbf{F_{60}}]^{2-}$ through solvent photooxidation. The increased [$\mathbf{F}_{60}$]$^{2-}$ concentration shifts the equilibrium so that disproportionation is no longer favored at 77 K.

The low-temperature behavior of $\mathbf{F_{60}}^0$ in 2-MeTHF was further explored by variable temperature ^{11}B- and ^{19}F-NMR collected from +65°C to -120°C. Based on the UV-visible spectrum, we assume complete conversion to [$\mathbf{F_{60}}$]$^{1-}$ at room temperature. The ^{11}B-NMR spectrum is featureless over the entire temperature range, as expected for paramagnetic [$\mathbf{F_{60}}$]$^{1-}$ (Figure 2.13). In line with previous reports,[21] the ^{19}F-NMR spectrum at ≥ +20°C shows two sharp resonances (1F, -158 ppm; 2F -165 ppm) corresponding to the meta and para positions on the perfluorophenyl rings. Additionally, a broad resonance is observed at -140 ppm, possibly stemming from the ortho position. Curiously, the fluorine resonances show significant broadening at lower temperatures and are near indistinguishable at -120°C (Figure 2.14).

The acid-base titration data and variable temperature UV-visible spectra suggest a disproportionation mechanism. Conversely, the lack of resonances in the variable temperature ^{11}B-NMR spectra indicate that the cluster remains paramagnetic. Low temperature and altered ionic strength is known to induce dimerization and other aggregation behaviors in some aromatic systems, which could lead to redistribution of charge and disproportionation.[22–25] We hypothesize that such disproportionated dimers/aggregates might form in 2-MeTHF at cryogenic temperatures, and could contribute to the broadening of the ^{19}F-NMR signals. The silent ^{11}B-NMR spectrum might be misleading, as the $\mathbf{F_{60}}^0$ and [$\mathbf{F_{60}}$]$^{2-}$ resonances could be too faint to be observable over the probe background. This explanation is corroborated by UV-visible spectra collected around -100°C, which indicate a low degree of disproportionation at the low-temperature limit of the NMR study.

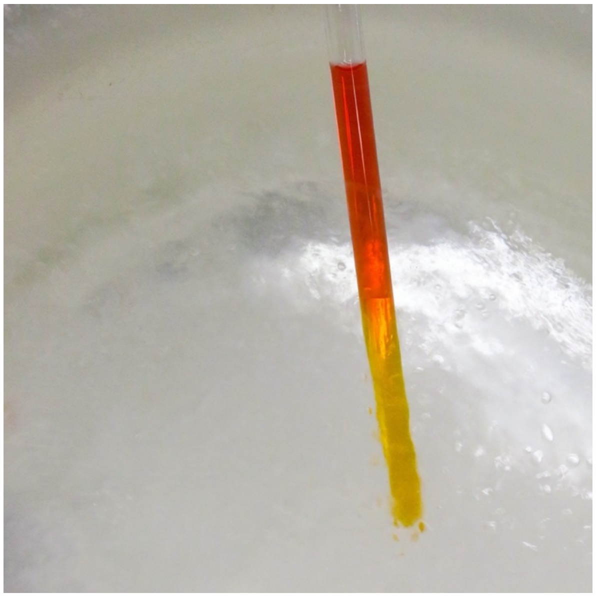

Figure 2.14. **F$_{60}$** in 2-MeTHF frozen in liquid nitrogen. The color shift is rapid and reversible.

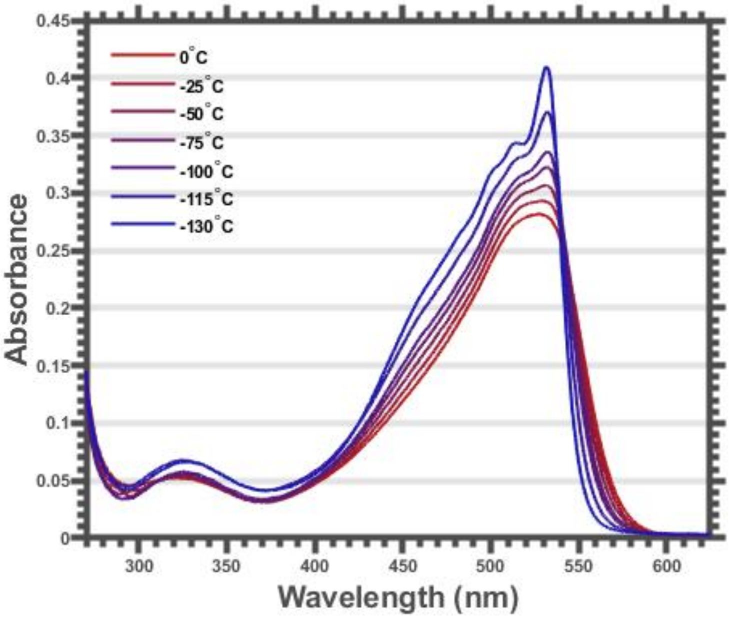

Figure 2.15. Variable temperature UV-visible spectra of **F$_{60}$** in 2-MeTHF collected from 0ºC to -130ºC. A 455 nm shoulder grows in at ≤ -100ºC.

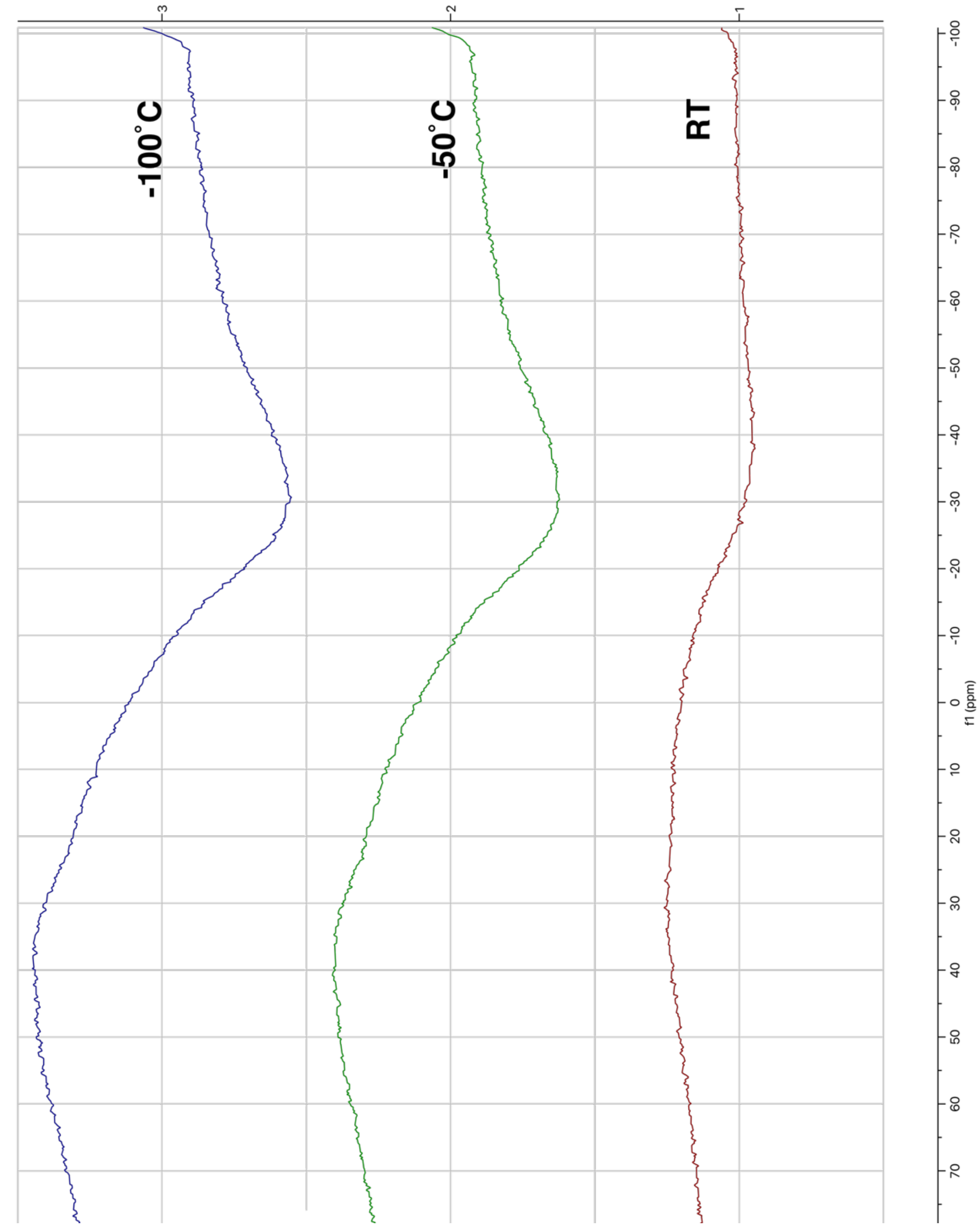

Figure 2.16. $\mathbf{F_{60}}^{0}$ in 2-MeTHF. ^{11}B-NMR collected at room temperature (red), -50°C (green) and -100°C (blue). Only the probe background signal is observed.

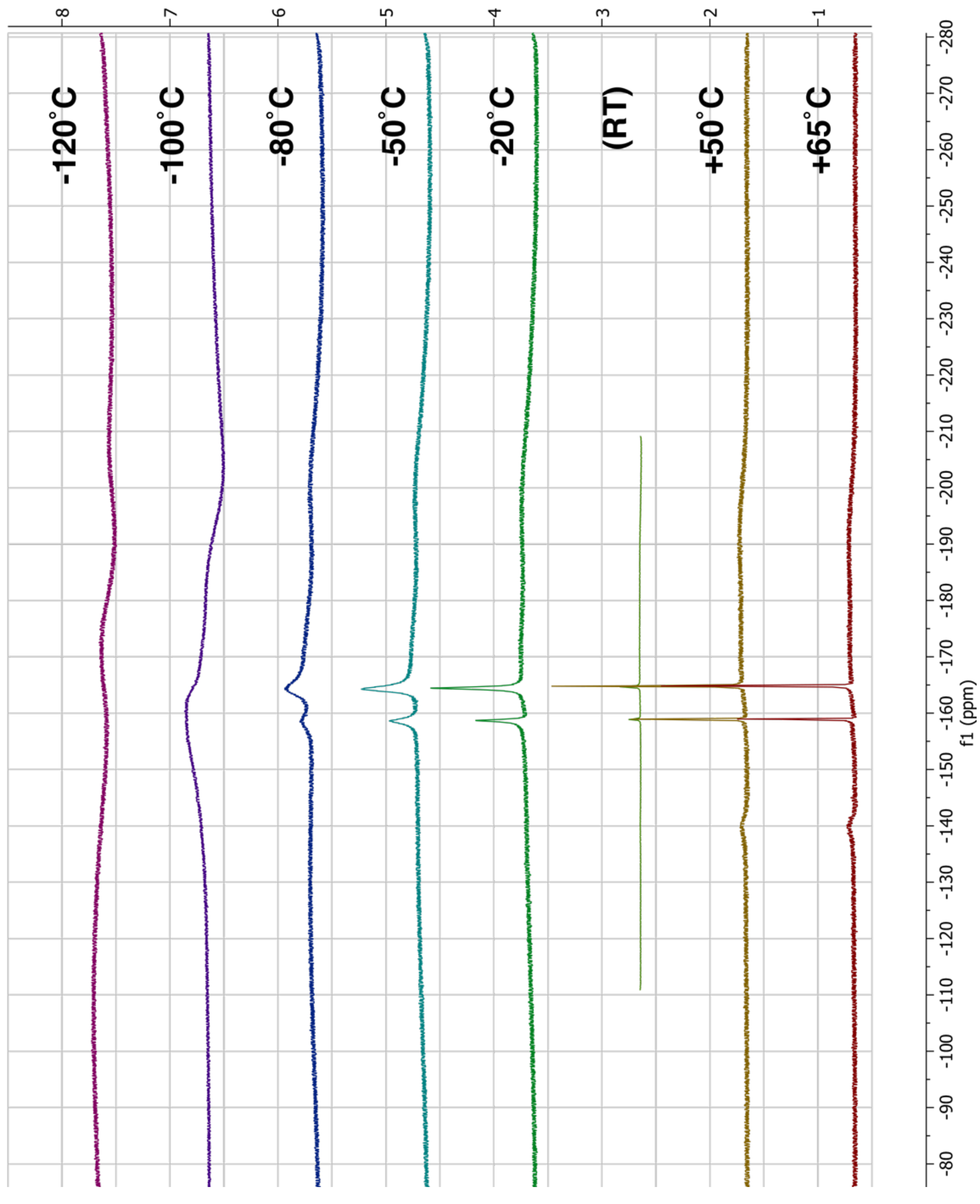

Figure 2.17. **F_{60}**^{0} in 2-MeTHF. Variable temperature ^{19}F-NMR spectra collected from +65°C to -120°C.

2.6 *hypercloso*-$B_{12}(OR)_{12}^0$ Emission

Although unable to definitively explain what causes the formation of the $[B_{12}]^{1-}$, we felt confident that obtaining reliable fluorescence spectra was dependent on preparation of samples containing only the 455 nm absorbing B_{12}^0 species. To determine optimal conditions, we explored two paths: (1) rigorous solvent purification and sample preparation and (2) exploration of alternative solvents. If formation of $[B_{12}]^{1-}$ by oxidation/photooxidation of impurities was the key issue, pure samples would be obtainable by sufficiently rigorous purification and sample preparation practices. However, if cluster-solvent interactions were involved, we would need to identify sufficiently non-interacting and oxidatively inert solvents.

We started by exploring the solvent purification path. Increasingly rigorous procedures were employed to prepare pure samples of $\mathbf{F_{60}^0}$ in benzene, toluene, 1,2-difluorobenzene and dichloromethane. Briefly, high-purity solvents were obtained (inhibitor free when relevant) and immediately dried over activated 3 Å molecular sieves for > 96 hours. After drying, solvents were distilled into Strauss flasks, discarding the initial and finals fractions. All manipulations were performed on a vacuum/argon manifold, with all glassware connected through glass joints. Ultra-high-purity argon, which was passed through oxygen and water scrubbers before entering the gas manifold, was used for all experiments. All glassware that came in contact with solution was cleaned in aqua regia before use. Following these procedures, no 525 nm shoulder was observed in the UV-visible spectra of $\mathbf{F_{60}}^0$ samples prepared under low-light conditions in dichloromethane, benzene and toluene. Upon prolonged and/or intense light-exposure, a minor 525 nm shoulder could be observed in both benzene and toluene. No fluorescence signal was observed above noise in any of these samples (450 nm excitation). UV-visible spectra of all $\mathbf{F_{60}}^0$ samples prepared in 1,2-difluorobenzene displayed a 525 nm shoulder, which grew when the sample was illuminated. Weak-to-medium intensity fluorescence, centered around 600 nm, was observed in these samples following 450 nm excitation. Further purification of 1,2-difluorobenzene, or use of solvents from different manufacturers, did not remove the 525 nm shoulder. These observations suggest that $[\mathbf{F_{60}}]^{1-}$ causes the 600 nm fluorescence. Solutions of $\mathbf{F_{60}}^{0}$ in 2-MeTHF, which appear to undergo complete conversion to $[\mathbf{F_{60}}]^{1-}$, provides further support of assigning the 600 nm fluorescence band to $[\mathbf{F_{60}}]^{1-}$. Figure 2.15 shows absorption, excitation and emission spectra of $\mathbf{F_{60}}$ in 2-MeTHF. The visible spectrum is identical to electrochemically generated $[\mathbf{F_{60}}]^{1-}$, and perfectly matched by the excitation spectrum.

As rigorous purification and sample preparation did not yield reliable fluorescence at room temperature, we started exploring alternative solvents. Dry and degassed octafluorotoluene was the only solvent were no formation of $[\mathbf{F_{60}}]^{1-}$ was observed at concentrations relevant for spectroscopy. Samples of $\mathbf{F_{60}}^{0}$ prepared in dry and degassed octafluorotoluene are stable for > 1 month under ambient lighting and show no spectral changes after prolonged laser illumination. Disappointingly, no fluorescence was observed for $\mathbf{F_{60}}^{0}$ solutions in octafluorotoluene at room temperature (450 nm excitation). We concluded that $\mathbf{F_{60}}^{0}$ does not display appreciable fluorescence at room temperature.

We turned our attention to low-temperature emission studies. Figure 2.16 shows emission spectra collected for $\mathbf{F_{60}}^{0}$ in toluene and 2-MeTHF glass at 77 K. In line with room-temperature data, $\mathbf{F_{60}}^{0}$ in toluene glass showed fluorescence centered around ~600 nm, likely stemming from trace $[\mathbf{F_{60}}]^{1-}$. In 2-MeTHF glass (freshly prepared), $\mathbf{F_{60}}^{0}$ displays low intensity fluorescence centered around 550 nm. This band could stem from $\mathbf{F_{60}}^{0}$, however, given the unusual temperature-dependent behavior of $\mathbf{F_{60}}^{0}$ in 2-MeTHF (Section 2.5) we felt these results did not provide a reliable representation of the neutral species. We decided to attempt 77 K studies of $[B_{12}]^0$ in octafluorotoluene. Neat octafluorotoluene does not glass well, but addition of ~10% perfluoro-methylcyclohexane results in clear glasses at 77 K. $\mathbf{F_{36}}^0$, $\mathbf{F_{60}}^0$ and $\mathbf{F_{72}}^0$ solutions in 10:1 octafluorotoluene/perfluoro-methylcyclohexane showed weak-to-medium intensity fluorescence at 77 K (Figure 2.17). $\mathbf{F_{36}}^0$ and $\mathbf{F_{72}}^0$ display bimodal emission, which we speculate could be due to the presence of two distinct conformations in solvent glasses. Dimerization mechanisms similar to what we suggested for $\mathbf{F_{60}}^0$ in 2-MeTHF (Section 2.5) may also be in play but seem less likely as the 77 K emission spectrum of $\mathbf{F_{60}}^0$ in 2-MeTHF is uncomplicated. Using the emission data at 77 K, we were able to calculate excited-state reduction potentials for $\mathbf{F_{36}}^0$ (~3.0 V), $\mathbf{F_{60}}^0$ (~ 3.2 V) and $\mathbf{F_{72}}^0$ (~ 3.3 V). Potentials are reported versus the standard calomel electrode (SCE).

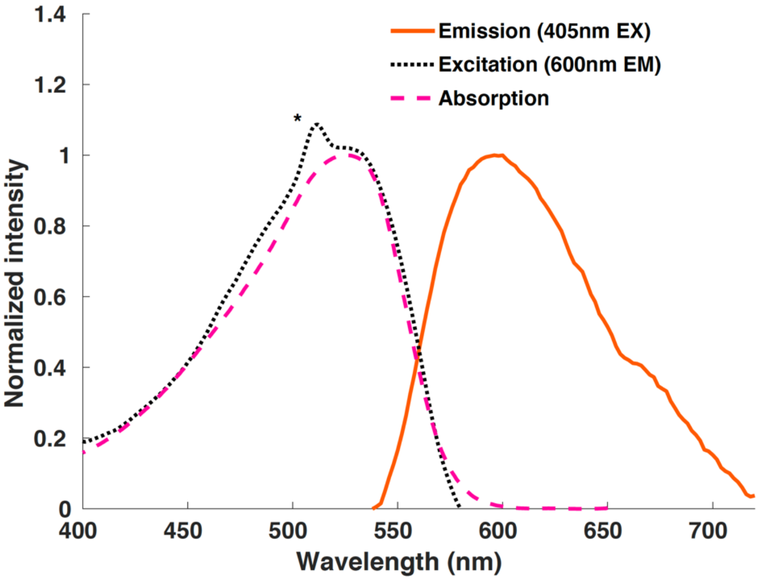

Figure 2.18. Absorption, excitation and emission spectra reported for $\mathbf{F_{60}}$ in 2-MeTHF. The excitation spectrum was collected monitoring 600 nm emission, while the emission spectrum was collected using 405 nm excitation.

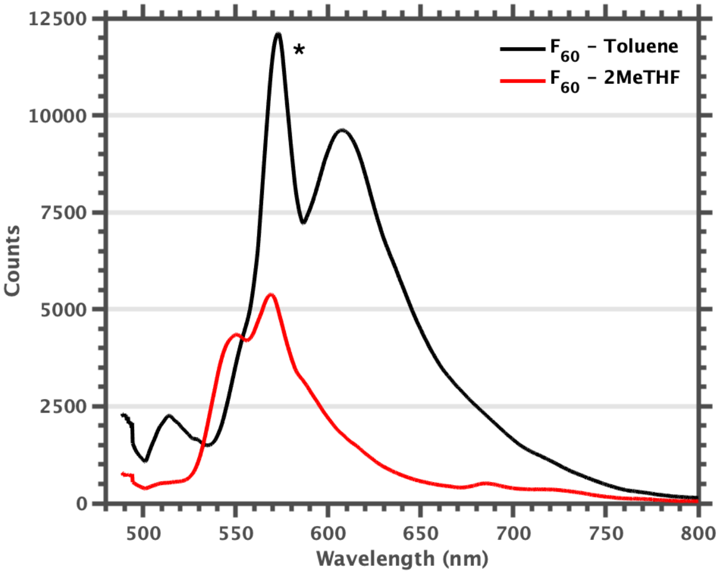

Figure 2.19. Emission spectrum of $\mathbf{F_{60}}^0$ in toluene and 2-MeTHF glass (77 K) excited at 457.9 nm. The peak denoted by * is caused by liquid nitrogen Raman scattering.

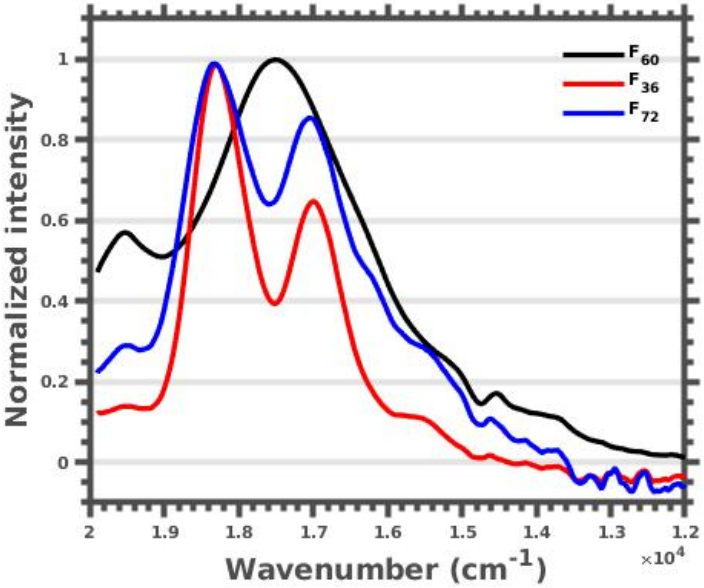

Figure 2.20. Emission spectra of $\mathbf{F_{36}}^0$, $\mathbf{F_{60}}^0$ and $\mathbf{F_{72}}^0$ in 10:1 octafluorotoluene/perfluoro-methylcyclohexane glass (77 K) excited at 457.9 nm.

2.7 Conclusions

Initial observations, reported in the Messina (2016) paper,[16] indicated that $[B_{12}]^0$ has lowest lying excited states with significant charge-transfer character and that the clusters exhibit complex emission stemming from multiple states. However, this was based on three assumptions that have later proved to be false (*vide supra*): (1) only the neutral clusters have strong ($> 10^4$ $M^{-1}cm^{-1}$) visible absorption bands, (2) the electronic transitions of interest must be of charge-transfer character to provide an excited state sufficiently long-lived to perform photochemistry in solution and (3) the clusters are relatively redox-stable in solution. The first assumption came from extinction coefficient measurements performed on isolated monoanionic $[B_{12}(OBz)_{12}]^{1-}$ and $[\mathbf{F_{60}}]^{1-}$ clusters. We now believe that the samples used for the reported extinction coefficient measurements were dominated the colorless dianionic species, which created the illusion of a relatively weak band 525 nm band. The true extinction coefficient of the 525 nm band is $> 10^4$ $M^{-1}cm^{-1}$. Viewing the 455 nm band as a charge-transfer transition makes sense considering the observed photochemistry, however, later work by us (see Chapter 4) has shown that this electronic transition is localized on the cluster core. Assumptions about the stability of the clusters in solution were based on that under the conditions used for photopolymerization reactions, which generally involved millimolar concentrations of the clusters, no noticeable color shifts occurred. At the much lower concentrations required for photophysical characterization illuminated samples quickly change from yellow to red-orange or purple due to cluster reduction.

Spectroelectrochemical data clearly shows that the 525 nm band belongs to $[\mathbf{F_{60}}]^{1-}$. It is our belief that the clusters participate in complex (photo)redox behaviors which explain most instances of $[\mathbf{F_{60}}]^{1-}$ formation. Under low-light conditions no 525 nm band is observed in the UV-visible spectrum of $\mathbf{F_{60}}^0$ in rigorously purified dichloromethane, benzene and toluene, suggesting that the 525 nm band seen in as-received solvents is primarily the result of spurious cluster reduction by impurities. However, after sufficient illumination the 525 nm band grows in even in samples prepared with rigorously purified solvents. These observations are readily explained by solvent photooxidation, consistent with the exceptionally high excited-state redox potential estimated for B_{12}^{0} clusters.

Although direct cluster reduction is a sufficient explanation under the conditions discussed above, interaction studies with haloarenes indicate that other mechanisms are also in play. Given the strong preference for [**F60**]$^{1-}$ in the presence of hexafluorobenzene and other highly halogenated arenes, it is likely that cluster-solvent interactions are involved. That said, it is possible that these observations are caused by impurities, although precautions have been taken to eliminate such contributions.

The room-temperature emission studies presented in this chapter indicate that the B_{12}^{0} excited state rapidly return to the ground state through non-radiative decay. Short lived excited states are not expected to substantially partake in solution based photoredox processes, as non-radiative decay outcompetes diffusion. However, electron transfer could proceed through a rapid tunneling mechanism if non-covalent cluster-monomer interactions occur in the ground state. The cluster-solvent interaction studies presented above, along with the computational work by Král and co-workers (Appendix A), support pre-association of clusters and monomers.

Although many question marks remain, the work presented here provided sufficient insight to guide us toward the computational and mechanistic studies presented in Appendix A. It would be interesting to further explore the intermolecular interactions and disproportionation mechanisms discussed in this chapter. However, we decided to, at least for the moment, leave these questions to the theoreticians. We felt our time was better spent exploring the electrochemical properties and electronic structure of $[B_{12}(OR)_{12}]$ clusters. That work is further discussed in Chapter 3 and 4.

2.8 Experimental Details

$B_{12}(OR)_{12}$ clusters

F_{36}, **F_{60}**, **F_{72}**, **F_{84}** were obtained from the Spokoyny lab and had been synthesized according to published procedures.[16,21]

UV-visible Spectroscopy

UV-visible spectra were collected on a Varian Cary 50 Bio spectrometer using a 1 cm path length quartz cuvettes, unless otherwise noted. All spectra were corrected by subtracting a solvent blank.

Electrochemistry

Sample preparation and electrochemical measurements were performed in an argon-filled glove box. Data was collected on a Gamry 600 Reference Potentiostat, using a small-volume electrochemical cell. Electrochemical grade $TBAPF_6$ (Sigma-Aldrich) had been previously recrystallized from hot ethanol and dried rigorously under vacuum. A d = 3.0 mm glassy carbon working electron (BASi), a Pt wire counter-electron and an Ag/AgCl reference electrode were used (BASi). The reference was prepared by placing a polished silver wire in a 0.01 M $AgNO_3$/0.2 M $TBAPF_6$ acetonitrile solution. A CoralPor (BASi) frit provided electrochemical contact between the reference solution and sample solution. Dichloromethane (Millipore) had been dried for > 84 hours over activated 3 Å molecular sieves (Sigma-Aldrich) and degassed through multiple freeze-pump-thaw cycles. Between each measurement the sample solution was thoroughly mixed, and the working electrode was polished with a Kimwipe (Kimtech) to remove any residue formed during preceding cycles. The EC-Lab software package (Biologic) was used to analyze the data.

Spectroelectrochemistry

The electrochemical setup was the same as described for the electrochemical experiments, with the exceptions noted below. Spectroelectrochemical data was collected on a Pine WaveNow potentiostat, using a 0.5 mm quartz spectroelectrochemistry (BASi) cell and gold mesh working electrode (BASi). Electrolytes were prepared at 0.1 M $TBAPF_6$. The experiments were conducted under ambient conditions. The electrolyte solution was degassed by argon bubbling.

In benzonitrile, the potential was held at +1.5 V to achieve full conversion to $\mathbf{F_{60}}^0$. The potential was the held at +0.2 V until $\mathbf{F_{60}}^0$ had been completely reduced to $[\mathbf{F_{60}}]^{1-}$. Finally, the potential was held at -0.5 V to reduce to $[\mathbf{F_{60}}]^{1-}$ to $[\mathbf{F_{60}}]^{2-}$. Complete conversion to $[\mathbf{F_{60}}]^{2-}$ was not achieved. In dichloromethane $\mathbf{F_{60}}^0$ was first reduced to $[\mathbf{F_{60}}]^{1-}$ by applying a -0.2 V bias (not shown). $[\mathbf{F_{60}}]^{2-}$ was generated by holding the potential at -0.5 V. $[\mathbf{F_{60}}]^{1-}$ was then fully recovered through applying a 0.85 V bias. Finally, $\mathbf{F_{60}}^0$ was regenerated by holding the potential at 2 V. Spectra were collected every 30 seconds.

Beer's Law Study

Toluene (Uvasol, Millipore), benzene (Uvasol, Millipore), chlorobenzene (Sigma-Aldrich) and dichlorobenzene (Sigma-Aldrich) were used as received. Stock solutions were prepared by dissolving $\mathbf{F_{60}}^0$ in toluene (3.6 mg, 0.72 mM), benzene (3.3 mg 0.66 mM), chlorobenzene (2.4 mg, 0.48 mM) and dichlorobenzene (2.4 mg 0.48 mM).

Aliquots of stock solution were added to achieve the desired $\mathbf{F_{60}}^0$ concentration. A flea stir bar was used to thoroughly mix the sample after each stock addition. The samples were given ample time to equilibrate.

Concentration Study

1,2-dichlorobenzene (Sigma-Aldrich) was dried over activated 3 Å molecular sieves for >48 hours before use. All manipulations were performed using standard air-free techniques.

A stock solution was prepared by dissolving 1.7 mg $\mathbf{F_{60}}^0$ in in 5 ml 1,2-dichlorobenzene. The solution was degassed by three 15 minute freeze-pump-thaw cycles. Neat solvent was separately freeze-pump-thawed over three 15 minute cycles, and 1.5 ml was transferred to septum sealed cuvette equipped with a flea stir bar. Stock solution was added 25 ul at a time using a gas-tight syringe. The sample was allowed to equilibrate under stirring after each addition. A spectrum was collected for each equilibrated solution.

Interaction with 1,2-Iodo-Tetrafluorobenzene

A stock solution of $\mathbf{F_{60}}^0$ in 1,2-difluorobenzene was prepared at approximately 50 μM concentration. A spectrum was collected of the neat $\mathbf{F_{60}}^0$ solution. Two 5 ml aliquots were taken aside for interaction experiments. ~2 mg (1 mM) 1,2-diiodo-tetrafluorobenzene was added to one of the 5 ml aliquots and ~200 mg (200 mM) 1,2-diiodotetrafluorobezene was added to the second 5 ml aliquot. The samples were given ample time to equilibrate. Final data were collected when the spectrum remained steady for several minutes.

A speck of $\mathbf{F_{84}}^0$ was added to a cuvette containing 3 ml 1,2-difluorobenzene. A spectrum was collected of the neat $\mathbf{F_{84}}^0$ solution. Then a small speck of 1,2-diiodo-tetrafluorobezene (< 1 mg) was added to the cuvette. After ample mixing and equilibration time a second spectrum was collected. Additional spectra were collected to assure that the sample had equilibrated.

Interaction with Hexafluorobenzene

A ~40 μM solution of $\mathbf{F_{60}}^0$ in chlorobenzene (Sigma-Aldrich) was transferred to a 1 cm path length quarts cuvette. Hexafluorobenzene (Sigma-Aldrich, NMR-grade) was added in 1 μl increments until a total of 18 μl had been added. Spectra were collected after each addition, first giving the sample ample time to equilibrate. A time-evolution series was collected by adding another 27 μl of hexafluorobenzene. Time points were collected until the spectrum stabilized.

Acid Titration

The initial solution was prepared by slow addition of a concentrated $\mathbf{F_{60}}^0$ solution to neat 1,2-dichlorobenzene, resulting in a sample dominated by $[\mathbf{F_{60}}]^{1-}$. A 1 vol% solution of trifluoroacetic acid was added to the sample in 25 μl increments until a total of 500 μl had been added. The sample was equilibrated under ambient lighting after each addition.

After completion of the acid titration, the sample was titrated with a 1 vol% solution of triethylamine in 1,2-dichlorobenzene, added in 25 μl increments until a total of 225 μl had been added. Unlike the acid titration steps, which required minutes of equilibration, the spectral changes upon triethylamine addition were near-instant. Attempts to add additional trifluoroacetic acid after the final data point resulted in formation of a white precipitate.

Variable Temperature Studies in 2-MeTHF

2-MeTHF (Sigma-Aldrich, anhydrous) was dried over activated 3 Å molecular sieves for > 48 hours and degassed through three 30 minute freeze-pump-thaw cycles. NMR samples were prepared in quartz J. Young tubes. A small speck of $\mathbf{F_{60}}^0$ was added to the tube and dried under vacuum for > 30 minutes, over three argon/vacuum cycles. Solvent was vacuum transferred to the J. Young tube. Complete conversion to $[\mathbf{F_{60}}]^{1-}$ was achieved by illuminating the sample with a 450 nm laser pointer (Roithner Lasertechnik). UV-visible samples were prepared in 1 cm path length screw-cap cuvettes inside a nitrogen-filled glovebox. Variable temperature NMR spectra were collected on a Varian 400 MHz Spectrometer with a broadband auto-tune OneProbe. A Varian Cary 50 UV-visible spectrometer equipped with a Unisoku CoolSpek cryostat was used to collect variable temperature UV-visible spectra. The samples were given ample time to equilibrate before each measurement. UV-visible spectra were corrected by subtracting solvent background spectra collect at each temperature point.

Visual observations were performed using X-band EPR tubes; no difference was observed between open-air and air-free samples. After preparation, the sample was illuminated using a 450 nm laser pointer to achieve complete conversion to $[\mathbf{F}_{60}]^{1-}$. The samples were submerged in liquid nitrogen to obtain a 2-MeTHF glass, resulting in an immediate color shift from deep purple to bright yellow. Thawing of the sample rapidly restored the color to deep purple.

Room-Temperature Emission

The following solvents were dried for > 96 hours and degassed though freeze-pump-thawing: toluene (Millipore), 2-MeTHF (Sigma-Aldrich), benzene (Millipore), chlorobenzene (Sigma-Aldrich), 1,2-difluorobenzene (Sigma-Aldrich), dichloromethane (Fischer., inhibitor free) and perfluorotoluene (TCI). Schlenk cuvettes with a separate compartment for sample preparation and degassing were used. All glassware was thoroughly oven-dried before use. Solid compounds were handled open-air but all steps following addition of solid to the sample compartment were performed using standard air-free techniques.

Under argon backflow a small amount of the cluster was added to the sample compartment. The solids were dried and degassed under vacuum. The solvent was vacuum transferred into the sample compartment, thawed and mixed to dissolve the solids. The sample solution was degassed by three 15 minute freeze-pump-thaw cycles, after which the solution was transfer to the cuvette compartment. Formation of $[B_{12}]^{1-}$ was assessed visually and by UV-visible spectroscopy.

Preliminary fluorescence spectra were collected on all samples, regardless of whether $[B_{12}]^{1-}$ was present or not. A FluoroLog Modular Spectrofluorometer (Horiba Jobin Yvon) was used to for photoluminescence measurements. Emitted light was passed through a monochromator and recorded by a PMT detector. Stronger 600 nm fluorescence was observed for samples containing more $[B_{12}]^{1-}$.

77 K Emission

Toluene (Millipore), 2-MeTHF (Sigma-Aldrich) and perfluorotoluene (TCI) and perfluoromethylcyclohexane (TCI) had been dried over 3 Å molecular sieves (> 48 hours) and degassed through at least three freeze-pump-thaw cycles. X-band quartz EPR tubes (ID = 3 mm, OD = 4 mm) were used to hold the samples. All glassware and cannulae had been thoroughly overdried before use. $\mathbf{F_{60}}$, $\mathbf{F_{72}}$, and $\mathbf{F_{84}}$ were handled open-air. All steps following addition of compound to the sample preparation vessel were performed under argon/vacuum using standard air-free techniques.

A small speck of compound was transferred to a 20 ml scintillation vial equipped with a septum cap. The solids were dried and degassed under vacuum for at least 30 minutes, minimum three argon/vacuum cycles. Solvent was added by cannula, the samples mixed and finally transferred to the EPR tube under argon backflow. The samples were immediately frozen in liquid nitrogen. A 457.9 nm excitation source (Coherent Innova 70) was used. Emitted light was directed to a

Melles Griot 13 FOS 200 Spectrometer through an optical fiber. A 457.9 nm long-pass cutoff filter was used to exclude excitation light. The reduction potentials of photo-excited B_{12}^{0} clusters were approximated[26] using eq. 2.2,

$$E_{red}^{*}{}^{0} = E_{red}{}^{0} + E_{0,0} \qquad (2.2)$$

where $E_{red}{}^{0}$ represents the ground-state 0/1- redox couple of and $E_{0,0}$ represents the wavelength of the onset of fluorescence. Redox values were calculated based on the Fc/Fc^{+} reference and converted to SCE, based on values reported by Connelly and Geiger,[27]. The potential of Fc/Fc^{+} referenced to SCE in CH_3CN with $TBAPF_6$ as the supporting electrolyte is 0.40 V.

BIBLIOGRAPHY

(1) Axtell, J. C.; Messina, M. S.; Liu, J.-Y.; Galaktionova, D.; Schwan, J.; Porter, T. M.; Savage, M. D.; Wixtrom, A. I.; Rheingold, A. L.; Kubiak, C. P.; et al. Photooxidative Generation of Dodecaborate-Based Weakly Coordinating Anions. *Inorg. Chem.* **2019**, *58* (16), 10516–10526. https://doi.org/10.1021/acs.inorgchem.9b00935.

(2) Lipscomb, W. N. Recent Studies of the Boron Hydrides. In *Advances in Inorganic Chemistry and Radiochemistry*; Emeléus, H. J., Sharpe, A. G., Eds.; Academic Press, 1959; Vol. 1, pp 117–156. https://doi.org/10.1016/S0065-2792(08)60253-8.

(3) Lipscomb, W. N.; Britton, D. Valence Structure of the Higher Borides. *J. Chem. Phys.* **1960**, *33* (1), 275–280. https://doi.org/10.1063/1.1731097.

(4) Eberhardt, W. H.; Crawford, B.; Lipscomb, W. N. The Valence Structure of the Boron Hydrides. *J. Chem. Phys.* **1954**, *22* (6), 989–1001. https://doi.org/10.1063/1.1740320.

(5) Hoffmann, R.; Lipscomb, W. N. Theory of Polyhedral Molecules. I. Physical Factorizations of the Secular Equation. *J. Chem. Phys.* **1962**, *36* (8), 2179–2189. https://doi.org/10.1063/1.1732849.

(6) Wunderlich, J. A.; Lipscomb, W. N. STRUCTURE OF B12H12-2 ION. *J. Am. Chem. Soc.* **1960**, *82* (16), 4427–4428. https://doi.org/10.1021/ja01501a076.

(7) Moore, E. B.; Lohr, L. L.; Lipscomb, W. N. Molecular Orbitals in Some Boron Compounds. *J. Chem. Phys.* **1961**, *35* (4), 1329–1334. https://doi.org/10.1063/1.1732046.

(8) Hoffmann, R.; Lipscomb, W. N. Boron Hydrides: LCAO—MO and Resonance Studies. *J. Chem. Phys.* **1962**, *37* (12), 2872–2883. https://doi.org/10.1063/1.1733113.

(9) Longuet-Higgins, H. C.; Roberts, M. D. V. The Electronic Structure of an Icosahedron of Boron Atoms. *Proc R Soc Lond A* **1955**, *230* (1180), 110–119. https://doi.org/10.1098/rspa.1955.0115.

(10) Peymann, T.; Knobler, C. B.; Hawthorne, M. F. An Unpaired Electron Incarcerated within an Icosahedral Borane Cage: Synthesis and Crystal Structure of the Blue, Air-Stable {[Closo-B12(CH3)12]·}– Radical. *Chem. Commun.* **1999**, *0* (20), 2039–2040. https://doi.org/10.1039/A905406E.

(11) Boeré, R. T.; Bolli, C.; Finze, M.; Himmelspach, A.; Knapp, C.; Roemmele, T. L. Quantum-Chemical and Electrochemical Investigation of the Electrochemical Windows of Halogenated Carborate Anions. *Chem. – Eur. J.* **2013**, *19* (5), 1784–1795. https://doi.org/10.1002/chem.201202475.

(12) Boeré, R. T.; Derendorf, J.; Jenne, C.; Kacprzak, S.; Keßler, M.; Riebau, R.; Riedel, S.; Roemmele, T. L.; Rühle, M.; Scherer, H.; et al. On the Oxidation of the Three-Dimensional Aromatics [B12X12]2− (X=F, Cl, Br, I). *Chem. – Eur. J.* **2014**, *20* (15), 4447–4459. https://doi.org/10.1002/chem.201304405.

(13) Boeré, R. T.; Kacprzak, S.; Keßler, M.; Knapp, C.; Riebau, R.; Riedel, S.; Roemmele, T. L.; Rühle, M.; Scherer, H.; Weber, S. Oxidation of Closo-[B12Cl12]2− to the Radical Anion [B12Cl12].− and to Neutral B12Cl12. *Angew. Chem. Int. Ed.* **2011**, *50* (2), 549–552. https://doi.org/10.1002/anie.201004755.

(14) Van, N.; Tiritiris, I.; Winter, R. F.; Sarkar, B.; Singh, P.; Duboc, C.; Muñoz-Castro, A.; Arratia-Pérez, R.; Kaim, W.; Schleid, T. Oxidative Perhydroxylation of [Closo-B12H12]2− to the Stable Inorganic Cluster Redox System [B12(OH)12]2−/.−: Experiment and Theory. *Chem. – Eur. J.* **2010**, *16* (37), 11242–11245. https://doi.org/10.1002/chem.201001374.

(15) Peymann, T.; Knobler, C. B.; Khan, S. I.; Hawthorne, M. F. Dodeca(Benzyloxy)Dodecaborane, B12(OCH2Ph)12: A Stable Derivative of Hypercloso-B12H12. *Angew. Chem. Int. Ed.* **2001**, *40* (9), 1664–1667. https://doi.org/10.1002/1521-3773(20010504)40:9<1664::AID-ANIE16640>3.0.CO;2-O.

(16) Messina, M. S.; Axtell, J. C.; Wang, Y.; Chong, P.; Wixtrom, A. I.; Kirlikovali, K. O.; Upton, B. M.; Hunter, B. M.; Shafaat, O. S.; Khan, S. I.; et al. Visible-Light-Induced Olefin Activation Using 3D Aromatic Boron-Rich Cluster Photooxidants. *J. Am. Chem. Soc.* **2016**, *138* (22), 6952–6955. https://doi.org/10.1021/jacs.6b03568.

(17) Williams, J. H.; Cockcroft, J. K.; Fitch, A. N. Structure of the Lowest Temperature Phase of the Solid Benzene–Hexafluorobenzene Adduct. *Angew. Chem. Int. Ed. Engl.* **1992**, *31* (12), 1655–1657. https://doi.org/10.1002/anie.199216551.

(18) Grimme, S. Do Special Noncovalent π–π Stacking Interactions Really Exist? *Angew. Chem. Int. Ed.* **2008**, *47* (18), 3430–3434. https://doi.org/10.1002/anie.200705157.

(19) Martinez, C. R.; Iverson, B. L. Rethinking the Term "Pi-Stacking." *Chem. Sci.* **2012**, *3* (7), 2191–2201. https://doi.org/10.1039/C2SC20045G.

(20) Muetterties, E. L.; Merrifield, R. E.; Miller, H. C.; Knoth, W. H.; Downing, J. R. Chemistry of Boranes. III.1 The Infrared and Raman Spectra of B12H12 - and Related Anions. *J. Am. Chem. Soc.* **1962**, *84* (13), 2506–2508. https://doi.org/10.1021/ja00872a011.

(21) Wixtrom, A. I.; Shao, Y.; Jung, D.; Machan, C. W.; Kevork, S. N.; Qian, E. A.; Axtell, J. C.; Khan, S. I.; Kubiak, C. P.; Spokoyny, A. M. Rapid Synthesis of Redox-Active Dodecaborane B12(OR)12 Clusters under Ambient Conditions. *Inorg. Chem. Front.* **2016**, *3* (5), 711–717. https://doi.org/10.1039/C5QI00263J.

(22) De Sorgo, M.; Wasserman, B.; Szwarc, M. Aggregation of Salts of Thianthrene Radical Cations. *J. Phys. Chem.* **1972**, *76* (23), 3468–3471. https://doi.org/10.1021/j100667a029.

(23) Penneau, J. F.; Stallman, B. J.; Kasai, P. H.; Miller, L. L. An Imide Anion Radical That Dimerizes and Assembles into .Pi.-Stacks in Solution. *Chem. Mater.* **1991**, *3* (5), 791–796. https://doi.org/10.1021/cm00017a013.

(24) Rapta, P.; Dunsch, L. Dimerisation of Organic Radical Ions and Redox Reactions of Dimers as Studied by Temperature-Dependent in Situ ESR/UV–Vis–NIR Spectroelectrochemistry. *J. Electroanal. Chem.* **2001**, *507* (1), 287–292. https://doi.org/10.1016/S0022-0728(01)00473-9.

(25) Nishinaga, T.; Komatsu, K. Persistent π Radical Cations: Self-Association and Its Steric Control in the Condensed Phase. *Org. Biomol. Chem.* **2005**, *3* (4), 561–569. https://doi.org/10.1039/B418872A.

(26) Gray, H. B.; Maverick, A. W. Solar Chemistry of Metal Complexes. *Science* **1981**, *214* (4526), 1201–1205. https://doi.org/10.1126/science.214.4526.1201.

(27) Connelly, N. G.; Geiger, W. E. Chemical Redox Agents for Organometallic Chemistry. *Chem. Rev.* **1996**, *96* (2), 877–910. https://doi.org/10.1021/cr940053x.

Chapter 3

THE $[B_{12}(OR)_{12}]^{1+}$ CATION

A manuscript based on the work presented in this chapter is being prepared by Stauber, J. M.; Schwan, L. J.; Xhang, X.; Axtell, J. C.; Jung, D.; McNicholas, B. J.; Oyala, P. H.; Winkler, J. R.; Miller, T. F.; Gray H. B.; Spokoyny, A.M. Evidence for the Existence of Cationic Dodecaborate-based Clusters.

*Chapter 3 discusses our discovery of a $[B_{12}(OR)_{12}]^{1+}$ species and initial attempts at isolating and characterizing this cationic cluster. Our investigations started with the observation of a third oxidation wave in the cyclic voltammogram of $B_{12}(OEt)_{12}$ ($\mathbf{4}^0$, Et =C_2H_5), which we assigned to a super-oxidized $[\mathbf{4}]^{1+}$ species. Further electrochemical investigation of **4** in 0.2 M $TBAPF_6$ dichloromethane electrolyte showed three reversible waves at $E_{1/2}(2-/1-) = -1.08$ V, $E_{1/2}(0/1-) = -0.454$ V and $E_{1/2}(1+/0) = +0.747$ V. Additionally, a strong irreversible wave is observed at > +1.2 V, which could indicate further oxidation to $[\mathbf{4}]^{2+}$. Electrochemically derived visible spectra of $[\mathbf{4}]^{1+}$ show a new broad absorption band at 707 nm and a strong 455 nm band (slightly blue-shifted from the 460 nm band of the neutral species). Preliminary attempts to chemically isolate $[\mathbf{4}]^{1+}$ indicated that tris(4-bromophenyl)ammoniumyl hexachloroantimonate was able to oxidize $\mathbf{4}^0$, but not sufficiently strong for isolation of the cation. Using the more powerful oxidant tris(2,4-dibromophenyl)ammoniumyl hexachloroantimonate, we were able to isolate $[B_{12}(OC_2H_2{}^iPr)_{12}][SbCl_6]$ ($[\mathbf{5}][SbCl_6]$). The isolated salts are not of sufficient purity for spectroscopic characterization; however, we were able to collect EPR spectra of $[\mathbf{4}]^{1+}$ and $[\mathbf{4}]^{1+}$ in-situ generated by addition of a substochiometric amount of tris(2,4-dibromophenyl)ammoniumyl hexachloroantimonate. The EPR spectrum indicates a delocalized SOMO, similar to what has been reported for the anionic hypocloso-$[B_{12}]$ clusters.*

3.1 Introduction

Early theoretical predictions by Longuet-Higgins and Lipscomb suggested that dodecaborate ($[B_{12}H_{12}]$) would not be stable as a neutral $B_{12}H_{12}$ species but might be stable in its dianionic $[B_{12}H_{12}]^{2-}$ state. These predictions considered a cluster in icosahedral (I_h) symmetry, where the highest occupied molecular orbital (HOMO) is a four-fold degenerate g_u set. Neutral or monoanionic dodecaborates do not have enough electrons to fill the HOMO(g_u), suggesting that these species would be unstable due to an energetically unfavorable open-shell cofiguration.[1–7] Lipscomb and co-workers were the first to confirm the existence of a stable dodecaborate through their isolation and structural characterization of *closo*-$[B_{12}H_{12}]^{2-}$. Later work has confirmed that oxidation of *closo*-$[B_{12}H_{12}]^{2-}$ leads to cluster decomposition or dimerization.[8] Wade generalized these results through the so-called 'Wade's rules', which predict the structure of polyhedral molecules based on the number of skeletal bonding electron pairs.[9,10]

Over the past two decades, a range of dodecaborate derivatives have been isolated as hypoelectronic *hypocloso*-$[B_{12}]^{1-}$ and *hypercloso*-B_{12}^{0} species (B_{12} denotes a generic dodecaborate cluster). Hawthorne first reported the isolation of *hypocloso*-$[B_{12}Me_{12}]^{1-}$ (Me = CH_3), followed by *hypocloso*-$[B_{12}(OBz)_{12}]^{1-}$ and *hypercloso*-$B_{12}(OBz)_{12}$ (Bz = $CH_2C_6H_5$).[11,12] Later work showed that perhydroxylated and perhalogenated dodecaborates could also be isolates as salts of *hypocloso*-$[B_{12}(OH)_{12}]^{1-}$ and *hypocloso*-$[B_{12}X_{12}]^{1-}$ (X = F, Cl, Br).[13,14] A key breakthrough came when Spokoyny and co-workers discovered a more convenient method for rapid synthesis of *hypercloso*-$B_{12}(OR)_{12}$.[15] The ability to readily produce large quantities of these compounds enabled in-depth exploration of their potential applications, most importantly the photopolymerization studies discussed in Appendix A, as well as recent reports on their use in charge-storage devices and as dopants in conducting polymers.[16–19]

The stability of hypoelectronic *hypocloso*-$[B_{12}]^{1-}$ and *hypercloso*-B_{12}^{0} species have been attributed to three factors: (1) a structural distortion lowering the symmetry from I_h to D_{3d} or T_d, which breaks the degeneracy of the HOMO(g_u) to lower the overall cluster energy, (2) steric protection of the cluster-confined frontier orbitals by bulky substituents and (3) electron donation from the substituents into the B-B bonding frontier orbitals. The effect of the structural distortion is shown in Figure 3.1 (assuming D_{3d} symmetry). Breaking of the g_u degeneracy yields a non-degenerate a_{1u} singly occupied molecular orbital (SOMO) in the case of *hypocloso*-$[B_{12}]^{1-}$ or lowest unoccupied molecular orbital (LUMO) in the case of *hypercloso*-B_{12}^{0}. Raising the energy of the a_{1u} and lowering the energy of the fully occupied e_g set leads to an energetically favorable state, stabilizing the cluster.[15–17,20] The role of electron donation is likely a major contributor, which will be discussed in more detail in Chapter 4.

Dodecaborate clusters oxidized beyond the *hypercloso*-B_{12}^{0} state have so far not been reported. The current paradigm states that that removal of an electron from the HOMO(a_{2u}) of *hypercloso*-B_{12}^{0} would undoubtedly lead to cluster decomposition. Here, we show that a super-oxidized cationic $[B_{12}]^{1+}$ state can be generated from $B_{12}(OR)_{12}$ when R = alkyl. Both electrochemical and chemical means have been used to generate $[B_{12}(OEt)_{12}]^{1+}$ and $[B_{12}(OC_2H_4{}^{i}Pr)_{12}]^{1+}$ (Et = CH_2CH_3, ${}^{i}Pr$ = isopropyl). These observations open up for interesting discussions on what the oxidation limit of dodecaborates is and what types of reactivities these super-oxidizes states can access.

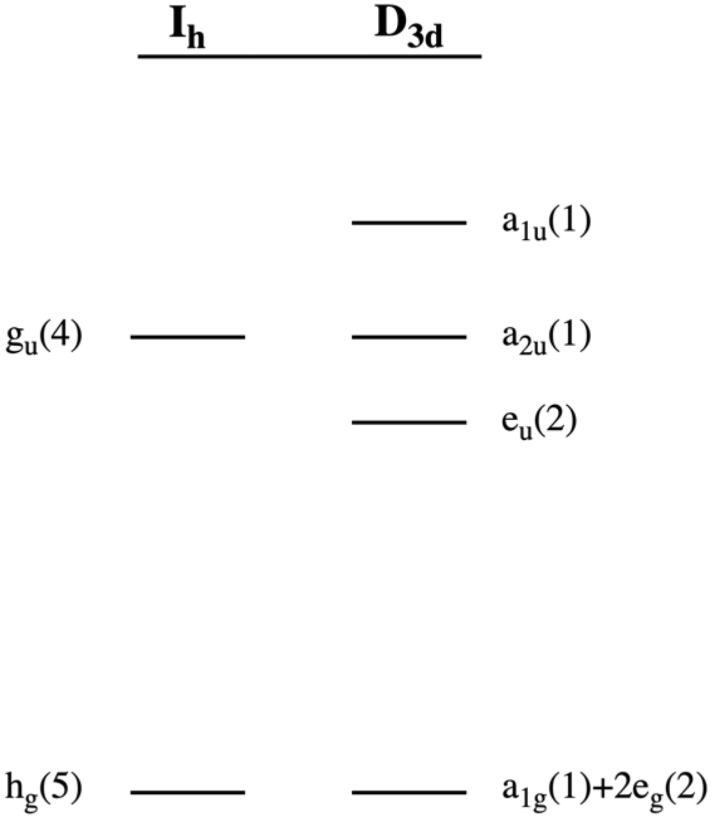

Figure 3.1. Hypoelectronic states are stabilized by a structural distortion, which lowers the overall energy of the cluster. The figure shows the *closo*-$[B_{12}]^{2-}$ HOMO(g_u) and HOMO-1(h_g) on the left. Symmetry lowering to D_{3d} transforms $g_u \rightarrow a_{1u}+a_{su}+e_u$ and $h_g \rightarrow a_{1g}+2e_g$. Raising of the partially filled or unfilled a_{1u} and lowering the filled e_u is energetically favorable in hypoelectronic clusters.

3.2 Electrochemical Generation of $[B_{12}(OR)_{12}]^{1+}$

The anodic cyclic voltammogram of $[B_{12}(OEt)_{12}]$ (**4**), collected in 0.2 M $TBAPF_6$ (tetrabutylammonium hexafluorophosphate) dichloromethane and acetonitrile electrolytes show two waves representing the known $[\mathbf{4}]^{1-/2-}$ and $[\mathbf{4}]^{1-/0}$ couples. The reduction potentials, $E_{1/2}$(1-/2-) = -1.08 V and $E_{1/2}$(0/-1) = -0.454 V in dichloromethane and $E_{1/2}$(1-/2-) = -0.94 V and $E_{1/2}$(0/-1) = -0.41 V in acetonitrile (all potentials reported versus the ferrocene-ferrocenium couple), are significantly less oxidizing than $[B_{12}(OBz)_{12}]$ (Bz = $CH_2C_6H_5$), which is the least oxidizing of the aryl-perfunctionalized clusters discussed in this thesis. Reported reduction potentials for $[B_{12}(OBz)_{12}]$ in dichloromethane are $E_{1/2}$(1-/2-) -0.7 V = and $E_{1/2}$(0/-1) = -0.2 V, around 300 mV more positive than **4**.[12,15] The unusually negative reduction potentials of **4**, compared to other known $[B_{12}(OR)_{12}]$ clusters, prompted us to explore the electrochemistry at highly oxidizing potentials. To our surprise, in dichloromethane, **4** shows a third reversible single-electron oxidation at $E_{1/2}$ = 0.747 V (Figure 3.2), which we assign to the $[\mathbf{4}]^{1+/0}$ couple. Cyclic voltammograms at scan rates between and 25–2500 mV/s were collected to explore the reversibility of the redox events. Figures 3.3–3.5 show individual cyclic voltammograms and plots of peak current (i_p) as a function of the square root of the scan rate (ν); the linear relationship confirms the electrochemical reversibility of all three couples. Furthermore, Figure 3.6 shows a cyclic voltammogram displaying a strong irreversible wave at E_p = +1.3 V. Comparison with a background scan collected for the 0.2 M $TBAPF_6$ dichloromethane electrolyte clearly shows that this wave involves **4**. We speculate that it corresponds to the $[\mathbf{4}]^{2+/1+}$ couple, and that $[\mathbf{4}]^{2+}$ partakes in rapid solvent or electrolyte oxidation reactions. In acetonitrile (Figure 3.7) neither of the $[\mathbf{4}]^{1-/2-}$ and $[\mathbf{4}]^{1-/0}$ waves are fully reversible and the $[\mathbf{4}]^{1+/0}$ couple appears completely irreversible. Table 3.1 summarizes the electrochemical data collected for **4** in dichloromethane. Voltammograms collected in dichloromethane outside the glovebox, without pre-drying the solvent, show similar results. The reversibility of the waves were not negatively affected by the presence of water (see Section 3.5).

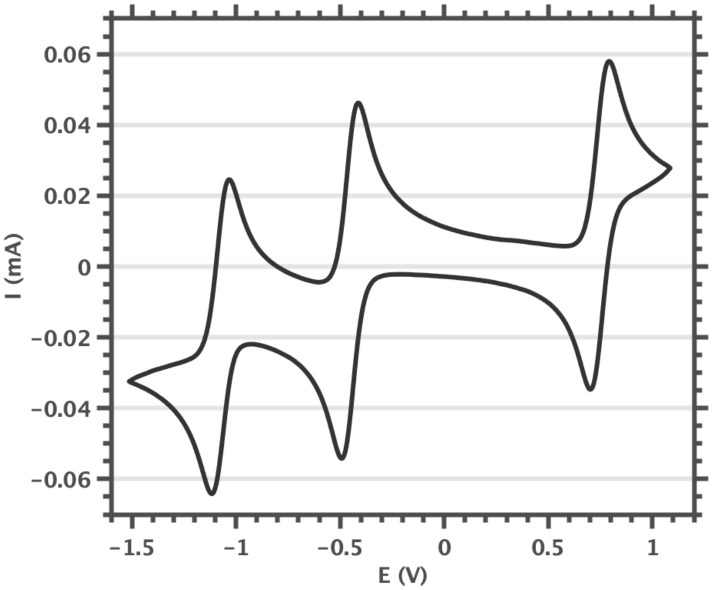

Figure 3.2. Cyclic voltammogram of 3.0 mM $B_{12}(OEt)_{12}$ (**4**^{0}) collected at 100 mV/s in 0.2 M $TBAPF_6$/dichloromethane under air-free conditions. Potential reported versus the ferrocene-ferrocenium couple.

.

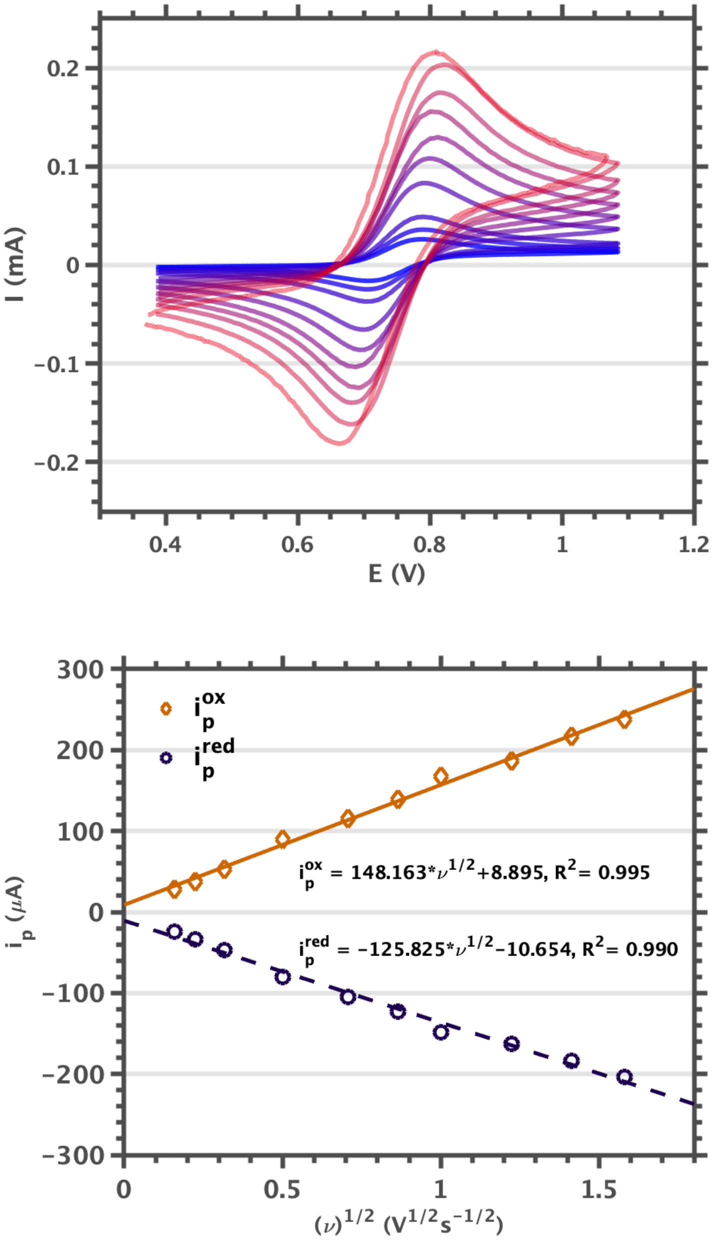

Figure 3.3. (Top) Cyclic voltammogram scan rate dependence of the [**4**]$^{1+/0}$ couple. 3.0 mM **4**^{0} in 0.2 M TBAPF$_6$/dichloromethane at 25 mV/s, 50 mV/s, 100 mV/s, 250 mV/s, 500 mV/s, 750 mV/s, 1000 mV/s, 1500 mV/s, 2000 mV/s and 2500 mV/s. (Bottom) Linear relationship between peak currents and scan rate. i_p^{ox} and i_p^{red} are the oxidative and reductive peak currents. ν is the scan rate.

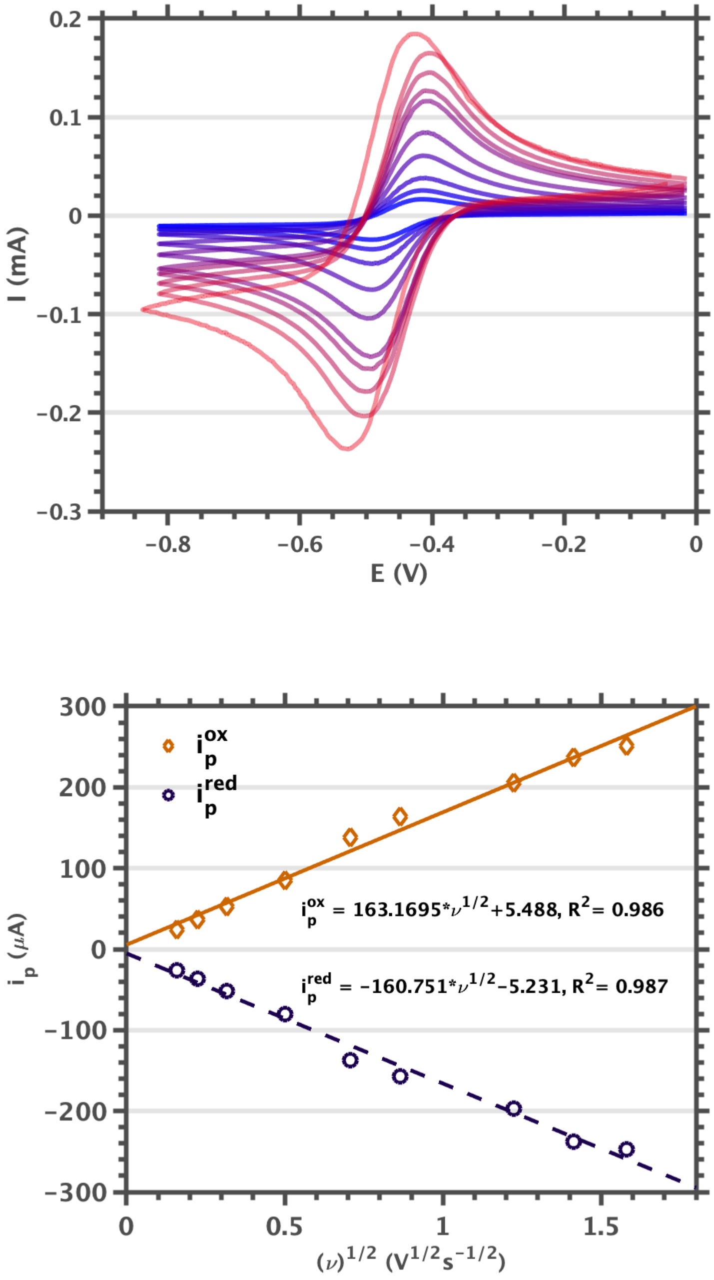

Figure 3.4. (Top) Cyclic voltammogram scan rate dependence of the [**4**]$^{0/1-}$ couple. 3.0 mM **4**^{0} in 0.2 M TBAPF$_6$/dichloromethane at 25 mV/s, 50 mV/s, 100 mV/s, 250 mV/s, 500 mV/s, 750 mV/s, 1000 mV/s, 1500 mV/s, 2000 mV/s and 2500 mV/s. (Bottom) Linear relationship between peak currents and scan rate. i_p^{ox} and i_p^{red} are the oxidative and reductive peak currents. ν is the scan rate.

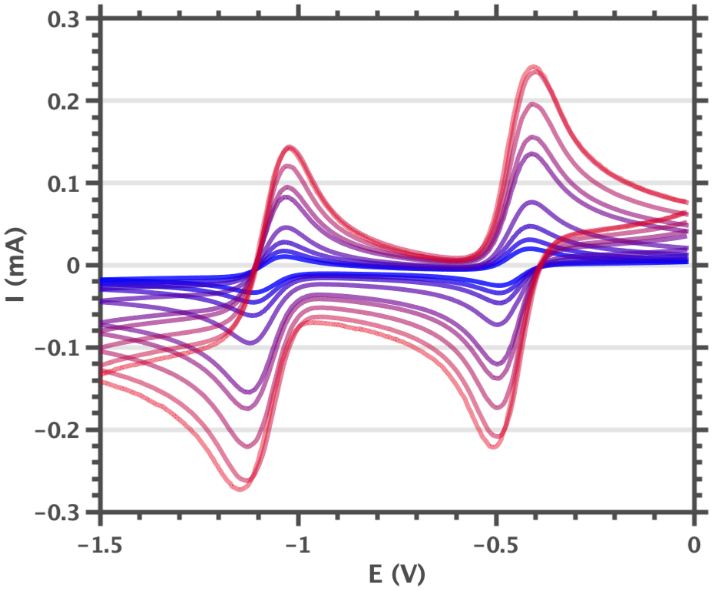

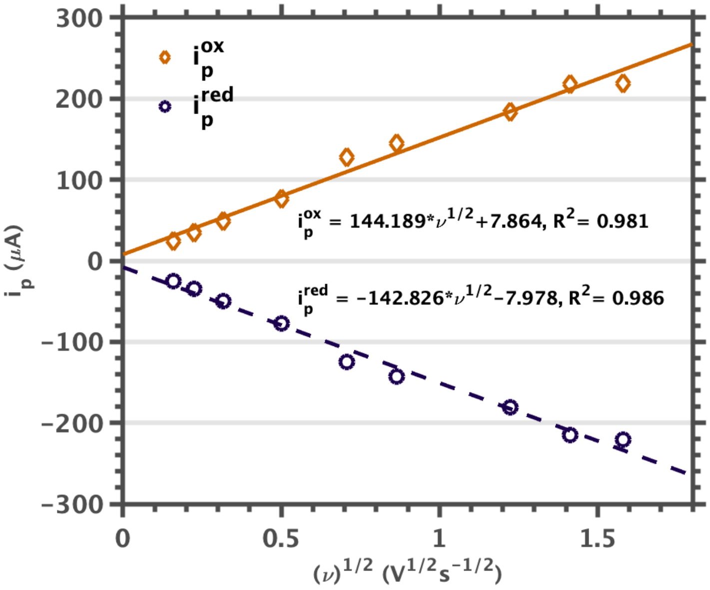

Figure 3.5. (Top) Cyclic voltammogram scan rate dependence of the [**4**]$^{1-/2-}$ couple. 3.0 mM **4**^{0} in 0.2 M TBAPF$_6$/dichloromethane at 25 mV/s, 50 mV/s, 100 mV/s, 250 mV/s, 500 mV/s, 750 mV/s, 1000 mV/s, 1500 mV/s, 2000 mV/s and 2500 mV/s. (Bottom) Linear relationship between peak currents and scan rate. i_p^{ox} and i_p^{red} are the oxidative and reductive peak currents. ν is the scan rate. The voltammogram was collected starting from **4**^{0}.

Table 3.1. (cont. next page) Electrochemical parameters for 3.0 mM **4**^{0} in 0.2 M TBAPF$_6$/dichloromethane. E_p^{ox} and E_p^{red} are the potentials at peak current for the respective oxidative and reductive waves. $E_{1/2}$ is the mean of the reductive and oxidative peak potential. i_p^{ox} and i_p^{red} are the peak currents observed at the absolute maximum of the respective oxidative and reductive waves. All potentials are reported versus the ferrocene-ferrocenium couple.

Couple	**ν**	**25 mV/s**	**50 mV/s**	**100 mV/s**	**250 mV/s**	**500 mV/s**
[**4**]$^{1-/2-}$	$E_{1/2}$ (V)	-1.072	-1.075	-1.075	-1.079	-1.085
	E_p^{ox} (V)	-1.030	-1.038	-1.037	-1.034	-1.038
	E_p^{red} (V)	-1.114	-1.113	-1.113	-1.125	-1.133
	i_p^{ox} (μA)	+24.67	+34.29	+49.15	+76.72	+127.7
	i_p^{red} (μA)	-24.90	-34.51	-49.50	-77.71	-124.6
[**4**]$^{0/1-}$	$E_{1/2}$ (V)	-0.452	-0.452	-0.454	-0.454	-0.454
	E_p^{ox} (V)	-0.414	-0.414	-0.418	-0.410	-0.410
	E_p^{red} (V)	-0.490	-0.490	-0.490	-0.498	-0.498
	i_p^{ox} (μA)	+24.21	+36.51	+52.57	+84.83	+138.3
	i_p^{red} (μA)	-25.77	-36.55	-52.11	-80.48	-137.2
[**4**]$^{1+/0}$	$E_{1/2}$ (mV)	+0.747	+0.749	+0.747	+0.747	+0.749
	E_p^{ox} (mV)	+0.785	+0.789	+0.785	+0.793	+0.797
	E_p^{red} (mV)	+0.709	+0.709	+0.709	+0.701	+0.701
	i_p^{ox} (μA)	+28.22	+37.50	+52.82	+90.00	+115.7
	i_p^{red} (μA)	-24.24	-33.51	-47.34	-80.64	-105.1

Couple	**ν**	**750 mV/s**	**1000 mV/s**	**1500 mV/s**	**2000 mV/s**	**2500 mV/s**
[**4**]$^{1-/2-}$	$E_{1/2}$ (V)	-1.083	-	-1.080	-1.081	-1.091
	E_p^{ox} (V)	-1.030	-	-1.030	-1.022	-1.027
	E_p^{red} (V)	-1.137	-	-1.129	-1.141	-1.155
	i_p^{ox} (μA)	+145.1	-	+184.0	+218.2	+219.0
	i_p^{red} (μA)	-143.1	-	-180.4	-215.2	-220.4
[**4**]$^{0/1-}$	$E_{1/2}$ (V)	-0.452	-	-0.454	-0.450	-0.456
	E_p^{ox} (V)	-0.410	-	-0.410	-0.402	-0.404
	E_p^{red} (V)	-0.494	-	-0.498	-0.497	-0.508
	i_p^{ox} (μA)	+163.6	-	+205.5	+236.8	+251.5
	i_p^{red} (μA)	-156.7	-	-197	-237.5	-247.6
[**4**]$^{1+/0}$	$E_{1/2}$ (mV)	+0.751	+0.747	+0.751	+0.757	+0.742
	E_p^{ox} (mV)	+0.813	+0.801	+0.813	+0.825	+0.813
	E_p^{red} (mV)	+0.689	+0.693	+0.689	+0.689	+0.672
	i_p^{ox} (μA)	+139.2	+167.9	+186.9	+217.3	+237.4
	i_p^{red} (μA)	-122.6	-148.6	-162.6	-184	203.4

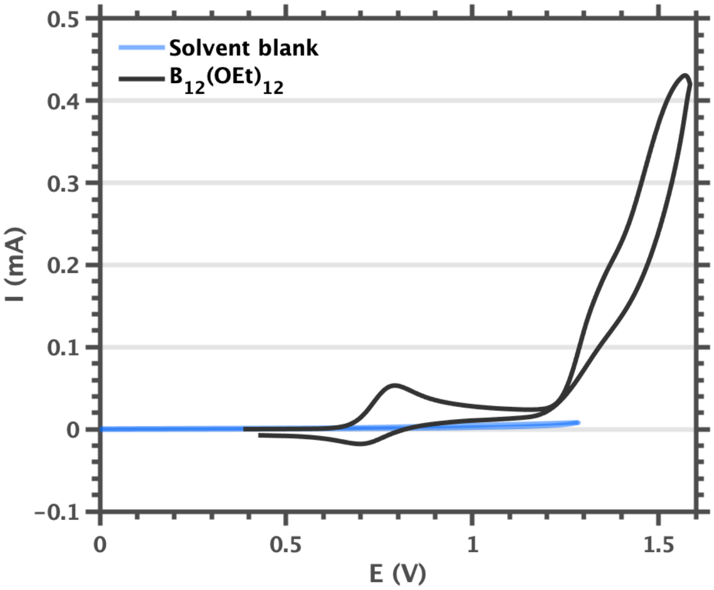

Figure 3.6. (Black trace) Cyclic voltammogram of 3.0 mM **4**^{0} collected at 100 mV/s in 0.2 M TBAPF$_6$/dichloromethane under air-free conditions. (Blue trace) Electrolyte background scan. Potential reported versus the ferrocene-ferrocenium couple.

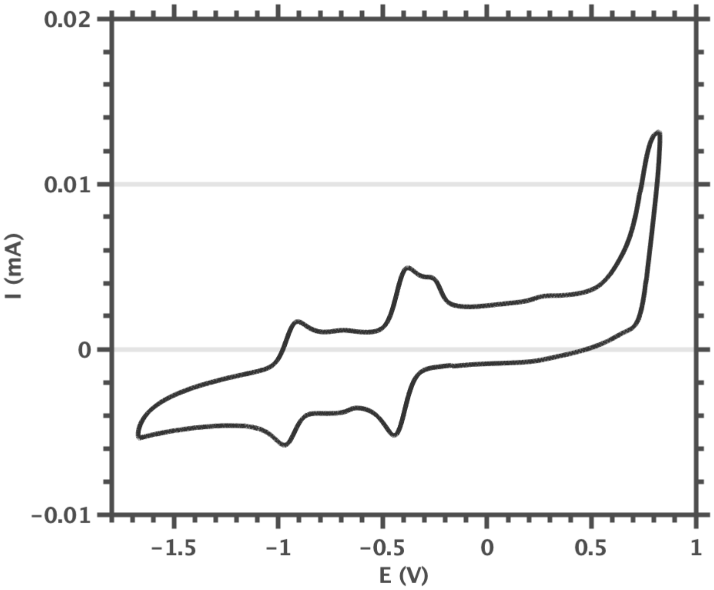

Figure 3.7. Cyclic voltammogram of 3.0 mM **4**^{0} collected at 100 mV/s in 0.2 M TBAPF$_6$/acetonitrile. Potential reported versus the ferrocene-ferrocenium couple.

Spectroelectrochemical characterization was performed to further probe the identity of the super-oxidized species. In a 0.1 M TBAPF$_6$ dichloromethane solution we were able to generate [**4**]$^{1+}$ by holding the potential at +1.2 V. Figure 3.8 shows spectra collected while holding the potential at (A) -0.5 V, (B) -1 V and (C) +1.2 V (after holding at +0.8 V to recover **4**^{0}). The strong visible absorption band of **4**^{0} at 460 nm blue-shifts very slightly to 455 nm upon oxidation to [**4**]$^{1+}$. Interestingly, [**4**]$^{1+}$ shows an additional broad lower-energy absorption band centered at 700 nm. Under the given conditions, [**4**]$^{1+}$ persists under applied bias but the visible spectrum indicates rapid reversible recovery of **4**^{0} when no potential is applied. Although significant non-coulombic currents were passed, the observed spectra indicate that we were able to reversibly cycle through all four oxidation states (2-/1-/0/1+). The spectral reversibility support assigning the super-oxidized species to [**4**]$^{1+}$. The non-coulombic currents likely stem from solvent oxidation or oxidation of adventitious water.

3.3 Chemical Generation of $[B_{12}(OR)_{12}]^{1+}$

Following our initial electrochemical and spectroelectrochemical observation of [**4**]$^{1+}$, we wanted to attempt isolating [**4**]$^{1+}$ through chemical means. A range of chemical oxidants were explored, including silver triflate, nitrosonium tetrafluoroborate, tungsten hexachloride and Magic Blue (tris(4-bromophenyl)ammoniumyl hexachloroantimonate). Only treatment with Magic Blue resulted in observable reactivity. Addition of Magic Blue to tetrahydrofuran (THF), dichloromethane and nitromethane solutions of **4**^{0} resulted in rapid consumption of the dark blue Magic Blue radical.[21] Visually observed color shifts suggested that [**4**]$^{1+}$ had been generated, but the species was too short-lived for spectroscopic characterization.

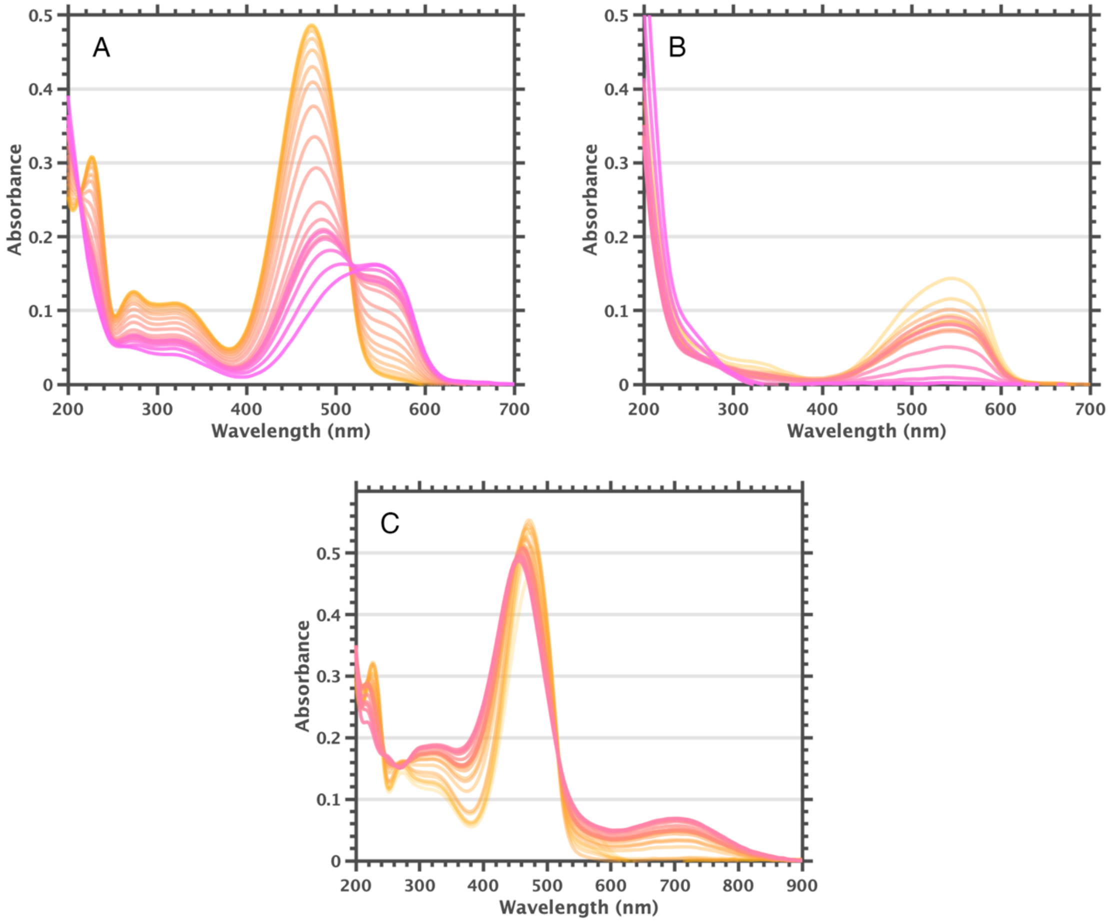

Figure 3.8 Electrochemically derived spectra of **4** in 0.1 M TBAPF$_6$/CH$_2$Cl$_2$. (A) Potential held at -0.5 V to generate [**4**]$^{1-}$. (B) Potential held at -1 V to generate [**4**]$^{2-}$. (C) Potential held at +1.2 V to generate [**4**]$^{1+}$. (**4**^{0} was first regenerated from [**4**]$^{2-}$ by holding the potential at +0.8 V). Potentials reported versus the ferrocene-ferrocenium couple.

Titration of a THF solution of $\mathbf{4}^0$ (60 μM) with Magic Blue, monitored by UV-visible spectroscopy, provided suggestive evidence of oxidation to $[\mathbf{4}]^{1+}$ followed by rapid solvent oxidation. Figure 3.9 shows UV-visible spectra taken after addition of 25 μl aliquots of a 0.64 mM solution of Magic Blue in THF. A total of 250 μl was added, yielding a 37.5 μM final concentration. The strong band growing in at 310 nm is indicative of the formation of neutral tris(4-bromophenyl)amine, suggesting that the oxidant had been consumed. The absence of the strong absorption bands characteristic of Magic Blue further confirmed that the oxidant had been consumed. Solutions of Magic Blue in THF without $\mathbf{4}^0$ last for hours without appreciable consumption of the oxidant, implying that $[\mathbf{4}]^{1+}$ plays a key role. Furthermore, this data suggests that $[\mathbf{4}]^{1+}$ act as an oxidation catalyst, given that no consumption of $\mathbf{4}^0$ is observed.

It is noteworthy that $[\mathbf{4}]^{1+}$ appears to be a potent catalyst, based on the electrochemical observations in acetonitrile and dichloromethane, as well as the suggested oxidation of solvent occurring after chemical oxidation of $\mathbf{4}^0$. In the case of Magic Blue, in addition to solvent oxidation, there is evidence that chemical transformations involving Magic Blue or the tris(4-bromopheyl)amine product may occur following formation of $[\mathbf{4}]^{1+}$. A crystal structure grown out of a solution of $\mathbf{4}^0$ and Magic Blue in dichloromethane shows the presence of a tris(4-bromophenyl)amine or tris(4-bromophenyl)ammoniumyl species with partial 2-bromination (Figure 3.8). Due to poor crystal quality we cannot derive reliable bond lengths, which prohibit differentiation of the amine and ammoniumyl radicals. We do not yet understand what causes 2-bromination, but postulate that $[\mathbf{4}]^{1+}$is involved in bromine transfer reactivity. That said, only a single small crystal was obtained containing the 2-brominated phenylamine, which could mean

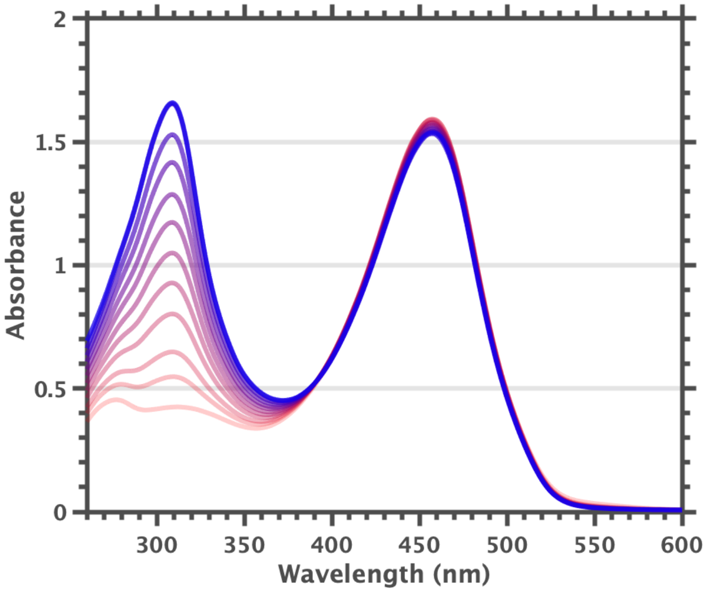

Figure 3.9: Spectrum of 60 μM **4**^{0} in THF titrated with a 0.64 mM solution of Magic Blue in THF. Each data point corresponds to a 25 μl addition of Magic Blue solution. A slight decrease in the 460 nm band is observed due to sample dilution.

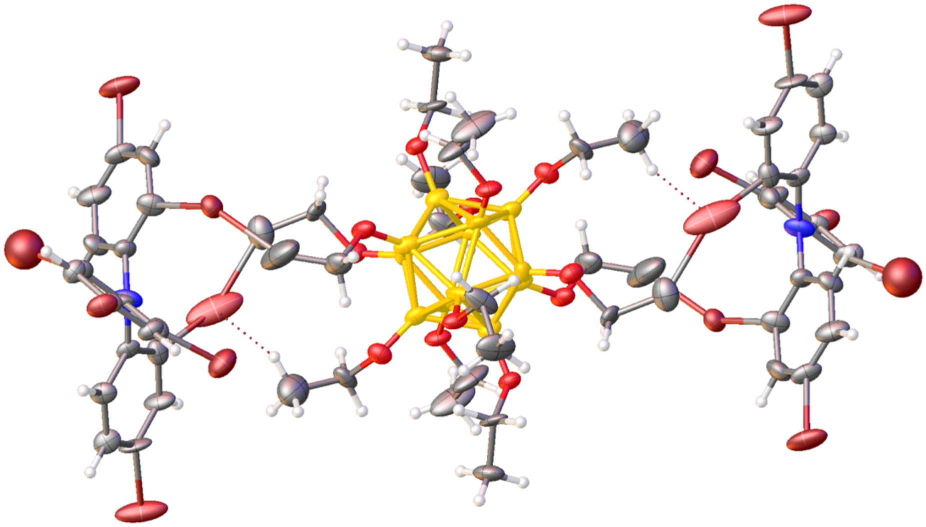

Figure 3.10: Crystal structure showing the unusual 2-bromianted phenyl groups of triphenylamines/ammoniumyls surrounding [**4**].

that it is only a minor side product. It is also plausible that commercial Magic Blue contains trace amounts of 2-brominated contaminants, which could be either in the ammoniumyl radical form or the uncharged amine form. A number of other crystals were collected from the sample, all displaying unit cells analogous to the known structure of **4**^{0}.

Based on the observations presented above, we hypothesized that Magic Blue is able to oxidize **4**^{0}, but not sufficiently strong of an oxidant to enable isolation of a [**4**]$^{1+}$ salt. We wondered if a more oxidizing ammoniumyl radical, such as tris(2,4-dibromophenyl)ammoniumyl hexachloroantimonate (henceforth referred to as Magic Green) would be more successful. The redox potential of Magic Blue is around +0.70 mV. 2-bromination provides Magic Green with an additional 440 mV of oxidizing power, bringing its redox potential to +1.14 mV (versus the ferrocene-ferrocenium couple).[22] Given that Magic Green is not commercially available and that the highly reactive nature of the reagents involved in synthesis demand expertise beyond our abilities, we asked for assistance from the Spokoyny lab.

We were excited to learn that using in-house prepared Magic Green, members of the Spokoyny lab had been able to isolate $[B_{12}(OC_2H_4{}^iPr)_{12}]^{1+}$ ([**5**]$^{1+}$) as a hexachloroantimonate salt. The salt had to be handled under rigorously dry and air-free conditions at all times and, even then, it decomposes over time (weeks). So far, [**5**][$SbCl_6$] salts of sufficient purity for spectroscopic characterization have not been obtained. However, we were able to collect electronic paramagnetic resonance (EPR) data on *in-situ* prepared [**4**]$^{1+}$ and [**5**]$^{1+}$. Both X-band continuous wave (CW) EPR spectra and pulsed Q-band ESE-EPR, HYSCORE and ENDOR spectra were collected on samples prepared by adding a substochiometric amount of Magic Green to toluene solutions of **4**^{0} and toluene/dichloromethane-*d*$_2$ solutions of **5**^{0}. The CW EPR spectrum of [**5**]$^{1+}$, shown in Figure 3.11, displays a broad unresolved signal around g = 2.0083, highly reminiscent of the monoanionic species previously described in the literature (*vide supra*). This indicates that the SOMO of $[B_{12}]^{1+}$ is highly delocalized, similar to what has been suggested for the SOMO of *hypocloso*-$[B_{12}]^{1-}$, and further validates our assignment of the super-oxidized species as $[B_{12}]^{1+}$. Additional EPR data and an in-depth analysis of the results can be found in Chapter 4.

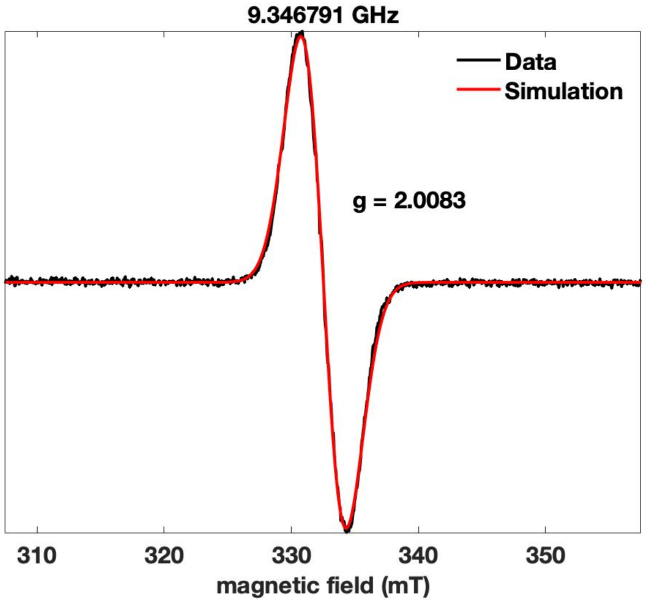

Figure 3.11. X-band CW EPR spectrum of [**5**]$^{1+}$ in toluene glass at 77 K. The cation was in-situ generated by reaction with a substochiometric amount of Magic Green.

3.4 Conclusions

We have shown that super-oxidized $[B_{12}(OR)_{12}]^{1+}$ (R = alkyl) species can be reversibly generated through electrochemical methods. Additionally, collaborators in the Spokoyny lab have been able to isolate [**5**]$[SbCl_6]$ using the strong ammoniumyl radical oxidant (Magic Green). The discovery of these super-oxidized dodecaborates is a significant breakthrough, as it was previously believed that depopulation of the *hypercloso*-B_{12}^{0} HOMO(a_{2u}) would lead to cluster decomposition. This also poses questions around what kind of reactivities these super-oxidized species can access, and, if even higher oxidation states can be isolated in clusters carrying sufficiently electron-donating substituents. These questions are stimulated by preliminary indications suggesting that [**4**]$^{1+}$ partake in catalytic oxidation reactions and that a [**4**]$^{2+}$ species can be electrochemically generated in dichloromethane. Further studies are currently underway to systematically describe the electrochemical, chemical and spectroscopic properties of $[B_{12}(OR)_{12}]^{1+}$ clusters.

3.5 Experimental Details

Compounds

4^0, **5**^{0}, [**5**][$SbCl_6$] and Magic Green were obtained from the Spokoyny lab.

Electrochemistry

Air-free electrochemistry

All sample preparation and measurements were performed inside an argon-filled glove box, which had been equipped with BNC ports to enable connection of an external potentiostat. Cyclic voltammograms of were collected on a Gamry Reference 600 potentiostat using a small-volume electrochemical cell. Electrochemical grade $TBAPF_6$ (Sigma-Aldrich) had been previously recrystallized from hot ethanol and dried under vacuum. A d = 3.0 mm glassy carbon working electron (BASi), a Pt wire counter-electrode and an Ag/AgCl reference electrode was used (BASi). The reference was prepared by placing a polished silver wire in a 0.01 M $AgNO_3$/0.2 M $TBAPF_6$ acetonitrile solution. A CoralPor (BASi) frit provided electrochemical contact between the reference solution and sample solution.

Dichloromethane (Millipore) and acetonitrile (Millipore) had been dried for > 84 hours over activated 3 Å molecular sieves (Sigma-Aldrich). After drying, the solvents were distilled and degassed through multiple freeze-pump-thaw cycles. Sample solutions were prepared at approximately 3.0 mM **4**^{0} in 0.2 M $TBAPF_6$ electrolyte. Between each measurement the sample solution was thoroughly mixed, and the working electrode was polished with a Kimwipe (Kimtech) to remove any residue formed during preceding cycles. A speck of ferrocene (Sigma-Aldrich, purified through sublimation) was added after the final measurement and a cyclic voltammogram was collected at a 100 mV/s. The ferrocene/ferrocenium wave was used as the reference.

The EC-Lab software package (Biologic) was used to analyze the data. Electrochemical parameters were obtained using the Wave Analysis function, taking care to select appropriate baselines. 100 mV/s scans were used to extract final E_p values. The parameters presented in Table 2.1 were derived from the individual wave data shown in Figure (3.3–3.5).

Open-air electrochemistry

Open-air experiments were performed using a CH Instruments potentiostat. Solutions were prepared at ~2 mM $\mathbf{4}^0$ in 0.1 M $TBAPF_6$ dichloromethane (Millipore, used as received) electrolyte. A small-volume electrochemical cell was used for all experiments (BASi) Electrochemical grade $TBAPF_6$ (Sigma-Aldrich) had been previously recrystallized from hot ethanol and dried rigorously under vacuum. A d = 3.0 mm glassy carbon working electron (BASi) , a Pt wire counter-electron and an Ag/AgCl reference electrode was used (BASi). The reference was prepared by placing a polished silver wire in a 0.01 M $AgNO_3$/0.1 M $TBAPF_6$ acetonitrile solution. A CoralPor (BASi) frit provided electrochemical contact between the reference solution and sample solution.

The sample solution was degassed by argon bubbling both before the initial measurement. The gas had first been saturated with dichloromethane by passing it through a bubbler containing dry solvent and activated 3 Å molecular sieves (Sigma-Aldrich). Between each measurement the sample solution was thoroughly mixed by argon bubbling and the working electrode was polished on a polishing pad (BASi). After the final measurement a speck of ferrocene (Sigma-Aldrich, purified through sublimation) was added. A cyclic voltammogram was collected at a 100 mV/s and the ferrocene/ferrocenium wave was used as the reference. The MATLAB software package (Mathworks) was used to analyze the data. Electrochemical parameters were obtained using a custom made scripts, taking care to select appropriate baselines. Cyclic voltammograms collected between 25 and 500 mV/s are shown in Figure 3.12. Figure 3.13–3.15 show plots of peak potential (i_p) as a function of the square root of scan rate (ν). The linear relationships confirm the reversibility of all three couples.

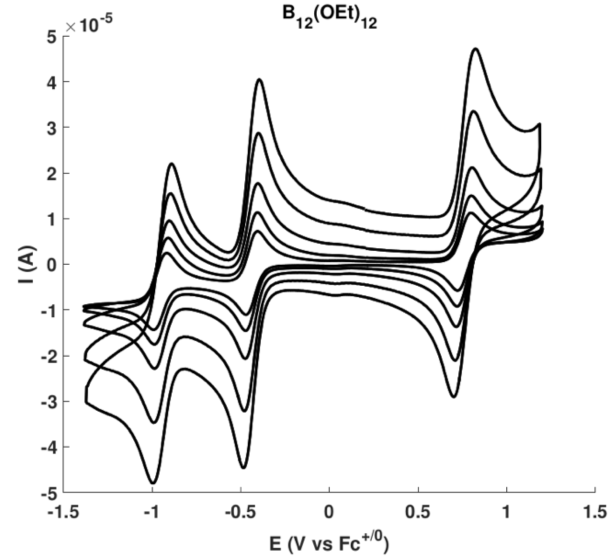

Figure 3.12: Cyclic voltammogram scan rate dependence. ~ 2mM (**4**^{0}) in 0.1 M TBAPF$_6$/dichloromethane at 25 mV/s, 50 mV/s, 100 mV/s, 250 mV/s and 500 mV/s.

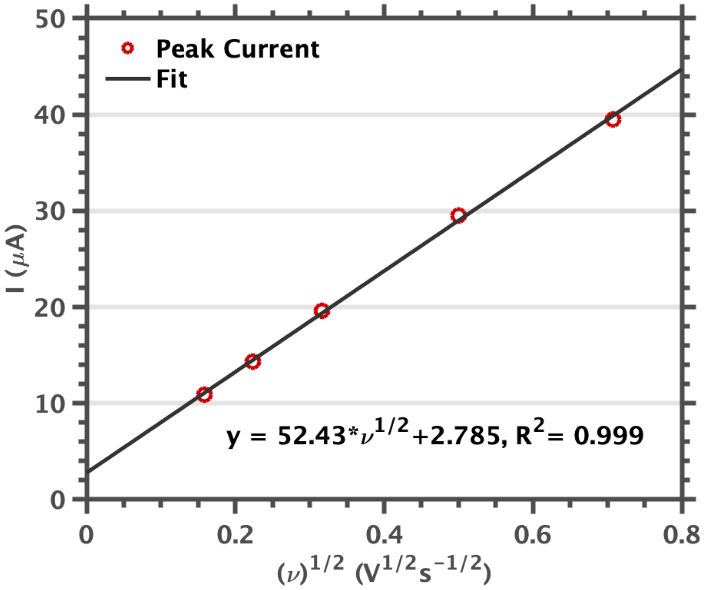

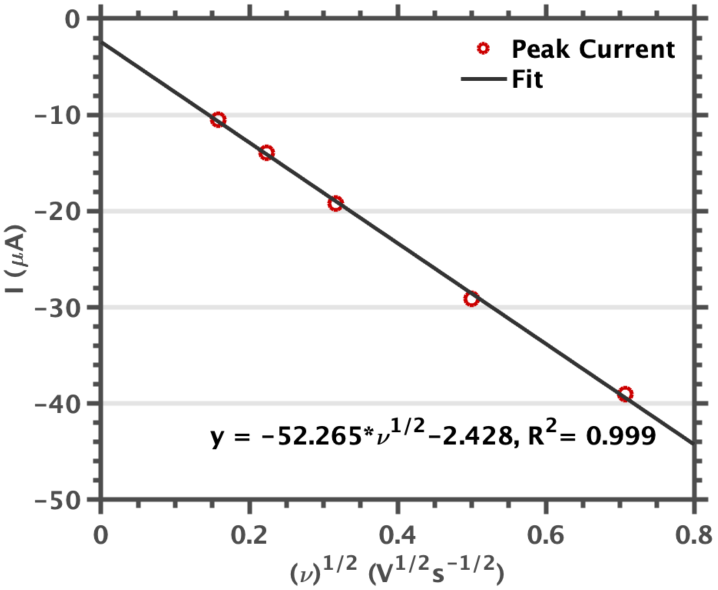

Figure 3.4. I_p vs $(\nu)^{1/2}$ plots for the [**4**]$^{1-/2-}$ couple. The top figure shows peak potentials observed for oxidation of [**4**]$^{2-}$ to [**4**]$^{1-}$ while the bottom figure shown peak potentials observed of reduction of [**4**]$^{1-}$ to [**4**]$^{2-}$.

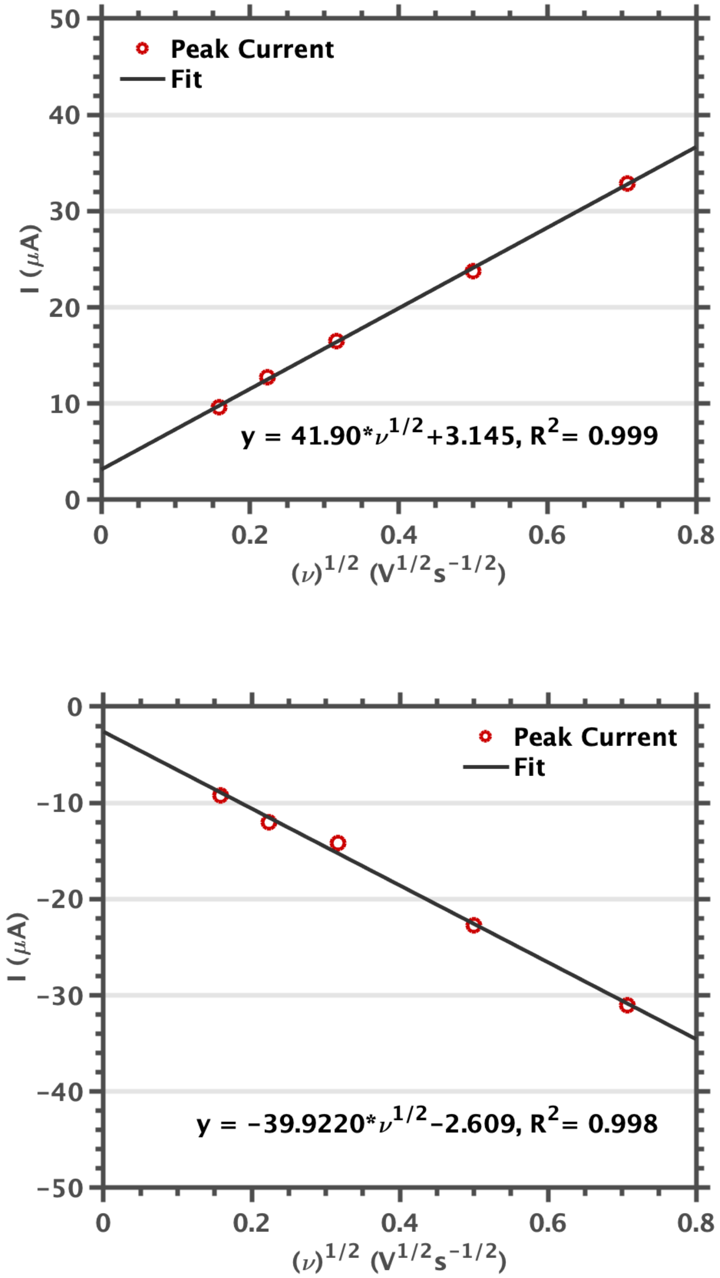

Figure 3.5. I_p vs $(n)^{1/2}$ plots for the $[\mathbf{4}]^{0/1-}$ couple. The top figure shows peak potentials observed for oxidation of $[\mathbf{4}]^{1-}$ to $\mathbf{4}^0$ while the bottom figure shown peak potentials observed of reduction of $\mathbf{4}^0$ to $[\mathbf{4}]^{1-}$.

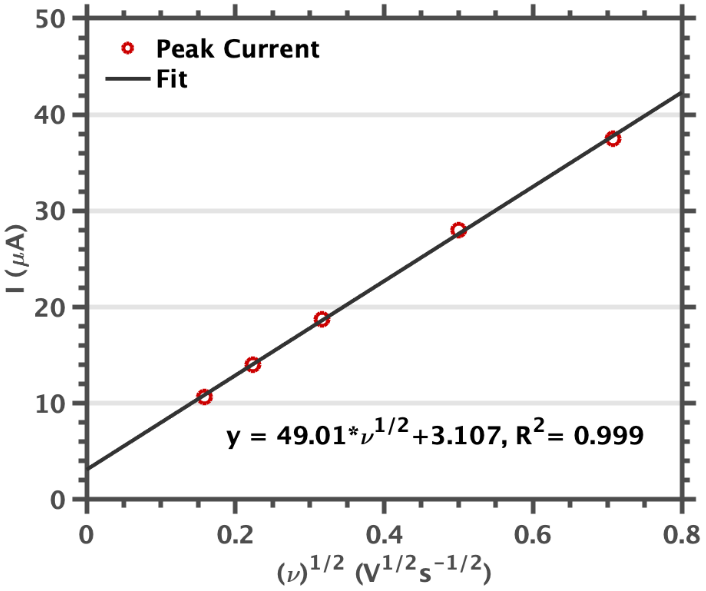

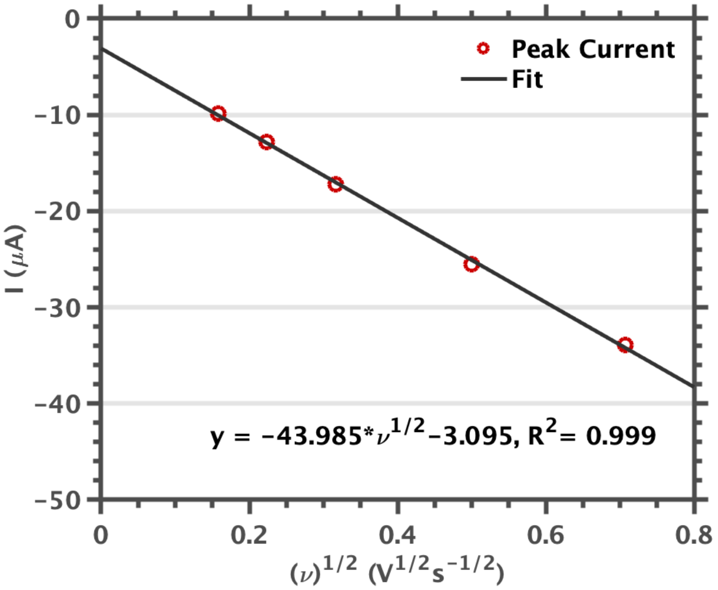

Figure 3.6. I_p vs $(n)^{1/2}$ plots for the $[\mathbf{4}]^{1+/0}$ couple. The top figure shows peak potentials observed for oxidation of $\mathbf{4}^0$ to $[\mathbf{4}]^{1+}$ while the bottom figure shown peak potentials observed of reduction of $[\mathbf{4}]^{1+}$ to $\mathbf{4}^0$.

Spectroelectrochemistry

Solution preparation and control cyclic voltammograms were performed as described above (open-air electrochemistry), with the modification that the **4**^{0} concentration was optimized for spectroelectrochemistry. A portable Pine WaveNow potentiostat was used to provide applied bias, while a Varian Cary 50 Bio UV-visible spectrometer was used to collect spectra. Data was collected using a 0.5 mm path length quartz spectroelectrochemical cell (BASi) and a gold mesh working electrode (BASi). Each potential was held until complete conversion to the desired oxidation state was apparent in the UV-visible spectrum. Due to the design of the spectroelectrochemistry cell, although attempts were made to keep the solution under argon at all times, we cannot guarantee rigorously air-free conditions.

Chemical oxidation

Reactivity was monitored by visual observations and UV-visible spectra collected on a Varian Cary 50 Bio UV-visible spectrometer. All experiments were performed under air-free conditions. Samples were prepared in Schlenk cuvettes to facilitate collection of UV-visible spectra without compromising the samples.

Solvents

3 Å Molecular sieves (Sigma-Aldrich) had been activated through heating to 180ºC under dynamic vacuum for > 12 hours. Activated sieves were stored under vacuum and the storage vessel was placed under positive argon pressure when sieves where being transferred to solvent drying vessels. Before addition of solvent, the solvent vessels and sieves were flame dried.

Nitromethane (Sigma-Aldrich) was dried for > 48 hours over activated 3 Å molecular sieves, followed by three > 30 minute freeze-pump-thaw cycles. Finally, the solvent was allowed to stand over sieves for an additional > 24 hours. An analogous procedure was applied to dry dichloromethane (Millipore). Tetrahydrofuran (Millipore) had been pre-dried on a commercial solvent purification system. The solvent was transferred to a Strauss flask and degassed through multiple freeze-pump-thaw cycles. The flask was then transferred into a nitrogen-filled glove box and the solvent further dried through stirring over NaK.

Nitrosonium tetrafluoroborate

A small speck of nitrosonium tetrafluoroborate (Sigma-Aldrich) was added to solutions of $\mathbf{4}^0$ in nitromethane, tetrahydrofuran and dichloromethane. No reactivity was observed.

Silver triflate

Solid silver triflate (Sigma-Aldrich) was added to solutions of $\mathbf{4}^0$ in nitromethane and dichloromethane. The UV-visible spectrum of the solution was monitored over hours. No reactivity was observed.

Magic Blue—$[(4\text{-Br-}C_6H_4)_3N]SbCl_6$

A solution of $\mathbf{4}^0$ in tetrahydrofuran and dichloromethane was prepared. A speck of Magic Blue (Sigma-Aldrich) was added. The solution immediately turned green but over minutes converted to a dark brown color, in line with what we expect for $[\mathbf{4}]^{1+}$.

A follow-up experiment was performed by titrating a 0.060 mM solution of $\mathbf{4}^0$ in tetrahydrofuran with a 0.64 mM solution of Magic Blue in tetrahydrofuran. 25 µl microliter additions were made. UV-visible spectra were collected after each addition, first allowing the sample to equilibrate. A total of 250 µl Magic Blue solution was added, yielding a final concentration 0.0365 mM

X-band CW Electronic Paramagnetic Resonance of $[5]^{1+}$

All manipulations were carried out inside a nitrogen-filled glove box. Samples were placed in X-band EPR tubes equipped with a J. Young valve and froze in liquid nitrogen immediately after removal from the glove box. Toluene (Millipore) had been dried on a commercial solvent purification system, followed by distillation and multiple freeze-pump-thaw cycles before transferring the solvent into the glove box. Inside the glove box, the solvent was stored over activated 3 Å molecular sieves (Sigma-Aldrich). Samples were prepared by dissolving 1.7 mg Magic Green and 3 mg $\mathbf{5}^0$ in 1 ml toluene. An aliquot of solution was transferred to the EPR tube, which was immediately sealed, removed from the glove box and frozen in liquid nitrogen.

X-band EPR spectra were obtained on a Bruker EMX spectrometer at 77 K in a liquid nitrogen dewar using Bruker Win-EPR software (ver. 3.0). Spectra were collected over a 1–8 mW power range, and 5 scans were averaged for each spectrum. Spectral simulation was performed using the EasySpin[23] Simulation toolbox with MATLAB 2019a .

BIBLIOGRAPHY

(1) Longuet-Higgins, H. C.; Roberts, M. D. V. The Electronic Structure of an Icosahedron of Boron Atoms. *Proc R Soc Lond A* **1955**, *230* (1180), 110–119. https://doi.org/10.1098/rspa.1955.0115.

(2) Lipscomb, W. N. Recent Studies of the Boron Hydrides. In *Advances in Inorganic Chemistry and Radiochemistry*; Emeléus, H. J., Sharpe, A. G., Eds.; Academic Press, 1959; Vol. 1, pp 117–156. https://doi.org/10.1016/S0065-2792(08)60253-8.

(3) Lipscomb, W. N.; Britton, D. Valence Structure of the Higher Borides. *J. Chem. Phys.* **1960**, *33* (1), 275–280. https://doi.org/10.1063/1.1731097.

(4) Hoffmann, R.; Lipscomb, W. N. Theory of Polyhedral Molecules. I. Physical Factorizations of the Secular Equation. *J. Chem. Phys.* **1962**, *36* (8), 2179–2189. https://doi.org/10.1063/1.1732849.

(5) Hoffmann, R.; Lipscomb, W. N. Boron Hydrides: LCAO—MO and Resonance Studies. *J. Chem. Phys.* **1962**, *37* (12), 2872–2883. https://doi.org/10.1063/1.1733113.

(6) Moore, E. B.; Lohr, L. L.; Lipscomb, W. N. Molecular Orbitals in Some Boron Compounds. *J. Chem. Phys.* **1961**, *35* (4), 1329–1334. https://doi.org/10.1063/1.1732046.

(7) Eberhardt, W. H.; Crawford, B.; Lipscomb, W. N. The Valence Structure of the Boron Hydrides. *J. Chem. Phys.* **1954**, *22* (6), 989–1001. https://doi.org/10.1063/1.1740320.

(8) Wiersema, R. J.; Middaugh, R. L. Electrochemical Preparation and Halogenation of 1,1'-.Mu.-Hydro-Bis(Undecahydro-Closo-Dodecaborate)(3-), B24H233-. *Inorg. Chem.* **1969**, *8* (10), 2074–2079. https://doi.org/10.1021/ic50080a009.

(9) Wade, K. The Structural Significance of the Number of Skeletal Bonding Electron-Pairs in Carboranes, the Higher Boranes and Borane Anions, and Various Transition-Metal Carbonyl Cluster Compounds. *J. Chem. Soc. Chem. Commun.* **1971**, No. 15, 792–793. https://doi.org/10.1039/C29710000792.

(10) J. Welch, A. The Significance and Impact of Wade's Rules. *Chem. Commun.* **2013**, *49* (35), 3615–3616. https://doi.org/10.1039/C3CC00069A.

(11) Peymann, T.; Knobler, C. B.; Hawthorne, M. F. An Unpaired Electron Incarcerated within an Icosahedral Borane Cage: Synthesis and Crystal Structure of the Blue, Air-Stable {[Closo-B12(CH3)12]·}– Radical. *Chem. Commun.* **1999**, *0* (20), 2039–2040. https://doi.org/10.1039/A905406E.

(12) Peymann, T.; Knobler, C. B.; Khan, S. I.; Hawthorne, M. F. Dodeca(Benzyloxy)Dodecaborane, B12(OCH2Ph)12: A Stable Derivative of Hypercloso-B12H12. *Angew. Chem. Int. Ed.* **2001**, *40* (9), 1664–1667. https://doi.org/10.1002/1521-3773(20010504)40:9<1664::AID-ANIE16640>3.0.CO;2-O.

(13) Van, N.; Tiritiris, I.; Winter, R. F.; Sarkar, B.; Singh, P.; Duboc, C.; Muñoz-Castro, A.; Arratia-Pérez, R.; Kaim, W.; Schleid, T. Oxidative Perhydroxylation of [Closo-B12H12]2− to the Stable Inorganic Cluster Redox System [B12(OH)12]2−/.−: Experiment and Theory. *Chem. – Eur. J.* **2010**, *16* (37), 11242–11245. https://doi.org/10.1002/chem.201001374.

(14) Boeré, R. T.; Derendorf, J.; Jenne, C.; Kacprzak, S.; Keßler, M.; Riebau, R.; Riedel, S.; Roemmele, T. L.; Rühle, M.; Scherer, H.; et al. On the Oxidation of the Three-Dimensional Aromatics [B12X12]2− (X=F, Cl, Br, I). *Chem. – Eur. J.* **2014**, *20* (15), 4447–4459. https://doi.org/10.1002/chem.201304405.

(15) Wixtrom, A. I.; Shao, Y.; Jung, D.; Machan, C. W.; Kevork, S. N.; Qian, E. A.; Axtell, J. C.; Khan, S. I.; Kubiak, C. P.; Spokoyny, A. M. Rapid Synthesis of Redox-Active Dodecaborane B12(OR)12 Clusters under Ambient Conditions. *Inorg. Chem. Front.* **2016**, *3* (5), 711–717. https://doi.org/10.1039/C5QI00263J.

(16) Messina, M. S.; Axtell, J. C.; Wang, Y.; Chong, P.; Wixtrom, A. I.; Kirlikovali, K. O.; Upton, B. M.; Hunter, B. M.; Shafaat, O. S.; Khan, S. I.; et al. Visible-Light-Induced Olefin Activation Using 3D Aromatic Boron-Rich Cluster Photooxidants. *J. Am. Chem. Soc.* **2016**, *138* (22), 6952–6955. https://doi.org/10.1021/jacs.6b03568.

(17) Axtell, J. C.; Messina, M. S.; Liu, J.-Y.; Galaktionova, D.; Schwan, J.; Porter, T. M.; Savage, M. D.; Wixtrom, A. I.; Rheingold, A. L.; Kubiak, C. P.; et al. Photooxidative Generation of Dodecaborate-Based Weakly Coordinating Anions. *Inorg. Chem.* **2019**, *58* (16), 10516–10526. https://doi.org/10.1021/acs.inorgchem.9b00935.

(18) Barton, J. L.; Wixtrom, A. I.; Kowalski, J. A.; Qian, E. A.; Jung, D.; Brushett, F. R.; Spokoyny, A. M. Perfunctionalized Dodecaborate Clusters as Stable Metal-Free Active Materials for Charge Storage. *ACS Appl. Energy Mater.* **2019**, *2* (7), 4907–4913. https://doi.org/10.1021/acsaem.9b00610.

(19) Aubry, T. J.; Axtell, J. C.; Basile, V. M.; Winchell, K. J.; Lindemuth, J. R.; Porter, T. M.; Liu, J.-Y.; Alexandrova, A. N.; Kubiak, C. P.; Tolbert, S. H.; et al. Dodecaborane-Based Dopants Designed to Shield Anion Electrostatics Lead to Increased Carrier Mobility in a Doped Conjugated Polymer. *Adv. Mater.* **2019**, *31* (11), 1805647. https://doi.org/10.1002/adma.201805647.

(20) Axtell, J. C.; Saleh, L. M. A.; Qian, E. A.; Wixtrom, A. I.; Spokoyny, A. M. Synthesis and Applications of Perfunctionalized Boron Clusters. *Inorg. Chem.* **2018**, *57* (5), 2333–2350. https://doi.org/10.1021/acs.inorgchem.7b02912.

(21) Quiroz-Guzman, M.; Brown, S. N. Tris(4-Bromo-phenyl)Aminium Hexa-chloridoantimonate (`Magic Blue’): A Strong Oxidant with Low Inner-Sphere Reorganization. *Acta Crystallogr. C* **2010**, *66* (7), m171–m173. https://doi.org/10.1107/S0108270110019748.

(22) Connelly, N. G.; Geiger, W. E. Chemical Redox Agents for Organometallic Chemistry. *Chem. Rev.* **1996**, *96* (2), 877–910. https://doi.org/10.1021/cr940053x.

(23) Stoll, S.; Schweiger, A. EasySpin, a Comprehensive Software Package for Spectral Simulation and Analysis in EPR. *J. Magn. Reson.* **2006**, *178* (1), 42–55. https://doi.org/10.1016/j.jmr.2005.08.013.

Intentionally left blank

Chapter 4

ELECTRONIC STRUCTURES OF PERFUNCTIONALIZED DODECABORATE CLUSTERS

A manuscript based on the work presented in this chapter is being prepared for submission by Schwan, L. J.; Oyala, P. H.; Stauber. J. M.; Axtell, J. C. Winkler, J. R.; Spokoyny, A. M.; Gray, H. B. Electronic Structures of Perfunctionalized Dodecaborate Clusters.

Chapter 4 discusses our exploration of the electronic structures of hypoelectronic [$B_{12}(OR)_{12}$] clusters. Previous work has been focused on computational descriptions, as experimental investigations were hampered by the broad and unresolved continuous wave EPR spectra typically observed for open shell hypocloso-[$B_{12}(OR)_{12}]^{1-}$ species. Here, we use pulsed Q-band EPR techniques, with particular focus on ENDOR spectroscopy, to quantify the hyperfine interactions in these compounds and provide an experimental description of the SOMO(a_{1u}) spin density distribution. Furthermore, following our discovery of super-oxidized dodecaborate cations, we extended our pulsed EPR work to investigate the spin density distribution of the SOMO(a_{2u}) of [$B_{12}(OR)_{12}]^{1+}$. Our work convincingly shows that the frontier orbitals of [$B_{12}(OR)_{12}$] clusters are confined to the cluster core and evenly delocalized across the 12 boron atoms. Comparisons between [$B_{12}(OR)_{12}]^{1+}$ cations and hypocloso-[$B_{12}(OR)_{12}]^{1-}$ anions further suggest that the spin density becomes more localized in more highly oxidized clusters. Besides our EPR investigations, we report UV–vis–NIR data which suggest that the visible and NIR transitions of hypoelectronic [$B_{12}(OR)_{12}$] clusters involve orbitals largely confined to the cluster core. Ongoing work aims to produce a more comprehensive description of the electronic transitions through expansion of our UV–vis–NIR studies, and to perform in-depth analysis of the pulsed EPR data for the super-oxidized [$B_{12}(OR)_{12}]^{1+}$ clusters.

4.1 Background

The discovery of a convenient process to perfunctionalize dodecaborate clusters, starting from dodecahydroxy-*closo*-dodecaborate (*closo*-$[B_{12}(OH)_{12}]^{2-}$), has led to the development of a range of aryloxy and alkyloxy-perfunctionalized dodecaborates ($[B_{12}(OR)_{12}]$; bracketing indicates an unspecified oxidation state if no oxidation number is given.).[1,2] While the parent *closo*-$[B_{12}H_{12}]^{2-}$ cluster is stable only in its dianionic closed-shell form,[3–7] the electron-donating OR groups allow $[B_{12}(OR)_{12}]$ to undergo two (aryl) or three (alkyl) reversible one-electron oxidations to form hypoelectronic *hypocloso*-$[B_{12}]^{1-}$ (25 electron), *hypercloso*-B_{12}^{0} (24 electron) and $[B_{12}]^{1+}$ (23 electron) cluster cores.[1,2,8] These clusters are promising candidates for a range of applications; recent examples include acting as combined photoinitiators and weakly coordinating proanions for cationic styrene polymerization[2,9], as well as for charge-storage devices[10] and as dopants in conducting polymers.[11] Here, we use pulsed electron paramagnetic resonance (EPR) techniques and UV-visible to near infrared (NIR) spectroscopies to investigate the electronic structure of five $[B_{12}(OR)_{12}]$ clusters: $[B_{12}(OCH_2C_6F_5)_{12}]$ ([**1**]), $[B_{12}(OCH_2(3,5\text{-}(CF_3)_2\text{-}C_6H_3)_{12}]$ ([**2**]), $[B_{12}(OBz)_{12}]$ ([**3**]), $[B_{12}(OEt)_{12}]$ ([**4**]). $[B_{12}(OC_2H_4{}^{i}Pr)_{12}]$ and ([**5**]) (Bz = $CH_2C_6H_5$, Et = C_2H_5, ^{i}Pr = C_3H_7).

The icosahedral *closo*-$[B_{12}H_{12}]^{2-}$ cluster is stabilized by a fully populated 4-fold degenerate B-B bonding HOMO(g_u) (highest occupied molecular orbital). Oxidation yields an unstable open shell species and leads to decomposition of the cluster.[3] However, some perfunctionalized dodecaborate clusters carrying electron-donating groups are able to accommodate hypoelectronic states. Examples include *hypocloso*-$[B_{12}(OR)_{12}]^{1-}$, *hypercloso*-$B_{12}(OR)_{12}$ (R = alkyl or aryl),[1,2,8,12,13] *hypocloso*-$[B_{12}Me_{12}]^{1-}$ (Me = CH_3)[14] and *hypocloso*-$[B_{12}X_{12}]^{1-}$ (X = F, Cl, Br, I).[15,16] Additionally, we recently discovered that $[B_{12}(OR)_{12}]$ clusters carrying certain alkyl substituents, such as [**4**] and [**5**], can accommodate a super-oxidized cationic $[B_{12}(OR)_{12}]^{1+}$ state (see Chapter 3).

Several factors contribute to the ability of $[B_{12}(OR)_{12}]$ clusters to support hypoelectronic oxidation states. Oxidized $[B_{12}H_{12}]$ species are not stable as depopulation of the four-fold degenerate B-B bonding HOMO(g_u) leads to an energetically unfavorable configuration. In hypoelectronic $[B_{12}(OR)_{12}]$ clusters, B-B bonding is enhanced through electron donation from the OR groups. Furthermore, structural distortion lowers the cluster core symmetry from I_h to D_{3d}, which splits the degenerate g_u set into orbitals of a_{1u} + a_{2u} + e_u symmetry. Raising the depopulated SOMO(a_{1u}) (singly occupied molecular orbital; in $[B_{12}]^{1-}$) or LUMO(a_{1u}) (lowest unoccupied molecular orbital; in B_{12}^0 and $[B_{12}]^{1+}$) and lowering of the fully populated HOMO-1(e_u) set (HOMO-1 refers to the second lowest energy occupied molecular orbital) reduces the overall energy of the cluster. Steric factors may also contribute to the stability of the cluster core, in particular when considering clusters carrying bulky fluoroaryl-substituents.[1,2,8,9,17,18] Motivated by the emerging applications and extraordinary ability to accommodate high oxidation states, we decided to perform an in-depth spectroscopic investigation of the electronic structures of $[B_{12}(OR)_{12}]$ clusters, hoping to provide comprehensive experimental descriptions of the frontier orbitals and electronic transitions of these clusters.

Attempts to examine the SOMO(a_{1u}) of monoanionic *hypocloso*-dodecaborate clusters using EPR spectroscopy have been restrained by the lack of resolution in continuous wave (CW) spectrum.[1,8,9,14] Even at high field strengths and low temperatures (285 GHz, 5 K) only very slight g-anisotropy is observed for $[B_{12}(OH)_{12}]^{1-}$.[17] It is generally believed that this is due to a highly delocalized SOMO, where the twelve near-equivalent boron nuclei give rise to a large number of overlapping hyperfine lines. This description has gained support from DFT calculations, although the details of the computational results vary significantly between different authors. We decided to investigate paramagnetic *hypocloso*-$[B_{12}(OR)_{12}]^{1-}$ and recently discovered $[B_{12}(OR)_{12}]^{1+}$ clusters using pulsed EPR techniques, hoping to verify the delocalized description of the frontier orbitals and show that the spin density is confined to the cluster core. To our knowledge this is the first time pulsed EPR data has been reported for paramagnetic dodecaborate clusters.

4.2 Pulsed EPR Investigation of *hypocloso*-$[B_{12}(OR)_{12}]^{1-}$

Q-band (34 GHz) EPR data was collected for the three anionic *hypocloso*-$[B_{12}(OR)_{12}]^{1-}$ clusters [**1**-**3**]$^{1-}$. [**1**]$^{1-}$ and [**2**]$^{1-}$ samples were prepared from their respective tetrabutylammonium (TBA) salts. Sufficiently pure salts of [**3**]$^{1-}$ have proven difficult to isolate, so we instead opted to prepare samples through *in-situ* reduction of **3**^{0} with triethylamine. As expected, Q-band Electron Spin Echo (ESE) EPR spectra of [**1**-**3**]$^{1-}$ show broad unresolved signals (Figure 4.1; g([**1**]$^{1-}$) = 2.00884, g([**2**]$^{1-}$) = 2.00883, g([**3**]$^{1-}$) = 2.00894), in line with reported X-band CW EPR spectra of *hypocloso*-$[B_{12}]^{1-}$ species. Davies Electron Nuclear Double Resonance (ENDOR) spectra for [**1**-**3**]$^{1-}$ are shown in Figure 4.2. The spectra were simulated as single class of rhombic $^{10/11}B$ hyperfine couplings ($|A_{x,y,z}$([**1**]$^{1-}$)$|$ = [0.1, 8.8, 12.9] MHz, $|A_{x,y,z}$([**2**]$^{1-}$)$|$ = [0.1, 9.4, 13.1] MHz, $|A_{x,y,z}$([**3**]$^{1-}$)$|$ = [0.1, 9.1, 12.6] MHz) and ^{1}H couplings ($|A_{x,y,z}$([**1**]$^{1-}$)$|$ = [1, 9.5, 6] MHz, $|A_{x,y,z}$([**2**]$^{1-}$)$|$ = [1, 9.5, 6] MHz, $|A_{x,y,z}$([**3**]$^{1-}$)$|$ = [1, 10, 6] MHz). g-values and hyperfine tensors are compared in Table 4.1. The simulations were refined using the Mims ENDOR spectra shown in Figure 4.3 and HYSCORE data. Figure 4.4 shows the [**3**]$^{1-}$ HYSCORE along with the results from simulations using the hyperfine tensors above. In addition to what can be observed in the Davies ENDOR, the Mims ENDOR spectra indicated a class of very weak hyperfine couplings to ^{19}F ($|A_{x,y,z}| < 0.5$Mhz) for both **[1]**$^{1-}$ and **[2]**$^{1-}$.

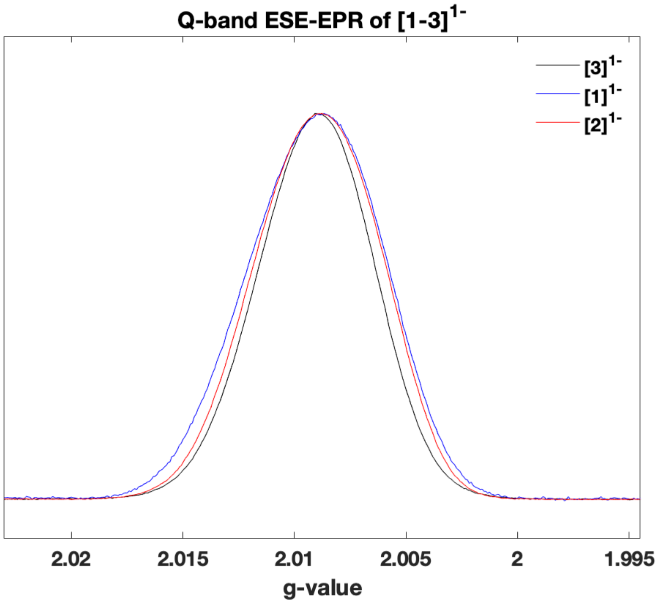

Figure 4.1. Q-band ESE-EPR spectra of [**1**-**3**]$^{1-}$ collected at 5 K and 34.11 GHz microwave frequency. Fitting of the ESE-EPR data yields isotropic g-values: g([**1**]$^{1-}$) = 2.00884, g([**2**]$^{1-}$) = 2.00883, g([**3**]$^{1-}$) = 2.00894.

The hyperfine coupling tensors are near identical between the three clusters, indicating a cluster core confined SOMO(a_{1u}) where the R-groups do not significantly perturb the spin density distribution. The very weak ^{19}F hyperfine coupling, which likely stems from through-space interactions, further substantiate a cluster core confined description. That we only observe a single class of $^{10/11}$B hyperfine interactions strongly supports describing the SOMO(a_{1u}) as evenly delocalized over twelve near-equivalent boron nuclei. Calculating quantitative spin densities remains a major challenge as it requires determining the relative orientation of all the contributing boron 2p orbitals. In this chapter, we have limited our quantitative calculations to the s-orbital spin densities, which can be readily obtained from the isotropic component of the hyperfine tensor. These calculations (see Section 4.6 for details) give a total boron 2s orbital spin density of ρ_{2s} = 3.4% (~0.3% on each of the 12 boron nuclei). Analogous calculations for the 24 proton 1s orbitals yield a total orbital spin density of ρ_{1s} = 9.9%. Rather than considering a SOMO(a_{1u}) extended beyond the oxygens, which would be inconsistent with the very weak ^{19}F hyperfine coupling, we believe the ^{1}H hyperfine interactions stem from hyperconjugation between β-protons and oxygen 2p spin density.

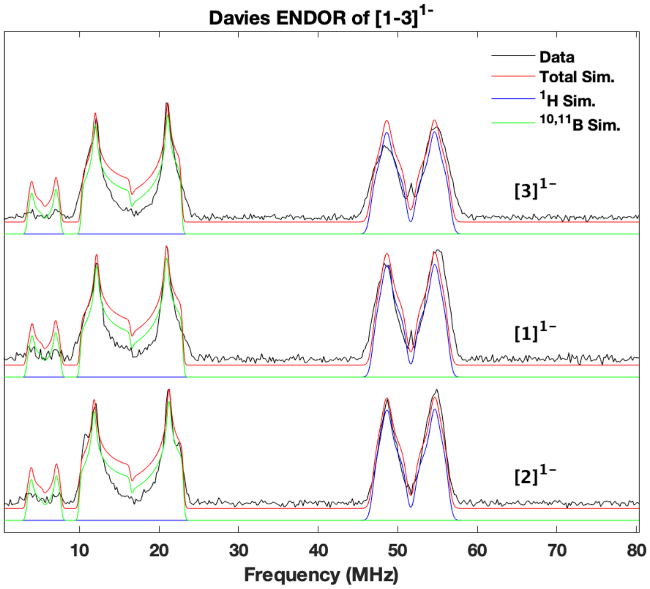

Figure 4.2. Davies ENDOR spectra of [**1**-**3**]$^{1-}$ collected at 5 K and 34.11 GHz microwave frequency. The colored lines show results from simulations using g([**1**]$^{1-}$) = 2.00884, g([**2**]$^{1-}$) = 2.00883, g([**3**]$^{1-}$) = 2.00894, and $^{10/11}$B hyperfine tensors $|A_{x,y,z}$([**1**]$^{1-}$)$|$ = [0.1, 8.8, 12.9] MHz, $|A_{x,y,z}$([**2**]$^{1-}$)$|$ = [0.1, 9.4, 13.1] MHz and $|A_{x,y,z}$([**3**]$^{1-}$)$|$ = [0.1, 9.1, 12.6] MHz, and ^{1}H hyperfine tensors $|A_{x,y,z}$([**1**]$^{1-}$)$|$ = [1, 9.5, 6] MHz, $|A_{x,y,z}$([**2**]$^{1-}$)$|$ = [1, 9.5, 6] MHz, $|A_{x,y,z}$([**3**]$^{1-}$)$|$ = [1, 10, 6] MHz. Blue lines represent the ^{1}H simulation, green lines the $^{10/11}$B simulation and red lines the total simulation combining both ^{1}H and $^{10/11}$B contributions.

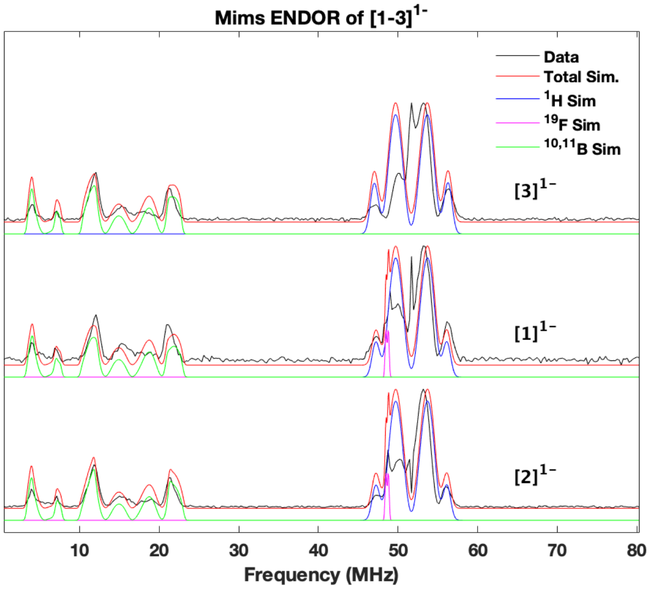

Figure 4.3. Mims ENDOR spectra of [**1**-**3**]$^{1-}$ collected at 5 K and 34.11 GHz microwave frequency. A very weak ^{19}F hyperfine coupling can be observed on the left side of the ^{1}H signal. The colored lines show results from simulations using g([**1**]$^{1-}$) = 2.00884, g([**2**]$^{1-}$) = 2.00883, g([**3**]$^{1-}$) = 2.00894, and the ^{19}F hyperfine tensor $A_{x,y,z}$ = [-0.25 0.5 -0.25] MHz, $^{10/11}$B hyperfine tensors $|A_{x,y,z}$([**1**]$^{1-}$)$|$ = [0.1, 8.8, 12.9] MHz, $|A_{x,y,z}$([**2**]$^{1-}$)$|$ = [0.1, 9.4, 13.1] MHz and $|A_{x,y,z}$([**3**]$^{1-}$)$|$ = [0.1, 9.1, 12.6] MHz, and ^{1}H hyperfine tensors $|A_{x,y,z}$([**1**]$^{1-}$)$|$ = [1, 9.5, 6] MHz, $|A_{x,y,z}$([**2**]$^{1-}$)$|$ = [1, 9.5, 6] MHz, $|A_{x,y,z}$([**3**]$^{1-}$)$|$ = [1, 10, 6] MHz. Blue lines represent the ^{1}H simulation, green lines the $^{10/11}$B simulation and red lines the total simulation combining both ^{1}H and $^{10/11}$B contributions.

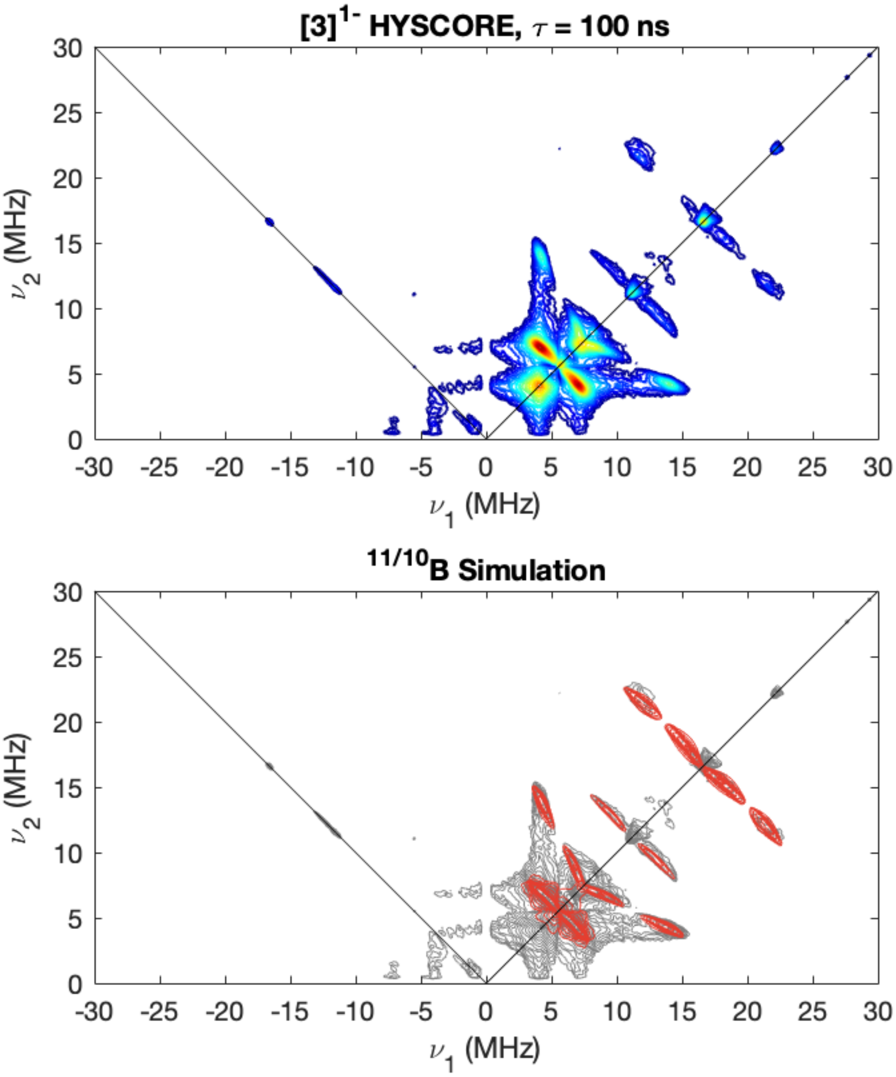

Figure 4.4. The top image shows HYSCORE data for [**3**]$^{1-}$ collected at 50 K and 34.11 GHz microwave frequency. Results for [**1**]$^{1-}$ and [**2**]$^{1-}$ are similar to the data presented here. The image figure shows the $^{10/11}$B simulation (red) obtained using g([**3**]$^{1-}$) = 2.00894 and a $|A_{x,y,z}$([**3**]$^{1-}$)$|$ = [0.1, 9.1, 12.6] MHz hyperfine tensor. The underlying gray contour map corresponds to the experimental data.

4.3 Pulsed EPR Investigation of Super-Oxidized $[B_{12}(OR)_{12}]^{1+}$ Clusters

Motivated by our successful application of pulsed EPR techniques to the *hypocloso*-$[B_{12}(OR)_{12}]^{1-}$ clusters, we decided to explore the recently discovered super-oxidized $[B_{12}(OR)_{12}]^{1+}$ cation. Samples of [**4**-**5**]$^{1+}$ were prepared through *in-situ* oxidation of **4**^{0} and **5**^{0} using a substochiometric amount of the strong oxidant tris(2,4-dibromophenyl)ammoniumyl hexachloroantimonate. Interestingly, the Q-band ESE-EPR spectrum, shown in Figure 4.5, of these species display some anisotropy in the g-tensor ($g_{x,y,z}$([**5**]$^{1+}$) = [2.0140 2.0082 2.0002]). This suggests that the cluster core is more distorted than in the [**1**-**3**]$^{1-}$ anions, which is not surprising given that further splitting the HOMO-1(e_u) set and the SOMO(a_{2u}) would likely result in a more stable cluster core. Figure 4.6 demonstrates the resemblance of the Davies ENDOR for [**4**-**5**]$^{1+}$ and [**3**]$^{1-}$, indicating that the SOMO distribution is similar in both the anion and the cation. Figure 4.7 and 4.8 shows simulations of the Davies ENDOR spectra and HYSCORE of [**5**]$^{1+}$, using hyperfine tensors relatively similar to those observed for [**1**-**3**]$^{1-}$ ($^{10/11}$B $|A_{x,y,z}$([**5**]$^{1+}$)$|$ = [0.1 8.5 13.5] MHz and ^{1}H $|A_{x,y,z}$([**5**]$^{1+}$)$|$ = [0.5 11 7] MHz). Interestingly, the HYSCORE of [**4**]$^{1+}$, for which we were able to obtain a significantly improved signal-to-noise, indicate that an additional class of weak ^{11}B hyperfine interactions are present (Figure 4.9). We are at this time unsure whether this weak signal indicates that [**4**]$^{1+}$ is more distorted than [**5**]$^{1+}$, or if we are simply not resolving the analogous features for [**5**]$^{1+}$ due to poor signal intensity. Figure 4.10 compares Davies ENDOR spectra of [**4**]$^{1+}$ at the high and low field edges. At the low field edge, the $^{10/11}$B signal appear broadened beyond detection, which is not suspiring given the broadness of the HYSCORE features in that quadrant. Simulations of the [**4**]$^{1+}$ data are currently underway.

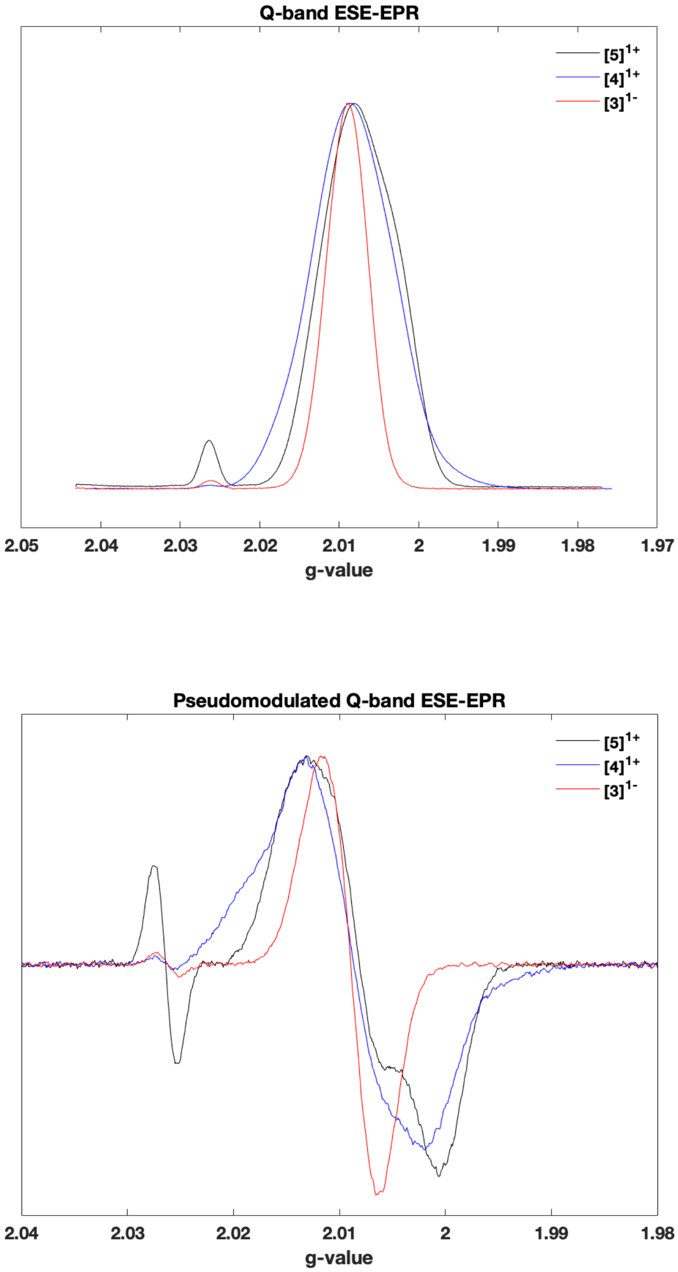

Figure 4.5. (Top) ESE-EPR spectra and (Bottom) pseudomodulated ESE-EPR spectra for [**4**-**5**]$^{1+}$ collected 32 K and 34.11 GHz ([**5**]$^{1+}$) or 34.13 GHz ([**4**]$^{1+}$) microwave frequency. Data for [**3**]$^{1-}$ is shown for comparison, demonstrating the significantly increased g-anisotropy. [**3**]$^{1-}$ data was collected at 5 K and 34.11 GHz microwave frequency. Fitting of the [**5**]$^{1+}$ ESE-EPR spectrum gives $g_{x,y,z}$([**5**]$^{1+}$) = [2.0140 2.0082 2.0002].

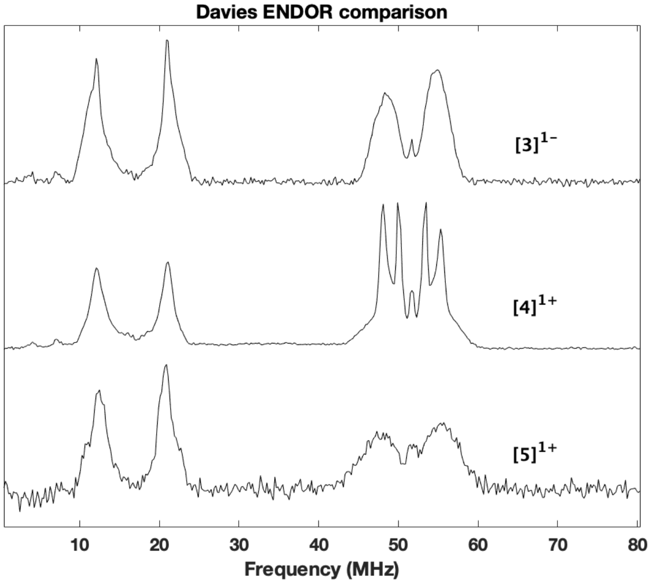

Figure 4.6. Davies ENDOR spectra for [**4**-**5**]$^{1+}$ compared to a spectrum collected for [**3**]$^{1+}$, demonstrating the similarities between the anion and cation data. Data was collected at 5 K ([**3**]$^{1-}$), 25 K ([**4**]$^{1+}$) and 18 K ([**3**]$^{1+}$). Microwave frequencies were the same as used for the ESE-EPR data (see Figure 4.5).

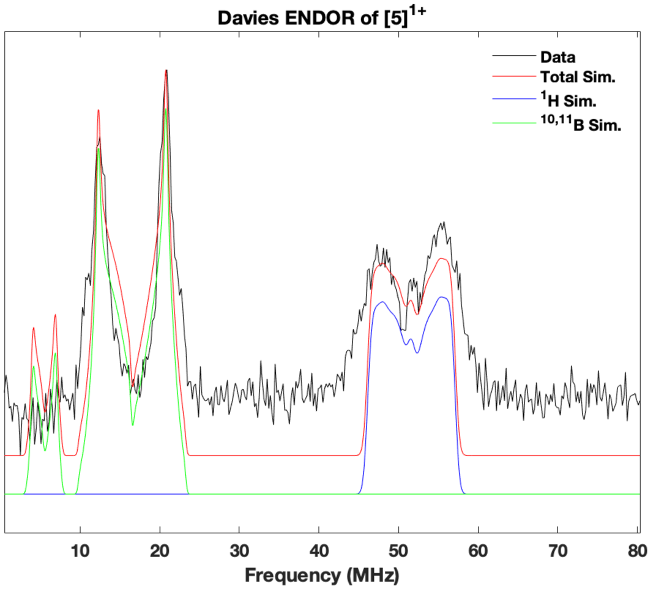

Figure 4.7. The black line shows the Davies ENDOR data for [**5**]$^{1+}$. The colored lines show simulations to $g_{x,y,z}$ = [2.0140 2.0082 2.0002] $^{10/11}$B $|A_{x,y,z}|$ = [0.1, 8.5, 13.5] MHz and ^{1}H $|A_{x,y,z}|$ = [0.5 11 7] MHz. Blue lines represent the ^{1}H simulation, green lines the $^{10/11}$B simulation and red lines the total simulation combining both ^{1}H and $^{10/11}$B contributions.

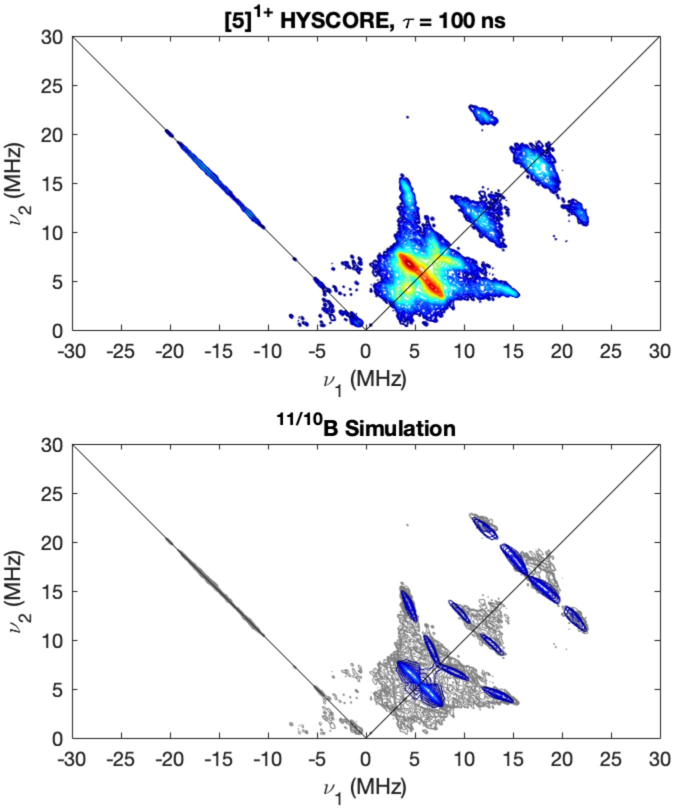

Figure 4.8. (Top) [**5**]$^{1+}$ HYSCORE collected at 32 K and 34.11 GHz microwave frequency. (Bottom) HYSCORE data in gray and simulation to $g_{x,y,z}$ = [2.0140 2.0082 2.0002] and $|A_{x,y,z}|$ = [0.1, 8.5, 13.5] MHz in color.

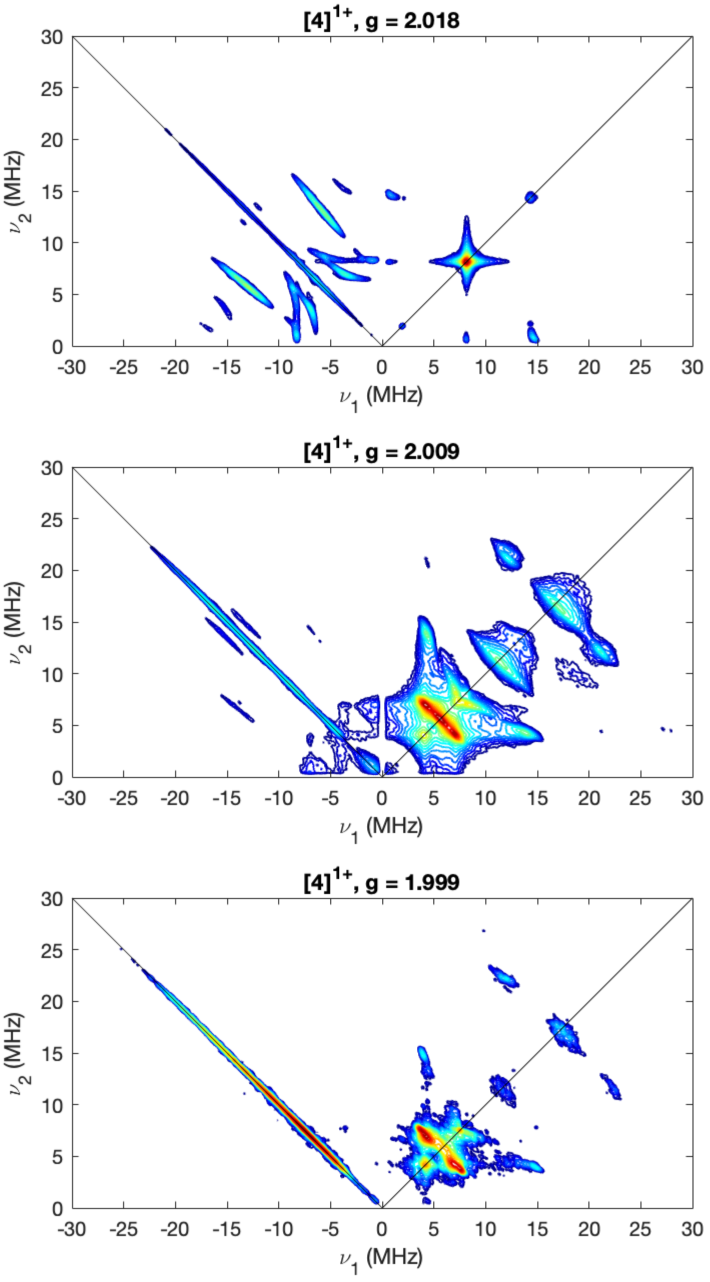

Figure 4.9. HYSCORE data collected for [**4**]$^{1+}$ at 25 K and 34.13 GHz microwave frequency. A broad feature appears in the left quadrant at the low field edge.

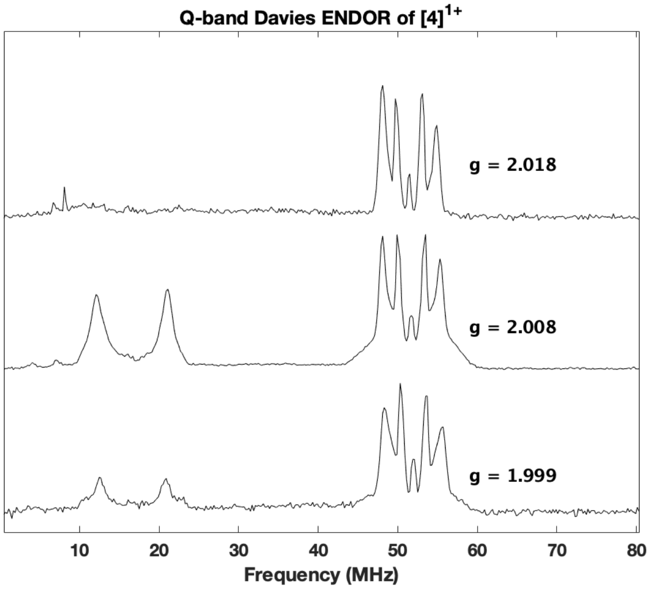

Figure 4.10. Comparison of Davies ENDOR spectra of [**4**]$^{1+}$ at the low field edge, mid field and high field edge. Data was collected at 25 K and 34.13 GHz microwave frequency. Analogous data collected for [**1**-**3**]$^{1-}$ do not show significant field dependence (see Section 4.6).

The mid field ENDOR spectra of [**4**-**5**]$^{1+}$ are comparable to spectra collected for the [**1**-**3**]$^{1-}$ anions, suggesting that the distribution of the SOMO(a_{2u}) is similar to the SOMO(a_{1u}) of the anions. This is further validated by the likeness of the simulated hyperfine tensors of [**5**]$^{1+}$ compared to [**1**-**3**]$^{1-}$. This is expected, as the SOMO (a_{1u} symmetry in $[B_{12}]^{1-}$ and a_{2u} symmetry in $[B_{12}]^{1+}$) stem from the same degenerate I_h symmetry HOMO(g_u) in both cases. However, the anisotropy in the ESE-EPR indicates that the SOMO(a_{2u}) is not equally distributed across all twelve boron nuclei. This is further supported by the ENDOR field dependence and the additional features in the HYSCORE of [**4**]$^{1+}$. This could be due to inherent differences in the orbital geometry between aryl-functionalized and alkyl-functionalized clusters, but a more probable cause is increased distortion in the cluster core of the more oxidized species. Although we have not yet been able to structurally characterize any super-oxidized $[B_{12}(OR)_{12})]^{1+}$ clusters, we postulate that the cluster core is elongated along the z-axis, resulting in a SOMO(a_{2u}) with the majority of the spin density centered around the equatorial belt. g-values and hyperfine tensors obtained for [**1**-**3**]$^{1-}$ and [**5**]$^{1+}$ are summarized in Table 4.1.

Table 4.1. g-values and hyperfine tensors obtained by simulation of ESE-EPR, ENDOR and HYSCORE data.

	$g_{x,y,z}$	^{1}H $\lvert A_{x,y,z}\rvert$ (MHz)	$^{10/11}$B $\lvert A_{x,y,z}\rvert$ (MHz)	^{19}F $\lvert A_{x,y,z}\rvert$ (MHz)
[**1**]$^{1-}$	2.00884	[1 9.5 6]	[0.1 8.8 12.9]	< 0.5
[**2**]$^{1-}$	2.00883	[1 9.5 6]	[0.1 9.4 13.1]	< 0.5
[**3**]$^{1-}$	2.00894	[1 10 6]	[0.1 9.1 12.6]	-
[**5**]$^{1+}$	[2.0140 2.0082 2.0002]	[0.5 11 7]	[0.1 8.5 13.5]	-

4.4 Electronic Transitions in $[B_{12}(OR)_{12}]$ Clusters

UV–vis–NIR spectra of $\mathbf{1}^0$, $\mathbf{2}^0$, TBA[**1**] and TBA[**2**] are shown Figure 4.11 and 4.12, while spectra of the alkyloxy functionalized clusters are shown in Figure 4.13 ($\mathbf{4}^0$ and $\mathbf{5}^0$) and 4.14 ($[\mathbf{4}]^{1+}$). The excitation energies and extinction coefficients are summarized in Table 4.2. The dianionic *closo*-$[B_{12}(OR)_{12}]^{2-}$ clusters are colorless, consistent with the large energy gap expected between the four-fold degenerate HOMO(g_u) and LUMO(g_g).[18] Depopulation of the HOMO gives rise to a strong visible absorption band (ES3). In the anionic TBA[**1**] and TBA[**2**] cluster ES3 appears around 525 nm ($1.9*10^5$ cm^{-1}, ~$1.5*10^4$ M^{-1} cm^{-1}), while in the neutral $\mathbf{1}^0$ and $\mathbf{2}^0$ clusters it is blue-shifted to around 455 nm ($2.2*10^5$ cm^{-1}, ~$3*10^4$ M^{-1} cm^{-1}). The alkyloxy-perfunctionalized $\mathbf{4}^0$ and $\mathbf{5}^0$ clusters show analogous absorption bands blue-shifted by 5-10 nm. Given that the energy of

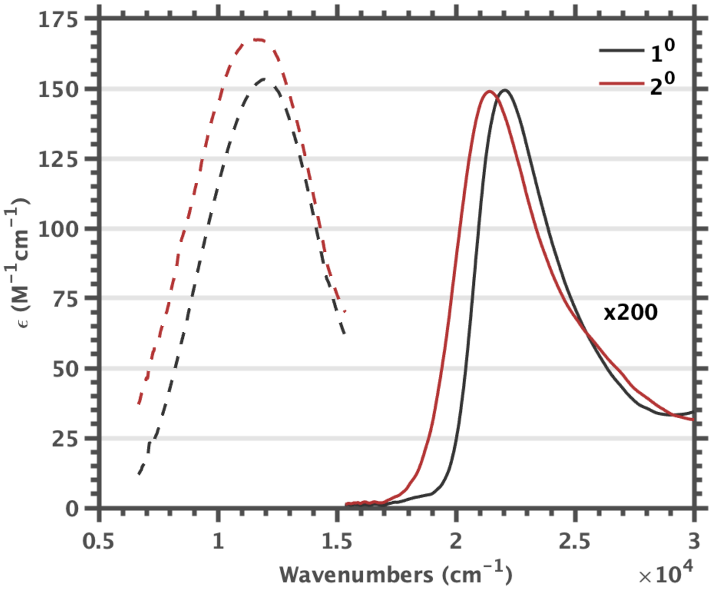

Figure 4.11. UV–vis–NIR spectra of $\mathbf{1}^0$ and $\mathbf{2}^0$ collected in dichloromethane-d_2. The visible band is displayed at approximately 1/200 of its actual extinction coefficient.

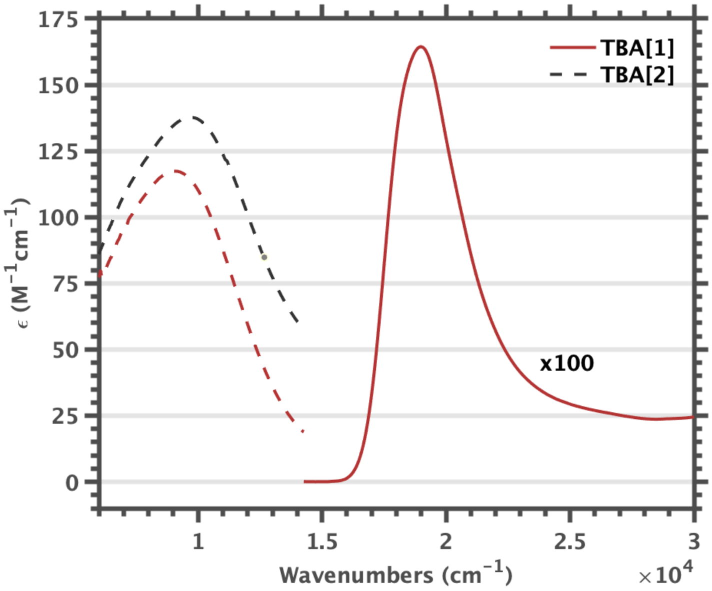

Figure 4.12. UV–vis–NIR spectra of TBA[**1**] and TBA[**2**] collected in dichloromethane-*d*$_2$. The visible band is displayed at approximately 1/100 of its actual extinction coefficient.

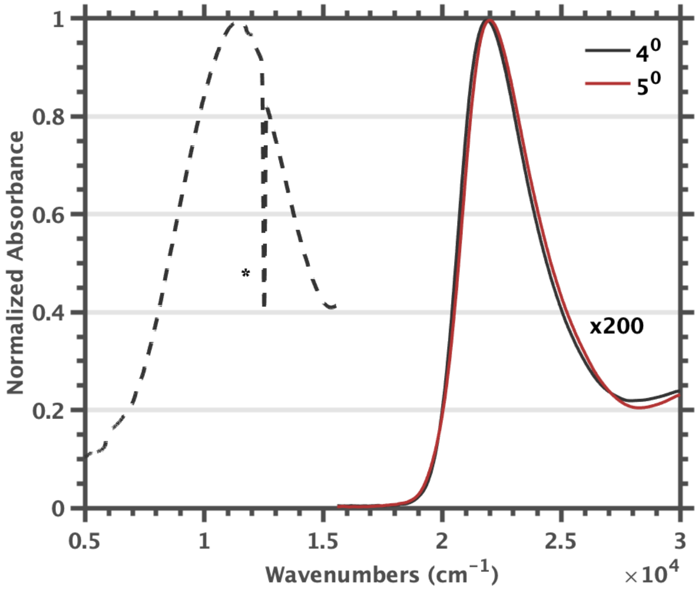

Figure 4.13. UV–vis–NIR spectra of **4**^{0} and **5**^{0} collected in dichloromethane-*d*$_2$. The visible band is displayed at approximately 1/100 of its actual intensity. Extinction coefficients are comparable to **1**^{0}-**2**^{0}.

ES3 is largely independent of R-group, we believe this transition must occur between cluster core-based orbitals. Most likely, the donor orbital stems from the five-fold degenerate I_h HOMO-1(h_g), which splits into one a_{1g} symmetry and two sets of e_g symmetry orbitals upon distortion to D_{3d}. The ground state of the closed-shell *hypercloso*-$B_{12}(OR)_{12}$ species is ${}^1A_{1g}$. Transitions from orbitals of a_{1g} or e_g symmetry would yield ${}^1A_{1u}$ or ${}^1E_u$ excited states. Orbital selection rules state that electronic transitions are allowed if and only if equation 4.1 contains the fully symmetric representation (a_{1g}).

$$\Gamma(\psi_e^*) \times \Gamma(\hat{\mu}_e) \times \Gamma(\psi_e) \tag{4.1}$$

where ψ_e^* is the excited-state wavefunction, ψ_e is the ground state wave function and $\hat{\mu}_e$ is the dipole moment operator ($\begin{pmatrix} a_{2u} \\ e_u \end{pmatrix}$ in D_{3d}).[19] Examining the excited states above, we get the expressions show in equations 4.2 and 4.3.

$$A_{1u} \leftarrow A_{1g}: A_{1u} \begin{pmatrix} a_{2u} \\ e_u \end{pmatrix} A_{1g} = \begin{pmatrix} a_{2g} \\ e_g \end{pmatrix} \tag{4.2}$$

$$E_u \leftarrow A_{1g}: E_u \begin{pmatrix} a_{2u} \\ e_u \end{pmatrix} A_{1g} = \begin{pmatrix} e_g \\ \boldsymbol{a_{1g}} + a_{2g} + e_g \end{pmatrix} \tag{4.3}$$

From these considerations, it becomes clear that only the ${}^1E_u \leftarrow {}^1A_{1g}$ transition is allowed. The high extinction coefficient of ES3 strongly suggests that it corresponds to this transition. Analogous considerations can be used to show that the ~525 nm ES3 in open-shell *hypocloso*-$[B_{12}(OR)_{12}]^{1-}$ clusters correspond to an ${}^2E_g \leftarrow {}^2A_{1u}$ transition.

Both neutral *hypercloso*-$B_{12}(OR)_{12}$ and anionic *hypocloso*-$[B_{12}(OR)_{12}]^{1-}$ clusters display weak NIR bands with extinction coefficients around 150 $M^{-1}cm^{-1}$ (ES1). These bands are shown along with the visible spectra in Figures 4.11–4.13. We suggest ES1 correspond to symmetry forbidden transitions between orbitals of g_u parentage, e.g. $^1A_{2g}\leftarrow{}^1A_{1g}$ or $^1E_g\leftarrow{}^1A_{1g}$ for *hypercloso*-$B_{12}(OR)_{12}$ and $^2A_{2u}\leftarrow{}^2A_{1u}$ or $^2E_u\leftarrow{}^2A_{2u}$ for *hypocloso*-$[B_{12}(OR)_{12}]$. Although we feel confident in our assignments, we cannot definitively say that ES1 does not involve orbitals with more ligand character, for example lone pairs on the oxygens.

Oxidation of $\mathbf{4}^0$ to the super-oxidized $[\mathbf{4}]^{1+}$ species slightly blue-shifts ES3 and gives rise to a new absorption band centered at 706 nm (ES2). In $[\mathbf{4}]^{1+}$ both the LUMO(a_{1u}) and SOMO(a_{2u}) can act as acceptor orbitals, which likely explain the appearance of the new absorption band. Similar to ES3, we suggest the donor orbital(s) in ES2 are of I_h HOMO-1(h_g) parentage. Forbidden lower-energy transitions analogous to ES1 are likely also accessible in $[B_{12}(OR)_{12}]^{1+}$ clusters, however, we have so far been unable to collect NIR spectra of $[\mathbf{4}]^{1+}$ and $[\mathbf{5}]^{1+}$ due to in-solution stability issues. Following the selection rule arguments discussed above, ES3 in $[B_{12}(OR)_{12}]^{1+}$ is likely an $^2E_g\leftarrow{}^2A_{2u}$ transition involving the same e_g symmetry donor orbitals as ES3 in *hypercloso*-$B_{12}(OR)_{12}$ and *hypocloso*-$[B_{12}(OR)_{12}]^{1-}$. The energy difference between ES2 and ES3 is Δ(ES3-ES2) $\approx$ 8000 cm^{-1}. It is interesting to compare this value to the ES1 energy, as both provide indications of the energy splitting between the LUMO(a_{1u}), SOMO(a_{2u}) and HOMO-1(e_u) orbitals. Given that the ES1 energy appears to increase as the clusters become more oxidized, we presume that the ES1 energy of $[\mathbf{4}]^{1+}$ is similar or larger than the ES1 energy of $\mathbf{4}^0$ (11500 cm^{-1}). This means that ES1 is at least 2500 cm^{-1} higher than Δ(ES3-ES2), which could indicate that the ES1 donor orbital is the HOMO-1(e_g) set, rather than the SOMO-1(a_{2u}). For ES2 eq. 4.4 and 4.5 show that transitions from orbitals of both a_{1g} and e_g symmetry could be allowed, assuming the SOMO(a_{2u}) is the acceptor orbital, which further complicates the analysis.

$$A_{1g} \leftarrow A_{2u}: A_{1g}\begin{pmatrix} a_{2u} \\ e_u \end{pmatrix} A_{2u} = \begin{pmatrix} \boldsymbol{a_{1g}} \\ e_g \end{pmatrix} \tag{4.4}$$

$$E_g \leftarrow A_{2u}: E_g\begin{pmatrix} a_{2u} \\ e_u \end{pmatrix} A_{2u} = \begin{pmatrix} e_g \\ \boldsymbol{a_{1g}}+a_{2g}+e_g \end{pmatrix} \tag{4.5}$$

Future spectroscopic work investigating NIR transitions in $[B_{12}(OR)_{12}]^{1+}$ may shed more light on the identity of these transitions.

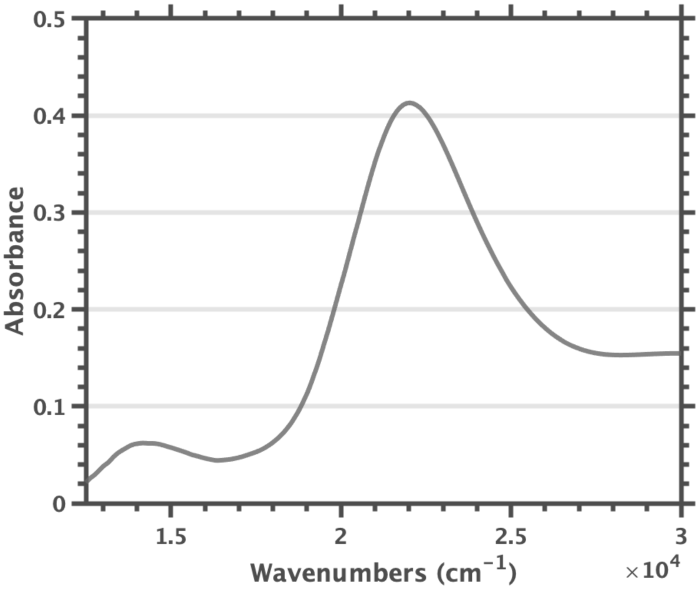

Figure 4.14. Electrochemically generated visible spectrum of [**4**]$^{1+}$ collected in 0.1 M tetrabutylammonium hexafluorophosphate dichloromethane electrolyte. Experimental details can be found in Chapter 3.

Table 4.2. Excitation energies and extinction coefficients (ε) obtained from UV–vis–NIR spectra. *k* is the excitation energy in cm-1, while λ is the excitation energy in M^{-1}cm^{-1}. ES1 is the lowest energy excited state, ES2 the second lowest energy excited state and ES3 the third lowest energy excited state (not considering triplets). ES2 is only observed in the [**4**]$^{1+}$ cation. We expect ES1 to be accessible in [**4**]$^{1+}$ but have so far not been able to experimentally observe it.

	ES1		**ES2**		**ES3**	
	***k* (cm^{-1}) [λ (nm)]**	**ε (M^{-1}cm^{-1})**	***k* (cm^{-1}) [λ (nm)]**	**ε (M^{-1}cm^{-1})**	***k* (cm^{-1}) [λ (nm)]**	**ε (M^{-1}cm^{-1})**
[**1**]$^{1-}$	9.69*10^{3} [1030]	140	-	-	2.20*10^{4} [455]	1.5*10^{4}
1^{0}	1.20*10^{4} [837]	150	-	-	2.21*10^{4} [453]	2.9*10^{4}
[**2**]$^{1-}$	9.06*10^{3} [1100]	120	-	-	1.90*10^{4} [527]	1.6*10^{4}
2^{0}	1.14*10^{4} [875]	170	-	-	2.18*10^{4} [457]	2.9*10^{4}
4^{0}	1.15*10^{4} [871]	~150	-	-	2.19*10^{4} [457]	3*10^{4}
[**4**]$^{1+}$	?	?	1.42*10^{4} [706]	~5*10^{3}	2.20*10^{4} [454]	~2.5*10^{4}
5^{0}	?	?	-	-	2.20*10^{4} [454]	3*10^{4}

4.5. Conclusions

The pulsed EPR work presented here provides strong experimental evidence supporting a cluster-confined but highly delocalized description of the $[B_{12}(OR)_{12}]$ frontier orbitals. In addition to offering an experimental description of the spin density, we suggest that the hyperfine tensors obtained from our simulations can help guide and improve the accuracy future computational studies. Furthermore, we hope other researcher will be inspired to apply similar methods to study the frontier orbitals of other hypoelectronic dodecaborates clusters such as *hypocloso*-$[B_{12}X_{12}]^{1-}$ and *hypocloso*-$[B_{12}Me_{12}]^{1-}$.

The NIR and visible absorption bands of $[B_{12}(OR)_{12}]$ clusters are best described as transitions between orbitals primarily confined to the cluster core. This is most evident for ES3, where the excitation energy is nearly independent of the R substituent. Additional work is required to definitively assign the transitions. Two key areas include obtaining NIR spectra of super-oxidized $[B_{12}(OR)_{12}]^{1+}$ clusters, which would provide further evidence of transitions between orbitals of I_h symmetry g_u parentage, and calculating of $E_{0,0}$ energies from emission spectra.

4.6 Experimental Details

Compounds

1^0-**5**^{0}, [TBA][**1**] and [TBA][**2**] were kindly gifted by the Spokoyny lab. We did not attempt study [**4**-**5**]$^{1-}$ as these species appear to disproportionate in solution.

Electron Paramagnetic Resonance

Sample preparation

All samples were prepared in quartz Q-band EPR tubes (Wilmad WG-221T-RB), ID = 1.1 mm, OD = 1.6 mm, L = 10 cm. A nitrogen-filled glove box was used for generation and manipulation of [**4**-**5**]$^{1+}$. Toluene (Millipore) had been dried on a commercial solvent purification system and further degassed through at least three freeze-pump-thaw cycles before introduction to the glove box. Inside the glove box, the solvent was stored over activated 3 Å molecular sieves (Sigma-Aldrich). Perfluorotoluene (TCI) and perfluoro-methylcyclohexane (TCI) were dried over 3 Å molecular sieves for > 84 hours, followed by distillation, discarding the initial and final fractions. Anhydrous diochloromethane-d_2 (Cambridge Isotope Labs) was used as received. Before use, the solvents were degassed by at least three freeze-pump-thaw cycles. Tris(2,4-dibromophenyl)ammoniumyl hexachloroantimonate was obtained from the Spokoyny lab.

[**1**]$^{1-}$: Sample prepared using standard air-free techniques. 8 mg of [TBA][**1**] was dissolved in 0.2 ml toluene. The solution was then diluted to 2 ml and transferred to a Q-band EPR tube. The sample was immediately frozen in liquid nitrogen.

[**2**]$^{1-}$: Sample prepared using standard air-free techniques. [TBA][**2**] was dissolved in 5:1 perfluorotoluene/perfluoro-methylcyclohexane and transferred to a Q-band EPR tube. The sample was immediately frozen in liquid nitrogen.

[**3**]$^{1-}$: Sample prepared open-air. 3 mg of **3**^{0} was added to 2 ml 1 mM triethylamine toluene solution. The sample was transferred to a Q-band EPR tube and immediately frozen in liquid nitrogen.

[**4**]$^{1+}$: Sample prepared inside a nitrogen-filled glove box. 4.5 mg tris(2,4-dibromophenyl)ammoniumyl hexachloroantimonate and 3.4 mg **4**^{0} was dissolved in a toluene/dichloromethane-d_2 mixture (1 ml toluene, 1 g dichloromethane-d_2). The solution was mixed until all of the oxidant had been consumed (determined visually). The sample was immediately transferred to a Q-band EPR tube and frozen in liquid nitrogen. The frozen sample was handled under ambient conditions, taking care not to thaw the solution.

[**5**]$^{1+}$: Sample prepared inside a nitrogen-filled glove box. 1.7 mg tris(2,4-dibromophenyl)ammoniumyl hexachloroantimonate and 3 mg **5**^{0} was dissolved in 1 ml toluene. The solution was mixed until all of the oxidant had been consumed (determined visually). The sample was immediately transferred to a Q-band EPR tube and frozen in liquid nitrogen. The frozen sample was handled under ambient conditions, taking care not to thaw the solution.

Pulsed EPR experiments

All pulsed EPR spectra were obtained on a Bruker (Billerica, MA) ELEXSYS E580 pulse EPR spectrometer equipped with a Bruker D2 ENDOR resonator and an ER 4118HV-CF5-L Flexline Cryogen-Free VT cryostat (ColdEdge, Allentown, PA) combined with an Oxford Instruments Mercury ITC. Descriptions of the ESE-EPR, Davies ENDOR, Mims ENDOR and HYSCORE experiments can be found in the literature.[20–27]

Simulation

MATLAB R2019a (MathWorks) was used along with the EasySpin[25] software package to simulate pulsed EPR data. ESE-EPR spectra were fitted using the Pepper function. ENDOR spectra were simulated using the Salt function and g-values from the ESE-EPR fitting. HYSCORE data was used to refine hyperfine tensors by simulation using the Saffron function.

Spin density calculations

The observed hyperfine tensors (**A**), contains both isotropic and anisotropic contributions. The mean of the hyperfine tensor corresponds to the isotropic contributions (a_{iso}). Subtracting a_{iso} from **A** yields the anisotropic contributions ($\boldsymbol{A}_{aniso}$). Considering the ^{11}B hyperfine tensor of [**1**]$^{1-}$ as an example:

$$\mathbf{A}\left({}^{11}B\right) = [0.1\ 8.8\ 12.9]\ \mathrm{MHz} = a_{iso} + \boldsymbol{A}_{aniso} = 7.3 + [-7.2\ 1.5\ 5.6]\ \mathrm{MHz} \qquad (4.6)$$

The s-orbital spin density can be readily calculated by dividing a_{iso} with the calculated isotropic hyperfine interaction for unit spin density (a_{iso}^{0}).[28] The anisotropic part of the hyperfine tensor represents contributions from non-spherical orbitals (p, d, f). To estimate spin densities from the anisotropic hyperfine, the isotropic hyperfine parameter (*P*) has to be considered along with an angular factor corresponding to the orbital in question. Such calculations are straightforward when the relative orientations of the orbitals are well defined. However, given the complexities involved in assigning p-orbital orientations in B_{12} clusters, we have opted to not attempt these calculations at this time. That said, work is underway to address these issues using both theoretical and computational approaches.

*ENDOR field dependence [**1-3**]$^{1-}$*

Spectra collected mid field and at the high and low field edges are shown in Figure 4.15-4.17.

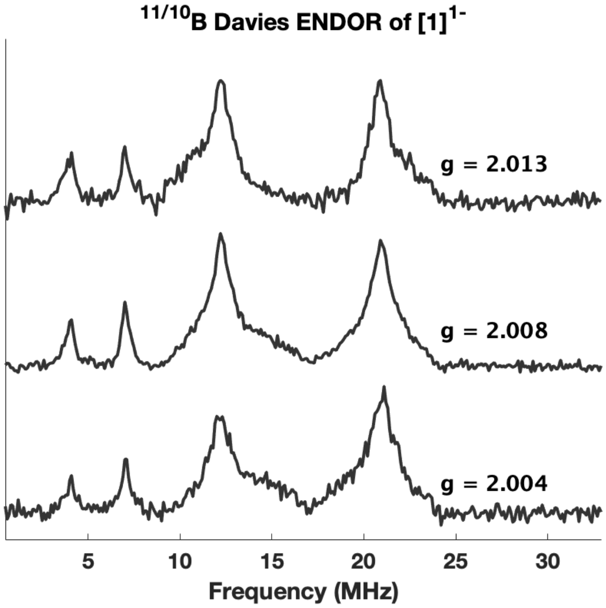

Figure 4.15. Field dependent Davies ENDOR spectra of [**1**]$^{1-}$ collected at 5 K and 34.11 GHz microwave frequency.

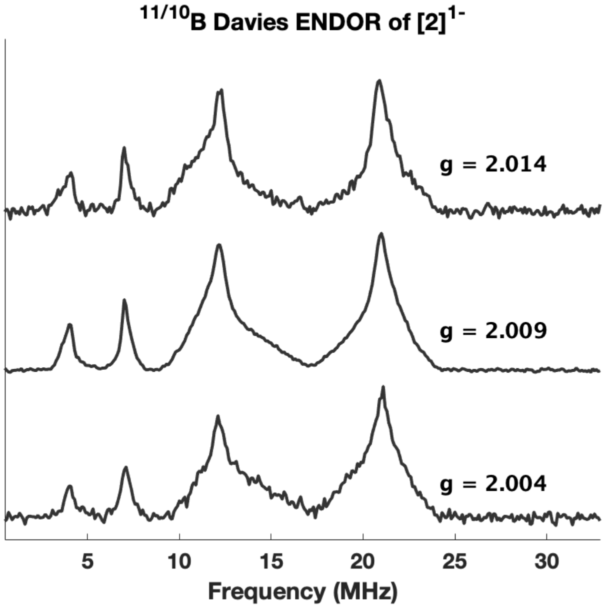

Figure 4.16. Field dependent Davies ENDOR spectra of [**2**]$^{1-}$ collected at 5 K and 34.12 GHz microwave frequency.

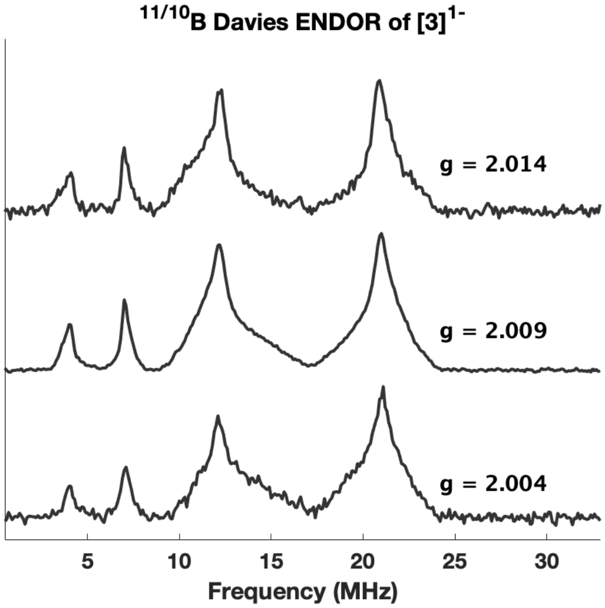

Figure 4.17. Field dependent Davies ENDOR spectra of [**3**]$^{1-}$ collected at 5 K and 34.11 GHz microwave frequency.

UV–vis–NIR Spectroscopy

All UV-vis-NIR Spectra were collected on a Varian Cary 500 UV-vis-NIR spectrometer in dual beam mode. Spectra were corrected for solvent backgrounds collected in 0% transmittance and 100% transmittance modes. Small-volume (~0.5 ml) quartz 1 cm path length cuvettes were used for high concentration NIR samples. Regular quartz 1 cm path length cuvettes were used to collect spectra in the UV-visible region. All spectra were collected in dichloromethane-d_2 (Cambridge Isotope Labs). The spectra did not change depending on if the samples were prepared air free (in a nitrogen-filled glove box) or open air.

BIBLIOGRAPHY

(1) Wixtrom, A. I.; Shao, Y.; Jung, D.; Machan, C. W.; Kevork, S. N.; Qian, E. A.; Axtell, J. C.; Khan, S. I.; Kubiak, C. P.; Spokoyny, A. M. Rapid Synthesis of Redox-Active Dodecaborane B12(OR)12 Clusters under Ambient Conditions. *Inorg. Chem. Front.* **2016**, *3* (5), 711–717. https://doi.org/10.1039/C5QI00263J.

(2) Messina, M. S.; Axtell, J. C.; Wang, Y.; Chong, P.; Wixtrom, A. I.; Kirlikovali, K. O.; Upton, B. M.; Hunter, B. M.; Shafaat, O. S.; Khan, S. I.; et al. Visible-Light-Induced Olefin Activation Using 3D Aromatic Boron-Rich Cluster Photooxidants. *J. Am. Chem. Soc.* **2016**, *138* (22), 6952–6955. https://doi.org/10.1021/jacs.6b03568.

(3) Longuet-Higgins, H. C.; Roberts, M. D. V. The Electronic Structure of an Icosahedron of Boron Atoms. *Proc R Soc Lond A* **1955**, *230* (1180), 110–119. https://doi.org/10.1098/rspa.1955.0115.

(4) Lipscomb, W. N. Recent Studies of the Boron Hydrides. In *Advances in Inorganic Chemistry and Radiochemistry*; Emeléus, H. J., Sharpe, A. G., Eds.; Academic Press, 1959; Vol. 1, pp 117–156. https://doi.org/10.1016/S0065-2792(08)60253-8.

(5) Wunderlich, J. A.; Lipscomb, W. N. STRUCTURE OF B12H12-2 ION. *J. Am. Chem. Soc.* **1960**, *82* (16), 4427–4428. https://doi.org/10.1021/ja01501a076.

(6) Lipscomb, W. N. The Boranes and Their Relatives. *Science* **1977**, *196* (4294), 1047–1055. https://doi.org/10.1126/science.196.4294.1047.

(7) Wiersema, R. J.; Middaugh, R. L. Electrochemical Preparation and Halogenation of 1,1'-.Mu.-Hydro-Bis(Undecahydro-Closo-Dodecaborate)(3-), B24H233-. *Inorg. Chem.* **1969**, *8* (10), 2074–2079. https://doi.org/10.1021/ic50080a009.

(8) Peymann, T.; Knobler, C. B.; Khan, S. I.; Hawthorne, M. F. Dodeca(Benzyloxy)Dodecaborane, B12(OCH2Ph)12: A Stable Derivative of Hypercloso-B12H12. *Angew. Chem. Int. Ed.* **2001**, *40* (9), 1664–1667. https://doi.org/10.1002/1521-3773(20010504)40:9<1664::AID-ANIE16640>3.0.CO;2-O.

(9) Axtell, J. C.; Messina, M. S.; Liu, J.-Y.; Galaktionova, D.; Schwan, J.; Porter, T. M.; Savage, M. D.; Wixtrom, A. I.; Rheingold, A. L.; Kubiak, C. P.; et al. Photooxidative Generation of Dodecaborate-Based Weakly Coordinating Anions. *Inorg. Chem.* **2019**, *58* (16), 10516–10526. https://doi.org/10.1021/acs.inorgchem.9b00935.

(10) Barton, J. L.; Wixtrom, A. I.; Kowalski, J. A.; Qian, E. A.; Jung, D.; Brushett, F. R.; Spokoyny, A. M. Perfunctionalized Dodecaborate Clusters as Stable Metal-Free Active Materials for Charge Storage. *ACS Appl. Energy Mater.* **2019**, *2* (7), 4907–4913. https://doi.org/10.1021/acsaem.9b00610.

(11) Aubry, T. J.; Axtell, J. C.; Basile, V. M.; Winchell, K. J.; Lindemuth, J. R.; Porter, T. M.; Liu, J.-Y.; Alexandrova, A. N.; Kubiak, C. P.; Tolbert, S. H.; et al. Dodecaborane-Based Dopants Designed to Shield Anion Electrostatics Lead to Increased Carrier Mobility in a Doped Conjugated Polymer. *Adv. Mater.* **2019**, *31* (11), 1805647. https://doi.org/10.1002/adma.201805647.

(12) Farha, O. K.; Julius, R. L.; Lee, M. W.; Huertas, R. E.; Knobler, C. B.; Hawthorne, M. F. Synthesis of Stable Dodecaalkoxy Derivatives of Hypercloso-B12H12. *J. Am. Chem. Soc.* **2005**, *127* (51), 18243–18251. https://doi.org/10.1021/ja0556373.

(13) Lee, M. W.; Farha, O. K.; Hawthorne, M. F.; Hansch, C. H. Alkoxy Derivatives of Dodecaborate: Discrete Nanomolecular Ions with Tunable Pseudometallic Properties. *Angew. Chem. Int. Ed.* **2007**, *46* (17), 3018–3022. https://doi.org/10.1002/anie.200605126.

(14) Peymann, T.; Knobler, C. B.; Hawthorne, M. F. An Unpaired Electron Incarcerated within an Icosahedral Borane Cage: Synthesis and Crystal Structure of the Blue, Air-Stable {[Closo-B12(CH3)12]·}− Radical. *Chem. Commun.* **1999**, *0* (20), 2039–2040. https://doi.org/10.1039/A905406E.

(15) Boeré, R. T.; Derendorf, J.; Jenne, C.; Kacprzak, S.; Keßler, M.; Riebau, R.; Riedel, S.; Roemmele, T. L.; Rühle, M.; Scherer, H.; et al. On the Oxidation of the Three-Dimensional Aromatics [B12X12]2− (X=F, Cl, Br, I). *Chem. – Eur. J.* **2014**, *20* (15), 4447–4459. https://doi.org/10.1002/chem.201304405.

(16) Boeré, R. T.; Kacprzak, S.; Keßler, M.; Knapp, C.; Riebau, R.; Riedel, S.; Roemmele, T. L.; Rühle, M.; Scherer, H.; Weber, S. Oxidation of Closo-[B12Cl12]2− to the Radical Anion [B12Cl12].− and to Neutral B12Cl12. *Angew. Chem. Int. Ed.* **2011**, *50* (2), 549–552. https://doi.org/10.1002/anie.201004755.

(17) Van, N.; Tiritiris, I.; Winter, R. F.; Sarkar, B.; Singh, P.; Duboc, C.; Muñoz-Castro, A.; Arratia-Pérez, R.; Kaim, W.; Schleid, T. Oxidative Perhydroxylation of [Closo-B12H12]2− to the Stable Inorganic Cluster Redox System [B12(OH)12]2−/.−: Experiment and Theory. *Chem. – Eur. J.* **2010**, *16* (37), 11242–11245. https://doi.org/10.1002/chem.201001374.

(18) Bambakidis, G.; Wagner, R. P. Electronic Structure and Binding Energy of the Icosahedral Boron Cluster B12†. *J. Phys. Chem. Solids* **1981**, *42* (11), 1023–1025. https://doi.org/10.1016/0022-3697(81)90068-8.

(19) Harris, D. C.; Bertolucci, M. D. *Symmetry and Spectroscopy: An Introduction to Vibrational and Electronic Spectroscopy*; New York: Oxford University Press, 1978.

(20) Mims, W. B. Pulsed Endor Experiments. *Proc. R. Soc. Lond. Ser. Math. Phys. Sci.* **1965**, *283* (1395), 452–457. https://doi.org/10.1098/rspa.1965.0034.

(21) Hyde, J. S.; Pasenkiewicz-Gierula, M.; Jesmanowicz, A.; Antholine, W. E. Pseudo Field Modulation in EPR Spectroscopy. *Appl. Magn. Reson.* **1990**, *1* (3), 483. https://doi.org/10.1007/BF03166028.

(22) Dikanov, S. A.; Tsvetkov, Y. Electron Spin Echo Envelope Modulation (ESEEM) Spectroscopy https://www.crcpress.com/Electron-Spin-Echo-Envelope-Modulation-ESEEM-Spectroscopy/Dikanov-Tsvetkov/p/book/9780849342240 (accessed Feb 27, 2020).

(23) Dikanov, S. A.; Xun, L.; Karpiel, A. B.; Tyryshkin, A. M.; Bowman, M. K. Orientationally-Selected Two-Dimensional ESEEM Spectroscopy of the Rieske-Type Iron−Sulfur Cluster in 2,4,5-Trichlorophenoxyacetate Monooxygenase from Burkholderia Cepacia AC1100. *J. Am. Chem. Soc.* **1996**, *118* (35), 8408–8416. https://doi.org/10.1021/ja960781x.

(24) Schweiger, A.; Jeschke, G. *Principles of Pulse Electron Paramagnetic Resonance*; Oxford University Press, 2001.

(25) Stoll, S.; Schweiger, A. EasySpin, a Comprehensive Software Package for Spectral Simulation and Analysis in EPR. *J. Magn. Reson.* **2006**, *178* (1), 42–55. https://doi.org/10.1016/j.jmr.2005.08.013.

(26) Tyryshkin, A. M.; Morton, J. J. L.; Ardavan, A.; Lyon, S. A. Davies Electron-Nuclear Double Resonance Revisited: Enhanced Sensitivity and Nuclear Spin Relaxation. *J. Chem. Phys.* **2006**, *124* (23), 234508. https://doi.org/10.1063/1.2204915.

(27) Buss, J. A.; Oyala, P. H.; Agapie, T. Terminal Molybdenum Phosphides with d Electrons: Radical Character Promotes Coupling Chemistry. *Angew. Chem. Int. Ed.* **2017**, *56* (46), 14502–14506. https://doi.org/10.1002/anie.201707921.

(28) Morton, J. R.; Preston, K. F. Atomic Parameters for Paramagnetic Resonance Data. *J. Magn. Reson. 1969* **1978**, *30* (3), 577–582. https://doi.org/10.1016/0022-2364(78)90284-6.

Chapter 5

FINISHING REMARKS

Chapters 2, 3 and 4 cover my exploration of hypoelectronic dodecaborate clusters. In Chapter 5, I provide a brief discussion of the results presented in this thesis along with a few words on the current state of dodecaborate research and my concluding thoughts.

Research into hypoelectronic dodecaborates have accelerated rapidly over the past decade. A range of promising applications are being explored, utilizing the strong visible absorption, noncoordinating properties and highly reversible redox behavior of these clusters. In this thesis I have presented an initial experimental foray into the electronic structure of hypoelectronic $[B_{12}(OR)_{12}]$ *clusters. Additionally, I have provided evidence indicating that a previously unknown super-oxidized* $[B_{12}(OR)_{12}]^{1+}$ *species can be isolated. My findings will be briefly discussed below, along with a quick outlook on where to go from here.*

5.1 Current State of Affairs

Over the past decade, there has been a marked increase in the interest for hypoelectronic dodecaborate clusters. Although icosahedral dodecaborate clusters were first isolated about 70 years ago, [1] no hypoelectronic analogues were reported until the late 1990s when the Hawthorne lab first isolated *hypocloso*-$[B_{12}Me_{12}]^{1-}$ (Me = CH_3),[2] *hypocloso*-$[B_{12}(OBz)_{12}]^{1-}$ and *hypercloso*-$B_{12}(OBz)_{12}$ (Bz = $CH_2C_6H_5$).[3] Developments in the years following these initial reports were limited to chemical isolation and electrochemical observation of additional hypoelectronic analogues, including a range of $[B_{12}(OR)_{12}]$ clusters[4] and the perhalogenated *hypocloso*-$[B_{12}X_{12}]^{1-}$ (X = F, Cl, Br, I) analogues.[5,6] A major breakthrough came when the Spokoyny lab published a more convenient route for microwave-assisted synthesis of *hypercloso*-$B_{12}(OR)_{12}$,[7] which was rapidly followed by publications outlining multiple interesting applications. Most notably, *hypercloso*-$B_{12}(OR)_{12}$ carrying fluoroaryl-substituents can act as powerful photoinitiators, capable of activating styrenes, as well as recalcitrant substrates like isobutylene.[8] Later work (see Appendix A) has shown that the anionic *hypocloso*-$[B_{12}(OR)_{12}]^{1-}$ species obtained after monomer photooxidation acts as weakly coordinating anions.[9] The reversible redox behavior and noncoordinating nature of $[B_{12}(OR)_{12}]$ has also led to promising application in charge-storage devices[10] and as dopants in conducting polymers.[11]

Systematic explorations of $[B_{12}(OR)_{12}]$ applications are complicated by the complex in-solution behaviors observed for the hypoelectronic clusters under many conditions. Chapter 2 gives some examples of the issues facing researchers exploring the properties and reactivity of these species. It took us about two years to get a good handle on the clusters, in the specific settings that we were interested in. Other researchers exploring the clusters under different conditions would likely have to go through similar iterative processes to find conditions that work for their needs.

5.2 Electronic Structure and Super-oxidized Clusters

In Chapters 3 and 4 we presented our work toward understanding the electronic structure of $[B_{12}(OR)_{12}]$ clusters, including the super-oxidized $[B_{12}(OR)_{12}]^{1+}$ species. Our observations lead to a few key conclusions:

1) the frontier orbitals of hypoelectronic $[B_{12}]$ clusters are confined to the cluster core and made up primarily by boron 2p orbitals, with some contributions from oxygen 2p orbitals

2) the spin density of both $[B_{12}]^{1-}$ and $[B_{12}]^{1+}$ is highly delocalized across the B_{12} pseudo-icosahedron

3) higher oxidation states lead to increased distortion, which is demonstrated by the added anisotropy and the appearance of an additional weak $^{10/11}B$ hyperfine coupling in the $[B_{12}]^{1+}$ EPR data

4) the visible and NIR electronic transitions most likely occur between orbitals largely confined to the cluster core, based on that the excitation energies are relatively independent of the R-groups.

Before moving on, I want to spend a few words explaining the EPR observations. Based on the $[B_{12}]^{1-}$ and $[B_{12}]^{1+}$ pulsed EPR data, it is clear that the HOMO(a_{1u}) and LUMO(a_{2u}) of B_{12}^0 are located on the cluster core, not stretching beyond the oxygen atoms. In particular, the very weak ^{19}F hyperfine interactions observed for the fluoroaryl derivatives show that no spin density is located on the aryl rings. That we only observe a single class of $^{10/11}B$ and ^{1}H hyperfine interactions in the $[B_{12}]^{1-}$ clusters strongly suggest that the a_{1u} symmetry orbital is evenly delocalized across the cluster core. Given that the $[B_{12}]^{1+}$ ENDOR spectra and the magnitude of the strong $^{10/11}B$ hyperfine tensor is highly reminiscent of $[B_{12}]^{1-}$, we feel confident also viewing the a_{2u} symmetry orbital as highly delocalized. However, we suggest that oxidation to $[B_{12}]^{1+}$ leads to significant distortion along the z-axis, which results in a SOMO(a_{2u}) where the spin density is concentrated in 2p orbitals from the equatorial boron atoms. The strong $^{10/11}B$ hyperfine interaction would then correspond to spin density evenly distributed across the equatorial boron atoms, while the weak coupling would stem from the boron atoms at the far edges in the z-direction.

It is interesting to think about why hypoelectronic $[B_{12}(OR)_{12}]$ clusters are stable, given that $[B_{12}H_{12}]^{2-}$ immediately decomposes upon oxidation. Symmetry lowering has been invoked by many authors, as raising the depopulated orbital and lowering the fully populated orbitals should lead to lowering of the overall cluster energy. The EPR results for $[B_{12}]^{1+}$, discussed above, substantiate this. Electron donation from the OR substituent has also been suggested as a key contributor to the stability. [3,12,13] Given that the redox potential of the clusters is highly dependent on the R-group identity, this seems reasonable.[4,7] It is interesting, however, that the B-B bonding frontier orbitals appear to have very little density on the R-groups. Our interpretation is that the electron donation into the B_{12} core primarily involves oxygen lone pairs, and that the role of the R-groups is primarily to modulate how tightly the oxygen holds on to its electrons.

5.3 Future Directions

Hypoelectronic dodecaborate clusters are interesting for a range of applications, as demonstrated in recent publications.[8–11] However, many question marks still remain. Following work will need to establish how the clusters act under various conditions, and develop systematic understand of their reactivity, photophysics and electrochemical properties. Once the field has matured, we believe a rich array of powerful applications will emerge.

The ability of alkyloxy-perfunctionalized clusters to maintain super-oxidized $[B_{12}]^{1+}$ states opens up to questions regarding what the true oxidation limits of dodecaborate clusters are. Cyclic voltammograms in dichloromethane do suggest a 4th oxidation for $[B_{12}(OEt)_{12}]$, which may indicate that $[B_{12}]^{2+}$ could be generated in sufficiently inert solvents. Electrochemical experiments in liquid SO_2 might shed light on whether the 4th wave corresponds to formation of $[B_{12}]^{2+}$, and to what extent such species are stable. It appears unlikely that further oxidation to $[B_{12}]^{3+}$ (and beyond) could be achieved without compromising the integrity of the B_{12} pseudo-icosahedron. Depopulation of the e_g set would weaken the effects of stabilization by symmetry lowering, which ought to result in immediate cluster decomposition. That said, we have now learned that $[B_{12}]^{1+}$ cores can be stable, which many would have argued against using similar reasoning. I look forward to seeing how this line of research develops.

Although the work presented in this thesis provides important insights into the electronic structure of hypoelectronic dodecaborates, many questions remain. I will mention a few crucial areas that need further exploration. Obtaining NIR spectra of $[B_{12}]^{1+}$ could provide the final piece required to definitively assign the electronic transitions discussed in Chapter 4. Furthermore, it is possible that multiple NIR bands would be observed, which would strongly support that hypoelectronic clusters display D_{3d} symmetry in solution (at least in the $[B_{12}]^{1+}$ state). More complex interpretation of the EPR data, involving modeling of the 2p orbital orientations or computational work, will be needed to quantitatively calculate the spin densities in orbitals of 2p parentage. Additionally, data collected for alkyloxy-perfunctionalized clusters in both their

$[B_{12}]^{1+}$ and $[B_{12}]^{1-}$ states is required for proper apples-to-apples comparisons. Finally, it would be very interesting to investigate the highest energy occupied molecular orbitals in all oxidation states using photoelectron spectroscopy, which has to our knowledge only been done for *closo*-$[B_{12}X_{12}]^{2-}$ clusters.[14]

The work presented in this thesis represents early attempts at describing the electronic structure and transitions of hypoelectronic dodecaborate clusters. I hope our observations will guide coming researchers wishing to perform more in-depth studies of the areas discussed here. I will be excited to learn what they find and whether our interpretations hold up to the test of time.

I wish the best of luck to any and all who choose to pursue these topics!

BIBLIOGRAPHY

(1) Wunderlich, J. A.; Lipscomb, W. N. STRUCTURE OF B12H12-2 ION. *J. Am. Chem. Soc.* **1960**, *82* (16), 4427–4428. https://doi.org/10.1021/ja01501a076.

(2) Peymann, T.; Knobler, C. B.; Hawthorne, M. F. An Unpaired Electron Incarcerated within an Icosahedral Borane Cage: Synthesis and Crystal Structure of the Blue, Air-Stable {[Closo-B12(CH3)12]·}− Radical. *Chem. Commun.* **1999**, *0* (20), 2039–2040. https://doi.org/10.1039/A905406E.

(3) Peymann, T.; Knobler, C. B.; Khan, S. I.; Hawthorne, M. F. Dodeca(Benzyloxy)Dodecaborane, B12(OCH2Ph)12: A Stable Derivative of Hypercloso-B12H12. *Angew. Chem. Int. Ed.* **2001**, *40* (9), 1664–1667. https://doi.org/10.1002/1521-3773(20010504)40:9<1664::AID-ANIE16640>3.0.CO;2-O.

(4) Lee, M. W.; Farha, O. K.; Hawthorne, M. F.; Hansch, C. H. Alkoxy Derivatives of Dodecaborate: Discrete Nanomolecular Ions with Tunable Pseudometallic Properties. *Angew. Chem. Int. Ed.* **2007**, *46* (17), 3018–3022. https://doi.org/10.1002/anie.200605126.

(5) Boeré, R. T.; Derendorf, J.; Jenne, C.; Kacprzak, S.; Keßler, M.; Riebau, R.; Riedel, S.; Roemmele, T. L.; Rühle, M.; Scherer, H.; et al. On the Oxidation of the Three-Dimensional Aromatics [B12X12]2− (X=F, Cl, Br, I). *Chem. – Eur. J.* **2014**, *20* (15), 4447–4459. https://doi.org/10.1002/chem.201304405.

(6) Boeré, R. T.; Kacprzak, S.; Keßler, M.; Knapp, C.; Riebau, R.; Riedel, S.; Roemmele, T. L.; Rühle, M.; Scherer, H.; Weber, S. Oxidation of Closo-[B12Cl12]2− to the Radical Anion [B12Cl12].− and to Neutral B12Cl12. *Angew. Chem. Int. Ed.* **2011**, *50* (2), 549–552. https://doi.org/10.1002/anie.201004755.

(7) Wixtrom, A. I.; Shao, Y.; Jung, D.; Machan, C. W.; Kevork, S. N.; Qian, E. A.; Axtell, J. C.; Khan, S. I.; Kubiak, C. P.; Spokoyny, A. M. Rapid Synthesis of Redox-Active Dodecaborane B12(OR)12 Clusters under Ambient Conditions. *Inorg. Chem. Front.* **2016**, *3* (5), 711–717. https://doi.org/10.1039/C5QI00263J.

(8) Messina, M. S.; Axtell, J. C.; Wang, Y.; Chong, P.; Wixtrom, A. I.; Kirlikovali, K. O.; Upton, B. M.; Hunter, B. M.; Shafaat, O. S.; Khan, S. I.; et al. Visible-Light-Induced Olefin Activation Using 3D Aromatic Boron-Rich Cluster Photooxidants. *J. Am. Chem. Soc.* **2016**, *138* (22), 6952–6955. https://doi.org/10.1021/jacs.6b03568.

(9) Axtell, J. C.; Messina, M. S.; Liu, J.-Y.; Galaktionova, D.; Schwan, J.; Porter, T. M.; Savage, M. D.; Wixtrom, A. I.; Rheingold, A. L.; Kubiak, C. P.; et al. Photooxidative Generation of Dodecaborate-Based Weakly Coordinating Anions. *Inorg. Chem.* **2019**, *58* (16), 10516–10526. https://doi.org/10.1021/acs.inorgchem.9b00935.

(10) Barton, J. L.; Wixtrom, A. I.; Kowalski, J. A.; Qian, E. A.; Jung, D.; Brushett, F. R.; Spokoyny, A. M. Perfunctionalized Dodecaborate Clusters as Stable Metal-Free Active Materials for Charge Storage. *ACS Appl. Energy Mater.* **2019**, *2* (7), 4907–4913. https://doi.org/10.1021/acsaem.9b00610.

(11) Aubry, T. J.; Axtell, J. C.; Basile, V. M.; Winchell, K. J.; Lindemuth, J. R.; Porter, T. M.; Liu, J.-Y.; Alexandrova, A. N.; Kubiak, C. P.; Tolbert, S. H.; et al. Dodecaborane-Based Dopants Designed to Shield Anion Electrostatics Lead to Increased Carrier Mobility in a Doped Conjugated Polymer. *Adv. Mater.* **2019**, *31* (11), 1805647. https://doi.org/10.1002/adma.201805647.

(12) Van, N.; Tiritiris, I.; Winter, R. F.; Sarkar, B.; Singh, P.; Duboc, C.; Muñoz-Castro, A.; Arratia-Pérez, R.; Kaim, W.; Schleid, T. Oxidative Perhydroxylation of [Closo-B12H12]2− to the Stable Inorganic Cluster Redox System [B12(OH)12]2−/.−: Experiment and Theory. *Chem. – Eur. J.* **2010**, *16* (37), 11242–11245. https://doi.org/10.1002/chem.201001374.

(13) Bambakidis, G.; Wagner, R. P. Electronic Structure and Binding Energy of the Icosahedral Boron Cluster B12†. *J. Phys. Chem. Solids* **1981**, *42* (11), 1023–1025. https://doi.org/10.1016/0022-3697(81)90068-8.

(14) Warneke, J.; Hou, G.-L.; Aprà, E.; Jenne, C.; Yang, Z.; Qin, Z.; Kowalski, K.; Wang, X.-B.; Xantheas, S. S. Electronic Structure and Stability of [B12X12]2– (X = F–At): A Combined Photoelectron Spectroscopic and Theoretical Study. *J. Am. Chem. Soc.* **2017**, *139* (41), 14749–14756. https://doi.org/10.1021/jacs.7b08598.

Appendix A

PHOTOOXIDATIVE GENERATION OF DODECABORATE-BASED WEAKLY COORDINATING ANIONS

Adapted with permission from Axtell, J. C.; Messina, M. S.; Liu, J.-Y.; Galaktionova, D.; Schwan, J.; Porter, T. M.; Savage, M. D.; Wixtrom, A. I.; Rheingold, A. L.; Kubiak, C. P.; et al. Photooxidative Generation of Dodecaborate-Based Weakly Coordinating Anions. *Inorg. Chem.* **2019**, *58* (16), 10516–10526. Copyright (2019) American Chemical Society. Supplemental information (SI) can be accessed online from the American Chemical Society (https://pubs.acs.org/doi/suppl/10.1021/acs.inorgchem.9b00935/suppl_file/ic9b00935_si_001.pdf).

Redox-active proanions of the type $B_{12}(OCH_2Ar)_{12}$ *[Ar =* C_6F_5 *(1), 4-*$CF_3C_6H_4$ *(2), 3,5-*$(CF_3)_2C_6H_3$ *(3)] are introduced in the context of an experimental and computational study of the visible-light initiated polymerization of a family of styrenes. Neutral, airstable proanions 1−3 were found to initiate styrene polymerization through single-electron oxidation under blue-light irradiation, resulting in polymers with number-average molecular weights (*M_n*) ranging from ∼6 to 100 kDa. Shorter polymer products were observed in the majority of experiments, except in the case of monomers containing 4-X (X = F, Cl, Br) substituents on the styrene monomer when polymerized in the presence of 1 in* CH_2Cl_2*. Only under these specific conditions are longer polymers (>100 kDa) observed, strongly supporting the formulation that reaction conditions significantly modulate the degree of ion pairing between the dodecaborate anion and cationic chain end. This also suggests that 1−3 behave as weakly coordinating anions (WCA) upon one-electron reduction because no incorporation of the cluster-based photoinitiators is observed in the polymeric products analyzed. Overall, this work is a conceptual realization of a single reagent that can serve as a strong photooxidant, subsequently forming a WCA*

A.1 Introduction

The concept and use of weakly coordinating anions (WCAs) have been known for many years within the chemical community. The unique properties of these species in particular, their electrochemical and kinetic stability have been leveraged to isolate highly reactive intermediates and facilitate unique chemical transformations. Applications of WCAs within the polymer community began with important discoveries employing noncoordinating borane anions [e.g., $B[3,5\text{-}(CF_3)_2C_6H_3]_4^-$ (BAr^F)] or proanions [e.g., $B(C_6F_5)_3$] in cationic polymerizations;[1−3] these types of reagents have been reviewed[4] and continue to be developed and applied in different areas of chemistry.[5] More recently, this concept has been extended to using heterogeneous supports, themselves, as WCAs to activate metal hydride or metal alkyl fragments, generating chemisorbed cationic metal catalysts.[6]

State-of-the-art WCAs, however, are not without their limitations. For example, even (fluoroaryl)borate anions have been shown to react with high-valent metal centers through ring-transfer reactions.[7] Highly Lewis acidic arylboranes, which have been used to generate WCAs in situ, readily form adducts with water[8] and have also been shown to engage in ringtransfer activity.[9] Waldvogel and co-workers recently disclosed an electrochemical study of BAr_4-based anions and detailed their instability toward arene−arene coupling at strongly oxidizing potentials.[10] Furthermore, many WCAs are introduced as salts, which are often synthetically nontrivial, and the formation of the desired ion pair can be complicated by incomplete salt metathesis or the formation of associated salt adducts.[4] Conceptually, access to WCAs from neutral precursors that can be triggered by external stimuli such as light would potentially ameliorate some of these challenges, although to our knowledge, no photoredox-active weakly coordinating proanions have been reported (Figure A.1).

Perfunctionalized dodecaborane clusters of the type $B_{12}(OCH_2Ar)_{12}$ (1; Ar = Ph, C_6F_5) initiate the polymerization of a range of styrenes as well as that of isobutylene.[11] We therefore wondered whether species of this type might breach new chemical space in the context of WCA chemistry.[12] In general, the use of icosahedral boron clusters typically the monoanionic carba-*closo*-undecaborate, $[CB_{11}H_{11}]^-$, and its functionalized derivatives as WCAs is well-known,[13] and they continue to be used to great effect, as shown, for example, in recent disclosures by Nelson and co-workers.[14] While $B_{12}(OCH_2Ar)_{12}$ species can be easily isolated as charge-neutral species, upon photoexcitation of certain derivatives with visible light, their extreme photooxidizing behavior [e.g., 2.98 V vs saturated calomel electrode (SCE) for 1] can activate substrates toward single electron transfer (ET), forming a substrate-based radical cation and a stable, cluster-based radical anion. Here we provide evidence for the WCA behavior of $[B_{12}(OCH_2Ar)_{12}]^-$, photooxidatively generated by the reaction of 1−3 with a variety of styrenes under blue-light-

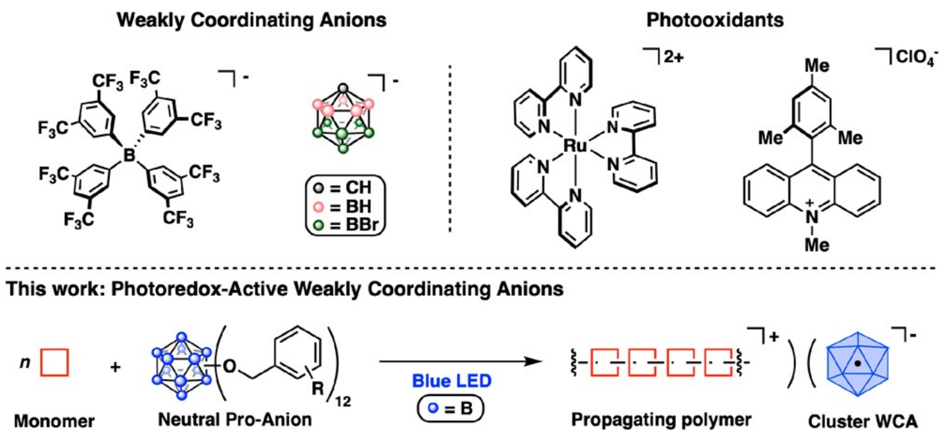

Figure A.1. Properties of WCAs and photooxidants harnessed simultaneously through the use of perfunctionalized photoredoxactive boron cluster proanions.

emitting diode (LED) irradiation. This study opens the door to previously unexplored photoredox-active WCAs.

A.2 Synthesis and Self-exchange Studies

A hallmark of 1 is the high photooxidizing potential displayed under blue-light irradiation, enabling reactivity toward species of otherwise appreciable oxidative stability. We wondered whether such behavior was general across other $B_{12}(OCH_2Ar)_{12}$ analogues bearing electron-withdrawing benzyl substituents: we suspected that similarly electron-deficient $B_{12}(OCH_2Ar)_{12}$ species $B_{12}(OCH_2\text{-}4\text{-}CF_3C_6H_4)_{12}$ (2)[15] and recently reported $B_{12}(OCH_2\text{-}3,5\text{-}(CF_3)_2C_6H_3)_{12}$ (3)[16] would be capable of initiating styrene polymerization. Indeed, 2 and 3 also initiate the polymerization of a number of styrene derivatives (*vide infra*). Although the syntheses of 1 and 2 are known, we have developed a more general and operationally straightforward protocol for neutral $B_{12}(OCH_2Ar)_{12}$ species containing electron-withdrawing Ar substituents: while $FeCl_3$ is a sufficiently strong oxidant to generate 1 and 2, it is not a strong enough oxidant under identical conditions to generate 3 from $[B_{12}(OCH_2\text{-}3,5\text{-}(CF_3)_2C_6H_3)_{12}]^{2-/-}$ ($[3]^{2-/-}$; note that, for $[\#]^{2-/-}$ (# = 1−3), the NBu_4^+ counterion is implied unless otherwise noted); in fact, $[3]^-$ is generated selectively by the treatment of $[3]^{2-/-}$ with $FeCl_3$.[15] We find that treating $[B_{12}(OCH_2Ar)_{12}]^{2-/-}$ mixtures of 1−3 with $NOBF_4$ in CH_3CN rapidly and cleanly generates the respective oxidized, charge-neutral species (Figure A.2 A).

Compound 3 crystallizes from hot toluene (see Figure A.2 B,C for a single-crystal X-ray structure and a space-filling diagram) and exhibits the most anodically shifted 0/1− redox couple (0.68 V vs Fc/Fc^+)[15] of any $B_{12}(OR)_{12}$ species reported to date (Figure A.2 D); as with other characterized

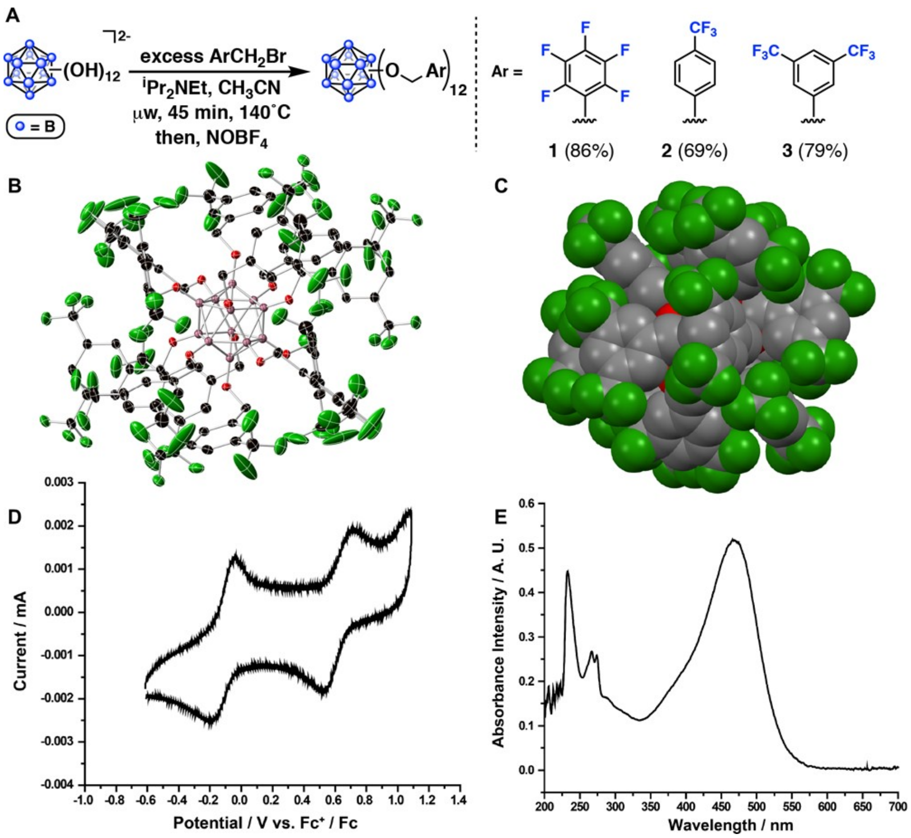

Figure A.2. (A) Synthetic protocol to generate neutral $B_{12}(OCH_2Ar)_{12}$ species from $[B_{12}(OH)_{12}]^{2-}$. Single-crystal X-ray structure (B; thermal ellipsoids at 50% probability) and space-filling model (C) of dodecaborane 3. (D and E) Cyclic voltammogram (CH_3CN) and UV−visible absorption spectrum (CH_2Cl_2) of 3.

$B_{12}(OCH_2Ar)_{12}$ species, 3 exhibits a strong absorption in the blue (~450 nm) region (Figure A.2 E). Bond angles and distances measured for 3 are consistent with structurally characterized *hypercloso*-$B_{12}(OR)_{12}$ species. Importantly, the oxidation reactions generating 1−3 using $NOBF_4$ can be carried out on gram scales to afford air-stable, neutral dodecaboranes in high yields. Our ability to cleanly isolate $[3]^-$ and 3 through the treatment of $[3]^{2-/-}$ with $FeCl_3$ and $NOBF_4$, respectively, prompted a solution-phase electron-self-exchange study using ^{19}F NMR spectroscopy in order to probe ET kinetics. We anticipated that such a study would shed light on ET between the cluster and substrate during styrene polymerization initiated by photoexcited $B_{12}(OCH_2Ar)_{12}$. At temperatures varying from 20 to 60 °C in 1,2-dichloroethane, we recently showed that electron self-exchange between [NBu_4][3] and 3 is slow on the NMR time scale, with $k_{ex} < 1.2 \times 10^3\ M^{-1}\ s^{-1}$.[16] It is known that electron self-exchange between the 0/1− redox pair in $Ru_3O(OAc)_6(CO)(L)_2$ clusters [where L = 4-cyanopyridine, pyridine, or 4-(dimethylamino)pyridine] is highly dependent on the degree of charge density residing on the ancillary pyridyl ligands.[17] Given the encumbering steric profile of pseudospherical 1−3 and considering that the highest occupied molecular orbital (HOMO) of $[3]^-$ and the lowest unoccupied molecular orbital (LUMO) of ground-state 3 are exclusively boron-cage-based,[16] we attribute this low rate of ET to poor electronic coupling between 3 and $[3]^-$ in the ground state. However, upon photoexcitation, these species possess oxidizing potentials exceeding 3 V versus SCE (*vide infra*), resulting in rapid hole transfer to the substrate. Ultimately, these qualities lay the groundwork for the development of sterically and electrochemically tunable neutral reagents that result in the generation of WCAs in situ through visible-light irradiation.

A.3 Styrene Polymerization

Our initial polymerization studies[11] with 1 in CH_2Cl_2 under blue-LED irradiation revealed good yields for moderate-toelectron-rich styrenes and dispersity values of ∼2, which might be expected for uncontrolled carbocationic polymerizations;[18] control experiments showed that these polymerizations do not proceed in the absence of 1 and that radical-based propagation modes are not likely. Interestingly, monomers with p-halide substituents displayed very high M_n and excellent yields, despite the inductively electron-withdrawing nature of the p-F and p-Cl substituents ($\sigma_p = 0.06$ and 0.23, respectively[19]), and were unexpected in comparison to other monomers: electronically similar monomers such as styrene [σ_p(H) = 0.00] and 3Cl-styrene [σ_m(Cl) = 0.37] gave significantly smaller M_n values.

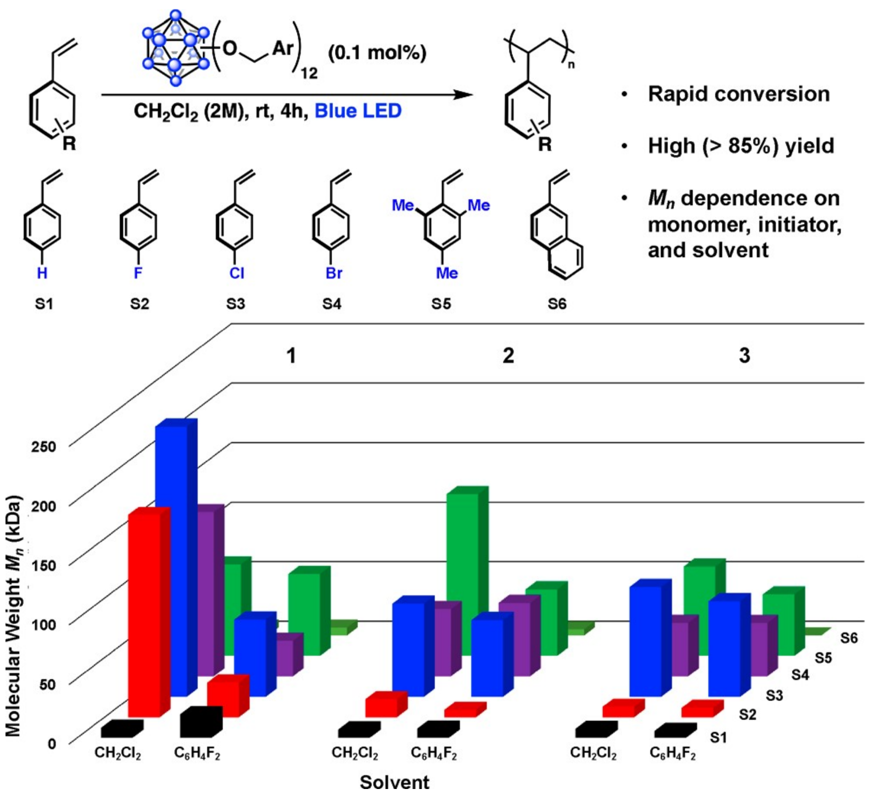

Figure A.3. Reaction conditions and monomer sets for photoinitiated polymerizations by 1−3. The bar chart depicts M_n values obtained for all polymerizations and reveals the unusually high M_n values obtained for S2−S4 in CH_2Cl_2 with 1. A numerical summary of these values with corresponding polymer yields can be found in the SI.

In order to better understand these results, we screened a family of vinylarenes with initiators 1−3 in CH_2Cl_2 and 1,2-difluorobenzene (Figure A.3) to probe generality, i.e., whether other perfunctionalized dodecaborates were also capable of initiating styrene polymerization via visible-light irradiation. Overall, we find that moderate M_n values are obtained in nearly all cases, consistent with an uncontrolled cationic polymerization involving a counteranion that does not effectively stabilize the cationic chain end:[18a] moderate M_n values were obtained for S1−S6 in 1,2-difluorobenzene for 1−3 under standard conditions; M_n values for a given monomer were also consistent for S1−S6 using 2 and 3 in CH_2Cl_2. For 1, while S1, S5, and S6 again displayed comparable M_n values when initiated in CH_2Cl_2, S2−S4, which contain 4-X (X = F, Cl, Br) substituents, displayed M_n values over 1 order of magnitude larger than that of in 1,2-difluorobenzene. In most cases, polydispersities range from ∼1.8 to 2.3 and appear to be independent of the trend observed for polymers generated using 1 and S2−S4 in CH_2Cl_2. Polymer analysis by matrix assisted laser desorption ionization mass spectrometry did not show incorporation of the initiator in any cases tested (see the Supporting Information (SI) for representative examples); this is consistent with previously obtained inductively coupled plasma mass spectrometry data[11] as well as the general inertness of the dodecaborate counterion in the presence of a reactive cationic chain end. We suggest that the unique distribution of polymer molecular weights based on the solvent, initiator, and monomer indicates both the weakly interacting behavior of the dodecaborate anions with the cationic chain end as well as an easily influenced equilibrium (*vide infra*) of these interactions from contact ion pairs to more efficiently solvated ion pairs; the location of this equilibrium ultimately determines the resulting M_n values.

A.4 Computational Analysis of Photoexcitation

Attempts to probe the proposed intermolecular interactions of the perfunctionalized dodecaboranes and a donor molecule (e.g., styrene) spectroscopically prior to ET so far have been unsuccessful, consistent with the short excited-state lifetime (τ = ∼360 ps for 1),[11] high excited-state reduction potential, and cluster-based HOMO and LUMO levels of 1−3 in the ground state (*vide infra*). Therefore, a computational evaluation of both isolated dodecaboranes as well as cluster−monomer interactions was undertaken.

We first initiated a computational study to evaluate the electronic properties of 1−3 as well as select monomers in order to identify qualities that might give rise to the unique performance of 1. First, we investigated whether the generation of high M_n polymers by 1 resulted simply from the difference in energy between the HOMO of the monomer and the lower energy, cluster-based donor orbital(s) responsible for blue-light absorption. As shown in Figure A.4, no clear correlation is observed between the monomer HOMO energy and polymer length for 1 in CH_2Cl_2. We calculated the ionization potentials of three representative monomers (S1, S3, and S5) and found that both in the gas phase and with a CH_2Cl_2 solvent model the energies for all three monomers are comparable and scale in the order of S1 > S3 > S5 (see the SI). In addition, the occupied orbitals involved in the visible-light (∼450 nm) absorption in all three initiators have similar parentages (Figure A.4 B) and oscillator strengths, with absorption maxima that closely reflect measured values (see the SI). This suggests that the donor and acceptor orbitals involved in visible-light absorption are not unique for 1 and therefore cannot, by themselves, explain the inconsistent behavior of 1 in producing polymers of only moderate M_n compared with 2 or 3 under otherwise identical conditions. Excited-state reduction potentials were estimated for 2 and 3 through fluorescence measurements in perfluorotoluene at 77 K and, in combination with ground-state potentials (which are, in fact, more anodic than 1 for the analogous 0/1− redox couples[15]), are higher than that of 1 (∼2.98 V vs SCE[11]), reaching values of ∼3.21 and ∼3.33 V versus SCE for 2 and 3, respectively (see the SI). In addition, electron affinity values for the arene fragments that correspond to 1−3 [C_6F_5H, $C_6H_5CF_3$, and m-$(CF_3)_2C_6H_4$, respectively] have comparable energies (Figure A.4 C and the SI); C_6F_5H has the highest value. Finally, extinction coefficients were measured at 450 nm for 1−3 in CH_2Cl_2, revealing that all three complexes absorb blue light with comparable efficiencies (∼20000−

25000 M^{-1} cm^{-1}); given the high concentration of monomer in these reactions (2 M), we assume that the efficiency of monomer oxidation by 1−3 is comparable across S1−S6. The structural-, photophysical-, and reactivity-based similarities of 1−3 imply that only a very specific set of conditions is required for a deviation in the observed polymerization trends, which is, in turn, strongly suggestive of the WCA behavior of the monoanionic dodecaborate species following hole transfer to monomer.

1 was also studied *in silico* in the presence of styrene substrate and explicit CH_2Cl_2 solvent (see the SI for details). Several positions of styrene in close proximity to the $-C_6F_5$ rings of 1 were identified, and time-dependent density functional theory (TD-DFT) calculations were then performed on the system at the B3LYP/6-31GS level of theory (Figure A.5); the results are consistent with DFT calculations shown in Figure A.4. Importantly, the donor molecular orbitals found in this simulation are positioned appropriately with respect to styrene to accept electron density following initiator photoexcitation, with some perturbation of the electronic structure observed at the $-C_6F_5$ rings (given the presence of the styrene molecule) with respect to calculations shown in Figure A.4.

Furthermore, the HOMO of the system is localized on styrene, again suggesting that ET from styrene upon cluster photoexcitation is mechanistically reasonable. Interestingly, when modeled in CH_3CN, both the HOMO and LUMO of the system are mostly located on the cluster core. This is consistent with our observation that <5% polystyrene is generated under typical reaction conditions with 1 when CH_3CN is employed as the solvent.

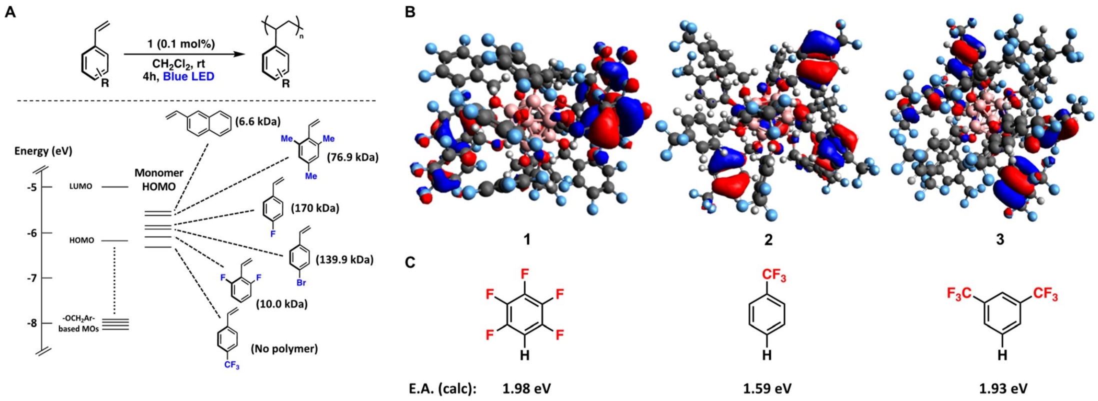

Figure A.4. (A) Relative energies of vinylarene HOMOs and corresponding M_n obtained with 1. (B) Representative donor molecular orbitals of 1−3 that are primarily oxygen-based with some contribution from the benzyl units. (C) Calculated electron affinity values for aryl substituents corresponding to 1-3.

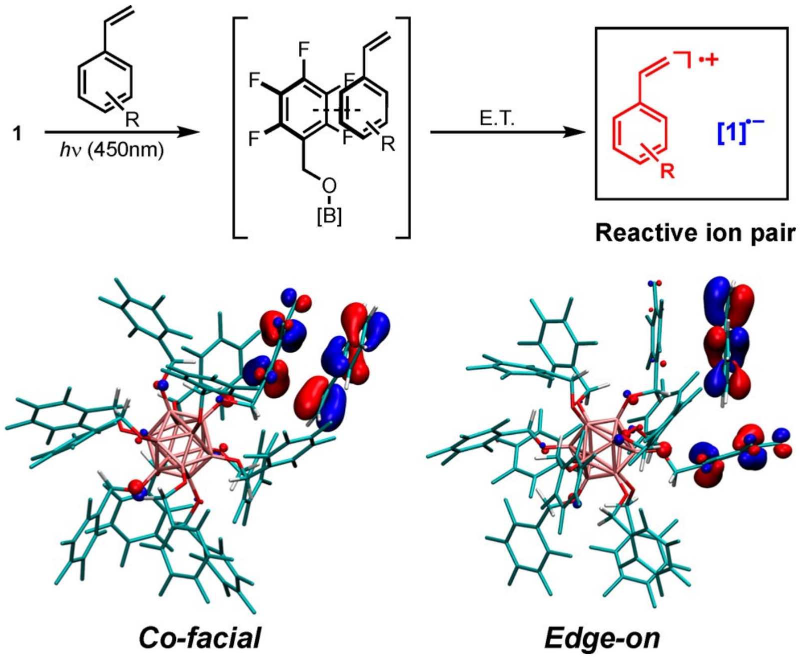

Figure A.5. TD-DFT calculation of 1 in the presence of styrene (B3LYP/6-31GS). In-phase cofacial and edge-on dispositions of the styrene-based HOMO relative to a 1-based molecular orbital suggest a possible pathway hole transfer to the substrate. Explicit CH_2Cl_2 has been removed for clarity (see the SI for details).

While we have not been able to experimentally identify either substrate preorganization or the relative orientations of the styrene and initiator, as shown in Figure A.5, they represent plausible modes of interaction by which ET may occur. However, it must also be noted that specific orientations are not required when invoking a tunneling mechanism for ET, which we suggest to be operative. It has been shown that electron tunneling can occur beyond 15 Å between the donor and acceptor even in the absence of covalent interactions;[20] while we have been unable to crystallographically characterize a donor−acceptor complex, the electron-self-exchange studies of 3 and $[3]^{-}$ (*vide supra*) confirm that ET can occur even between dodecaborates, likely through tunneling. On the basis of the solid state crystal structure of 3, the closest intermolecular B−C or O−C distances (analogous to initiator−substrate distances) are well within 15 Å. Ultimately, these data indicate that the dodecaborane excited state[21] is quenched by very rapid hole transfer to the substrate.

A.5 Discussion of Photoinitiated Polymerization Studies

The above analyses suggest that the physical properties of the initiators, monomers, and media, by themselves, are likely not responsible for the anomalous M_n results but rather that a combination of properties, either prior to or during polymerization, accounts for the observed molecular weight differences. Nevertheless, this implies that 1 possesses a structural or electronic feature that is less prominent or absent in 2 and 3 or is potentially magnified to a greater degree than 2 or 3 in CH_2Cl_2 in the presence of S2−S4. We turned to a time-point analysis of polymerizations conducted in the presence of 1 with various styrenes to further interrogate this system. The results are shown in Figure A.6. The polymerizations of S1, S4, and S5 (1 M in CH_2Cl_2) were initiated by 1 under blue-LED irradiation at room temperature. As expected, the rapidity of conversion scaled with the relative electron-richness of the monomer (S5 > S1 > S4).

Interestingly, gel permeation chromatography analysis of the same time points revealed that while the M_n values for poly-S1 and poly-S5 remained fairly consistent and low (~ 20 and ~50 kDa, respectively) during the course of polymerization, M_n for poly-S4 began at ~190 kDa and gradually decreased during the time frame in which aliquots were taken. This suggests that the ratio of the propagation rate to chain-transfer rate for S4 is fundamentally different from that for S1 and S5 and that this ratio reaches a steady state much later in the polymerization. This is potentially indicative of some additional factor (e.g., intermolecular interactions) that affects one or both terms of this ratio that is less prominent or absent with S1 and S5 under identical conditions. While we note that adventitious water can act as a powerful chain-transfer agent in carbocationic polymerizations, the clear dependence of M_n on the solvent and initiator suggests that the components of the reaction are more relevant to the observed polymer metrics.

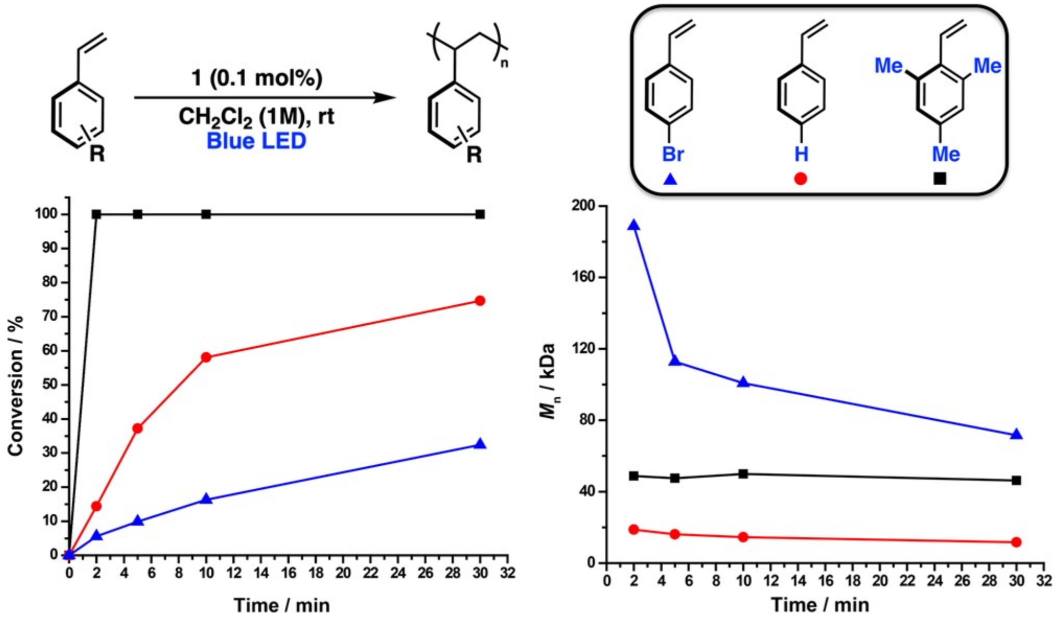

Figure A.6. Polymerization of electronically diverse styrenes showing more rapid conversion for more electron-rich substrates but a higher initial M_n followed by a gradual decrease for S4 as opposed to those of S1 and S5, which remain constant during the reaction.

The decay of M_n over time would be consistent with an increasing number of termination events relative to insertion events per time as the monomer depletes, particularly for an uncontrolled carbocationic polymerization of styrenes. While in photochemically initiated reactions, in particular, the initiator concentration is critical, we suggest that potential fluctuation in these values is not a dominant factor because only select polymers generated in the presence of 1 in CH_2Cl_2 show high M_n values. Electron-withdrawing functional groups should render the β-proton of the propagating cationic chain more acidic than those in $[\text{poly-S1}]^+$ or $[\text{poly-S5}]^+$, making it increasingly susceptible to loss of H^+. However, it is unclear why the M_n values for poly-S1 and poly-S5 do not also gradually decrease over time but instead remain constant during the course of the polymerization. The presence of poorly stabilized, free ion chain ends, which rapidly terminate, is consistent with this latter observation;[22] this scenario is analogous to decreased chain-end stabilization with decreasing solvent polarity, which also results in a larger number of chaintransfer events and lower-molecular-weight polymers in cationic polymerizations, as noted by Nuyken and co-workers.[23] Conversely, this also suggests that some degree of control, likely through more effective ion pairing, is imparted under the polymerization conditions of 1 and S4 in CH_2Cl_2, ultimately reducing chain transfer at early time points and giving rise to higher M_w values.

We find that the conversion of S1 in the presence of 1 in CH_2Cl_2 is slower than that of 1,2-difluorobenzene. While according to Reichardt's $E_T(30)$ scale, CH_2Cl_2 and 1,2-difluorobenzene have comparable polarities,[24] this difference in the propagation rate has been observed in photoinitiated polymerizations of styrenes and isobutylene and has been attributed to differences in ion pairing as a result of varying medium polarity.[22,25] It was concluded in these cases that faster propagation resulted from free ions and slower propagation resulted from ion pairs. Furthermore, it was shown that free ions produced smaller M_n polymers than the ion pairs in these photoinitiated polymerizations. Interestingly, in the case of 1 and S4, we observe similar rates of conversion in both CH_2Cl_2 and 1,2-difluorobenzene, while M_n of CH_2Cl_2 at early time points reached up to ~190 versus ~60 kDa in 1,2-difluorobenzene under the same conditions (Figure A.7). This indicates that solvophobic effects similarly affect polymerizations of S4 by 1, likely as a result of the strength of ion pairing of oligo- or poly-S4, specifically, with 1. This result is consistent with the slightly higher dielectric constant of 1,2-difluorobenzene compared to CH_2Cl_2. To understand whether the similarity in the propagation rates was a function of the combination of S4 and 1 or dependent on S4 alone, we performed a similar set of experiments with 2 and S4. Here, we find that, in CH_2Cl_2, the initial M_n values at low conversion are high (~240 kDa) and gradually taper, whereas those in 1,2-difluorobenzene start much lower and likewise taper. Compared to 1 and S4, however, M_n drops much more rapidly as conversion increases. This suggests that S4 (and likely S2 and S3) exhibits similar behavior in the presence of 2 but that the proposed interactions are much less pronounced than those in the presence of 1. Beyond solvophobic effects, it is also possible that 1,2-difluorobenzene materially interferes with ion pairing, particularly in the case of 1 and S2−S4 (*vide infra*).

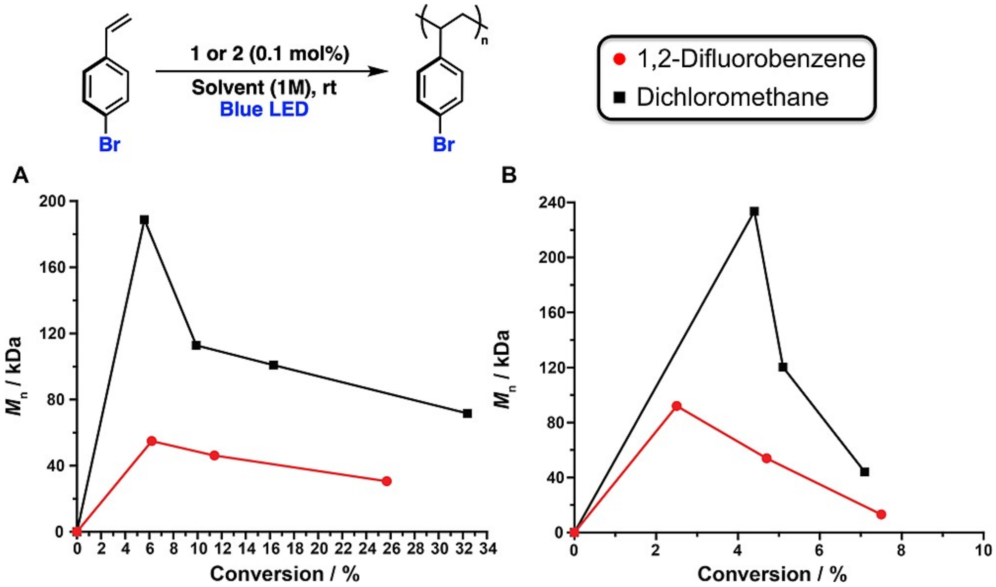

Figure A.7. M_n versus conversion plots for the polymerization of S4 initiated by 1 (A) and 2 (B). While in both cases M_n starts at ~240 kDa in CH_2Cl_2, M_n decreases much more rapidly when initiated by 2.

Halide functional groups are capable of resonance stabilization of aromatic systems such that they behave as ortho- and para-directing substituents in electrophilic aromatic substitutions despite their inductively electron-withdrawing nature. Importantly, in these cases, the position, rather than simply the π-donating ability, of a halide substituent is critical in the observed reactivity and substitution pattern based on canonical resonance forms that are available along the reaction coordinate. We considered that these substituents might be electronically stabilizing oligomeric or polymeric intermediates toward β-H^+ loss through resonance contributions, generating higher M_w fragments at early time points before chain transfer becomes more prominent as monomer depletes. Lenz and co-workers previously noted the potential importance of resonance effects of p-halide substituents in the carbocationic polymerization of p-X-α-methylstyrenes (X = F, Cl).[26] Lewis et al. have also suggested this possibility.[27] While the presence and position of the halide in S2−S4 is clearly important, the consideration of resonance stabilization imparted by these functional groups still cannot explain the observation of high M_w in CH_2Cl_2 with 1 only. Because there is a clear solvent effect on conversion (Figure A.6) in which polymerization occurs more rapidly in 1,2-difluorobenzene versus CH_2Cl_2 for S1 (see the SI), we posit that CH_2Cl_2 favors a more tightly held ion pair between 1 and oligo- or poly-S2−S4, giving rise to polymers of high M_w and M_n for S2−S4. We suggest that the nature of this ion pair, in addition to the requisite electrostatic attraction, is through aromatic donor−acceptor interactions between the arene ring(s) of oligo- or poly-S2−S4 and the pentafluorophenyl substituents of 1 that are not present in 2 or 3.

Intermolecular aromatic interactions have been widely observed[28] and used in the context of materials science,[29] molecular recognition,[30] biology,[31] and reaction chemistry.[32] Some of the most recognizable are those between electron-rich and (fluorinated) electron-poor aromatic rings (Ar^F), which are believed to result, in part, from inversion of the electronic quadrupole of Ar^F relative to that of more electron-rich arenes, leading to favorable aromatic donor−acceptor interactions;[33] electrostatic, charge-transfer, and solvophobic effects have also been implicated in the facilitation of these aromatic interactions.[34] For example, in their study of interactions between C_6F_6 and C_6H_5X arenes, Hunter and co-workers favored an electrostatic model of intermolecular arene interactions because of the linear correlation of the binding affinity with Hammett constants of substituted arene derivatives.[35] Gung and co-workers found deviations in this trend and also implicated significant charge-transfer effects in addition to electrostatic effects in order to fully explain the free energy of attraction between pentafluorobenzoate and 3,5-dinitrobenzoate groups with monofunctionalized arenes in a substituted triptycene manifold.[36] In addition, they posit that monosubstituted aryl rings as a donor−acceptor pair are not sufficiently electronically perturbed to engage in arene−arene interactions of meaningful magnitude; rather, electronic extremes such as $-C_6F_5$ or $-3,5\text{-}(NO_2)_2\text{-}C_6H_3$ moieties are necessary. Furthermore, Sherill and co-workers have shown that dispersion interactions can significantly contribute to the strength of the arene−arene interactions in face-to-face and edge-on arrangements of aryl rings.[37] The nonnegligible effect of the solvent on intermolecular interactions has been detailed,[33b,38] often in the context of effects on the electrostatic interactions or analyte desolvation. Finally, Cockroft and co-workers have also detailed the importance of substituent solvation in modulating the electrostatic potentials of aromatic systems.[39] While we cannot definitively identify the specific type of intermolecular interactions in the present case, based on our computational data of monomer interactions with 1 (see Figure A.5) and the high local density of aryl substituents in 1−3 (particularly the $-C_6F_5$ rings in 1), electrostatic, dispersion, charge-transfer, and solvophobic effects likely all contribute to the interactions of monomer with the ring periphery of the dodecaborate photoinitiators and are most prominent between S2 and S4 with 1 in CH_2Cl_2.[40]

Ion pairing under carbocationic polymerization conditions has historically been described through the Weinstein spectrum of ionicity[25b] and an associated equilibrium between dormant, contact ion pair, and fully solvated ions of a propagating cationic chain end and its corresponding anion. Biasing the equilibrium toward a contact ion pair through the addition of a "common ion"[25b,41] approximates the conditions under which controlled ("living") carbocationic polymerization might be observed. We attempted to probe this equilibrium by employing readily accessible $[3]^-$ as an additive in polymerizations initiated by 3. If ion pairing is essential, one would expect that the addition of free $[3]^-$ would drive the equilibrium toward a contact ion pair of propagating cationic polymer and counterion, giving rise to more controlled polymerizations with higher M_n.[42] The addition of S5 to a 1,2-difluorobenzene solution containing 0.1 mol % 3 and 0.1 mol % $[3]^-$, followed by blue-LED irradiation for 4 h and quenching with methanol, resulted in the expected precipitation of polymer. Upon workup, the isolated poly-S5 was found to display M_n values nearly double that obtained in the absence of $[3]^-$ (M_n = 101 vs 51.6 kDa; see the SI).

A similar experiment was conducted with S1 in 1,2difluorobenzene, again revealing poly-S1 with approximately double the M_n relative to standard conditions (see the SI). Control polymerization experiments with $[3]^-$ were performed and found not to initiate S1 polymerization under standard conditions, suggesting that 3 is completely responsible for the initial reactivity and oxidation of the styrene monomers. We also found that the addition of 0.1 mol % NBu_4BArF_4[43] to 3 and S1 under standard polymerization conditions in 1,2difluorobenzene also resulted in polymers of increased molecular weight (Figure A.8). Notably, increasing the amount of $[3]^-$ in S1 polymerization experiments beyond 0.1 mol % does not result in a further increase of M_n. These experiments highlight the importance of ion-pair equilibria (Figure A.9) in the resulting M_n and that, in comparison to 1 and S2−S4, the interactions between 2 or 3 and S2−S4 are significantly weaker in CH_2Cl_2 and result in poly-S2−S4 of much lower M_n. The requirement of biasing these equilibria to observe higher M_n is consistent with the ionicity spectrum concept and the role of monoanionic 1−3 as WCAs.

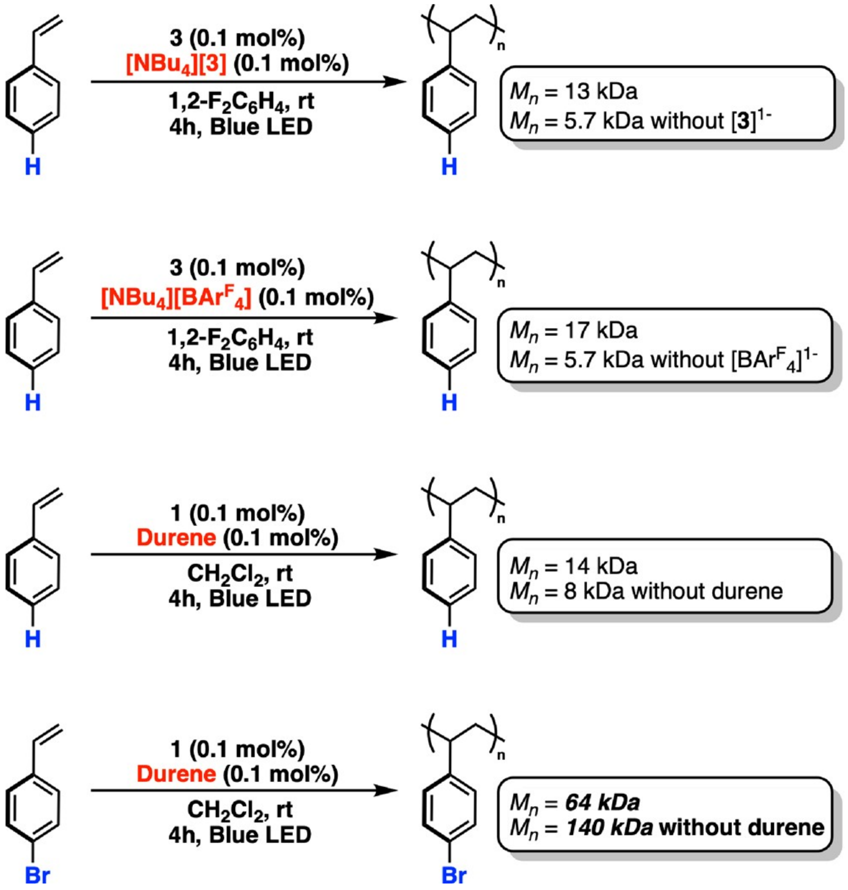

Figure A.8. Control polymerization experiments by 1 and 3, with select additives suggesting the importance of ion pairing in polymer molecular weights.

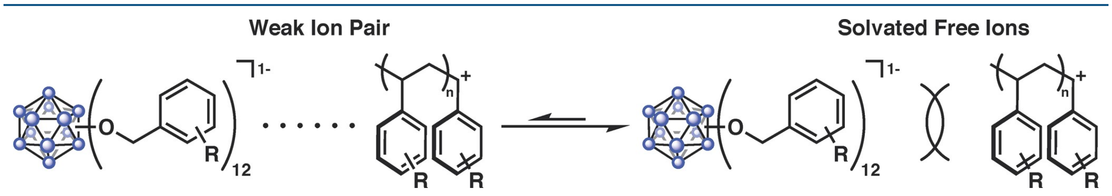

Figure A.9. Proposed equilibrium between solvated and contact ion pairs between propagating polymer and dodecaborate WCAs 1−3.

In the carbocationic polymerization of styrene by $SnCl_4$, Overman and Newton observed that the addition of either durene or hexamethylbenzene resulted in an increase in M_n of the resulting polystyrene. They note: "No explanation of the atypical behavior of these methylbenzenes is readily apparent, but it is thought that there is a possibility that catalyst or catalyst-cocatalyst complexing with the aromatic compounds might affect the reaction when the aromatic compounds are as highly basic as these methylbenzenes."[44] We wondered whether such complexation might involve interactions of durene with the propagating chain. We found that the addition of durene (1 equiv relative to 1) to the polymerization of S1 by 1 under standard conditions only slightly increased the molecular weight of the resulting polymer (average 14 vs 8 kDa) but did not significantly alter the yield of the resulting polystyrene compared to the polymerization of styrene by 1 alone. While subtle, this M_n difference could implicate aromatic donor−acceptor interactions as operative in enhancing the M_n values; importantly, both durene and styrene are devoid of any Lewis basic substituents that might also be implicated as contributors to the M_n increase (*vide supra*). In an analogous reaction, durene (1 equiv relative to 1) was used as an additive in the polymerization of S4 by 1. In this case, we found that M_n and M_w were halved compared to poly-S4 produced in the absence of durene, while the overall yield of the reaction was still comparable (Figure A.8). This suggests that durene interferes with the reaction overall, either by reducing the rate of propagation on the time scale of chain transfer or by increasing the rate of chain transfer on the time scale of propagation. Given the discussion above, we suggest that durene competitively interacts with oligo- or poly-S4 under the reaction conditions, preventing association with 1 and giving rise to lower M_w. We must also consider the possibility that similar interferences occur in the 1,2-difluorobenzene solvent, giving rise to low M_n for poly-S2−S4 initiated by 1 in this medium. Overall, the specific reaction conditions required to generate the anomalous polymerization results obtained with 1 and the generally consistent results obtained in all other cases are indicative of the WCA behavior of $[1]^{-}$−$[3]^{-}$.

A.6 Conclusion

Our work highlights the intricacies associated with the strength of ion-pairing interactions of the propagating cationic polymer chain and a dodecaborate-based WCA as a function of the initiator, monomer, and solvent. Importantly, and despite the anomalous behavior of 1, we can sterically and electronically diversify the dodecaborate proanions through the careful molecular design of the substituents appended onto the dodecaborate core to generate analogues such as 2 or 3: these proanions still display strong photooxidizing potentials with nearly identical λ_{max}, molar absorptivities, and oscillator strengths for relevant visible-light transitions compared to 1, and the monoanions generated through styrene oxidation appear devoid of significant intermolecular interactions with the cationic chain end. Charge-transfer excitation from the benzyloxy substituents to the cluster ultimately provides a driving force for ET from the olefin substrate. Furthermore, as a result of (1) the delocalization of unpaired electron density in these anions across the 12 boron atoms of the cage, (2) the cluster-based frontier molecular orbitals in both neutral and monoanionic ground states, and (3) the steric protection afforded by the organic substituents bound to each boron vertex of 1−3, these WCAs remain chemically intact during the course of the cationic polymerization that occurs as a consequence of their photooxidizing ability. Overall, this supports the ability of $[1]^{-}$−$[3]^{-}$ to behave as competent WCAs.

In our view, the photooxidative generation of $[1]^{-}$−$[3]^{-}$ akin to "redox-active $[BAr^{F}_{4}]^{-}$" analogues represents a fundamentally new approach to accessing WCAs, simply through visible-light irradiation. While there exist many visible-light photooxidants that have enjoyed steady use in the catalytic realm,[45] none possesses the extreme photooxidizing potentials displayed by 1−3. While traditional BAr_4-based WCAs would be unstable toward oxidative coupling, the species presented here are themselves responsible for the oxidative strength and are compatible with these potentials. Ultimately, we envision the application of these and similar species[46] beyond polymer synthesis[16,47] to leverage the unique combination of a strong photooxidant and a WCA embodied in a single-cluster-based reagent, potentially providing access to otherwise inaccessible properties.

BIBLIOGRAPHY

(1) Yang, X.; Stern, C. L.; Marks, T. J. Cation-like" Homogeneous Olefin Polymerization Catalysts Based upon Zirconocene Alkyls and Tris(pentafluorophenyl)borane. J. Am. Chem. Soc. 1991, 113, 3623− 3625.

(2) Pellecchia, C.; Immirzi, A.; Grassi, A.; Zambelli, A. Base-Free Cationic Mono(cyclopentadienyl)zirconium Complexes: Synthesis, Structural Characterization, and Catalytic Activity in Olefin Polymerization. Organometallics 1993, 12, 4473−4478.

(3) (a) Shaffer, T. D.; Ashbaugh, J. R. Noncoordinating Anions in Carbocationic Polymerization. J. Polym. Sci., Part A: Polym. Chem. 1997, 35, 329−344. (b) Wang, Q.; Quyoum, R.; Gillis, D. J.; Tudoret, M.-J.; Jeremic, D.; Hunter, B. K.; Baird, M. C. Ethylene, Styrene, and α - Methylstyrene Polymerization by Mono-(pentamethylcyclopentadienyl) (Cp*) Complexes of Titanium, Zirconium, and Hafnium: Roles of Cationic Complexes of the Type $[Cp^*MR_2]^+$ (R = Alkyl) as Both Coordination Polymerization Catalysts and Carbocationic Polymerization Initiators. Organometallics 1996, 15, 693−703. (c) Quyoum, R.; Wang, Q.; Tudoret, M.-J.; Baird, M. C.; Gillis, D. J. η^5-$C_5Me_5TiMe_3B(C_6F_5)_3$: A Carbocationic Olefin Polymerization Initiator Masquerading as a Ziegler-Natta Catalyst. J. Am. Chem. Soc. 1994, 116, 6435−6436. (d) Wang, Q.; Baird, M. C. Carbocationic Initiation of Polymerization of Vinyl Ethers and N-Vinylcarbazole Induced by $(\eta^5\text{-}C_5Me_5)TiMe_2(\mu\text{-}Me)B(C_6F_5)_3$. The First Examples of Polymerization of This Class of Electron-Rich Olefins by a Metallocene-like Initiator. Macromolecules 1995, 28, 8021−8027.

(4) (a) Krossing, I.; Reisinger, A. Chemistry with Weakly Coordinating Fluorinated Alkoxyaluminate Anions:Gas Phase Cations in Condensed Phases? Coord. Chem. Rev. 2006, 250, 2721− 2744. (b) Ewart, S. W.; Baird, M. C. Olefin Polymerization by Pentamethylcyclopentadienyl TrimethylTitanium, Cp^*TiMe_3. Top. Catal. 1999, 7, 1−8. (c) Bochmann, M. Kinetic and Mechanistic Aspects of Metallocene Polymerization Catalysts. J. Organomet. Chem. 2004, 689, 3982−3998. (d) Bochmann, M. The Chemistry of Catalyst Activation: The Case of Group 4 Polymerization Catalysts. Organometallics 2010, 29, 4711−4740. (e) Bochmann, M. Highly Electrophilic Organometallics for Carbocationic Polymerizations: From Anion Engineering to New Polymer Materials. Acc. Chem. Res. 2010, 43, 1267−1278. (f) Beck, W.; Sünkel, K. Metal Complexes of Weakly Coordinating Anions. Precursors of Strong Cationic Organometallic Lewis Acids. Chem. Rev. 1988, 88, 1405−1421.

(5) (a) Li, Y.; Cokoja, M.; Kühn, F. E. Inorganic/Organometallic Catalysts and Initiators Involving Weakly Coordinating Anions for Isobutene Polymerization. Coord. Chem. Rev. 2011, 255, 1541−1557. (b) LaPointe, R. E.; Roof, G. R.; Abboud, K. A.; Klosin, J.

New Family of Weakly Coordinating Anions. J. Am. Chem. Soc. 2000, 122, 9560− 9561. (c) Piers, W. E. The Chemistry of Perfluoroaryl Boranes. Adv. Organomet. Chem. 2004, 52, 1−76. (d) Pan, B.; Gabbaï, F. P. $[Sb(C_6F_5)_4][C(C_6F_5)_4]$: An Air Stable, Lewis Acidic Stibonium Salt That Activates Strong Element-Fluorine Bonds. J. Am. Chem. Soc. 2014, 136, 9564−9567. (e) Johnson, A. M.; Contrella, N. D.; Sampson, J. R.; Zheng, M.; Jordan, R. F. Allosteric Effects in Ethylene Polymerization Catalysis. Enhancement of Performance of Phisphine-Phosphinate and Phosphine-Phosphonate Palladium Alkyl Catalysts by Remote Binding of $B(C_6F_5)_3$. Organometallics 2017, 36, 4990− 5002. (f) Bernsdorf, A.; Brand, H.; Hellmann, R.; Köckerling, M.; Schulz, A.; Villinger, A.; Voss, K. Synthesis, Structure, and Bonding of Weakly Coordinating Anions Based on CN Adducts. J. Am. Chem. Soc. 2009, 131, 8958−8970. (g) Lancaster, S. J.; Walker, D. A.; ThorntonPett, M.; Bochmann, M. New Weakly Coordinating Counter Anions for High Activity Polymerization Catalysts: $[(C_6F_5)_3B{-}CN{-}B(C_6F_5)_3]^-$ and $[Ni\{CNB(C_6F_5)_3\}_4]^{2-}$. Chem. Commun. 1999, 1533− 1534. (h) Yin, Q.; Soltani, Y.; Melen, R. L.; Oestreich, M. BAr^{F}_{3}Catalyzed Imine Hydroboration with Pinacolborane Not Requiring the Assistance of an Additional Lewis Base. Organometallics 2017, 36, 2381−2384. (i) Chen, E. Y.-X.; Marks, T. J. Cocatalysts for Metal Catalyzed Olefin Polymerization: Activators, Activation Processes, and Structure-Activity Relationships. Chem. Rev. 2000, 100, 1391− 1434. (j) Ghosh, S. K.; Ojeda, A. S.; Guerrero-Leal, J.; Bhuvanesh, N.; Gladysz, J. A. New Media for Classical Coordination Chemistry: Phase Transfer of Werner and Related Polycations into Highly Nonpolar Fluorous Solvents. Inorg. Chem. 2013, 52, 9369−9378. (k) Riddlestone, I. M.; Kraft, A.; Schaefer, J.; Krossing, I. Taming the Cationic Beast: Novel Developments in the Synthesis and Application of Weakly Coordinating Anions. Angew. Chem., Int. Ed. 2018, 57, 13982−14024. (l) Klikovits, N.; Knaack, P.; Bomze, D.; Krossing, I.; Liska, R. Novel Photoacid Generators for Cationic Photopolymerization. Polym. Chem. 2017, 8, 4414−4421.

(6) (a) Tafazolian, H.; Culver, D. B.; Conley, M. P. A Well-Defined Ni(II) α-Diimine Catalyst Supported on Sulfated Zirconia for Polymerization Catalysis. Organometallics 2017, 36, 2385−2388. (b) Stalzer, M. M.; Delferro, M.; Marks, T. J. Supported Single-Site Organometallic Catalysts for the Synthesis of High-Performance Polyolefins. Catal. Lett. 2015, 145, 3−14. (c) Ahn, H.; Marks, T. J. Supported Organometallics. Highly Electrophilic Cationic Metallocene Hydrogenation and Polymerization Catalysts Formed via Protonolytic Chemisorption on Sulfated Zirconia. J. Am. Chem. Soc. 1998, 120, 13533−13534. (d) Williams, L. A.; Guo, N.; Motta, A.; Delferro, M.; Fragala, I. L.; Miller, J. T.; Marks, T. J. Surface Structure-Chemical Characterization of a Single-Site d^0 Heterogeneous Arene Hydrogenation Catalyst Having 100% Active Sites. Proc. Natl. Acad. Sci. U. S. A. 2013, 110, 413−418.

(7) (a) Weber, S. G.; Zahner, D.; Rominger, F.; Straub, B. F. A Cationic Gold Complex Cleaves $BArF_{24}$. Chem. Commun. 2012, 48, 11325−11327. (b) Salem, H.; Shimon, L. J.

W.; Leitus, G.; Weiner, L.; Milstein, D. B−C Bond Cleavage of BAr$_F$ Anion Upon Oxidation of Rhodium(I) with AgBAr$_F$. Phosphinite Rhodium(I), Rhodium(II), and Rhodium(III) Pincer Complexes. Organometallics 2008, 27, 2293−2299. (c) Konze, W. V.; Scott, B. L.; Kubas, G. J. First Example of B−C Bond Cleavage in the BAr$_F$ ($B[C_6H_3(CF_3)_2\text{-}3,5]_4$) Anion Mediated by a Transition Metal Species, trans-$[(PPh_3)_2Pt(Me)(OEt_2)]^+$. Chem. Commun. 1999, 1807−1808. (d) Bochmann, M.; Sarsfield, M. J. Reaction of AlR_3 with $[CPh_3][B(C_6F_5)_4]$: Facile Degradation of $[B(C_6F_5)_4]^-$ by Transient "$[AlR_2]^+$. Organometallics 1998, 17, 5908−5912.

(8) For a study on borane adducts of water, see: (a) Bergquist, C.; Bridgewater, B. M.; Harlan, C. J.; Norton, J. R.; Friesner, R. A.; Parkin, G. Aqua, Alcohol, and Acetonitrile Adducts of Tris(perfluorophenyl)borane: Evaluation of Brønsted Acidity and Ligand Lability with Experimental and Computational Methods. J. Am. Chem. Soc. 2000, 122, 10581−10590. (b) Danopoulos, A. A.; Galsworthy, J. R.; Green, M. L. H.; Doerrer, L. H.; Cafferkey, S.; Hursthouse, M. Equilibria in the $B(C_6F_5)_3\text{-}H_2O$ System: Synthesis and Crystal Structures of $H_2O{\cdot}B(C_6F_5)_3$ and the Anions $[HOB(C_6F_5)_3]^-$ and $[(F_5C_6)_3B(\mu\text{-}OH){\cdot}B(C_6F_5)_3]^-$. Chem. Commun. 1998, 2529−2560. (c) Doerrer, L. H.; Green, M. L. H. Oxidation of $[M(\eta\text{-}C_5H_5)_2]$, M = Cr, Fe or Co, by the New Brønsted acid $H_2O{\cdot}B(C_6F_5)_3$ Yielding the Salts $[M(\eta\text{-}C_5H_5)_2]^+A^-$, where $A = [(C_6F_5)_3B(\mu\text{-}OH)B(C_6F_5)_3]^-$ or $[(C_6F_5)_3B{\cdots}H_2OB(C_6F_5)_3]$-. J. Chem. Soc., Dalton Trans. 1999, 4325− 4329.

(9) (a) Hewavitharanage, P.; Danilov, E. O.; Neckers, D. C. Pentafluorophenyl Transfer: A New Group-Transfer Reaction in Organoborate Salts. J. Org. Chem. 2005, 70, 10653−10659. (b) Kalamarides, H. A.; Iyer, S.; Lipian, J.; Rhodes, L. F.; Day, C. Pentafluoroaryl Transfer from Tris(pentafluorophenyl)boron Hydrate to Nickel. Synthesis and X-ray Crystal Structure of $(PPh_2CH_2C(O)Ph)Ni(C_6F_5)_2$. Organometallics 2000, 19, 3983−3990.

(10) (a) Beil, S. B.; Mȯhle, S.; Enders, P.; Waldvogel, S. R. Electrochemical Instability of Highly Fluorinated Tetraphenyl Borates and the Synthesis of their Respective Biphenyls. Chem. Commun. 2018, 54, 6128−6131. (b) Lawrence, E. J.; Oganesyan, V. S.; Wildgoose, G. G.; Ashley, A. E. Exploring the Fate of the Tris(Pentafluorophenyl)-Borane Radical Anion in Weakly Coordinating Solvents. Dalton Trans. 2013, 42, 782−789. (c) Ashley, A. E.; Herrington, T. J.; Wildgoose, G. G.; Zaher, H.; Thompson, A. L.; Rees, N. H.; Kramer, T.; Ö ’Hare, D. Separating Electrophilicity and Lewis Acidity: The Synthesis, Characterization, and Electrochemistry of the Electron Deficient Tris(aryl)boranes $B(C_6F_5)_{3\text{-}n}(C_6Cl_5)_n$ (n = 1−3). J. Am. Chem. Soc. 2011, 133, 14727−14740.

(11) Messina, M. S.; Axtell, J. C.; Wang, Y.; Chong, P.; Wixtrom, A. I.; Kirlikovali, K. O.; Upton, B. M.; Hunter, B. M.; Shafaat, O. S.; Khan, S. I.; Winkler, J. R.; Gray, H. B.; Alexandrova, A. N.; Maynard, H. D.; Spokoyny, A. M. Visible-Light-Induced Olefin

Activation Using 3D Aromatic Boron-Rich Cluster Photooxidants. J. Am. Chem. Soc. 2016, 138, 6952−6955.

(12) (a) Gu, X.; Ozerov, O. V. Exhaustive Chlorination of $[B_{12}H_{12}]^{2}$without Chlorine Gas and the Use of $[B_{12}Cl_{12}]^{2-}$ as a Supporting Anion in Catalytic Hydrodefluorination of Aliphatic C−F Bonds. Inorg. Chem. 2011, 50, 2726−2728. (b) Wegener, M.; Huber, F.; Bolli, C.; Jenne, C.; Kirsch, S. F. Silver- Free Activation of Ligated Gold(I) Chlorides: The Use of $[Me_3NB_{12}Cl_{11}]$ as a Weakly Coordinating Anion in Homogeneous Gold Catalysis. Chem. - Eur. J. 2015, 21, 1328−1336. (c) Kessler, M.; Knapp, C.; Zogaj, A. Cationic Dialkyl Metal Compounds of Group 13 Elements (E = Al, Ga, In) Stabilized by the Weakly Coordinating Dianion, $[B_{12}Cl_{12}]^{2-}$. Organometallics 2011, 30, 3786−3792. (d) Axtell, J. C.; Saleh, L. M. A.; Qian, E. A.; Wixtrom, A. I.; Spokoyny, A. M. Synthesis and Applications of Perfunctionalized Boron Clusters. Inorg. Chem. 2018, 57, 2333−2350.

(13) (a) Strauss, S. H. The Search for Larger and More Weakly Coordinating Anions. Chem. Rev. 1993, 93, 927−942. (b) Reed, C. A. Carboranes: A New Class of Weakly Coordinating Anions for Strong Electrophiles, Oxidants, and Superacids. Acc. Chem. Res. 1998, 31, 133−139. (c) Douvris, C.; Michl, J. Update 1 of: Chemistry of the Carba-closo-dodecaborate(−) Anion, $CB_{11}H_{12}$-. Chem. Rev. 2013, 113, PR179−PR233. (d) Douvris, C.; Ozerov, O. V. Hydrodefluorination of Perfluoroalkyl Groups Using Silylium-Carborane Catalysts. Science 2008, 321, 1188−1190. (e) Nava, M. J.; Reed, C. A. High Yield CDerivatization of Weakly Coordinating Carborane Anions. Inorg. Chem. 2010, 49, 4726−4728. (f) Dziedzic, R. M.; Waddington, M. A.; Lee, S. E.; Kleinsasser, J.; Plumley, J. B.; Ewing, W. C.; Bosley, B. D.; Lavallo, V.; Peng, T. L.; Spokoyny, A. M. Reversible Silver Electrodeposition from Boron Cluster Ionic Liquid (BCIL) Electrolytes. ACS Appl. Mater. Interfaces 2018, 10, 6825−6830. (g) Krossing, I.; Raabe, I. Noncoordinating Anions − Fact or Fiction? A Survey of Likely Candidates. Angew. Chem., Int. Ed. 2004, 43, 2066−2090. (h) Reed, C. A. H^+, CH_3^+, and R_3Si^+ Carborane Reagents: When Triflates Fail. Acc. Chem. Res. 2010, 43, 121−128. (i) Kitazawa, Y.; Takita, R.; Yoshida, K.; Muranaka, A.; Matsubara, S.; Uchiyama, M. Naked" Lithium Cation: Strongly Activated Metal Cations Facilitated by Carborane Anions. J. Org. Chem. 2017, 82, 1931−1935. (j) Ivanov, S. V.; Peryshkov, D. V.; Miller, S. M.; Anderson, O. P.; Rappe, A. K.; Strauss, S. H. Synthesis, Structure, and Reactivity of $AlMe_2(1\text{-}Me\text{-}CB_{11}F_{11})$: An $AlMe_2^+$ Cation-like Species Bonded to a Superweak Anion. J. Fluorine Chem. 2012, 143, 99−102. (k) Fisher, S. P.; Tomich, A. W.; Lovera, S. O.; Kleinsasser, J. F.; Guo, J.; Asay, M. J.; Nelson, H. M.; Lavallo, V. Nonclassical Applications of closoCarborane Anions: From Main Group Chemistry and Catalysis to Energy Storage. Chem. Rev. 2019, DOI: 10.1021/acs.chemrev.8b00551.

(14) (a) Popov, S.; Shao, B.; Bagdasarian, A. L.; Benton, T. R.; Zou, L.; Yang, Z.; Houk, K. N.; Nelson, H. M. Teaching an Old Carbocation New Tricks: Intermolecular C−H Insertion

Reactions of Vinyl Cations. Science 2018, 361, 381−387. (b) Shao, B.; Bagdasarian, A. L.; Popov, S.; Nelson, H. M. Arylation of Hydrocarbons Enabled by Organosilicon Reagents and Weakly Coordinating Anions. Science 2017, 355, 1403−1407.

(15) Wixtrom, A. I.; Shao, Y.; Jung, D.; Machan, C. W.; Kevork, S. N.; Qian, E. A.; Axtell, J. C.; Khan, S. I.; Kubiak, C. P.; Spokoyny, A. M. Rapid Synthesis of Redox-Active Dodecaborane $B_{12}(OR)_{12}$ Clusters under Ambient Conditions. Inorg. Chem. Front. 2016, 3, 711−717.

(16) Aubry, T. J.; Axtell, J. C.; Basile, V. M.; Winchell, K. J.; Lindemuth, J. R.; Porter, T. M.; Liu, J.-Y.; Alexandrova, A. N.; Kubiak, C. P.; Tolbert, S. H.; Spokoyny, A. M.; Schwartz, B. J. DodecaboraneBased Dopants Designed to Shield Anion Electrostatics Lead to Increased Carrier Capacity in a Doped Conjugated Polymer. Adv. Mater. 2019, 31, 1805647.

(17) (a) Goeltz, J. C.; Hanson, C. J.; Kubiak, C. P. Rates of Electron Self-Exchange Reactions between Oxo-Centered Ruthenium Clusters Are Determined by Orbital Overlap. Inorg. Chem. 2009, 48, 4763− 4767. (b) Goeltz, J. C.; Benson, E. E.; Kubiak, C. P. Electronic Structural Effects in Self-Exchange Reactions. J. Phys. Chem. B 2010, 114, 14729−14734. (c) Porter, T. M.; Canzi, G. C.; Chabolla, S. A.; Kubiak, C. P. Tuning Electron Delocalization and Transfer Rates in Mixed-Valent Ru3O Complexes through “Push−Pull” Effects. J. Phys. Chem. A 2016, 120, 6309−6316.

(18) (a) Kanazawa, A.; Shibutani, S.; Yoshinari, N.; Konno, T.; Kanaoka, S.; Aoshima, S. Structure Effects of Lewis Acids on the Living Cationic Polymerization of p-Methoxystyrene: Distinct Difference in Polymerization Behavior from Vinyl Ethers. Macromolecules 2012, 45, 7749−7757. Note: Initial studies revealed that the polymerizations proceeded in the presence of atmospheric oxygen as well as radical traps (see ref 11). Inhibition of S5 polymerization by 1 in the presence of 2,6-$^tBu_2$-C_5H_3N was also observed, indicating the importance of H^+ in chain termination/reinitiation, which is common in uncontrolled carbocationic polymerizations. In addition, the cationic polymerization originating from cation radicals has been studied. For example, see: (b) Pilar, J.; Marek, M.; Toman, L. The Formation of Radical Cations of Styrene and α-Methylstyrene in the Irradiation of Mixtures of These Monomers with $TiCl_4$ and $SnCl_4$ in a Semicrystalline Heptane Matrix. J. Polym. Sci., Polym. Chem. Ed. 1980, 18, 3193−3197. (c) Akbulut, U.; Fernandez, J. E.; Birke, R. L. Electroinitiated Cationic Polymerization of Styrene by Direct Electron Transfer. J. Polym. Sci., Polym. Chem. Ed. 1975, 13, 133−149. (d) Sparapany, J. J. Ion−Molecule Reactions in Liquid Hydrocarbons via Photoionization with Vacuum Ultraviolet Radiation. The Polymerization of Isobutene. J. Am. Chem. Soc. 1966, 88, 1357− 1362. (e) Michaudel, Q.; Kottisch, V.; Fors, B. P. Cationic

Polymerization: From Photoinitiation to Photocontrol. Angew. Chem., Int. Ed. 2017, 56, 9670−9679.

(19) Hansch, C.; Leo, A.; Taft, R. W. A Survey of Hammett Substituent Constants and Resonance and Field Parameters. Chem. Rev. 1991, 91, 165−195.

(20) Wenger, O. S.; Leigh, B. S.; Villahermosa, R. M.; Gray, H. B.; Winkler, J. R. Electron Tunneling Through Organic Molecules in Frozen Glasses. Science 2005, 307, 99−102.

(21) Boeré, R. T.; Derendorf, J.; Jenne, C.; Kacprzak, S.; Keßler, M.; Riebau, R.; Riedel, S.; Roemmele, T. L.; Rühle, M.; Scherer, H.; VentSchmidt, T.; Warneke, J.; Weber, S. On the Oxidation of the Three-Dimensional Aromatics $[B_{12}X_{12}]^{2-}$ (X = F, Cl, Br, I). Chem. - Eur. J. 2014, 20, 4447−4459.

(22) Yamamoto, Y.; Irie, M.; Hayashi, K. Photoinduced Ionic Polymerization. VI. Molecular Weight Distribution in Cationic Polymerization of a-Methystyrene. Polym. J. 1976, 8, 437−441.

(23) Vierle, M.; Zhang, Y.; Santos, A. M.; Köhler, K.; Haeßner, C.; Herdtweck, E.; Bohnenpoll, M.; Nuyken, O.; Kühn, F. E. SolventLigated Manganese(II) Complexes for the Homopolymerization of Isobutene and the Copolymerization of Isobutene and Isoprene. Chem. - Eur. J. 2004, 10, 6323−6332.

(24) Reichardt, C. Solvatochromic Dyes as Solvent Polarity Indicators. Chem. Rev. 1994, 94, 2319−2358.

(25) (a) Suzuki, M.; Yamamoto, Y.; Irie, M.; Hayashi, K. Polymerization of Styrene Initiated By Photoexcited Charge-Transfer Complex. J. Macromol. Sci., Chem. 1976, 10, 1607−1622. (b) Pernecker, T.; Kennedy, J. P. Living Carbocationic Polymerization. XLVI. Living Isobutylene Polymerization Induced by the Common Ion Effect. Polym. Bull. 1991, 26, 305−312.

(26) (a) Lenz, R. W.; Faullimel, J. G.; Jonte, J. M.; Fisher, D. J. Characterization of the Active Centers in the Cationic Polymerization of p-Substituted α-Methylstyrenes. Makromol. Chem., Macromol. Symp. 1988, 13-14, 255−269. (b) Lenz, R. W.; Fisher, D. J.; Jonte, J. M. Cationic Polymerization of Para-Substituted α-Methylstyrenes. 6. Solvent Polarity Effects on Polymer Tacticity. Macromolecules 1985, 18, 1659−1663.

(27) Lewis, M.; Bagwill, C.; Hardebeck, L. K. E.; Wireduaah, S. The Use of Hammett Constants to Understand the Non-Covalent Binding of Aromatics. Comput. Struct. Biotechnol. J. 2012, 1, e201204004.

(28) Meyer, E. A.; Castellano, R. K.; Diederich, F. Interactions with Aromatic Rings in Chemical and Biological Recognition. Angew. Chem., Int. Ed. 2003, 42, 1210−1250.

(29) (a) Shao, S.; Hu, J.; Wang, X.; Wang, L.; Jing, X.; Wang, F. Blue Thermally Activated Delayed Fluorescence Polymers with Nonconjugated Backbone and Through-Space Charge Transfer Effect. J. Am. Chem. Soc. 2017, 139, 17739−17742. (b) Sun, L.; Campbell, M. G.; Dinca, M. Electrically Conductive Porous Metal-Organic Frameworks. Angew. Chem., Int. Ed. 2016, 55, 3566−3579. (c) Yao, Z.-F.; Wang, J.-Y.; Pei, J. Control of π−π Stacking via Crystal Engineering in Organic Conjugated Small Molecule Crystals. Cryst. Growth Des. 2018, 18, 7−15.

(30) (a) Cozzi, F.; Ponzini, F.; Annunziata, R.; Cinquini, M.; Siegel, J. S. Polar Interactions between Stacked π Systems in Fluorinated 1,8Diarylnaphthalenes: Importance of Quadrupole Moments in Molecular Recognition. Angew. Chem., Int. Ed. Engl. 1995, 34, 1019−1020. (b) Salonen, L. M.; Ellermann, M.; Diederich, F. Aromatic Rings in Chemical and Biological Recognition: Energetics and Structures. Angew. Chem., Int. Ed. 2011, 50, 4808−4842.

(31) (a) Patrick, C. R.; Prosser, G. S. A Molecular Complex of Benzene and Hexafluorobenzene. Nature 1960, 187, 1021. (b) Burley, S. K.; Petsko, G. A. Aromatic-Aromatic Interaction: A Mechanism of Protein Structure Stabilization. Science 1985, 229, 23−28. (c) Pace, C. J.; Gao, J. Exploring and Exploiting Polar−π Interactions with Polar Aromatic Amino Acids. Acc. Chem. Res. 2013, 46, 907−915.

(32) (a) Coates, G. W.; Dunn, A. R.; Henling, L. M.; Dougherty, D. A.; Grubbs, R. H. Phenyl−Pentafluorophenyl Stacking Interactions: A New Strategy for Supermolecule Construction. Angew. Chem., Int. Ed. Engl. 1997, 36, 248−251. (b) Senaweera, S.; Weaver, J. D. S_NAr Catalysis Enhanced by an Aromatic Donor-Acceptor Interaction; Facile Access to Chlorinated Polyfluoroarenes. Chem. Commun. 2017, 53, 7545−7548.

(33) (a) Williams, J. H.; Cockcroft, J. K.; Fitch, A. N. Structure of the Lowest Temperature Phase of the Solid Benzene−Hexafluorobenzene Adduct. Angew. Chem., Int. Ed. Engl. 1992, 31, 1655−1657. (b) Martinez, C. R.; Iverson, B. L. Rethinking the Term "Pi-Stacking. Chem. Sci. 2012, 3, 2191−2201. (c) Grimme, S. Do Special Noncovalent π−π Stacking Interactions Really Exist? Angew. Chem., Int. Ed. 2008, 47, 3430−3434.

(34) (a) Ringer, A. L.; Sherrill, C. D. Substituents Effects in Sandwich Configurations of Multiply Substituted Benzene Dimers Are Not Solely Governed by Electrostatic Control. J. Am. Chem. Soc. 2009, 131, 4574−4575. (b) Meyer, E. A.; Castellano, R. K.; Diederich, F. Interactions with Aromatic Rings in Chemical and Biological Recognition. Angew. Chem., Int. Ed. 2003, 42, 1210−1250. (c) Hunter, C. A.; Sanders, J. K. M. The Nature of π−π Interactions. J. Am. Chem. Soc. 1990, 112, 5525−5534. (d) Hwang, J. w.; Li, P.;

Shimizu, K. D. Synergy Between Experimental and Computational Studies of Aromatic Stacking Interactions. Org. Biomol. Chem. 2017, 15, 1554−1564.

(35) Cockroft, S. L.; Hunter, C. A.; Lawson, K. R.; Perkins, J.; Urch, C. J. Electrostatic Control of Aromatic Stacking Interactions. J. Am. Chem. Soc. 2005, 127, 8594−8595.

(36) (a) Gung, B. W.; Patel, M.; Xue, X. A Threshold for Charge Transfer in Aromatic Interactions? A Quantitative Study of π-Stacking Interactions. J. Org. Chem. 2005, 70, 10532−10537. (b) Gung, B. W.; Amicangelo, J. C. Substituent Effects in C_6F_6-C_6H_5X Stacking Interactions. J. Org. Chem. 2006, 71, 9261−9270.

(37) (a) Ringer, A. L.; Sinnokrot, M. O.; Lively, R. P.; Sherrill, C. D. The Effect of Multiple Substituents on Sandwich and T-Shaped π-π Interactions. Chem. - Eur. J. 2006, 12, 3821−3828. (b) Sinnokrot, M. O.; Sherrill, C. D. Unexpected Substituent Effects in Face-to-Face πStacking Interactions. J. Phys. Chem. A 2003, 107, 8377−8379.

(38) (a) Smithrud, D. B.; Diederich, F. Strength of Molecular Complexation of Apolar Solutes in water and in Organic Solvents Is Predictable by Linear Free Energy Relationships: A General Model for Solvation Effects on Apolar Binding. J. Am. Chem. Soc. 1990, 112, 339−343. (b) Chapman, K. T.; Still, W. C. A Remarkable Effect of Solvent Size on the Stability of a Molecular Complex. J. Am. Chem. Soc. 1989, 111, 3075−3077. (c) Canceill, J.; Lacombe, L.; Collet, A. A New Cryptophane Forming Unusually Stable Inclusion Complexes with Neutral Guests in a Lipophilic Solvent. J. Am. Chem. Soc. 1986, 108, 4230−4232.

(39) Muchowska, K. B.; Adam, C.; Mati, I. K.; Cockroft, S. L. Electrostatic Modulation of Aromatic Rings via Explicit Solvation of Substituents. J. Am. Chem. Soc. 2013, 135, 9976−9979.

(40) For additional discussions of intermolecular aromatic interactions, see: (a) Sinnokrot, M. O.; Sherrill, C. D. Substituent Effects in π−π Interactions: Sandwich and T-Shaped Configurations. J. Am. Chem. Soc. 2004, 126, 7690−7697. (b) Paliwal, S.; Geib, S.; Wilcox, C. S. Molecular Torsion Balance for Weak Molecular Recognition Forces. Effects of "Tilted-T" Edge-to-Face Aromatic Interactions on Conformational Selection and Solid-State Structure. J. Am. J. Am. Chem. Soc. 1994, 116, 4497−4498. (c) Kim, E.-I.; Paliwal, S.; Wilcox, C. S. Measurements of Molecular Electrostatic Field Effects in Edge-to-Face Aromatic Interactions and CH-π Interactions with implications for Protein Folding and Molecular Recognition. J. Am. Chem. Soc. 1998, 120, 11192−11193. (d) Nishio, M.; Umezawa, Y.; Hirota, M.; Takeuchi, Y. The CH/π Interaction: Significance in Molecular Recognition. Tetrahedron 1995, 51, 8665−8701. (e) Yang, L.; Adam, C.; Nichol, G. S.; Cockroft, S. L. How Much do van der Waal Dispersion Forces Contribute to Molecular Recognition in Solution? Nat. Chem. 2013, 5, 1006−1010. (f) Cockroft, S.

L.; Hunter, C. A. Desolvation Tips the Balance: Solvent Effects on Aromatic Interactions. Chem. Commun. 2006, 3806−3808.

(41) (a) Nagy, A.; Majoros, I.; Kennedy, J. P. Living Carbocationic Polymerization. LXII. Living Polymerization of Styrene, p-Methylstyrene and p-Chlorostyrene Induced by the Common Ion Effect. J. Polym. Sci., Part A: Polym. Chem. 1997, 35, 3341−3347. (b) Higashimura, T.; Ishihama, Y.; Sawamoto, M. Living Cationic Polymerization of Styrene: New Initiating Systems Based on Added Halide Salts and the Nature of the Growing Species. Macromolecules 1993, 26, 744−751.

(42) Higashimura, T.; Aoshima, S.; Sawamoto, M. New Initiators for Living Cationic Polymerization of Vinyl Compounds. Makromol. Chem., Macromol. Symp. 1988, 13-14, 457−471.

(43) (a) Nishida, H.; Takada, N.; Yoshimura, M.; Sonoda, T.; Kobayashi, H. Tetrakis[3,5-bis(trifluoromethyl)phenyl]borate. Highly Lipophilic Stable Anionic Agent for Solvent-extraction of Cations. Bull. Chem. Soc. Jpn. 1984, 57, 2600−2604. (b) Hill, M. G.; Lamanna, W. M.; Mann, K. R. Tetrabutylammonium Tetrakis[3,5-bis(trifluoromethyl)phenyl]borate as a Noncoordinating Electrolyte: Reversible 1e$^-$ Oxidations of Ruthenocene, Osmocene, and $Rh_2(TM4)_4^{2+}$ (TM4 = 2,5-Diisocyano-2,5-dimethylhexane). Inorg. Chem. 1991, 30, 4687−4690.

(44) Overberger, C. G.; Newton, M. G. Ionic Polymerization. XV. Further Molecular Terminating Agents in the Cationic Polymerization of Styrene. J. Am. Chem. Soc. 1960, 82, 3622−3626.

(45) (a) Prier, C. K.; Rankic, D. A.; MacMillan, D. W. C. Visible Light Photoredox Catalysis with Transition Metal Complexes: Applications in Organic Synthesis. Chem. Rev. 2013, 113, 5322− 5363. (b) Narayanam, J. M. R.; Stephenson, C. R. J. Visible Light Photoredox Catalysis: Applications in Organic Synthesis. Chem. Soc. Rev. 2011, 40, 102−113. (c) Du, Y.; Pearson, R. M.; Lim, C. H.; Sartor, S. M.; Ryan, M. D.; Yang, H.; Damrauer, N. H.; Miyake, G. M. Srongly Reducing Visible Light Organic Photoredox Catalysts as Sustainable Alternatives to Precious Metals. Chem. - Eur. J. 2017, 23, 10962−10968.

(46) (a) Wixtrom, A. I.; Parvez, Z.; Savage, M. A.; Qian, E. A.; Jung, D.; Khan, S. I.; Rheingold, A. L.; Spokoyny, A. M. Tuning the Electrochemical Potential of Perfunctionalized Dodecaborate Clusters Through Vertex Differentiation. Chem. Commun. 2018, 54, 5867− 5870. (b) Axtell, J. C.; Kirlikovali, K. O.; Jung, D.; Dziedzic, R. M.; Rheingold, A. L.; Spokoyny, A. M. Metal-Free Peralkylation of the closo-Hexaborate Anion. Organometallics 2017, 36, 1204−1210.

(47) Jung, D.; Saleh, L. M. A.; Berkson, Z. J.; El-Kady, M. F.; Hwang, J. Y.; Mohamed, N.; Wixtrom, A. I.; Titarenko, E.; Shao, Y.; McCarthy, K.; Guo, J.; Martini, I. B.; Kraemer, S.; Wegener, E. C.; Saint-Cricq, P.; Ruehle, B.; Langeslay, R. R.; Delferro, M.; Brosmer, J. L.; Hendon, C. H.; Gallagher-Jones, M.; Rodriguez, J.; Chapman, K. W.; Miller, J. T.; Duan, X.; Kaner, R. B.; Zink, J. I.; Chmelka, B. F.; Spokoyny, A. M. A Molecular Cross-Linking Approach for Hydrid Metal Oxides. Nat. Mater. 2018, 17, 341−348.